Structure Engineering of Self- and Directed-Assembled conjugated polymers

Yuyin Xi

A dissertation

submitted in partial fulfillment of the

requirements for the degree of

Doctor of Philosophy

University of Washington

2018

Reading Committee:

Lilo D. Pozzo, Chair

Christine K. Luscombe

Stuart Adler

Program Authorized to Offer Degree:
Chemical Engineering

University of Washington

Abstract

Structure Engineering of Self- and Directed-Assembled conjugated polymers

Yuyin Xi

Chair of the Supervisory Committee:
Associate Professor Lilo D. Pozzo

Department of Chemical Engineering

Due to their unique electrical, optical and mechanical properties, conjugated polymers are promising candidates for a variety of devices, including transistors, optoelectronics, sensors, batteries, memories, spintronics and bioelectronics. However, further development of those applications calls for effective charge transport of conjugated polymers. Engineering their assembly to form ordered structures is key to enhancing the electrical properties. In this dissertation, external electric and acoustic fields have been demonstrated to effectively direct polymer assembly into fibers and the addition of polar poor solvents can self-assemble donor-acceptor conjugated polymers into nanoribbons with long-range order. To form detailed correlations between external controllable variables and the resulted nanostructures, a systematic

investigation on the effects of tuning electric field frequency and amplitude, acoustic field peak negative pressure, as well as poor solvent polarity, is performed. Structure-property relationships are formed and mechanistic discussions on directed- and self- assembly are presented. Different polymers are explored to form general molecular design guidelines that can be beneficial to structure manipulation. This work provides insights into engineering structures for enhanced charge transport by controlling the assembly of conjugated polymers.

TABLE OF CONTENTS

LIST OF FIGURES

LIST OF TABLES

ACKNOWLEDGEMENTS

I appreciate the guidance and support from my advisor, Prof. Lilo D. Pozzo. Thanks for being such a great mentor to always keep me on track in research. She always has time to stop by in the lab to give valuable comments on experimental results and foresees promising directions. Her passion in science encourages me to keep going.

I feel blessed to be a member of a group of talented people. I'd like to thank Dr. Greg M. Newbloom and Dr. Jeff J. Richards for valuable inputs for my experiments during the past five years. Specially, many thanks go to Dr. Pablo de la Iglesia, who is being really patient to me and introduced me to the world of board games. I also appreciate the support from Dr. David S. Li and Caitlyn M. Wolf for being my "Accountabilabuddies". Thanks to the rest of the group members, Dr. Kathlene Weigandt, Kiran Kanekal, Jaime Rodrigues, Yi-Ting Lee, Ryan Katilani, and Kacper Lachowski. They make this journey lovely and enjoyable. In addition, Thanks Dr. Shuang Li from Prof. Guozhong Cao's group for training me on solid state battery assembly and testing. I would also like to thank the endless help I received from instrument scientists at NIST, Dr. Paul Butler and Dr. Yun Liu.

I am lucky to be guided by my previous research advisor, Dr. Fan Ren, who helps me build a lot of good habits and gets me started in research. My forever friends, Dr. Lu Liu and Dr. Shu Shang for sharing happiness and sorrow together with me. Specially, Dr. Lu Liu provided me with a lot of valuable life advices.

Finally, I acknowledge the primary financial support from Department of Energy, Office of Basic Energy Sciences under award number DE-SC0010282. I also thank a fellowship and several travel

grants I received from Clean Energy Institute in the University of Washington. I appreciate the financial support from Polydrop during the first year of my research.

DEDICATION

To my parents, Tongxiang Xi and Rongying Xi, for never giving up on me.

And to my fiancée, Lei Lei, for her unwavering support.

Chapter 1. Introduction & Motivation

Materials have always been of vital importance during the human evolution history from prehistory to nowadays, since it influences both the cognitive and cultural aspects of mankind. [1] In ancient times, the usage of stone and wood (100,000 B.C.), bronze (3000 B.C.), and iron (1000 B.C.) marked the start of each period of the three-age-system. [1] The choice of different materials not only changes the way people farm, but also affects how people fight wars. [2] More recently, the discovery of silicon as semiconducting material (1950 s') gave birth to the so-called "Computer age", which greatly changed the way people live. [1,3] It has been reported that until 2007, more than 94% of the telecommunication and memory are based on digital technologies. [3] During the past two decades, material development is greatly emphasized in science. The emergence of a new material is always associated with many advanced technologies. Three Nobel Prizes were awarded to the discovery of new materials such as fullerenes (1996), conductive polymers (2000), and graphene (2010). [4] It is interesting to note that both fullerenes and graphene are consisting of merely carbon atoms, but atoms are organized to spheres in fullerenes, whereas graphene is a thin sheet of ordered covalently bonded carbons. The final molecule shape determines their properties, as well as their applications. Spherical fullerenes are often used as acceptors due to its specific energy state for organic photovoltaics (OPVs). [5] The excellent electronic properties of thin sheet graphene is often utilized for applications such as transistors, electrodes, or sensors. [6] Another interesting shape in the carbon allotropes family is nanotubes (CNTs). On top of the electronic properties, CNTs also exhibited extraordinary mechanical strength, whose measured modulus of a single tube is more than 10 times higher than any fibers produced in industry. [7]

Similar to that molecular shape determines its properties, the nano- and micro-structures (larger structures) formed by ordering molecules also plays a decisive role in affecting their final properties. Ways to assemble molecules into larger structures with different shapes, various sizes, and diverse patterns have been greatly focused for realizing practical devices in the macroscopic scale and improving their performances. For example, people have been studying on ordering fullerene spheres into nanoribbons or nanofibers to enhance the charge transport mobility and at the same time maintain high surface area. [8,9] In order to enhance the mechanical and electrical properties, CNTs have been aligned to sheet form or prepared to rope structures. [10] At the same time, the relatively large structures formed by molecules can even lead to new applications. The arrangement of CNTs into certain order can also realize stimuli responsive properties, such as electrochromatism and photo-induced deformation. [10–12] The alignment of graphene by magnetic field lead to anisotropic optical properties and the self-alignment of graphene oxide results in excellent efficiency of electromagnetic interface (EMI) shielding. [13,14]

This chapter starts with the discussion of the strong correlation between structures and properties, followed by typical ways of forming assembled structures, including self- and direct- assembly. What is more, the importance of nano- and macro- structures formed by conjugated polymers and their properties will be discussed.

1.1 SELF- AND DIRECTED-ASSEMBLY

People have devoted a lot of efforts to come up with numerous brilliant ideas to manipulate the structures of materials to achieve desired functions. One of an interesting example comes to poly (vinylidene fluoride) (PVDF), a common piezoelectric material that converts mechanical energy (pressure) to electrical signal. By simply produce the materials in webs consisting nanofibers

through electrospinning, the sensitivity to both audible sound pressure level and frequencies have been greatly enhanced. [15] The unidirectional aligned PVDF nanofibers can otherwise enable the applications for energy generators or wearable sensors for detecting bending. [16,17]

In order to generate different kinds of structures of various material systems, many techniques can be used, including electrospinning, etching, chemical vapor deposition (CVD), nanoimprint, crystallization, and electrostatic assembly. [15,18–21,22,23] Typically, those techniques can be classified into two approaches: bottom-up and top-down method. The top-down method always starts with bulk material and walks its way down to the final forms using techniques like etching and milling. [22,23] A typical example of using top-down approach is the photolithography process in semiconductor fabrication industry. The photoresist (PR) is usually coated on wafer scale and a PR removal procedure results in certain patterns. [23] In contrast, the bottom-up approach refers to a process that assembles smaller pieces together to form larger structures. [23,24] Conjugated polymers are often used through solution process, which requires the dissolution of the polymers first, so it usually utilizes a bottom-up approach. [24] Compared to top-down methods, the bottom-up approach has better control of the small size features in nanometer scales. [23]

The assembly of molecules through bottom-up approach have two basic strategies: self-assembly and directed-assembly. Self-assembly is a spontaneous process of forming nanoparticles or large colloidal aggregates with molecules. [25] The self-assembly of monolayer of molecules has been used to modify the surface energy of silicon dioxide and subsequent deposited film morphology for organic field effect transistor fabrication (OFETs). [26] Self-assembly is also used to obtain different structures of the material to achieve certain functions. For example, it is used to induce crystallization of conjugated polymers in solutions to enhance charge transport.[27] The supersaturation in solutions could drive polymers to form colloidal network or organogels,

depending on the polymer concentrations. [27–30] The supersaturation can simply be tuned by temperatures, polymer concentrations, and solvent qualities. [31] In chapter 5, the self-assembly of a high mobility conjugated polymer to form nanoribbons will be discussed. In contrast, the directed-assembly requires energy input from external sources. [25] The external fields can be electric, shear, capillary or acoustic field. [31,32,33,34] Based on the interactions of the external fields to the systems, it can provide guidance to the system to form anisotropic structures (electric, shear, capillary forces), which can be useful for optical and electrical applications. It is also possible that the external fields provide the energy to overcome energy barrier and accelerate the assembly process (electric and acoustic fields). In Chapter 3, the electric field on the alignment of conjugated polymer system will be discussed and the acoustic field in the acceleration of crystallization of polymers will be presented in Chapter 4.

1.2 THE IMPORTANCE OF NANOSTRUCTURES IN CONJUGATED POLYMERS

The discovery and development of conjugated polymers (CPs) was awarded the Nobel prize in 2000.[4] The conductive nature combined with the unique properties, i.e. flexibility, light weight, low cost, and large scale processability make them perfect candidates for organic electronics, such as organic photovoltaics (OPVs), organic light emitting diodes (OLEDs), and organic field effect transistors (OFETs). [5,31,32] However, the charge transport has always been a problem, since CPs have multiple degrees of freedom and complex structures can be formed during the fabrication process. [35] Figure 1.1 shows molecular structure of a typical conjugated polymer: poly(3-hexylthiophene) (P3HT). The alkyl side chain is electrically insulating and the backbone allows delocalization of charges. It is a fast process to conduct charge along the polymer chains, but it is a slow process to hop from chain to chain. [35] The contour length of conjugated polymers are usually on the order of sub-100 nm, which is several orders of magnitude shorter than the useful distance

for practical applications. [36] In order to achieve efficient charge transport, effective interchain charge transport is required. Fortunately, conjugated polymers can form crystalline domains that substantially extends the charge transport distances. Moreover, the crystallization of conjugated polymers can be easily manipulated by self-assembly or directed-assembly techniques during solution process. It is thus important to induce crystallization through π-π stacking to achieve fast interchain transport through π orbital overlapping. This requires the assembly of polymer chains into larger ordered structures. The previous work in our group has demonstrated effective charge transport through an engineered fibril network and enhanced hole mobility has been observed long the conjugated polymer fiber direction. [27,29,30,37,32] Through directed-assembly, the anisotropic structures formed by conjugated polymers could also induce optical properties at the same time. The uni-directionally aligned conjugated polymers have been utilized to make polarized photovoltaics for harvesting energies from liquid crystal displays. [38]

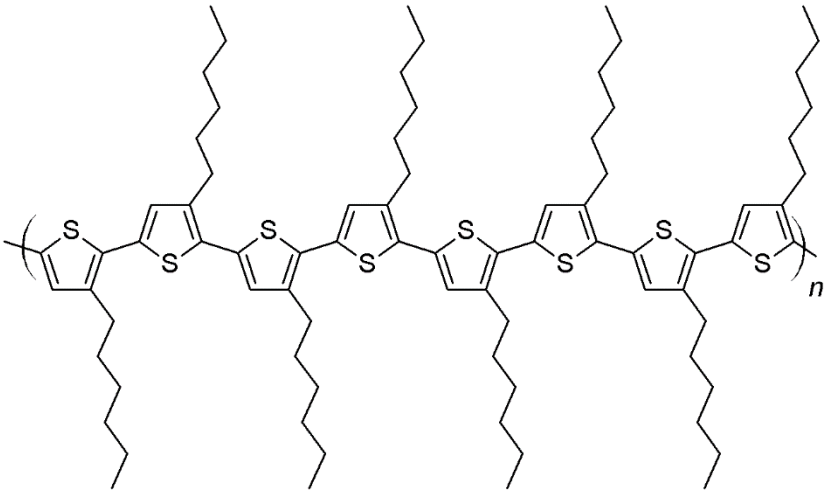

Figure 1.1. Molecular structure of poly (3-hexylthiophene)

1.3 TYPES OF NANOSTRUCTURES FORMED BY ASSEMBLY

Small molecules can be assembled into large structures with various shapes by self- and directed-assembly to achieve certain functions. Based on the work the author has conducted so far, various structures whose dimensionality ranging from 1-dimentional to 3-dimentional can be formed using assembly, including nanofibers, nanoribbons, nanosheets, spheres, and spherulites. Figure 1.2 shows the electron microscopic images of the different structures formed by conductive polymers or fullerenes. Different shapes are suitable for different applications. For conjugated polymers, the assembly into nanofibers or nanoribbons are desired, as the π-π stacking allows long-range charge transport. Also, nanofibers and nanoribbons both possess high aspect ratio structure, as well as a huge surface area, which is beneficial for organic photovoltaics (OPVs), since the large surface area is useful for effective exciton dissociation. Meanwhile, the aligned anisotropic structures can be used to achieve unique optical (polarizer) properties. For phenyl-C61-butyric acid methyl ester (PCBM), the spherical molecules are engineered to form sheets through a reprecipitation process. [8] The assembled structure can facilitate charge transport and at the same time on similar size range of exciton dissociation. [8] Other than the above structures, conjugated polymers with different side chains could result in completely different structures. For regio-random P3HT, they can aggregate into spherical clusters after solution evaporation and poly(3,3’’’-diakylquarterthiophene) (PQT-12) could result in spherulites structures. Consequently, it is crucial to control the assemble structures in multi-length scales through engineering processing conditions.

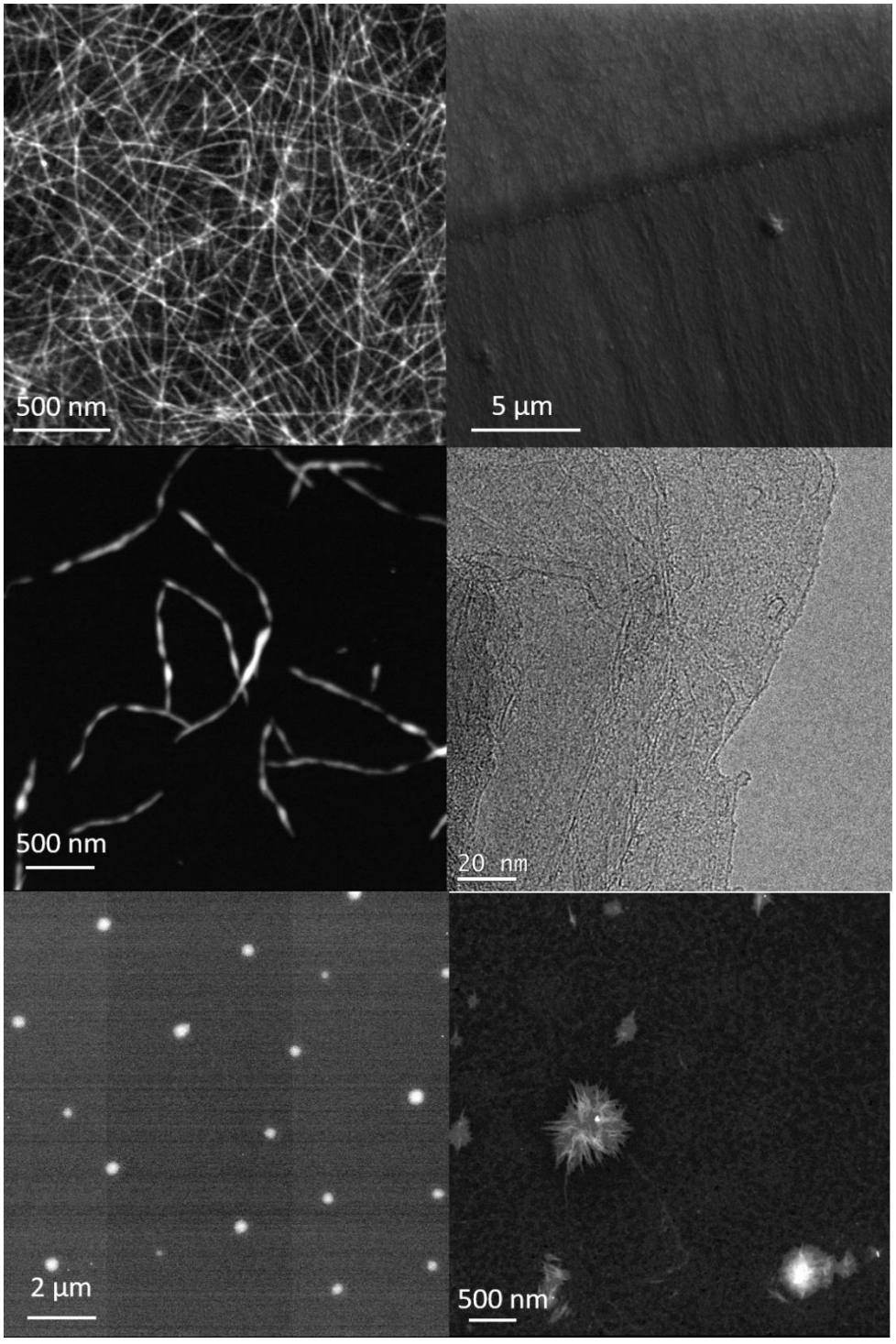

Figure 1.2. (a) sTEM image of P3HT nanofibers and (b) SEM image of aligned P3HT fiber bundles. (c) sTEM image of nanoribbons formed by PCDTPT. (d) TEM image of nanosheets formed by PCBM and (e) sTEM image of spherical aggregates formed by regiorandom P3HT (f) spherulites formed by PQT-12.

1.4 REFERENCES

(1) Herrmann, B. W. A. Review New Materials ± The Potential of Modern Synthetic Chemistry *. **1998**, 549–558 DOI: 10.1002.

(2) Whipps, H. How the iron age changed the world https://www.livescience.com/2339-iron-age-changed-world.html.

(3) Hilbert, M.; Lopez, P. The World's Technological Capacity to Store, Communicate, and Compute Information. *Science (80-.).* **2011**, *332* (6025), 60–65 DOI: 10.1126/science.1200970.

(4) No Title https://www.nobelprize.org/.

(5) Sulas, D. B.; Yao, K.; Intemann, J. J.; Williams, S. T.; Li, C.-Z.; Chueh, C.-C.; Richards, J. J.; Xi, Y.; Pozzo, L. D.; Schlenker, C. W.; Jen, A. K.-Y.; Ginger, D. S. Open-Circuit Voltage Losses in Selenium-Substituted Organic Photovoltaic Devices from Increased Density of Charge-Transfer States. *Chem. Mater.* **2015**, *27* (19), 6583–6591 DOI: 10.1021/acs.chemmater.5b02133.

(6) Allen, M. J.; Tung, V. C.; Kaner, R. B. Honeycomb Carbon: A Review of Graphene. *Chem. Rev.* **2010**, *110* (1), 132–145 DOI: 10.1021/cr900070d.

(7) Volder, M. F. L. De; De Volder, M. F. L.; Tawfick, S. H.; Baughman, R. H.; Hart, a. J. Carbon Nanotubes: Present and Future Commercial Applications. *Science (80-.).* **2013**, *339* (6119), 535–539 DOI: 10.1126/science.1222453.

(8) Gracia-Espino, E.; Barzegar, H. R.; Sharifi, T.; Yan, A.; Zettl, A.; Wågberg, T. Fabrication of One-Dimensional Zigzag [6,6]-Phenyl-C 61 -Butyric Acid Methyl Ester Nanoribbons from Two-Dimensional Nanosheets. *ACS Nano* **2015**, *9* (10), 10516–10522 DOI: 10.1021/acsnano.5b04972.

(9) Zheng, L.; Han, Y. Solvated Crystals Based on [6,6]-Phenyl-C 61 -Butyric Acid Methyl Ester (PCBM) with the Hexagonal Structure and Their Phase Transformation. *J. Phys. Chem. B* **2012**, *116* (5), 1598–1604 DOI: 10.1021/jp210937h.

(10) Sun, X.; Chen, T.; Yang, Z.; Peng, H. The Alignment of Carbon Nanotubes: An Effective Route To Extend Their Excellent Properties to Macroscopic Scale. *Acc. Chem. Res.* **2013**, *46* (2), 539–549 DOI: 10.1021/ar300221r.

(11) Peng, H.; Sun, X.; Cai, F.; Chen, X.; Zhu, Y.; Liao, G.; Chen, D.; Li, Q.; Lu, Y.; Zhu, Y.; Jia, Q. Electrochromatic Carbon Nanotube/Polydiacetylene Nanocomposite Fibres. *Nat. Nanotechnol.* **2009**, *4* (11), 738–741 DOI: 10.1038/nnano.2009.264.

(12) Wang, W.; Sun, X.; Wu, W.; Peng, H.; Yu, Y. Photoinduced Deformation of Crosslinked Liquid-Crystalline Polymer Film Oriented by a Highly Aligned Carbon Nanotube Sheet. *Angew. Chemie - Int. Ed.* **2012**, *51* (19), 4644–4647 DOI: 10.1002/anie.201200723.

(13) Lin, F.; Zhu, Z.; Zhou, X.; Qiu, W.; Niu, C.; Hu, J.; Dahal, K.; Wang, Y.; Zhao, Z.; Ren, Z.; Litvinov, D.; Liu, Z.; Wang, Z. M.; Bao, J. Orientation Control of Graphene Flakes by Magnetic Field: Broad Device Applications of Macroscopically Aligned Graphene. *Adv. Mater.* **2017**, *29* (1), 1–6 DOI: 10.1002/adma.201604453.

(14) Yousefi, N.; Sun, X.; Lin, X.; Shen, X.; Jia, J.; Zhang, B.; Tang, B.; Chan, M.; Kim, J. K. Highly Aligned Graphene/Polymer Nanocomposites with Excellent Dielectric Properties for High-Performance Electromagnetic Interference Shielding. *Adv. Mater.* **2014**, *26* (31), 5480–5487 DOI: 10.1002/adma.201305293.

(15) Lang, C.; Fang, J.; Shao, H.; Ding, X.; Lin, T. High-Sensitivity Acoustic Sensors from Nanofibre Webs. *Nat. Commun.* **2016**, *7*, 11108 DOI: 10.1038/ncomms11108.

(16) Biomechanical, H. Hybrid Nanogenerator for Concurrently. **2010**, *4* (7), 3647–3652.

(17) Persano, L.; Dagdeviren, C.; Su, Y.; Zhang, Y.; Girardo, S.; Pisignano, D.; Huang, Y.; Rogers, J. a. High Performance Piezoelectric Devices Based on Aligned Arrays of Nanofibers of Poly(Vinylidenefluoride-Co-Trifluoroethylene). *Nat. Commun.* **2013**, *4*, 1633 DOI: 10.1038/ncomms2639.

(18) Liu, L.; Lo, C.-F.; Xi, Y.; Ren, F.; Pearton, S. J.; Laboutin, O.; Cao, Y.; Johnson, J. W.; Kravchenko, I. I. Effect of Buffer Structures on AlGaN/GaN High Electron Mobility Transistor Reliability. *J. Vac. Sci. Technol. B Microelectron. Nanom. Struct.* **2013**, *31* (1), 011805.

(19) Xi, Y.; Liu, L.; Ren, F.; Pearton, S. J.; Kim, J.; Dabiran, A.; Chow, P. P. Methane Detection Using Pt-Gated AlGaN/GaN High Electron Mobility Transistor Based Schottky Diodes. *J. Vac. Sci. Technol. B Microelectron. Nanom. Struct.* **2013**, *31* (3), 032203.

(20) Li, J.-H.; Xi, Y.; Pozzo, L. D.; Xu, J.-T.; Luscombe, C. K. Macroscopically Aligned Nanowire Arrays of π-Conjugated Polymers via Shear-Enhanced Crystallization. *J. Mater. Chem. C* **2017** DOI: 10.1039/C7TC01419H.

(21) Lo, C. F.; Xi, Y.; Liu, L.; Pearton, S. J.; Doré, S.; Hsu, C. H.; Dabiran, A. M.; Chow, P. P.; Ren, F. Effect of Temperature on CO Sensing Response in Air Ambient by Using Zno Nanorod-Gated AlGaN/GaN High Electron Mobility Transistors. *Sensors Actuators, B Chem.* **2013**, *176*, 708–712.

(22) Hofmann, S.; Ducati, C.; Neill, R. J.; Piscanec, S.; Ferrari, A. C.; Geng, J.; Dunin-Borkowski, R. E.; Robertson, J. Gold Catalyzed Growth of Silicon Nanowires by Plasma Enhanced Chemical Vapor Deposition. *J. Appl. Phys.* **2003**, *94* (9), 6005–6012 DOI: 10.1063/1.1614432.

(23) Hah, J. H.; Mayya, S.; Hata, M.; Jang, Y.-K.; Kim, H.-W.; Ryoo, M.; Woo, S.-G.; Cho, H.-K.; Moon, J.-T. Converging Lithography by Combination of Electrostatic Layer-by-Layer Self-Assembly and 193 Nm Photolithography: Top-down Meets Bottom-Up. *J. Vac. Sci. Technol. B Microelectron. Nanom. Struct.* **2006**, *24* (5), 2209 DOI: 10.1116/1.2244541.

(24) Jiang, S.; Duan, G.; Kuhn, U.; Mörl, M.; Altstädt, V.; Yarin, A. L.; Greiner, A. Spongy Gels by a Top-Down Approach from Polymer Fibrous Sponges. *Angew. Chemie - Int. Ed.* **2017**, *56* (12), 3285–3288 DOI: 10.1002/anie.201611787.

(25) Israelavhvili, J. N. No Title. In *Intermolecular and surface forces*; 2009; p 628.

(26) Hutchins, D. O.; Weidner, T.; Baio, J.; Polishak, B.; Acton, O.; Cernetic, N.; Ma, H.; Jen, A. K.-Y. Effects of Self-Assembled Monolayer Structural Order, Surface Homogeneity and Surface Energy on Pentacene Morphology and Thin Film Transistor Device Performance. *J. Mater. Chem. C* **2013**, *1* (1), 101–113 DOI: 10.1039/C2TC00378C.

(27) Newbloom, G. M.; Kim, F. S.; Jenekhe, S. a.; Pozzo, D. C. Mesoscale Morphology and Charge Transport in Colloidal Networks of Poly(3-Hexylthiophene). *Macromolecules* **2011**, *44* (10), 3801–3809 DOI: 10.1021/ma2000515.

(28) Iglesia, P. D. La; Pozzo, D. C. Effects of Supersaturation on the Structure and Properties of Poly(9,9-Dioctyl Fluorene) Organogels. *Soft Matter* **2013**, *9* (47), 11214 DOI: 10.1039/c3sm51753e.

(29) Newbloom, G. M.; Weigandt, K. M.; Pozzo, D. C. Electrical, Mechanical, and Structural Characterization of Self-Assembly in Poly(3-Hexylthiophene) Organogel Networks. *Macromolecules* **2012**, *45*, 3452–3462 DOI: 10.1021/ma202564k.

(30) Newbloom, G. M.; de la Iglesia, P.; Pozzo, L. D. Controlled Gelation of Poly(3-Alkylthiophene)s in Bulk and in Thin-Films Using Low Volatility Solvent/Poor-Solvent Mixtures. *Soft Matter* **2014**, *10* (44), 8945–8954 DOI: 10.1039/c4sm00960f.

(31) Xi, Y.; Pozzo, L. D. Electric Field Directed Formation of Aligned Conjugated Polymer Fibers. *Soft Matter* **2017**, *13*, 3894–3908 DOI: 10.1039/C7SM00485K.

(32) Li, J.-H.; Xi, Y.; Pozzo, L. D.; Xu, J.-T.; Luscombe, C. K. Macroscopically Aligned Nanowire Arrays of π-Conjugated Polymers via Shear-Enhanced Crystallization. *J. Mater. Chem. C* **2017** DOI: 10.1039/C7TC01419H.

(33) Diao, Y.; Tee, B. C.-K.; Giri, G.; Xu, J.; Kim, D. H.; Becerril, H. a; Stoltenberg, R. M.; Lee, T. H.; Xue, G.; Mannsfeld, S. C. B.; Bao, Z. Solution Coating of Large-Area Organic Semiconductor Thin Films with Aligned Single-Crystalline Domains. *Nat. Mater.* **2013**, *12* (7), 665–671 DOI: 10.1038/nmat3650.

(34) Luo, C.; Kyaw, A. K. K.; Perez, L. a.; Patel, S.; Wang, M.; Grimm, B.; Bazan, G. C.; Kramer, E. J.; Heeger, A. J. General Strategy for Self-Assembly of Highly Oriented Nanocrystalline Semiconducting Polymers with High Mobility. *Nano Lett.* **2014**, *14* (5), 2764–2771 DOI: 10.1021/nl500758w.

(35) Noriega, R.; Rivnay, J.; Vandewal, K.; Koch, F. P. V.; Stingelin, N.; Smith, P.; Toney, M. F.; Salleo, A. A General Relationship between Disorder, Aggregation and Charge Transport in Conjugated Polymers. *Nat. Mater.* **2013**, *12* (11), 1038–1044 DOI: 10.1038/nmat3722.

(36) Newbloom, G. M.; Hoffmann, S. M.; West, A. F.; Gile, M. C.; Sista, P.; Cheung, H. C.; Luscombe, C. K.; Pfaendtner, J.; Pozzo, L. D. Solvatochromism and Conformational Changes in Fully Dissolved Poly(3-Alkylthiophene)S. *Langmuir* **2015**, *31* (1), 458–468 DOI: 10.1021/la503666x.

(37) Newbloom, G. M.; Weigandt, K. M.; Pozzo, D. C. Structure and Property Development of Poly(3-Hexylthiophene) Organogels Probed with Combined Rheology, Conductivity and Small Angle Neutron Scattering. *Soft Matter* **2012**, *8* (34), 8854 DOI: 10.1039/c2sm26114f.

(38) Zhu, R.; Kumar, A.; Yang, Y. Polarizing Organic Photovoltaics. *Adv. Mater.* **2011**, *23* (36), 4193–4198 DOI: 10.1002/adma.201101514.

Chapter 2. Theory & Methods

2.1 SMALL ANGLE NEUTRON SCATTERING (SANS)

SANS is a nondestructive method that probes structures from several nanometers to a couple hundred nanometers which is useful in areas such as polymers, complex fluids, and biology. [1] For conjugated polymers, SANS is a great tool to quantitatively understand the structures in solutions, especially in halogenated solvents. The good solvent for conjugated polymers are usually chlorinated solvents, which absorbs x-ray and cannot be easily characterized with enough contrast.

2.1.1 Basic theories of small angle scattering

The interaction between the irradiation source (such as light, x-ray, or neutron) and the scattering medium gives rise to the scattering vector q. The schematic of the relationship of the propagation vectors of incident beam (k_i), transmitted beam (k_t), scattered beam (k_s) and the scattering vector (q) is shown in Figure 2.1. The angle between the scattered beam and the incident beam is scattering angle θ. The scattering vector is defined as the difference between the propagation vector of scattered and incident scattering radiation. The magnitude of propagation vector is $2\pi/\lambda$, where λ is the wavelength of the incident beam. [2] The scattering vector is defined in equation (2.1). There are three assumptions associated with this definition. (1) The scattering beam only accounts for a small portion of the incident beam (Born approximation). (2) The multiple scattering can be neglected. (3) Only a small amount of energy is transferred after scattering, which makes all of the propagation vectors the same value. [2]

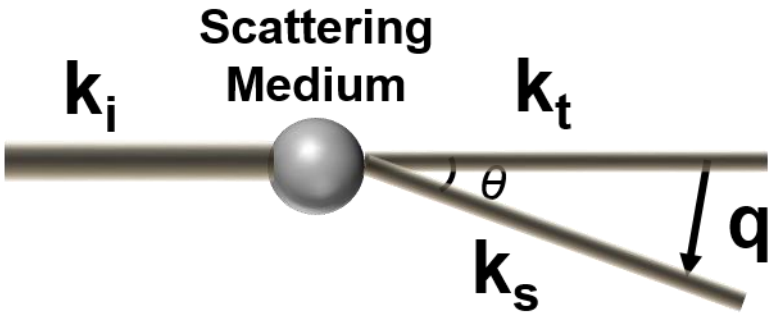

Figure 2.1. Propagation vectors of incident beam, scattering beam, transmitted beam and scattering vector.

$$q = k_s - k_i = \frac{4\pi}{\lambda}\sin\frac{\theta}{2} \tag{2.1}$$

2.1.2 Instrumentation

In order to interpret the data quantitatively, a relationship between the normalized scattering intensity and the structure of scattering medium needs to be developed. [2] **Figure 2.2** shows a typical instrument setup of a scattering experiment. The slit is used to define the aperture size of an incident beam with intensity I_i. The scattering intensity is recorded by a detector that is spaced apart from the sample with a distance of L. Differential scattering cross-section ($d\sigma$) over the unit solid angle ($d\Omega$) is defined based on the intensity of the incident beam and the that of the scattering beam I_s in equation (2.2). Its value normalized by the volume of the sample *V* gives the absolute scattering intensity (equation (2.3)), which is important for extracting structural information and correlation between scattered particles. [2] The absolute scattering intensity can be experimentally

determined if the sample thickness, transmission, and the ratio of scattered flux over the total flux are measured. [2]

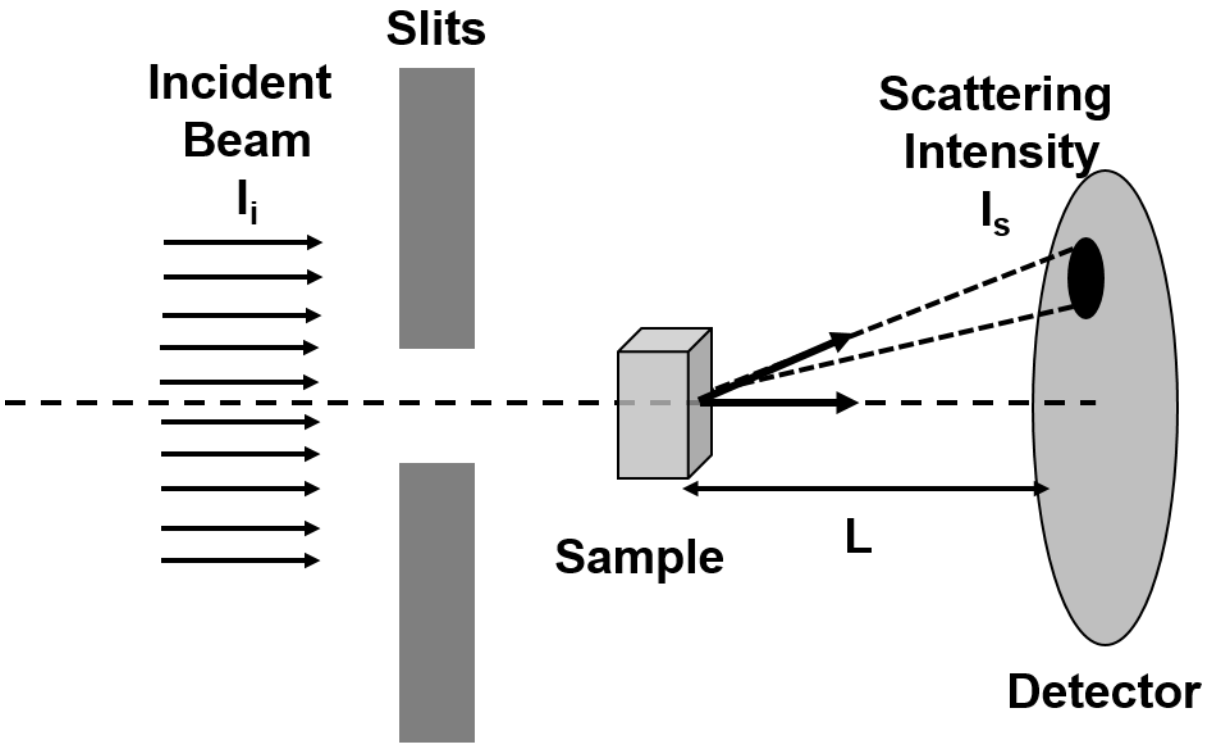

Figure 2.2. Schematic drawing of typical setup of a typical scattering experiment.

$$\frac{d\sigma}{d\Omega} = \frac{I_S}{I_i} L \tag{2.2}$$

$$I(cm^{-1}) = \frac{1}{V}\frac{d\sigma}{d\Omega} = \frac{d\Sigma}{d\Omega} \tag{2.3}$$

2.1.3 Form Factor Fitting

After obtaining the absolute scattering intensity, various models can be used to fit the form factors of the system to extrapolate quantitatively averaged information about the structure. This relation

is described in equation (2.4), which also requires the knowledge of the scattering properties of the samples.

$$I(cm^{-1}) = \frac{d\Sigma}{d\Omega} = n\Delta\rho^2 VP(q)S(q) \tag{2.4}$$

$$\rho = \frac{\sum_i bi}{V_s} \tag{2.5}$$

Where *n* is the number density of the scattering species, $\Delta\rho$ is the scattering length density (SLD) difference between the sample species and the solvent, *V* is the volume of the sample particle, *P(q)* is the form factor and *S(q)* is the structure factor of the system. [2] The SLD is defined in equation 2.5, where the summation of *b* is the scattering lengths over all atoms and V_s is the sample volume. The scattering length is closely related to the ratio of scattering intensity (I_s) over incident beam intensity (I_i). [2] The structural information can be obtained from the form factor and the interaction between particles within the sample is contained in the structure factor. [2] For dilute polymer solutions, the structure factor *S(q)* can be treated as 1. The number density of the sample, SLD difference and volume of the scattering species can be easily determined from the experiment set-up. The form factor can be fitted based on the shape of the samples. Below are some typically used form factors of various shape models for polymer solutions.

2.1.3.1 Dissolved polymers with excluded volume effect

Different from random walk model, excluded volume effect takes the fact that the space occupied by one monomer cannot be occupied by others into account, which is widely used to fit the fully dissolved polymer coils. [2–6] The form factor of the model can be defined from equation (2.6) through equation (2.8). [7]

$$P_{PExV}(q) = \frac{1}{\nu U^{\frac{1}{2\nu}}}\gamma\left(\frac{1}{2\nu}, U\right) - \frac{1}{\nu U^{\frac{1}{\nu}}}\gamma\left(\frac{1}{\nu}, U\right) \quad (2.6)$$

$$\gamma(x, U) = \int_0^U dt\, \exp(-t)t^{x-1} \quad (2.7)$$

$$U = \frac{q^2 R_g^2 (2\nu+1)(2\nu+2)}{6} \quad (2.8)$$

Where ν is the inverse of the Porod exponent and R_g is the radius of gyration.

2.1.3.2 Parallelepiped model

Parallelepiped model can be used to model nanofibers assuming rectangular cross-section. Its orientation can be described by two angles and they are integrated over all degrees. [8] Previous work from our group has successfully applied this model to describe the cross-sectional size of conjugated polymer nanofibers in a colloidal network or organogels. [3–6,9]

$$P_{PP}(q) = \frac{2}{\pi}\int_0^{2\pi}\int_0^{2\pi}\left[\left(\frac{\sin(qA\sin\alpha\cos\beta)}{qA\sin\alpha\cos\beta}\right)\left(\frac{\sin(qB\sin\alpha\cos\beta)}{qB\sin\alpha\cos\beta}\right)\left(\frac{\sin(qC\cos\alpha)}{qC\cos\alpha}\right)\right]^2 \sin\alpha\, d\alpha d\beta \quad (2.9)$$

Whereas a, b and c represent the dimensions of the parallelepiped shape, which is depicted in Figure 2.3. a and b are the sides of the cross-section and c is the length of the parallelepiped.

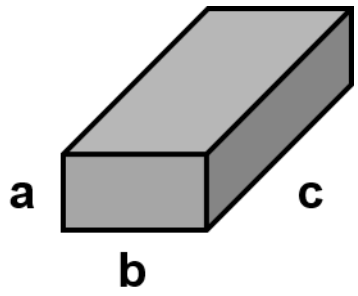

Figure 2.3. Schematic drawing parallelepiped shape labeled with three dimensions.

2.2 GRAZING-INCIDENCE SMALL ANGLE X-RAY SCATTERING (GISAXS)

X-ray is an electromagnetic wave that can be used for the characterization of polymer chain orientation and extrapolating information about crystal structure dimensions. A specific type of s-ray scattering, GISAXS, is widely used to probe polymer packing in solid thin films. The information obtained from GISAXS experiments is useful in understanding how the structure affects performance of organic electronics. [10–14] Figure 2.5 shows the typical experimental setup. The x-ray beam is aligned with an incident angle α_i with respect to the polymer thin film sample. When the incident angle α_i is smaller than a critical angle α_c of the material of thin film (polymers), the beam gets total external reflection. The critical angle for silicon is 0.223° and that of a polystyrene film is 0.153° for an x-ray beam with a wavelength of 1.54 Å. [15] Thus a tilt angle of 0.2° would penetrate through the polymer film, but get reflected from the polymer/silicon interface. Conjugated polymers can form very crystalline domains, which is favorable for charge transport over long distance. Figure 2.4 shows schematic drawing of conjugated polymer chains along with their lamella and π-π stacking distances. When polymers formed crystals, those repeated distances can be captured by GISAXS with scattering peaks at different positions.

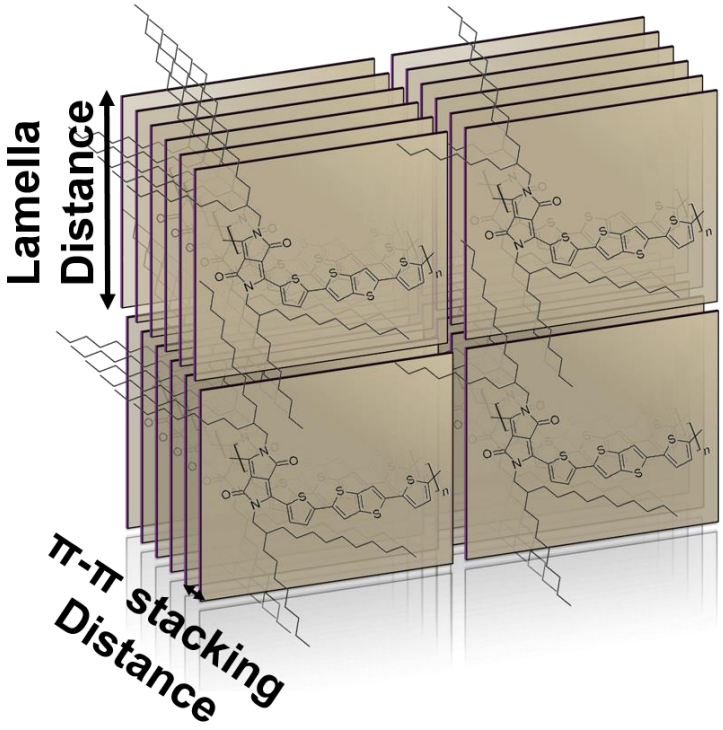

Figure 2.4. Schematic drawing of crystal structures formed by polymer packing associated with the characterization distances (i.e. lamella and π-π stacking).

The scattering pattern can be recorded with a 2-D detector, which is shown in Figure 2.5. Typical peak positions of π-π stacking and lamella peaks of conjugated polymer films are labeled in Figure 2.5. The processing conditions or the polymer molecular structure can strongly affect the packing distance between polymer chains. Moreover, the intensity distribution along the semicircle of each scattering peak (azimuthal angle between -90° and 90°) indicates the polymer chain packing orientation with respect to the substrate. Thus it is usually useful to compare the 1-D scattering profiles integrated along both out-of-plane and in-plane directions.

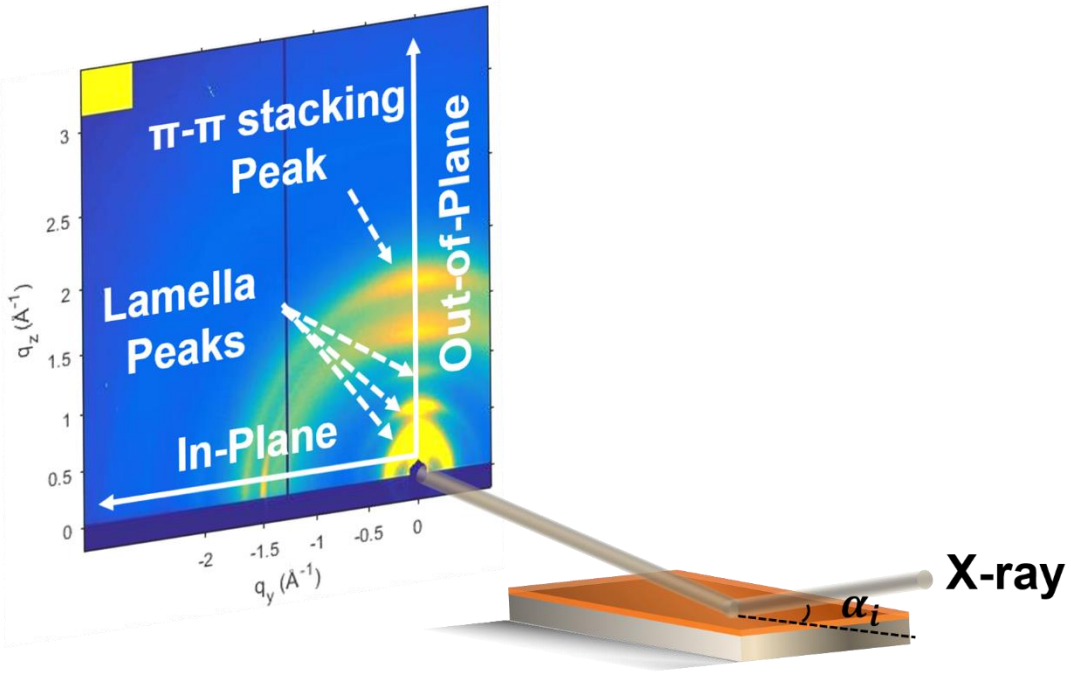

Figure 2.5. GISAXS Experimental setup for characterizing thin films.

Examples of polymer chain orientation analysis can be found in Figure 2.6. Those are scattering patterns of DPPDTT polymer films processed with different solution processes. In Figure 2.6 (a), the π-π stacking peak has a strong intensity along the out-of-plane direction. This indicates that the polymer chains favor 'face-on' orientation, which is depicted in the schematic drawing below. In contrast, the π-π stacking peak shows a relatively strong intensity in the in-plane direction in Figure 2.6 (b), which corresponds to an 'Edge-on' orientation of the polymer chains. Figure 2.6 (c) shows a uniform distribution of the π-π stacking peak over all azimuthal angles. This can be interpreted as a random orientation of the crystals over all directions.

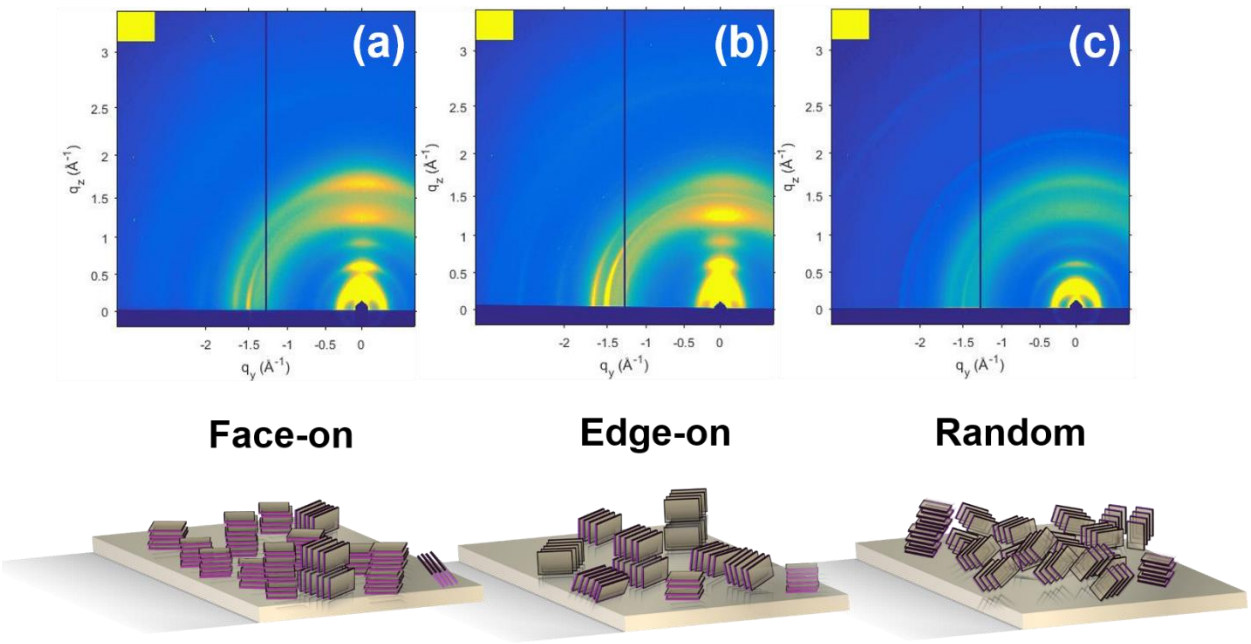

Figure 2.6. GISAXS 2-D scattering profile of polymer sample DPPDTT processed from different solvent conditions and the corresponding schematic drawing of polymer chain packing orientation with respect to the substrate interpreted from the scattering profile.

2.3 SCANNING TRANSMISSION ELECTRON MICROSCOPY (STEM)

sTEM can be used to visualize the shape or structure formed from several nanometers to a few micrometers. It is a great technique to get a qualitative understanding of the shape of the sample. Compared to TEM, scanning mode gives a better contrast for imaging conjugated polymer formed nano-structures on pure carbon grids. Figure 2.7 compares the TEM and sTEM images of P3HT nanofibers formed in 1,2-dichlorobenzene (o-DCB) under ultrasound. It is clear that the sample in the sTEM mode has a better contrast and is easier to focus. Figure 2.8 shows major components of the sTEM instrument. [16] The condenser lens is used to focus the electron beam to the sample and the contrast can be enhanced by inserting the objective aperture. [17] The objective length is used to increase the magnification of the image. [17] sTEM is imaged with dark field detector.

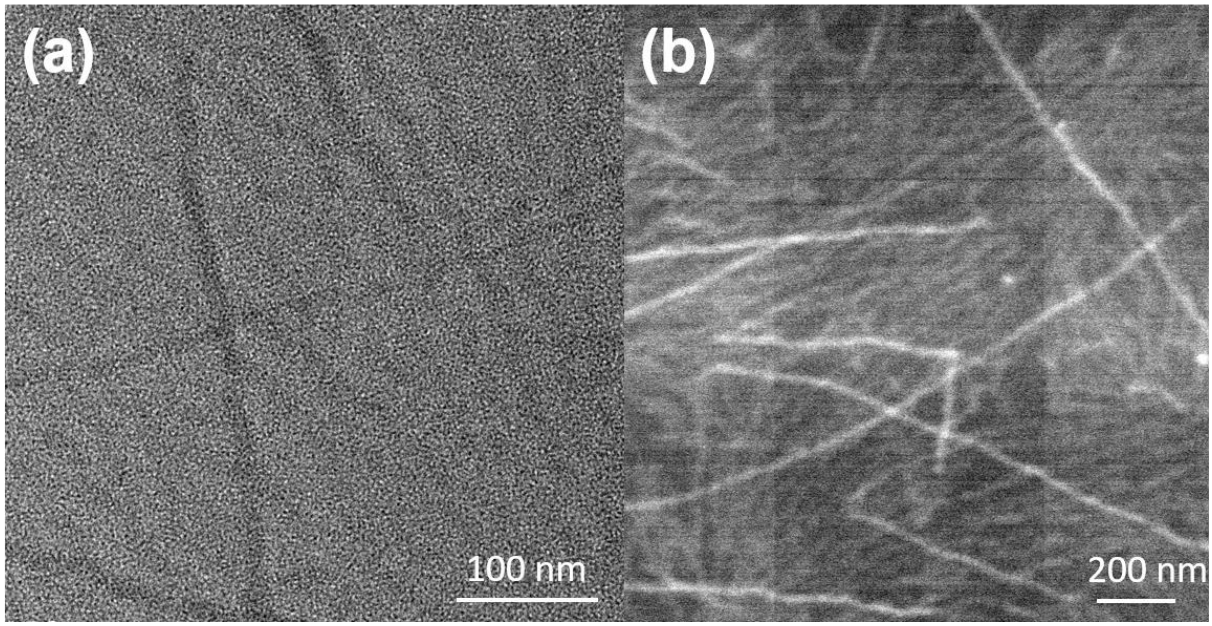

Figure 2.7. Images of 10 mg/ml P3HT sonicated in sonication bath for 30min taken with (a) TEM and (b) sTEM mode.

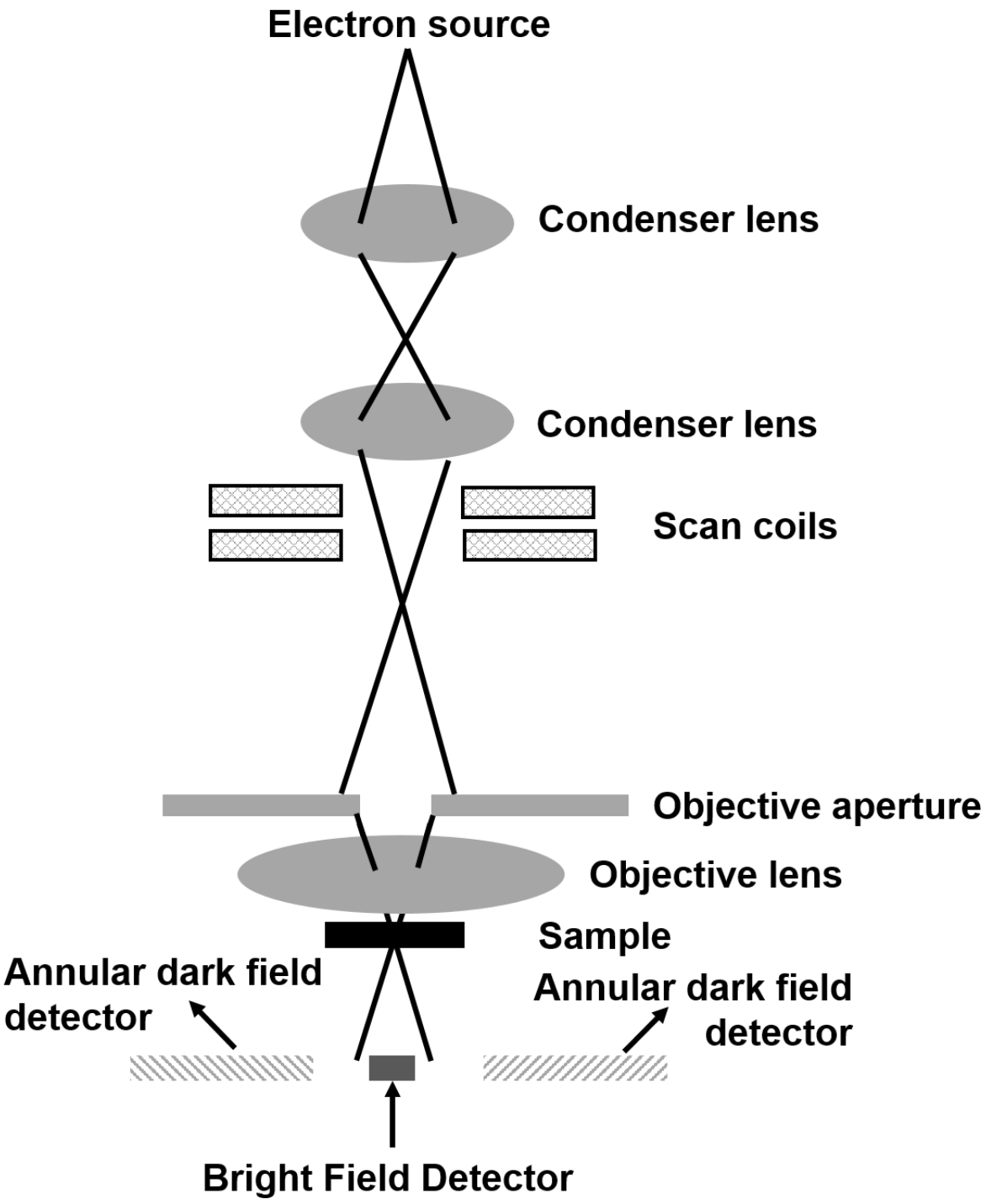

Figure 2.8. Schematic drawing of the major component of sTEM instrument.

2.4 UV-VISIBLE SPECTROSCOPY

UV-visible spectroscopy is a powerful yet fast measurement to obtain the absorbance information of a sample as a function of wavelength. This technique measures samples directly in solutions and the information provided can be analyzed in a quantitative way.[18] It measures the UV-range and covers the whole wavelength of visible light (200 nm- 1100 nm). This is especially useful for a lot of conjugated polymers, since most of them absorb light in this range. Based on the formation of new peaks or the shifts of the existing peak, the information regarding both fully dissolved polymers and assembled nanofibers in solutions can be obtained. [4,19,20] The experiment setup measures the intensity of the incident light (I_0) and detects the intensity of the transmitted light (I_t) as a function of wavelength. The absorbance (Abs) is defined based on the above measured intensities in equation 2. 10. The absorbance can be used to calculate the concentration of the sample (c), given the path length (L) used and the extinction coefficient (ε) calculated. This relation is described by Beer-Lambert law in equation 2.10.

$$Abs = lg\frac{I_0}{I_t} = \varepsilon Lc \tag{2.10}$$

For certain systems, specific models have been developed to accurately fit the spectrum to provide quantitative information. For example, fully P3HT in solutions exhibits a single absorption peak at ~460 nm. When they aggregate to form nanofibers, additional peaks are raised at ~ 600 nm to make the solution visibly dark. Figure 2.6 shows a comparison of the P3HT spectrum collected for fully dissolved state and nanofibers. Based on the absorption peak area of the additional peaks, Frank-Condon fit can be used to model the aggregates and extrapolate its percentage over the total polymer amount. [20,21] The model is shown as in equation (2.11). [20]

$$A = \sum_{m=0}\left(\frac{e^{-S}S^m}{m!}\right)\left(1 - \frac{We^{-S}}{2E_p}\sum_{n\neq m}\frac{S^n}{n!}(n-m)\right)^2 \Gamma(h\omega - E_{0-0} - mE_p) \quad (2.11)$$

Where n is the vibrational quantum number, S is Huang-Rhys factor, W is the exciton bandwidth of aggregates, Ep is the energy of main intramolecular vibration. The exciton bandwidth is a value that reflects how ordered the polymer chains are assembled. The lower the value, the more ordered the system is. The W value can be estimated based on a much simpler version of Frank-Condon fit, equation (2.12), which only takes the two absorption peaks of 0-0 and 0-1. Those two peaks are also labeled in Figure 2.9.

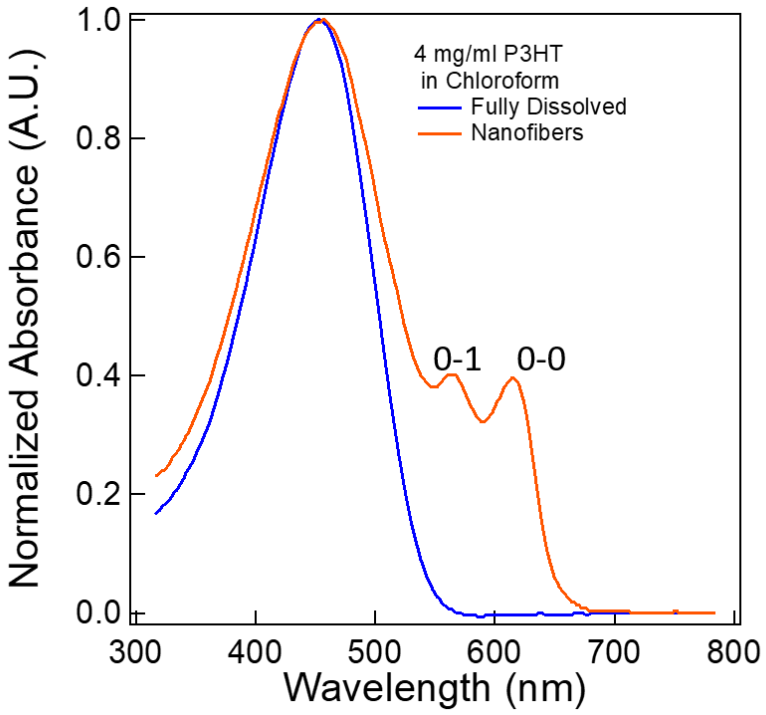

Figure 2.9. UV-vis spectra of fully dissolved P3HT and P3HT nanofibers in solutions.

$$\frac{A_{0-0}}{A_{0-1}} \approx \left(\frac{1-0.24\frac{W}{E_p}}{1+0.073\frac{W}{E_p}}\right)^2 \quad (2.12)$$

2.5 RHEOLOGY

Rheology is a widely used technique to characterize the mechanic properties of fluids, colloidal suspensions, gels or cells. [3,9,22] In the case in **Figure 2.10**, shear force F is exerted on material with a cross-sectional dimension of A to induce lateral displacement of x. The parameters labeled in **Figure 2.10** are used to define shear stress (τ), shear strain (γ) and shear rate ($\dot{\gamma}$) from equation (2.13) to (2.15). The shear stress is the force exerted per area.

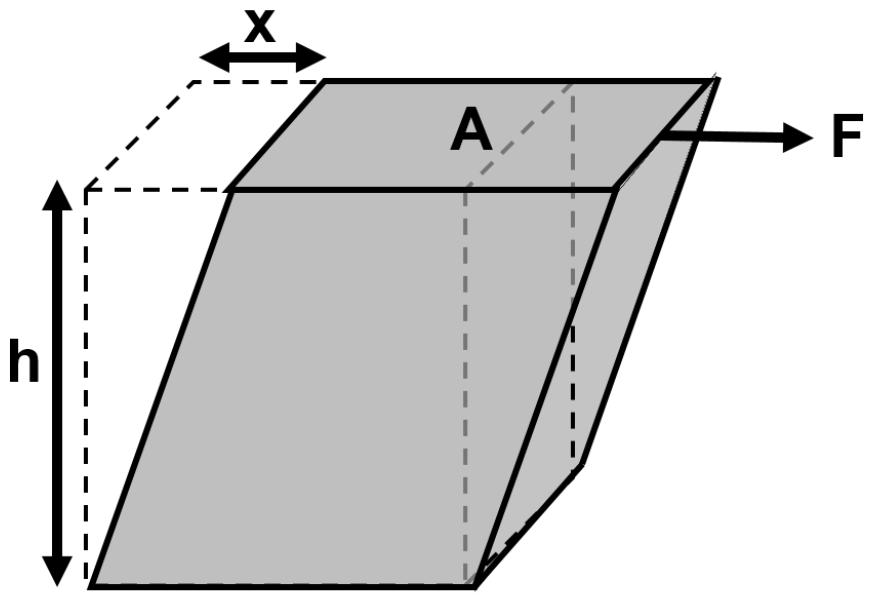

Figure 2.10. Schematic drawing of basic rheology parameters.

$$\tau = \frac{F}{A} \tag{2.13}$$

$$\gamma = \frac{x}{h} \tag{2.14}$$

$$\dot{\gamma} = \frac{d\gamma}{dt} \tag{2.15}$$

For oscillatory rheology test, the sinusoidal strain is applied and the stress needed is measured. This test is conducted within linear viscoelastic regime, so that the measured strain is also a sinusoidal wave function, but may be in a different phase from the applied strain signal. This response can be fitted with a component that in-phase with the strain and component off-phase with it. The prefactor of the in-phase component is called storage modulus (G') and that of the off-phase component is named loss modulus (G''). The liquid sample always has G'' > G'. When G' exceeds G'', the sample transits to a gel. The larger the G' value, the stronger the gel is.

2.6 IMPEDANCE SPECTROSCOPY

Impedance spectroscopy is another non-destructive technique that allows probing the electrical property of a sample. The experiment applies an AC potential with frequency ω (equation (2.16)) as an input to the system and measures the current. In a linear system, the current response of the AC potential is also sinusoidal, but there might be a phase shift φ(equation (2.17)). [23] The ratio of voltage over current is complex impedance Z^*, whose real part is Z_{real} and imaginary part is Z_{imag} (equation (2.18)). By plotting the real part on the x-axis and imaginary part on the y-axis, a Nyquist plot can be obtained. Another commonly used data representation is through Bode plot, where the impedance magnitude and phase angle are plotted as a function of frequency.

$$V(t) = V_A \sin \omega t \tag{2.16}$$

$$I(t) = I_A \sin(\omega t + \varphi) \tag{2.17}$$

$$Z^* = \frac{V(t)}{I(t)} = Z_A \frac{\sin(\omega t)}{\sin(\omega t + \varphi)} = Z_{real} + jZ_{imag} \tag{2.18}$$

Similar to complex impedance, complex permittivity of the material can also be expressed as a function of real part ε' (dielectric constant) and imaginary part ε'' (loss factor). [23] They can be related in equation (2.19). The dielectric constant represents the ability of the system to store energy and it is a measure of how well the dipole in the material is aligned to the external electric field perturbation. It relates to the capacitance of the system in equation (2.19), where C is the capacitance, d is the distance between two electrodes, ε_0 is vacuum permittivity, and A is the contact area. In contrast, ε'' reflects the conductivity of the system and is defined in Equation (2.20), where ρ is the resistivity and ω is AC radial frequency.

$$\varepsilon^* = \varepsilon' - j\varepsilon'' \tag{2.18}$$

$$\varepsilon' = \frac{Cd}{\varepsilon_0 A} \tag{2.19}$$

$$\varepsilon'' = \frac{1}{\varepsilon_0 \rho \omega} \tag{2.20}$$

2.7 REFERENCES

(1) Hammouda, B. *Probing Nanoscale Structures-The SANS Toolbox*.

(2) Pusey, P. N. Introduction to Scattering Experiments. In *Neutrons, x-rays and light: scaattering methods applied to soft condensed matter*.

(3) Newbloom, G. M.; Weigandt, K. M.; Pozzo, D. C. Structure and Property Development of poly(3-Hexylthiophene) Organogels Probed with Combined Rheology, Conductivity and Small Angle Neutron Scattering. *Soft Matter* **2012**, *8* (34), 8854 DOI: 10.1039/c2sm26114f.

(4) Newbloom, G. M.; Kim, F. S.; Jenekhe, S. a.; Pozzo, D. C. Mesoscale Morphology and

Charge Transport in Colloidal Networks of poly(3-Hexylthiophene). *Macromolecules* **2011**, *44* (10), 3801–3809 DOI: 10.1021/ma2000515.

(5) Newbloom, G. M.; Weigandt, K. M.; Pozzo, D. C. Electrical, Mechanical, and Structural Characterization of Self-Assembly in poly(3-Hexylthiophene) Organogel Networks. *Macromolecules* **2012**, *45*, 3452–3462 DOI: 10.1021/ma202564k.

(6) Newbloom, G. M.; de la Iglesia, P.; Pozzo, L. D. Controlled Gelation of poly(3-Alkylthiophene)s in Bulk and in Thin-Films Using Low Volatility Solvent/poor-Solvent Mixtures. *Soft Matter* **2014**, *10* (44), 8945–8954 DOI: 10.1039/c4sm00960f.

(7) 1993_Hammouda_Adv_Polym_Sci.Pdf. In *Advances in polymer science*; 1993; pp 87–133.

(8) Mittelbach, P.; Porod, G. No Title. *Acta Phys. Austriaca* **1961**, *14*, 185–211.

(9) Iglesia, P. D. La; Pozzo, D. C. Effects of Supersaturation on the Structure and Properties of poly(9,9-Dioctyl Fluorene) Organogels. *Soft Matter* **2013**, *9* (47), 11214 DOI: 10.1039/c3sm51753e.

(10) Li, J.-H.; Xi, Y.; Pozzo, L. D.; Xu, J.-T.; Luscombe, C. K. Macroscopically Aligned Nanowire Arrays of π-Conjugated Polymers via Shear-Enhanced Crystallization. *J. Mater. Chem. C* **2017**, *5* (21), 5128–5134 DOI: 10.1039/C7TC01419H.

(11) Wu, C.-H.; Chueh, C.-C.; Xi, Y.-Y.; Zhong, H.-L.; Gao, G.-P.; Wang, Z.-H.; Pozzo, L. D.; Wen, T.-C.; Jen, A. K.-Y. Influence of Molecular Geometry of Perylene Diimide Dimers and Polymers on Bulk Heterojunction Morphology Toward High-Performance Nonfullerene Polymer Solar Cells. *Adv. Funct. Mater.* **2015**, *25* (33), 5326–5332 DOI: 10.1002/adfm.201501971.

(12) Yu, J.; Xi, Y.; Chueh, C.-C.; Xu, J.-Q.; Zhong, H.; Lin, F.; Jo, S. B.; Pozzo, L. D.; Tang, W.; Jen, A. K.-Y. Boosting Performance of Inverted Organic Solar Cells by Using a Planar Coronene Based Electron-Transporting Layer. *Nano Energy* **2017**, *39*, 454–460 DOI: 10.1016/j.nanoen.2017.07.031.

(13) Yu, J.; Xi, Y.; Chueh, C.-C.; Zhao, D.; Lin, F.; Pozzo, L. D.; Tang, W.; Jen, A. K.-Y. A Room-Temperature Processable PDI-Based Electron-Transporting Layer for Enhanced Performance in PDI-Based Non-Fullerene Solar Cells. *Adv. Mater. Interfaces* **2016**, *3* (18), 1600476 DOI: 10.1002/admi.201600476.

(14) Sulas, D. B.; Yao, K.; Intemann, J. J.; Williams, S. T.; Li, C.-Z.; Chueh, C.-C.; Richards, J. J.; Xi, Y.; Pozzo, L. D.; Schlenker, C. W.; Jen, A. K.-Y.; Ginger, D. S. Open-Circuit Voltage Losses in Selenium-Substituted Organic Photovoltaic Devices from Increased Density of Charge-Transfer States. *Chem. Mater.* **2015**, *27* (19), 6583–6591 DOI: 10.1021/acs.chemmater.5b02133.

(15) Tolan, M. *X-Ray Scattering from Soft-Matter Thin Films*; Springer-Verlag Berlin Heidelberg, 1999.

(16) No Title. In *Scanning Transmission Electron Microscopy Imaging and Analysis*; 2011.

(17) Transmission Electron Microscopy https://cmrf.research.uiowa.edu/transmission-electron-microscopy.

(18) Kleinhenz, N.; Persson, N.; Xue, Z.; Chu, P. H.; Wang, G.; Yuan, Z.; McBride, M. A.; Choi, D.; Grover, M. A.; Reichmanis, E. Ordering of Poly(3-Hexylthiophene) in Solutions and Films: Effects of Fiber Length and Grain Boundaries on Anisotropy and Mobility. *Chem. Mater.* **2016**, *28* (11), 3905–3913 DOI: 10.1021/acs.chemmater.6b01163.

(19) Newbloom, G. M.; Hoffmann, S. M.; West, A. F.; Gile, M. C.; Sista, P.; Cheung, H. K. C.; Luscombe, C. K.; Pfaendtner, J.; Pozzo, L. D. Solvatochromism and Conformational Changes in Fully Dissolved poly(3-Alkylthiophene)s. *Langmuir* **2015**, *31* (1), 458–468 DOI: 10.1021/la503666x.

(20) Clark, J.; Chang, J. F.; Spano, F. C.; Friend, R. H.; Silva, C. Determining Exciton Bandwidth and Film Microstructure in Polythiophene Films Using Linear Absorption Spectroscopy. *Appl. Phys. Lett.* **2009**, *94* (16), 2007–2010 DOI: 10.1063/1.3110904.

(21) Spano, F. C. Absorption in Regio-Regular poly(3-Hexyl)thiophene Thin Films: Fermi Resonances, Interband Coupling and Disorder. *Chem. Phys.* **2006**, *325* (1), 22–35 DOI: 10.1016/j.chemphys.2005.08.019.

(22) Philippova, O. E.; Shibaev, A. V.; Muravlev, D. A.; Mityuk, D. Y. Structure and Rheology of Solutions and Gels of Stiff Polyelectrolyte at High Salt Concentration. *Macromolecules* **2016**, *49* (16), 6031–6040 DOI: 10.1021/acs.macromol.6b01392.

(23) Lvovich, V. F. *Impedance Spectroscopy*; John Wiley & Sons, Inc., 2012.

Chapter 3. Electric Field Directed Formation of Aligned Conjugated Polymer Fibers

3.1 INTRODUCTION AND MOTIVATION

Conjugated polymers (CPs) have attracted tremendous attention due to their capacity for solution processing, which makes them viable economic and scalable routes for mass produced electronic devices.[1,2] CPs are also lightweight and flexible, which makes them attractive for flexible electronic applications where inorganic materials cannot meet specifications, such as artificial electronic skin, tactile sensing and flexible displays.[3–5] Unfortunately, when compared to their inorganic counterparts, the electronic performance of CPs in electronic devices still lags significantly behind. After years of steady improvements, single junction organic photovoltaics (OPVs) can yield power conversion efficiency over 10% and hole mobility values can reach above 30 cm^2/V-s.[6,7] Yet, there is a large need for further improvements since these metrics are still not fully competitive with inorganic counterparts.[6–11]

Molecular alignment provides an effective way to significantly enhance charge transport, which is essential to improving performance of organic electronic devices. For example, after alignment is achieved for conductive polymers, OFET mobility values can increase by more than one order of magnitude up to a record 47 cm^2/V-s. [6,12,13]Aligned structures have also played an important role in the fabrication of optical and opto-electronic devices. Polarizers[14] and concealed imaging systems[15] were demonstrated with uniaxially oriented conductive polymers. Switchable polarizers based on electrochromism[16] were also designed and could be used in smart windows. Polarized light emitting diodes (OLEDs) for liquid crystal displays (LCDs) could further reduce energy consumption.[17,18] Polarizing organic photovoltaics (OPVs) act as polarizers while also harvesting

energy from blocked polarization states.[19] In addition to these, controlled alignment of nanofibers could facilitate the production of microscopic circuitry from organic components.

The need for effective polymer alignment has led to the exploration of several methods including recrystallization by vapor treatment,[20] mechanical rubbing,[19,21] directional epitaxial crystallization,[22,23] nanoimprinting,[24–26] Langmuir-Blodgett films,[27] and blade shearing.[13] Still, most of the currently reported alignment methods are either difficult to scale up or hard to control. In contrast, alignment with electric fields can be a more promising approach because it is economic, easily tunable, accurately controlled, and can be integrated with large scale processing. For example, electrospinning, has now been successfully implemented in several large scale industrial production processes for more than 60 years.[28,29] Here, the simple components required for applying electric fields and the continuous nature of the spinning process keep the costs low. Thus, the use of electric field processing has already proven to be a highly tunable approach to produce advanced materials in commercial quantities.

Although potentially useful, the application of electric fields to align conjugated polymers (CPs) has not been systematically studied by the scientific community. In contrast, electric field alignment has been widely demonstrated and analyzed in-depth in the literature for several other systems including block copolymers,[30–32] cellulose fibers,[33] carbon nanotubes[34–36] and metallic nanorods or nanowires.[37–39] Although limited in numbers, there are also a few pioneering reports demonstrating successful electric field alignment of various CP systems.[40–42] In the context of OFETs fabrication, enhanced charge transport mobility was also demonstrated for aligned Poly(3-hexylthiophene) (P3HT) suggesting that this technique could be technologically useful.[43,44] However, in these reports, alignment was only analyzed over a single electric field type and fibers were only aligned over small distances (0.5 to 4 μm). Therefore, at this point, the forces at play in

the alignment of CP nanofibers under electric fields are still not fully understood and this prevents the effective application and extension of this technique to other systems.

In this work, we systematically analyze CP alignment using various types of electric fields and demonstrate that primary alignment is due to dielectrophoretic (DEP) forces. We also show that electrophoretic forces can play an important role in this process but, on their own, they are incapable of producing good quality CP alignment. Electrophoresis acts on charged particles at low electric field frequencies(<10 Hz), but it becomes less significant than dielectrophoresis (DEP) as frequency gets higher because the net displacement of the particles are canceled out by fast-switching field.[45] In contrast, DEP originates from forces due to a non-uniform external field acting on polarizable particles, which may or may not have charges or be conductive. DEP has been used to align metallic nanoparticles and it is routinely used in biosciences to selectively separate cells and other biological components.[45] Recently, DEP theory was also successfully implemented to explain and predict the optimum AC electric field conditions for alignment of small organic semiconductor (OSC) molecules. [46] The DEP force is strongly affected by gradients of electric fields so that it also depends on electrode geometry. Moreover, the size and shape of the particles is also known to affect the magnitude of the force, with larger and elongated particles experiencing larger DEP forces and torques.[45,47,48,49] Moreover, both the magnitude of force and the orientation of DEP torques can have a strong frequency dependencies for cases of dielectric particles with ohmic conductivities.[49]

In this work, regio regular poly-3-hexyl-thiophene (P3HT) is chosen as a model system to help us understand the origin of electric field alignment in conjugated polymers. P3HT is known to crystallize to form nanofibers and organogels under certain conditions and we demonstrate that this property is also an important factor in the alignment process.[50–53] We also show that controlled

polymer crystallization rates and AC electric fields of specific magnitude and frequency result in optimal alignment of conjugated polymer fibers. Moreover, the alignment is found to persist over micro-meter and nanometer scales. This work also demonstrates that electrical and mechanical properties are significantly altered by the electric field alignment process. Finally, we show that electric field alignment can be applied to several conjugated polymer systems and can be used over a wide range of polymer concentrations.

3.2 EXPERIMENTAL

3.2.1 *Materials*

Two lots of Poly(3-hexylthiophene) (P3HT) were purchased from Rieke Metals (Lincoln, NE): RMI-001E, lot# PTL12-67 (regioregularity=96%, M_w=71k, PDI=2.2) and RMI-001EE, lot# PTL14-85 (regioregularity=96%, M_w=69k, PDI=2.3). The SANS experiment was conducted with lot# PTL12-67 and the rest of the data was collected using lot# PTL14-85. The polymers were used after centrifugal purification of nanofibers to remove a significant fraction of the material that would not crystallize.[51] To achieve this, the original polymer was fully dissolved in toluene at ~80 °C at a concentration of 5mg/ml. It was then cooled down to 5ºC and allowed to fully self-assemble into nanofibers for more than 12 hrs. The samples were then centrifuged at ~7000 rpm for 30 min to sediment all of the fibers that were formed. The supernatant that contained an amorphous fraction of polymer was decanted and replaced with fresh toluene. The whole procedure was repeated 5 times before drying the purified sample for use. Gel permeation chromatography (GPC) was used to measure the M_w and PDI of the polymer using polystyrene standards. The molecular weight values of purified P3HT are similar to that of the original samples.

All other chemicals and solvents were used as received. Poly(3-butylthiophene-2,5-diyl) (P3BT), Poly(3-octylthiophene-2,5-diyl) (P3OT), Poly(3-decylthiophene-2,5-diyl) (P3DT), and Poly(3-dodecylthiophene-2,5-diyl) (P3DDT) were purchased from Rieke Metals. Poly(3,3’’’-didodecyl quarter thiophene) (PQT-12) and Poly[2,5-bis(3-dodecylthiophen-2-yl)thieno[3,2-b]thiophene] (PBTTT-C12) were purchased from Solaris Chem. The molecular weight and lot numbers are listed in Table 3.1. Hydrogenated solvents: dodecane (99%) and 1,2-dichlorobenzene (99%) were purchased from Sigma-Aldrich (St Louis, MO). Toluene (99.9%), chloroform (99.9%), acetone (99.7%) and 2-proponal (99.9%) were purchased from Fisher Scientific (Hampton, NH). Deuterated solvents: d4-1,2-dichlorobenzene (D>99%) and d26-dodecane (D>98%) were purchased from Cambridge Isotopes (Tewksbury, MA).

Table 3.1. Molecular weight and polydispersity index of polymer samples.

Polymers	Lot #	M_w	PDI
P3BT	BS19-36	41k	2.3
P3OT	PTL11-39	63k	1.9
P3DT	PTL11-77	57k	2.1
P3DDT	BS21-87	39k	1.8
PQT-12	DL158	40k	1.7
PBTTT-C12	16C0103	20k	1.55
Regiorandom P3HT	BS20-92	63k	2.4

3.2.2 *Optical Microscopy*

Silver was deposited *via* vacuum evaporation (10^{-7} Torr) over glass slides with a shadow mask that defined a 125 μm gap between parallel electrodes. An AC electric field was applied, depending on the voltage, with either an Agilent e4980a LCR meter or with a bipolar operational power supply amplifier (Kepco BOP 1000M) using a function generator (BK precision 4040DDS) as an input signal. An inverted microscope (Zeiss Axiovert 40 CFL) was coupled with a Lumenara camera (LU075M-ID) to take videos or images during the application of the electric field. Fast Fourier transform (FFT) of some images were performed using the software ImageJ.[54]

3.2.3 *Scanning Electron Microscopy*

An FEI XL830 dual beam scanning electron microscope was used to take SEM images. The substrate that was the same that was used to take optical microscopic images. The sample consisted of 0.3 mg/ml P3HT in 45 wt% dodecane and 55 wt% 1,2-dichlorobenzene. After alignment and drying, a thin layer of ~8 nm gold and palladium was evaporated onto the surface to enhance the conductivity of the sample in order to prevent charging during imaging.

3.2.4 *Rheology*

An Anton Paar MCR 301 stress controlled rheometer configured in a 25 mm parallel plate geometry with a gap of 0.5 mm was used for all rheological experiments. The parallel plates have ceramic insulation that electrically separates them from the instrument body and electronics. Electrical contact was made possible by a gold wire that loosely connected to the upper plate shaft while minimizing friction. The wire exerted a small but constant friction component on the shaft, which results in a measurable modulus for the fully dissolved polymers at early stages in the

measurement. In spite of this, the friction exerted by the samples as they form fibers is significantly larger than the friction of the wire and allows for estimation of the one-dimensional crystallization kinetics for all samples. The bottom plate was also connected by a wire and was electrically insulated from the rest of the instrument by a ceramic spacer. A schematic of the rheological setup can be found in previous publications [52]. This setup allows for the application of electric fields to achieve fiber alignment and also allows for analysis with dielectric spectroscopy after alignment is complete. A small shear strain perturbation with a frequency of 1Hz and amplitude of 0.25% strain, which is within the linear viscoelastic limit, were used for all tested samples[51,53]. At the start of every measurement, the rheometer plates were preheated to 60 °C before the fully dissolved sample (~80 °C) was loaded. A thin layer of a perfluorinated liquid (Fomblin Y 25/6) was added to the exposed edges of the sample to prevent solvent evaporation during testing. This was also similar to previously reported procedures that allowed for long time analysis (days) of volatile organic solvent samples [53]. Samples were then heated up to 80 °C, by using a Peltier heating/cooling element, to fully dissolve all of the polymer. They were then cooled down to 20 °C at a rate of 15 °C/min to induce the one-dimensional crystallization process. Data collection and electric fields were initiated as soon as the system started to cool down. It is worth noting that the cooling period (~240 seconds) is significantly shorter than the duration of the crystallization process (10^4 seconds).

3.2.5 *Small Angle Neutron Scattering (SANS)*

SANS experiments were conducted at the NIST Center for Neutron Research (NCNR) in Gaithersburg, MD. The SANS instrument NG7 was configured to cover a q-range of $0.003<q(Å^{-1})<0.5$, with two detector distances (13.5 m and 1m) and two different sample environments. These

q-values were chosen to allow probing of nanofiber alignment over distances corresponding from tens to hundreds of nanometers. A previously developed parallel plate cell [52] was used to probe the 'parallel' sample orientation (*i.e.* electric field parallel to the neutron beam). The cell consisted of an insulating polyether ether ketone (PEEK) body that holds two titanium metal plates acting as parallel electrodes with a gap of 1 mm. A new cell was also designed for the 'perpendicular' configuration (*i.e.* electric field perpendicular to the neutron beam). In this cell, the separation between electrodes was 1 mm and the size of the rectangular slit that defined the neutron beam was 0.5 by 0.8 mm. A laser-engraved quartz microscope slide with external dimensions of 1 - 50.8 - 25.4 mm (Ted Pella, Redding, CA) was used as an insulating spacer between two titanium electrodes that were attached with epoxy to encapsulate the sample. The dimensions of the inner rectangular sample enclosure are 12.7 by 25.4 mm. A small hole was also engraved with a laser cutter to facilitate loading the samples.

After filling with a dissolved polymer sample, the injection hole was sealed with epoxy to prevent any evaporation during the SANS test. Electric fields were applied, using variable voltage and frequency, with either a Keithley 2400 Source-Meter or a bipolar operational power supply amplifier (Kepco BOP 1000M) with an input signal from a function generator (Agilent 33220A). The samples were maintained at ~80 °C for more than one hour before testing in order to fully dissolve the polymer. During SANS tests, the temperature of the sample was controlled by a 10-position Heating/Cooling Block (10CB) with a recirculating heater/chiller. SANS data was reduced according to standard protocols[55] and, when possible, fit to a suitable model with SasView[51–53,56].

3.2.6 *X-ray diffraction (XRD)*

Samples were prepared by drop casting a 3.5 µL hot polymer solution over glass substrates containing two silver electrodes separated by a 1.58 mm gap. The electric field was applied for a duration of 30 min and, after alignment, the samples were dried in air before measurements. XRD experiments were conducted using a Bruker-D8 instrument with a Hi-Star 2-D detector and a Cu Kα x-ray source. The diameter of the circular x-ray beam was 300 µm. Out-of-plane scattering profiles were collected with an x-ray incident angle of $\omega=2.5°$ and 2θ ranging from 4° to 28°. The frame tilt angle was fixed at $\chi=90°$. The in-plane data was obtained using the following angles: $\omega=10°$, 2θ from 4° to 28° and $\chi=10°$. Scattering data that is 'perpendicular' (Figure 7(c)) and 'parallel' (Figure 7(d)) to the electrodes were realized by rotating the sample stage at $\varphi=0°$ and 90°, respectively.

3.2.7 *Atomic force microscopy (AFM)*

AFM images were recorded *via* Bruker Dimension Icon-PT atomic force microscope with peak force tapping mode. A scan of a 10 µm × 10 µm area was used. Samples for AFM were prepared by drop casting P3HT dissolved in 35 wt% dodecane and 65 wt% 1,2-dichlorobenzene solution over substrates with embedded parallel electrodes. To produce the AFM image in Figure 3.1, a Si wafer was used having a 200 nm thermally grown SiO_2 layer and patterned layers of chromium (12 nm) and gold (50 nm) in a parallel electrode system with a 100 µm gap. Gold and cadmium layers were patterned by a standard photolithography process. The frequency sweep experiments in Figure 3.8 and Figure 3.9 were conducted using P3HT samples coated over glass microscope slides with silver electrodes separated by 125 µm. The electric fields were applied for 20 min,

followed by a hexane wash to remove the high boiling point solvents. The samples were dried in air overnight before taking AFM images.

3.2.8 *Dielectric Spectroscopy*

AC dielectric spectroscopy experiment was carried out with Agilent e4980a LCR meter. The frequency range was between 20 Hz and 2 MHz with a perturbation voltage of just 20 mV. All the samples were measured between two stainless steel parallel plates as described in the rheology methods section. The possibility of electrode polarization affecting the results was also assessed with controlled experiments that are described in Figure 8.2. It was determined that electrode polarization effects did not significantly affect the data.

3.3 RESULTS

Real time microscopy videos can be found online [57], illustrate the evolution of aligned fiber growth under electric fields for 0.3 mg/ml of P3HT solution in 45 wt% dodecane solvent balanced with 55 wt% 1,2-dichlorobenzene and for 30 mg/ml P3HT solution in 25 wt% dodecane solvent balanced with 75 wt% 1,2-dichlorobenzene. Dodecane, a poor solvent for P3HT, was used to manipulate the supersaturation as previously demonstrated for organogels.[53,58] The polymer solution was fully dissolved at ~80 °C before drop-casting over a substrate held at 20 °C. An alternating electric field of 250 Hz and 160 V/mm was then immediately applied for the duration of the experiment. Initially, polymers remained dissolved because the temperature was not low enough for nucleation and crystallization to occur. A highly transparent and homogeneous solution was observed at the beginning of the experiment. Upon cooling, the solution underwent a clear

one-dimensional crystallization process[50] with polymer chains growing on nucleation sites in the electrodes to form micron-sized fiber structures that were visible under the optical microscope. The fibers grew in the direction parallel to the electric fields, starting from the edge of the 3 also demonstrate that the electric field alignment can work over distances up to several millimeters and with electrodes with highly complex geometries. In order to quantify and compare the alignment at different conditions, a fast Fourier transform (FFT) was used to process microscopy images in this work. Figure 3.1 (d) shows an example of aligned fibers in the raw optical microscopic image and Figure 3.1 (e) is its corresponding FFT image. Figure 8.3 Illustrates artificially generated alignment to better understand the FFT images.

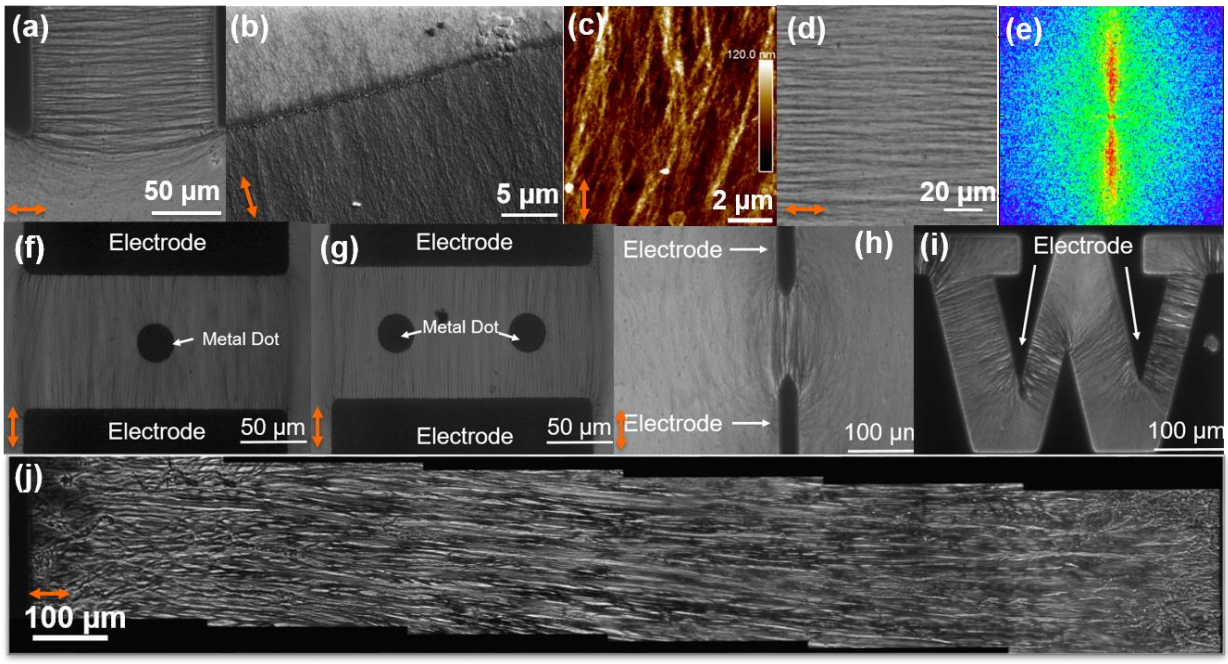

Figure 3.1. (a) Optical microscopic image of 160 V/mm 250 Hz electric field aligned P3HT, (b) SEM image of P3HT aligned with 160 V/mm 250 Hz, (c) AFM image of fibers aligned under 200 V/mm 2500 Hz, (d) Optical microscopic image of 160 V/mm 250 Hz electric field aligned P3HT and (e) its corresponding FFT. (f) ~ (i) Microscopy images of P3HT aligned using complex electrode geometries (j) Stitched optical microscopic images of 200 V/mm 250 Hz aligned P3HT

over 1.58mm gap. The arrow at the bottom left corner of each image indicates the direction of electric field.

The magnitude and frequency of the AC electric fields were systematically varied in order to identify their effect on the growth and alignment of P3HT fibers. Frequency was found to reach an optimum value for fiber alignment at ~250 Hz. Moreover, fiber alignment of good quality was only found to occur between 25 and 2500 Hz. Fast Fourier transforms (FFT) were also applied to raw images to facilitate comparisons of alignment quality (i.e. insets of Figure 3.2a). The electric field direction in all images was parallel to the x-axis. Since fiber growth was also parallel to the electric field, a high intensity is observed in the vertical direction (y-axis) of the FFT images. This is exactly analogous to the interpretation of x-ray or neutron scattering data from aligned rod-like objects.[59,60] An annular integration was performed within the range shown in Figure 3.2(a) 250Hz in order to quantify and compare the extent of alignment using one-dimensional profiles. The results of the integrations are shown in Figure 3.2(c). From this analysis, it became clear that the strongest alignment occurred at an intermediate frequency of 250 Hz. At this frequency, two dots appear in the FFT images, indicating strong alignment and a repeating characteristic fiber separation distance. This feature can be considered equivalent to Bragg peaks emerging in diffraction experiments due to aligned lamellar or cylindrical structures.[59,60] FFT images corresponding to higher (2.5 kHz) or lower (25 Hz) frequencies also resulted in alignment. However, the strong correlation in the separation distance was lost under these conditions. A much larger frequency of 250 kHz resulted in a homogenous structure with no alignment. DC fields (0 Hz) also resulted in loss of fiber alignment. An example video of real-time fiber formation under DC electric fields can be found in our publication. [57] It shows that the fibers are branched and relatively thick compared to those aligned with AC fields. The spacing between fibers is also inhomogeneous and alignment quality is very poor.

The amplitude of the electric field was also varied at a fixed frequency of 250 Hz in order to explore its influence on fiber alignment. In Figure 3.2(b), raw and FFT images are shown for experiments corresponding to amplitudes from 40 to 480 V/mm. The same integration area was used to generate one-dimensional profiles in Figure 3.2(d). The data suggests that the best alignment occurred at strengths of ~160 V/mm.

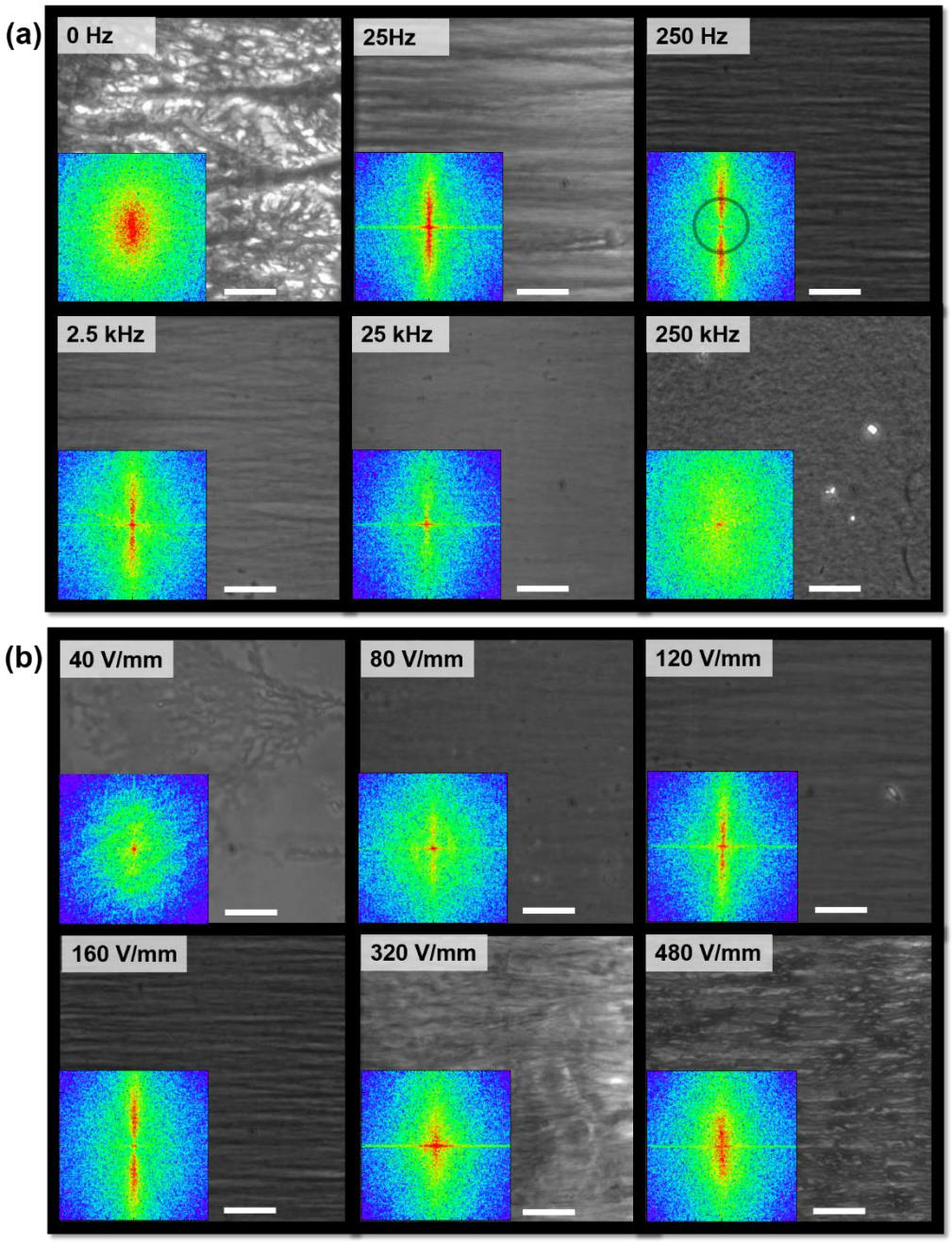
(a)
0 Hz
25Hz
250 Hz
2.5 kHz
25 kHz
250 kHz
(b)
40 V/mm
80 V/mm
120 V/mm
160 V/mm
320 V/mm
480 V/mm

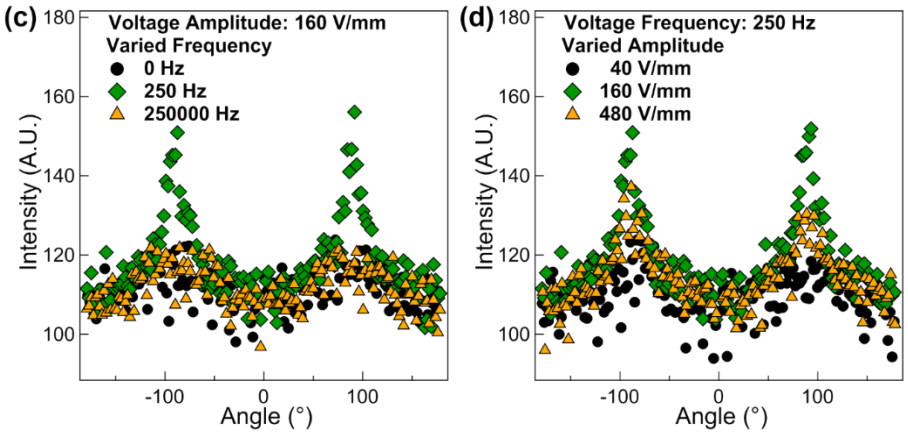

Figure 3.2. Microscope images of the fibers formed with 1 mg/ml P3HT in 25 wt% dodecane mixed with DCB under (a) varied frequencies between 0 and 250 kHz at fixed amplitude fixed at 160 V/mm and (b) variable amplitudes from 40 to 480 V/mm at 250Hz between two silver electrodes with a separation of 125µm. The scale bars represent 20 µm distance. The insets showed the corresponding fast Fourier transform images. Annular integrations of the 2-D FFT images corresponding to (c) fixed amplitude with varying frequencies and (d) constant frequency with changing amplitudes.

Besides electric field amplitude and frequency, the effect of changing supersaturation and crystallization kinetics was also studied by changing P3HT concentrations and by varying the dodecane ratio in the dichlorobenzene mixture (i.e. altering solvent quality). Detailed results from optical microscopy images of alignment are shown in Figure 3.3 ~ Figure 3.7. Alignment was observed over a wide range of P3HT concentrations from 1 to 30 mg/ml but the quality of the film would vary. In addition, control over polymer concentration and solvent quality was found to be important to achieving a high degree of alignment.

The effect of changing crystallization kinetics was investigated by varying P3HT concentrations as is shown in Figure 3.3. Although fiber alignment was observed at all concentrations, the degree of order varied significantly. In FFT images, the vertical lines at higher concentrations shifted

towards lower k_y values, which corresponded to increased size and broader distribution. It is interesting to note that the optimum electric field condition would not change with increasing concentrations. Experiments performed with variable frequency and amplitude using a more concentrated sample (30 mg/ml P3HT) resulted the same optimum conditions as for 1 mg/ml P3HT. The optical microscopic images and the corresponding FFT images of the electric field sweep of 30 mg/ml P3HT are shown in Figure 3.4 ~ Figure 3.6.

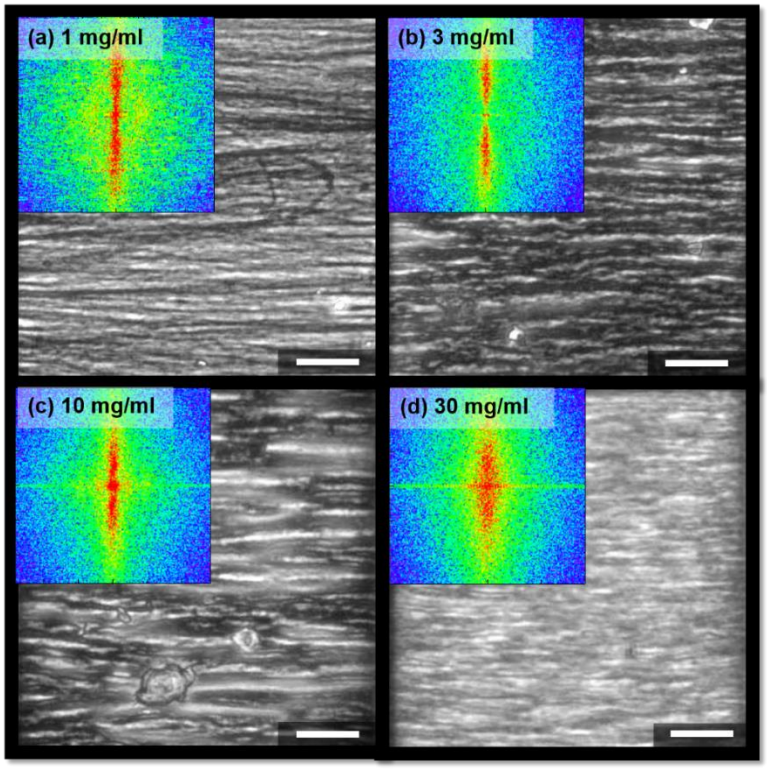

Figure 3.3. Microscopic images of P3HT fibers aligned under 160V/mm 250Hz in 25% wt dodecane mixed with dichlorobenzene at concentrations of (a) 1 (b) 3 (c) 10 (d) 30 mg/ml. The insets showed the corresponding FFT of each concentration. The scale bars represent 20 μm.

Experiments with variable frequency and amplitude were also performed using samples with larger P3HT concentration. Figure 3.4 and Figure 3.5 demonstrate that an optimum condition for alignment is also observed for these samples. Annular integrations were summarized in Figure 3.6

for different electric field conditions. Interestingly, these conditions seem to be very close to the optimum frequency (250 Hz) and amplitude (160 V/mm) that were observed at the lower P3HT concentrations (1 mg/mL) that are shown in Figure 3.2. However, it is important to note that the quality of the aligment was significantly higher when lower concentrations of polymer were being used. It is very likely that this is also due to the difficulties that arrise when trying to image the thicker and more opaque samples that result when using the higher concentrations of P3HT.

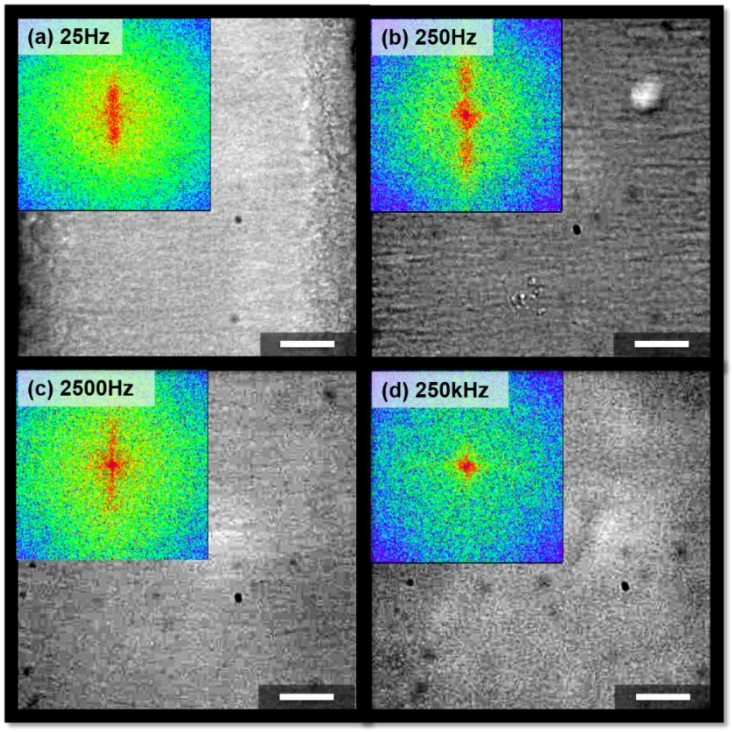

Figure 3.4. Microscopic images of 30mg/ml P3HT in 25% dodecane balanced with 75 wt% 1,2-dichlorobenzene under 160V/mm and (a) 25 (b) 250 (c) 2500 (d) 250000 Hz electric fields. The insets showed the corresponding FFT images and the scale bars represent 20 µm.

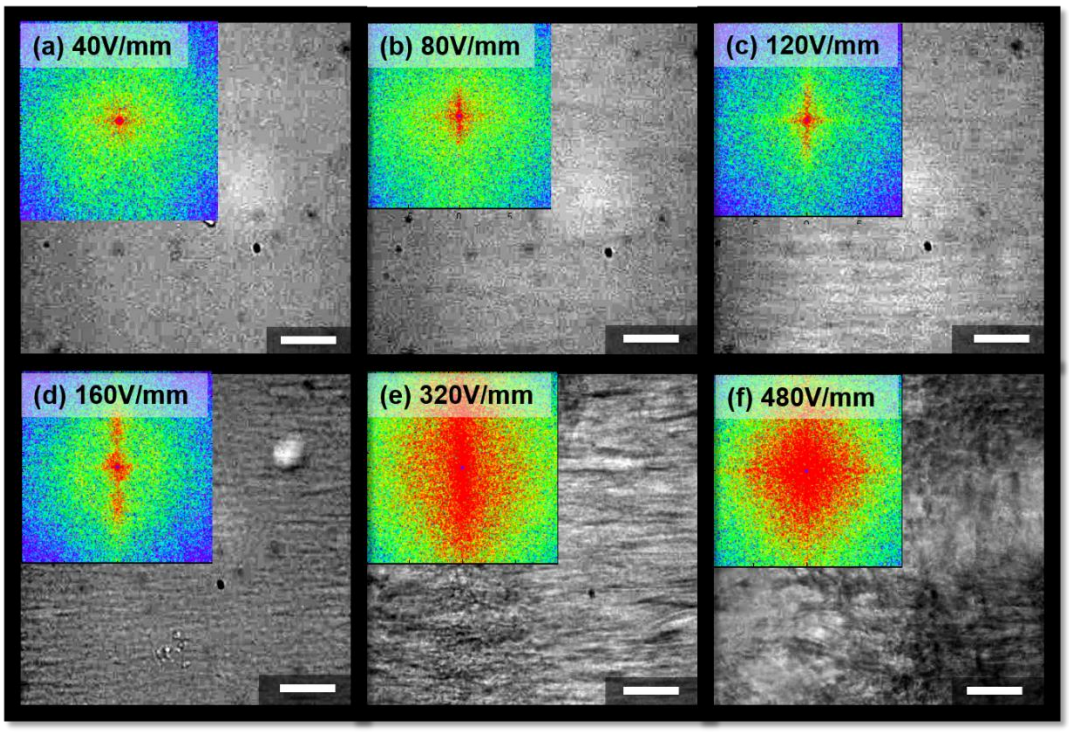

Figure 3.5. Microscopic images of 30 mg/ml P3HT in 25% wt dodecane mixed with 75 wt% 1,2-dichlorobenzene under 250Hz and (a)40 (b) 80 (c) 120 (d) 160 (e) 320 (f) 480 V/mm electric fields applied between two silver electrodes with 125µm gap. The insets show the FFT of the optical imgaes and the scale bars represent 20 µm.

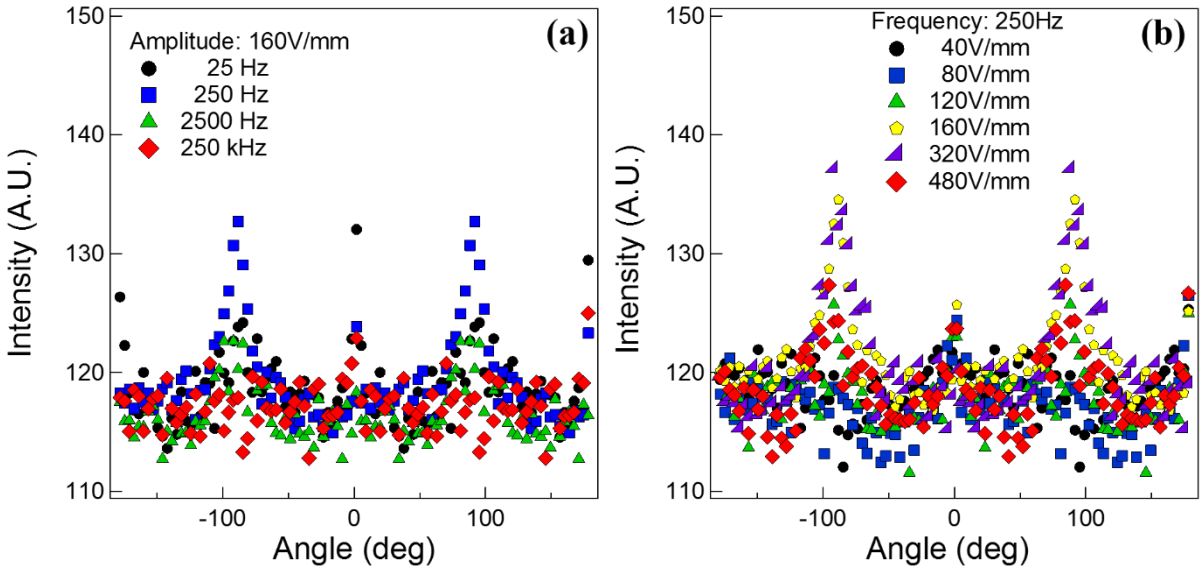

Figure 3.6. Annular integrations of the 2-D FFT images in Figure 3.4 and Figure 3.5 of electric fields (a) fixed amplitude with varying frequencies and (b) constant frequency with changing amplitude.

Dodecane is a poor solvent for P3HT so that a higher fraction in the solvent results in higher supersaturation and faster nucleation and growth for the fibers.[58,61,62] Figure 3.7 shows the results of experiments performed for a series of samples (30 mg/mL P3HT) having different dodecane ratios under identical electric field conditions (250 Hz and 200 V/mm). In pure dichlorobenzene solutions, Figure 3.7(a), P3HT remained fully dissolved and no self-assembly occurred before the evaporation of the solvent. As a result, FFT images are homogeneous and no alignment or fiber formation is visible. When the dodecane content was increased, the formation of aligned fibers was observable and reached a maximum alignment at a dodecane fraction of 25 wt%. In contrast, when the dodecane ratio was increased to 40 wt%, the supersaturation was very high and the kinetics of crystallization was too fast to allow for organized alignment to occur. An elastic

organogel formed quickly and fibers interconnected before the DEP force was able to transport them along the electric field gradient.

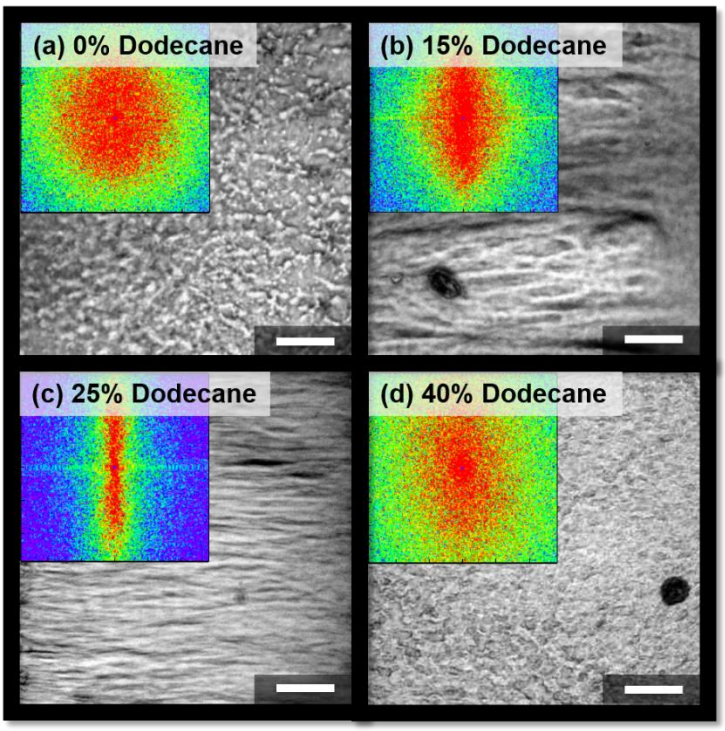

Figure 3.7. Microscopic images of P3HT fibers after gelation in mixed solvents of (a) 0% (b) 15% (c) 25% and (d) 40%wt dodecane balanced with dichlorobenzene under 250Hz 200V/mm electric field. The insets are the corresponding FFT images and the scale bars represent 20 µm.

In order to obtain information on fiber alignment over nanometer scales, atomic force microscopy was also utilized. Samples with both 1 and 0.1 mg/ml concentrations were prepared and aligned under variable frequencies and the results are shown in Figure 3.8 and Figure 3.9. AFM results are consistent with those of optical microscopy images showing evidence of the existence of an optimum frequency for alignment. To further complement AFM experiments, small angle neutron scattering (SANS) was also used to provide detailed information of the samples over nanometer sizes. Figure 3.10(a) shows a schematic of the setup used for neutron scattering experiments. The

sample environment was a cell with an engraved quartz slide (1 mm thick) sandwiched between two titanium plates acting as electrodes. The dimensions of the engraved sample enclosure were 1” by 0.5” as shown in Figure 3(a). The incident neutron beam in this configuration was perpendicular to the electric field. The resulting SANS scattering patterns after electric field application are shown in Figure 3.10(b). The 2-D scattering pattern was also reduced to a 1-D profile by integrating along the annular region centered at q=0.01 $Å^{-1}$. This allows for quantitative comparison of alignment under different field conditions. In general, results were also consistent with microscopy experiments despite the significantly larger electrode separation distance. Optimum alignment conditions were again found at 250Hz with electric field amplitudes between 200 and 400 V/mm. The q-range of the 2-D scattering patterns corresponds to probing characteristic dimensions between ~20 and ~200 nm in real space. For comparison, typical dimensions of P3HT nanofibers are ~5 by ~25 nm in cross-section and several micrometers in length.[50] Thus, this instrument configuration characterizes the largest structures that are possible to probe with SANS, which are also more likely to show clear indications of fiber alignment. In order to further extract quantitative information from the SANS data, 2-D fitting was performed on profiles with clear signs of alignment under electric field conditions (i.e. 200 V/mm and 400 V/mm at 250 Hz). The details and results of the 2D fits are shown in Figure 8.4 and Figure 8.5. This analysis shows that the fiber cross-sectional size is similar for both aligned conditions. However, there were differences in the level of alignment that was achieved since the electric field with larger amplitude resulted in more aligned fibers with smaller angular variations. SANS experiments successfully demonstrate that alignment of P3HT fibers persists from micrometer (microscopy) to nanometer scales. SANS experiments on samples exposed to direct current (DC) fields led to a homogeneous pattern showing no signs of alignment.

Figure 3.8 shows the atomic force microscopic images of 1 mg/ml P3HT aligned at variable frequencies. In Figure 3.8 (a) to (c) it is clear that the micron size fibers, which consist of bundled nanofibers, are aligned unidirectionally and formed at lower frequencies (i.e. 25 Hz and 250 Hz). The height of the fiber bundles formed at 25 Hz is higher than that of 250 Hz on the surface. At higher frequencies (i.e. 2.5-250 kHz) corresponding to Figure 3.8 (d) to (f), the long-range order deteriorates gradually and the fiber heights are reduced. To rule out the possibility that this loss of order at high frequencies was due to the formation of very thick samples, samples at much lower P3HT concentrations (0.1 mg/ml) were also prepared and analyzed with AFM. These results are shown in Figure 3.9. A dependence of alignment on frequency was also found for these samples and no alignment was observed above 2.5 kHz.

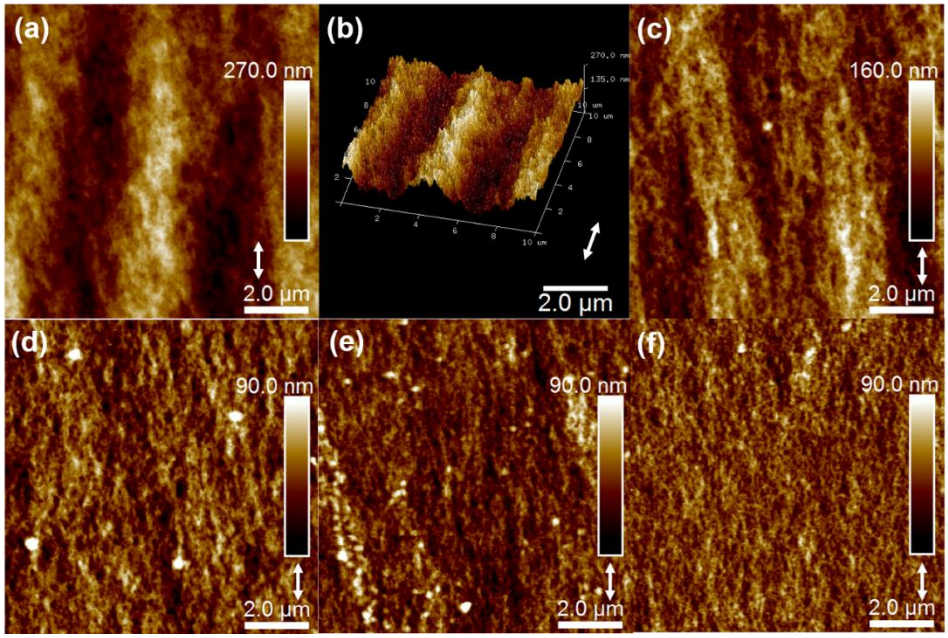

Figure 3.8. AFM images of 1 mg/ml P3HT in 25 wt% dodecane and 75 wt% 1,2-dichlorobenzene aligned under 160V/mm and (a) 25 Hz, (c) 250 Hz, (d) 2.5 kHz, (e) 25 kHz, and (f) 250 kHz electric field. Figure 5(b) is the 3-D view of Figure 5(a). The arrow at the bottom right corner of each image represents the direction of the electric field.

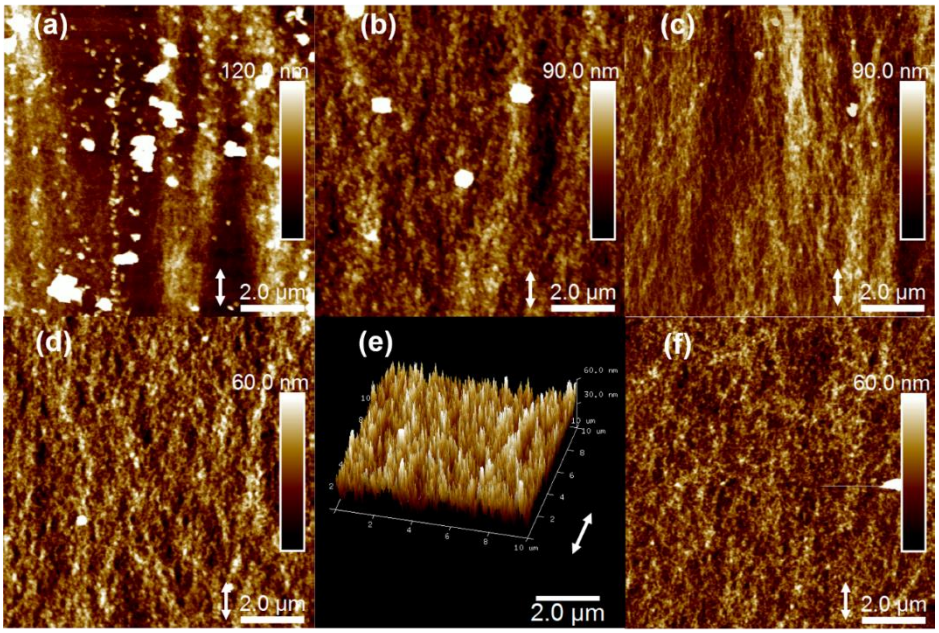

Figure 3.9. AFM images of 0.1 mg/ml P3HT in 25 wt% dodecane and 75 wt% 1,2-dichlorobenzene aligned under 160V/mm and (a) 25 Hz, (b) 250 Hz, (c) 2.5 kHz, (d) 25 kHz, and (f) 250 kHz electric field. (e) is the 3-D view of (d). The arrows at the bottom right corner indicate the direction of electric fields.

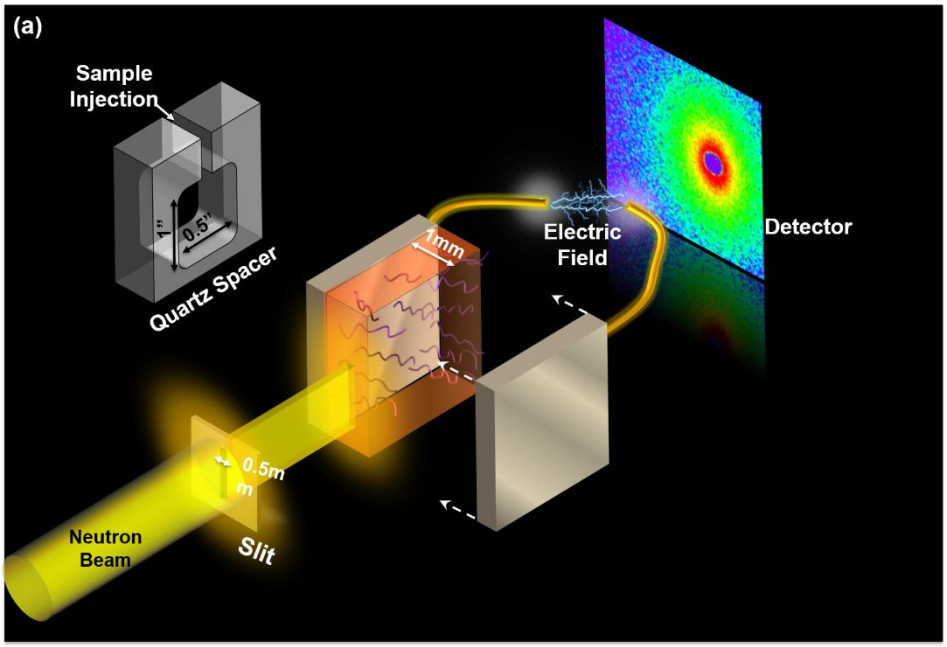

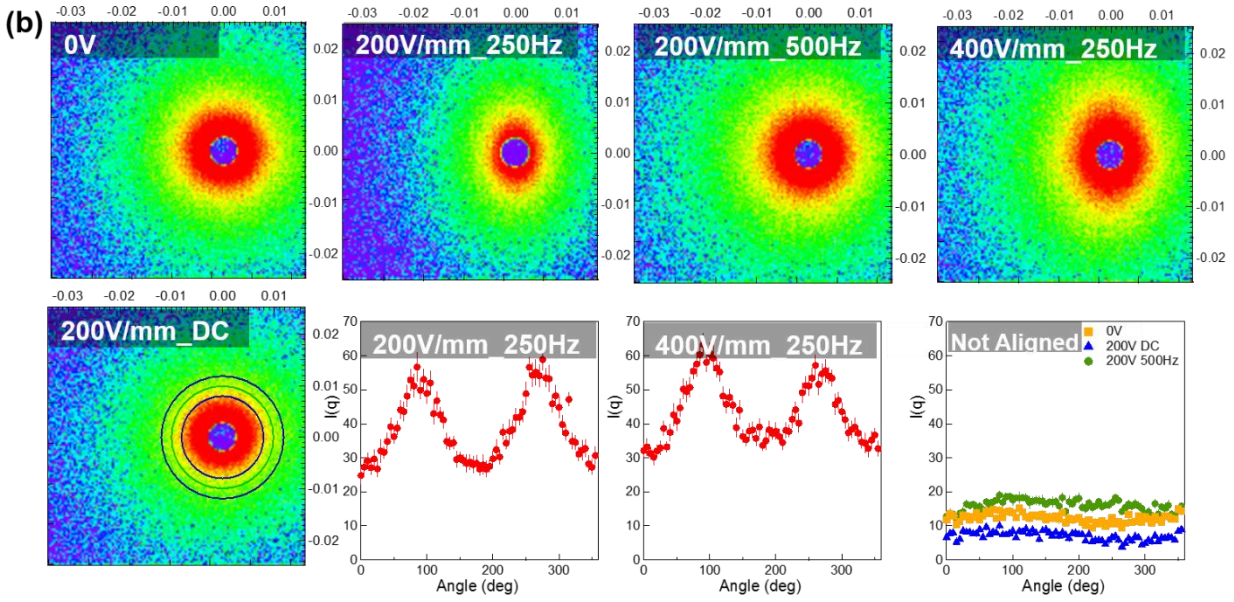

Figure 3.10. (a) Schematic representation of the SANS experiment with incident beam perpendicular to the electric field. (b) SANS 2-D patterns of P3HT fibers aligned under 0 V, 200 V/mm 250 Hz, 200 V/mm 500 Hz, 400 V/mm 250 Hz and 200 V/mm DC electric field at 13 m detector distance. Annular integrating was performed at q=0.01 $Å^{-1}$ as shown for the sample of 200 V/mm DC.

Since P3HT nanofibers are usually one-dimensional crystal structures, XRD experiments can provide insight on the relative orientation of individual polymer chains after electric field alignment. Figure 3.11 (a) and (b) shows both in-plane and out-of-plane scans of the x-ray beam perpendicular and parallel to the electrodes. Schematics shown in Figure 3.11 (c) and (d) help to explain the different orientations that were used in the experiments. An anisotropic structure was observed, leading to differences in the scattering profiles for different sample orientations (*i.e.* parallel or perpendicular to the electrode) with respect to the x-ray direction. In Figure 3.11(a), only the electric field aligned sample, abbreviated as EF, showed well defined lamella peaks at the orientation where the x-ray beam was parallel to electrodes. This was an indication of high

crystallinity. Neither of these conditions showed π-π stacking peaks at 2θ=23º for the out-of-plane scan, which suggests that the thiophene rings were mostly oriented perpendicular to the substrate (*i.e.* 'edge-on' conformation). In Figure 3.11(b), the in-plane π-π stacking peak was very well defined when the x-ray beam was parallel to the electrodes for aligned samples, whereas no peaks appear with the beam parallel to the electrodes. In contrast, samples without applying electric field (*i.e.* no electric field or NEF) exhibited clearly defined π-π stacking peaks for both orientations. Moreover, both of the π-π stacking peaks were lower than the peaks in the electric field aligned sample with the x-ray beam oriented parallel to the electrodes. This suggests that the π-π stacking direction was along the fiber growth direction for aligned samples and randomly oriented in the absence of an electric field. This also explains the difference in lamellar peaks observed in the out-of-plane scan in Figure 3.11(a). It was noticed that the beam parallel to the electrodes had sharper lamellar peaks than the perpendicular case. Since the thiophene plane was perpendicular to the substrate (*i.e.* edge-on) and the π-π stacking direction was along fiber growth direction, lower intensity peaks are expected with the beam perpendicular to the electrodes due to a shorter correlation along the width of the fibers *versus* along the length. The proposed orientation of the electrically aligned fibers is shown in the schematic (Figure 3.14) in the discussion section. The lamellar and π-π stacking peaks were also fit to a Gaussian function in order to quantify their location and to estimate their characteristic distances from Bragg's law. This analysis shows that the lamellar spacing distance (lamellar = 1.66 nm) remains constant regardless of the electric field conditions. The π-π stacking distances showed a very small increase between samples aligned with electric fields (π-π stacking = 0.39 nm) when compared to a sample that was not exposed to electric fields (π-π stacking = 0.38 nm).

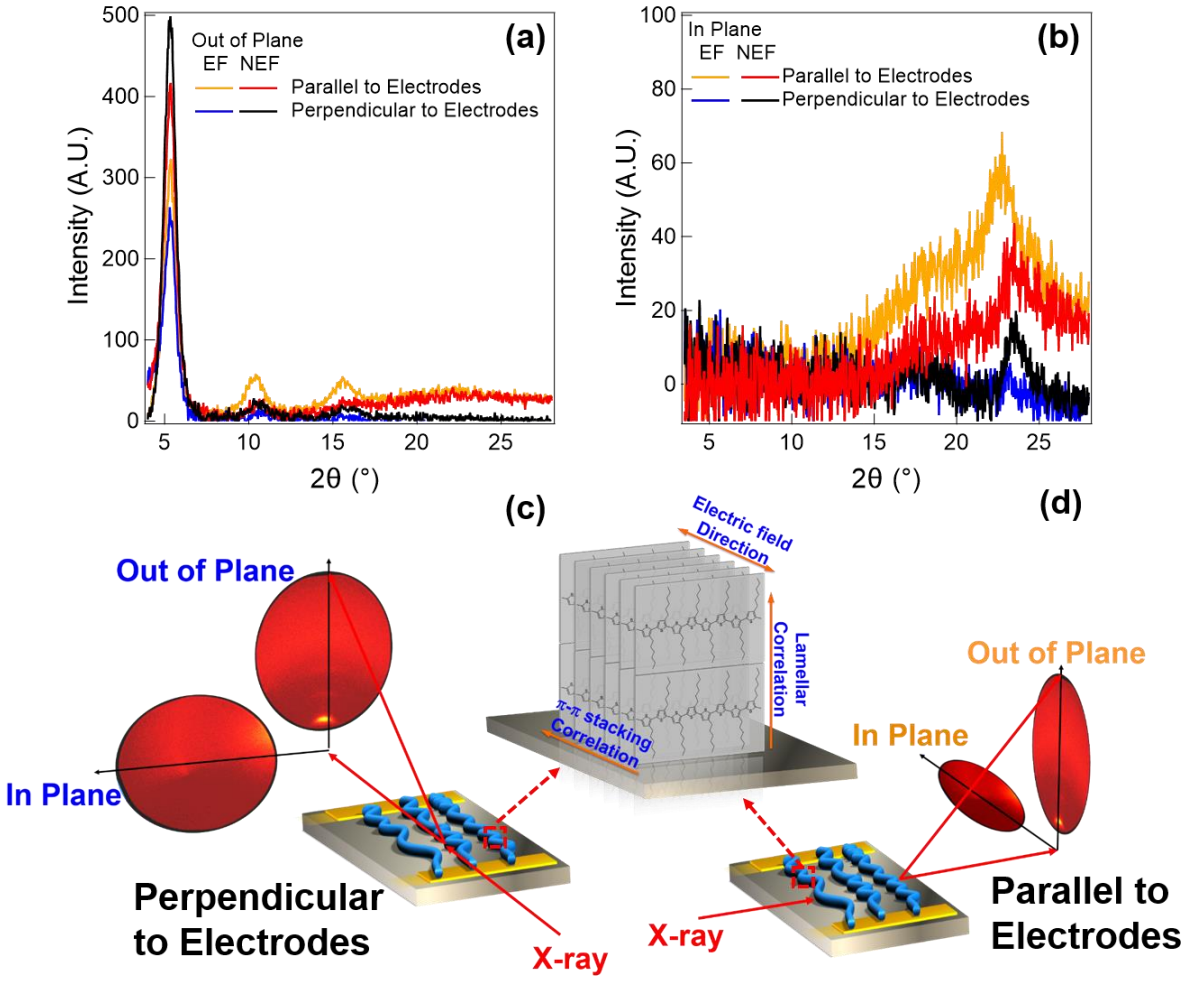

Figure 3.11. XRD of (a) Out-of-plane and (b) in-plane scans of the 200 V/mm 250Hz electric field aligned 3 mg/ml P3HT samples in 25 wt% dodecane mixed with DCB, as well as the reference samples without applying electric field. Schematics in (c) and (d) show the geometry of x-ray beam relative to the sample orientation, as well as the detector position for configurations both 'perpendicular' and 'parallel' to electrodes.

Changes in shear modulus for samples formed under different conditions were also monitored by small amplitude oscillatory rheology with and without electric fields in Figure 3.12. Error bars (*i.e.* one standard deviation) are calculated from three repetitions (Figure 8.6). In these experiments, the complex shear modulus (G*) was recorded as a function of time as the sample was cooled to

induce nanofiber formation while an electric field was applied between the parallel plates of the instrument. In all experiments, samples started as viscous polymers solutions followed by a rapid increase of the modulus, which was an indication of the initiation of crystallization and gelation. More than 80% of the increase in modulus occurs within the first 3000s. As indicated by Liu, *et al*., the slope of the complex modulus at the time it starts to gel (t_g) is proportional to the growth rate of the crystalline structures (i.e. nanofibers) that give rise to the increase in modulus.[62,63] Using this model, estimates of the fractal dimension (D_f^R) can also be extracted from the kinetics of crystallization originating from the modulus data.[63] Equation (3.1) corresponds to the analysis proposed by Liu, *et al.*, where G^* is the time-dependent complex modulus, t_g is the gelation time and k^0 is a constant that is related to both the crystal growth rate v_g and the fractal dimension D_f^R. Results from this analysis, corresponding to samples with and without electric field alignment, are listed in Table 3.2. The full analysis of the experimental data is also shown in the Figure 8.7. The fractal dimension for AC electric field aligned samples was close to 1, indicating unidirectional growing structures. In contrast, in the absence of an electric field the value was 1.3, which was significantly higher. Moreover, the modulus of fibers formed under an AC electric field was more than 1.6 times higher than that of the reference sample with no field. In contrast, DC electric fields weakened the structure and reduced the final modulus by about 10 times. A fractal dimension of 1 was also obtained for samples aligned in DC fields but the analysis has significant uncertainty due to the very weak nature of this organogel. Optical microscopy (Figure 3.2) and movie online [57] show that gelation under DC electric fields results in highly branched and disordered structures.

A separate set of fractal dimension values could also be estimated by fitting the SANS data ($\boldsymbol{D_f^S}$) over the low-q region (0.0033 to 0.007 $Å^{-1}$) while using a power law function. Fits to the SANS data are shown in the Figure 8.8 and the results of the analysis are also included in Table 3.2. Due

to the anisotropic patterns that are observed in aligned samples, the extraction of fractal dimension values is performed along the horizontal axis of the 2D data, which corresponds to the long axis of the fibers. Annular integration can be used for samples exposed no fields and to DC field conditions because there is no anisotropy or signs of alignment. The fractal dimensions obtained from SANS consistently show larger values than those obtained from rheology. However, the general trend is consistent with the observation that fibers aligned under electric fields are closer to a linear structure (i.e. $D_f \sim 1$) than those at all other conditions. It must be noted that rheology estimates fractal dimension from modelling the rate of growth of fibers that lead to mechanical changes. In contrast, SANS allows for a direct characterization of the fractal fiber structure but only with sensitivity over smaller length scales due to the limited q-range. Notably, when extracting fractal dimensions from rheology for DC electric fields, the measured modulus was 10 times lower than that of samples in AC fields or in the absence of electric fields. This indicated very weak percolation, and resulted in significant uncertainty when extracting a fractal dimension using rheology for the DC sample. This also lead to a large discrepancy between SANS and rheology for these samples. The fractal dimension of DC sample (D_f^S) obtained from SANS data is above 3, which indicates Porod scattering resulting from large aggregates formation.

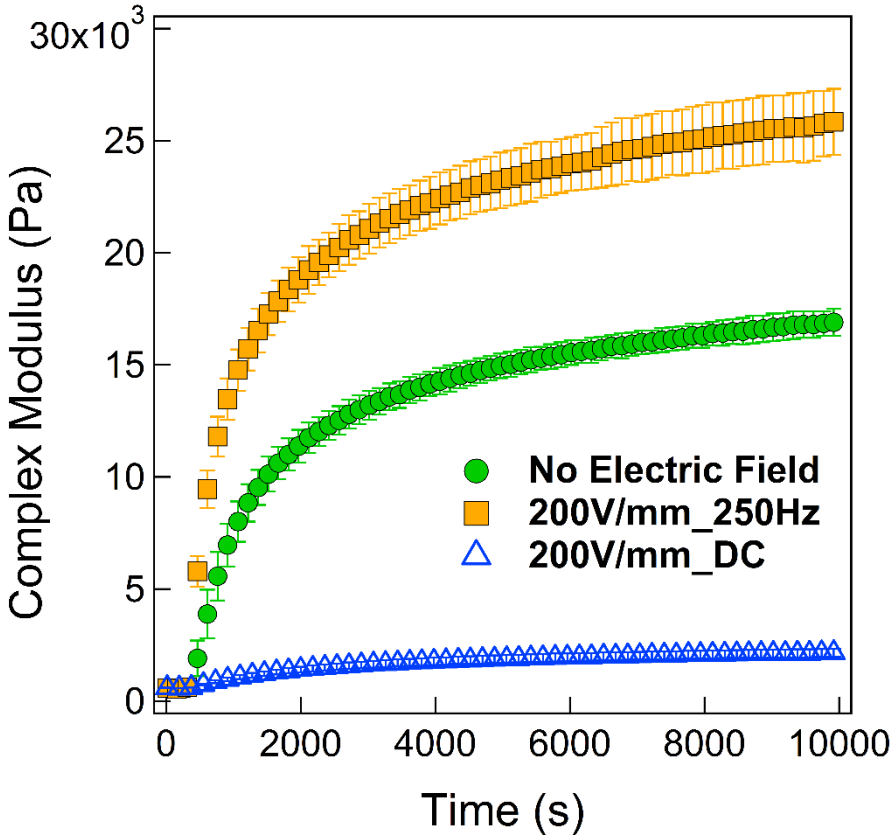

Figure 3.12. Complex modulus for 30 mg/ml P3HT samples in 25 wt% dodecane mixed with DCB formed with 0, 200 V/mm 250Hz and 200 V/mm DC electric fields as a function of time.

$$\ln\left[1-\frac{G^*(t)-G_0^*}{G^*(max)-G_0^*}\right]=-k^0(t-t_g)^{D_f} \qquad (3.1)$$

Table 3.2. Fractal dimension (D_f^R) and constant k^0 obtained from rheology measurement, as well as fractal dimension (D_f^S) extrapolated from power law fitting of SANS data.

	0V	200V/mm 250Hz	200V/mm DC
D_f^R	1.31	1.03	1.00
D_f^S	2.59	1.20	3.16
$k^0\times10^4$	1.45	11.86	4.88

Impedance spectroscopy was also performed on samples after completion of the rheological experiments in order to probe for enhancement of the electrical conductivity. Figure 3.13 shows impedance spectroscopy data for P3HT organogels formed with AC, DC and without electric fields. Figure 3.13(a) shows the Nyquist plot of the gels 30 min after electric field application. Similar to the reduced shear modulus, the application of DC electric fields also drastically reduced the electrical conductance. The impedance of the sample under DC fields increased by a factor of 10. Figure 3.13(b) shows the dielectric permittivity (□') as a function of frequency. The major difference appeared between 20 and 100 kHz. AC aligned organogels showed the highest permittivity, especially in the low frequency region (< 1 kHz), whereas applying DC fields would reduce the permittivity by about one order of magnitude. The dielectric loss, ε", as a function of frequency is also plotted in the Figure 8.9 (a). The imaginary and real parts of the conductivity are also shown in Figure 8.9 (b) and (c), respectively. It is clear that the AC electric field enhances the conductivity and the DC field significantly reduces it across the whole range of frequencies probed.

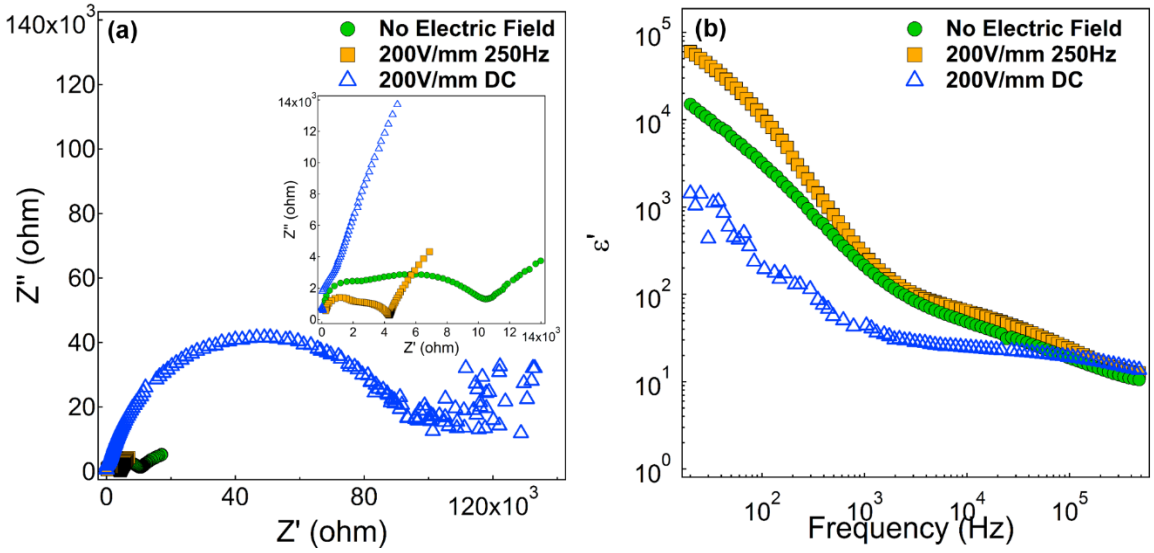

Figure 3.13. (a) Nyquist plots of 30 mg/ml P3HT organogels in 25 wt% dodecane mixed with DCB that have been formed with AC, DC, and no electric field in the rheology setup. Inset shows an enlarged plot of the same data. (b) Permittivity as a function of frequency for the same samples.

3.4 Discussion

3.4.1 *Influence of dielectrophoresis (DEP) on fiber alignment*

We propose that the primary mechanism of fiber alignment is due to dielectrophoresis (DEP) as shown in Figure 3.14. However, we also note that electrophoresis is also possible and can play an important role in the alignment process at low frequencies, which will be discussed further in section 3.4.3. The DEP force is known to be proportional to particle size and to the electric field gradients. At high temperatures (~80 °C) and in good solvents, the conjugated polymers are fully dissolved and too small to experience strong DEP forces. Upon cooling down samples or reducing solvent quality, supersaturation drives polymer chains to crystallize and to form larger fibers.[51–53] Nucleation of new fibers can happen in the bulk or start from the edge of the electrodes, where

nucleation may be further enhanced by high electric field gradients. It has been previously reported, for several other systems, that electric fields can help enhance nucleation.[64–67] Growing fibers, will eventually reach a critical size where the DEP force becomes strong enough to induce transport towards the edge of the electrodes, where the largest electric field gradients are observed. At the same time, for anisotropic particles, such as P3HT nanofibers, DEP torques can also emerge due to these gradients and they will tend to orient the long axis along the field lines. Consequently, fibers will grow mostly in the direction perpendicular to the electrodes with the polymer chains aligned perpendicular to the electric field direction. Moreover, since the polymer is conductive, fibers that grow from the edge of the electrodes will further alter the local electric field and produce large gradients at the tip of the fiber. Therefore, the tips of growing fibers eventually produce the strongest localized DEP forces enabling increased accumulation of polymer material and further accelerating growth.

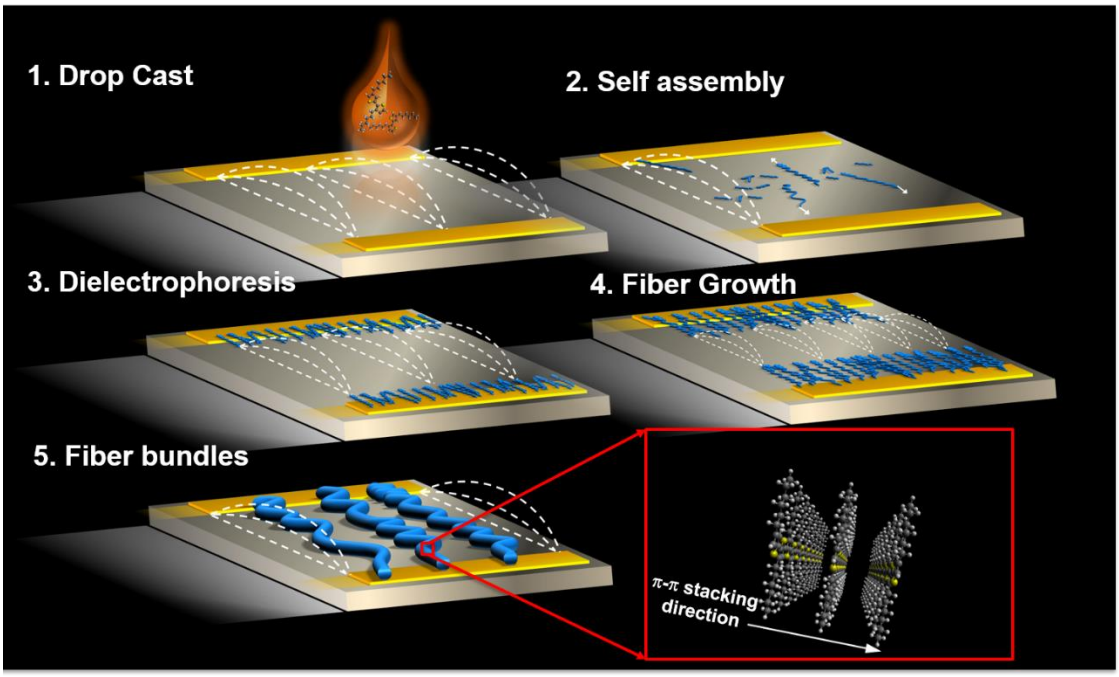

Figure 3.14. Proposed mechanism of directed fiber growth and alignment under electric fields, including one-dimensional crystallization of nanofibers, dielectrophoretic advection, and growth.

3.4.2 *Estimation of DEP forces and torques acting on growing fibers*

The quantitative estimation of the relationships between DEP force and the determining parameters for elongated particles, which are approximated as ellipsoids, are shown in equation(3.2)(3.2)to (3.4), where P_{eff} is the effective dipole moment, $\boldsymbol{\varepsilon_1}$ is the dielectric constant of P3HT, $K(\omega)$ is the Clausius-Mossotti function, a, b, c are the axis dimensions of ellipsoids and ∇E is the gradient of the electric field. [48,49] It is worth noting that compared with spherical particles, the elongated structures can significantly increase the DEP force by several orders of magnitude. [48] In equation (3.4), the parameters ε_1, σ_1 are the dielectric permittivity and conductivity of the particles and ε_2 and σ_2 correspond to the medium, L_α is the depolarization factor, which can be

calculated from equation (3.5), and ω is the angular frequency. The real part of Clausius-Mossotti function is also plotted in Figure 8.12.

$$F_{DEP} = P_{eff} \cdot \nabla E \quad (3.2)$$

$$F_{DEP} = 2\pi\varepsilon_1 a^2 b Re|\underline{K(\omega)}|\nabla E^2 \quad (3.3)$$

$$\underline{K(\omega)} = \frac{(\underline{\varepsilon}_2 - \underline{\varepsilon}_1) - j(\sigma_2 - \sigma_1)/\omega}{3[\underline{\varepsilon}_1 + (\underline{\varepsilon}_2 - \underline{\varepsilon}_1)L_\alpha] - 3j[\sigma_1 + (\sigma_2 - \sigma_1)L_\alpha]/\omega} \quad (3.4)$$

$$L_\alpha = \frac{abc}{2}\int_0^\infty \frac{ds}{(s+a^2)\sqrt{(s+a^2)(s+b^2)(s+c^2)}} \quad (3.5)$$

In order to estimate the magnitude of DEP forces, the spatial distribution of the electric field gradients for planar electrodes (AFM, microscopy) and parallel plates (SANS, Rheology) were first obtained from finite element analysis (FEM) (Figure 8.10 and Figure 8.11). FEM allowed us to quantify and estimate the local electric fields based on geometric parameters for each electrode configuration and the results were used to determine the direction of particle movement under DEP forces. Since the presence of conductive nanofibers is expected to significantly affect the electric field gradients, the electric field distribution that is calculated from FEM is only relevant to the early stages of alignment. Interestingly, although the gradient of the electric fields between two perfectly flat parallel plates is ideally uniform, the roughness of the electrodes can introduce high local electric field gradients that can lead to fiber nucleation. A detailed discussion of the electric field gradients can be found in 8.2.6.

In addition to the DEP force, torques on the nanofibers generated by DEP were also considered. The stable orientation of a dielectric ellipsoid with ohmic loss in an external electric field depends on the frequency.[49] Torques were calculated from equation (3.6), which is a function of the particle shape, permittivity, and conductivity of both the particles and the medium.[49] The subscripts α, β, γ are in the order of x→y→z→x, based on the convention of the right-handed coordination system. $E_{0,\beta}$ and $E_{0,\gamma}$ represent the electric field components on corresponding axes.

The sign of the torque components on each of the three axes (*i.e.* $<T^e>_x$, $<T^e>_y$, and $<T^e>_z$), which depend on $\left(L_\alpha - L_\beta\right)Re[\underline{K_\beta}\underline{K_\gamma}]$, determine the most stable orientation of the particles. The stable orientation corresponding to every possible combination of the torque signs on each axis are summarized by Jones.[49] For our system, these terms are plotted as a function of frequency in Figure 8.12, assuming a 200 nm long nanofiber with a cross-sectional dimension of 4 nm by 20 nm. [50] Over all of the probed frequency ranges, $<T^e>_x$ and $<T^e>_z$ are both positive and $<T^e>_y$ is negative. This means that the most stable particle orientation for our system is always with the long fiber length oriented along the electric field direction.[49] A decrease in torque at high frequencies can also serve to explain the loss of alignment that is observed in experiments (Figure 3.2).

$$< T^e >_\alpha = \frac{2}{3}\pi abc\varepsilon_1\left(L_\alpha - L_\beta\right)E_{0,\beta}E_{0,\gamma}Re[\underline{K_\beta}\underline{K_\gamma}] \qquad (3.6)$$

3.4.3 *Effect of electric field frequency and amplitude, particle size, and supersaturation on fiber alignment*

The strong frequency dependence shown in Figure 3.2(a) and in the SANS measurements (Figure 3(b)) suggest that the mechanism of directional assembly is governed by DEP. The DEP force is a function of frequency dependent parameters, such as the relative dielectric permittivity and conductivity, between P3HT and the suspending medium. The estimated force is shown in Figure 8 as a function of frequency. Here, it is assumed that the permittivity and conductivity of the P3HT chains and nanofibers are the same as that of the bulk P3HT organogels, which are obtained from dielectric spectroscopy measurements in Figure 6. The results show that the DEP force increases with decreasing frequency, which leads to the loss of alignment above ~1 kHz. At frequencies lower than 25 Hz, the origin of the reduced alignment is attributed to a competing electrophoresis effect that takes place simultaneously to DEP. It has been confirmed by zeta potential

measurements (Figure 8.13) that P3HT nanofibers are positively charged (~100 mV) under these conditions. The origin of these charges is still uncertain but it could be due to partial doping of the polymers. Still, it is important to note that DEP force can act on all particles in non-uniform electric field, no matter if they are charged or not, while electrophoresis requires that the particles have significant surface charges. Video S3 shows characteristic fiber growth in a DC field, which always results in poor quality alignment. Interestingly, in the video some fibers originate from the positive electrode, which shares the same charge as P3HT fibers. In addition, growing fibers that are thin and mobile are clearly pulled towards the negative electrode. Our hypothesis is that, at lower frequencies, both electrophoresis and DEP are playing important simultaneous roles in the alignment process. The appearance of fibers at a random and heterogeneous spacing from the edge of the electrodes suggests that local features in the electrodes lead to preferential nucleation. We believe that the shape and microstructure of the electrodes can affect local field gradients and increase local DEP in these spots. At the same time, evidence of electrophoresis is also clearly observed when fibers are pulled towards the negative electrode. This results in the formation of thick and disorganized fiber arrays for all DC experiments performed in this work. At a medium to high AC field frequency (> 25 Hz), electrophoresis is largely suppressed because the electric field is reversed quickly, relative to transport time-scales, but DEP continues to play a significant role. The decline of electrophoresis at high frequencies has been previously demonstrated by Burt et al. using charged bacteria. [68] Electrophoresis was observed to compete with dielectrophoresis at 1 Hz but only DEP dominated when the frequency was increased beyond 10 Hz. Therefore, at higher frequencies, DEP leads to the formation of homogeneous and highly oriented fiber arrays. However, if the frequency is increased to very high values (>100 kHz) the DEP force also starts to decay due to the decrease in dielectric permittivity of the material (Figure 3.13(b)). At this high

frequency range, both electrophoresis and DEP are suppressed and this leads to the loss of alignment as fibers continue to crystallize but are randomly oriented.

At low frequencies, it is also possible that electroosmosis plays a role in affecting the fiber alignment, especially at high electric field amplitude, since the fluid movement can exert a shear force on polymer. In fact, some signs of electroosmosis in the form of fluid movement are observed when using high field amplitudes (2000 V/mm) and low frequencies (<5 Hz). However, just like electrophoresis, the fast switch of the electric field at higher frequencies (>25 Hz) also leads to a vanishing net fluid motion due to electroosmosis. Therefore, electroosmosis does not contribute significantly to the net polymer motion at the high frequencies (~250 Hz) where good quality alignment is observed.

Figure 3.15 also shows a decreased DEP force with a reduced particle size. The DEP force for a P3HT domain of size approximating that of single polymer chains (*i.e.* R_g ~ 10 nm) is extremely small. This helps explain why it is important to first induce nanofiber growth in order to produce highly aligned arrays via DEP. Figure 8 also shows that the magnitude of the DEP force increases very rapidly with small increases in size of the P3HT domains. Small increases in domain size, due to crystallization, would be sufficient to induce significant DEP transport towards regions of high field gradient. As fibers grow, the DEP force increases until reaching a critical fiber size where significant directional advection occurs.

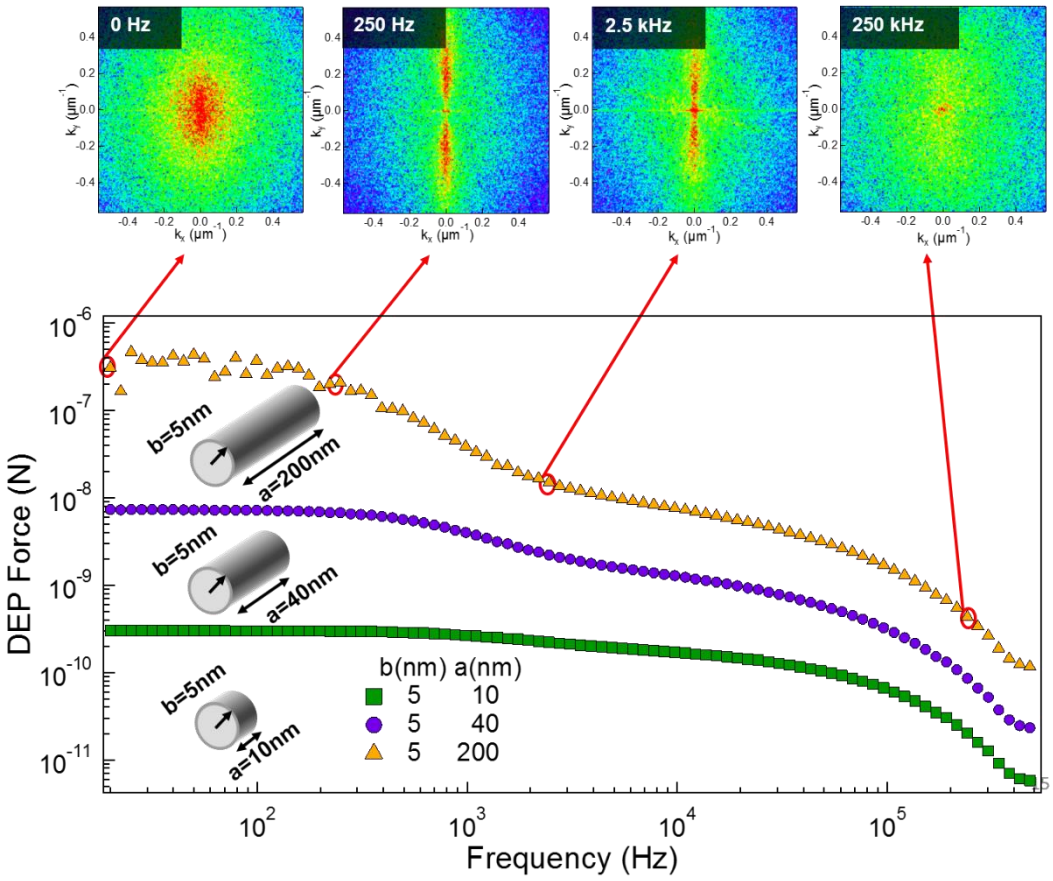

Figure 3.15. Comparison of estimated DEP force for P3HT nanofibers of different sizes. The smallest fiber are of similar dimension to a P3HT coil (R_g ~ 10 nm).[69] Here 'a' represents the length and 'b' is the radius of the cross section. FFT of aligned fibers collected at different frequencies are labeled on the DEP force curve as inserts.

In addition to frequency, the amplitude of the electric field was also observed to strongly affect fiber alignment. The observation of an optimum amplitude in optical microscopy (Figure 3.2 (b)) and SANS (Figure 3.10 (b)), is attributed to a competition between the rate of DEP transport and the rate of nanofiber crystallization due to supersaturation. When polymer domains are very small (*e.g.* single dissolved chains) the DEP force is also small (Figure 3.15) and unable to move particles until they grow large enough for this effect to dominate over diffusion. In the opposite extreme, when fibers grow fast and DEP forces are weak (i.e. low amplitudes), they quickly achieve large sizes that increase friction with other growing fibers and with the substrate preventing their

transport and orientation. This produces large immobile P3HT fibers that are randomly oriented and similar to the organogels that form in the absence of an electric field. When the electric field increases, aligned fiber structures start to appear at ~80 V/mm (Figure 3.2(b)) due to the increase in DEP force equation (3.3). Fibers continue to become more highly oriented and thinner as the electric field is further increased until the optimum condition at ~160 V/mm. For very high electric fields, alignment and order are again reduced, presumably due to the formation of defective structures leading to thicker and poorly aligned fibers (Figure 3.2(b)).

The importance of the competition between DEP and crystallization rates is also evident in samples with variable composition. The driving force for crystallization can be controlled by changing solvent quality, polymer concentration and/or temperature.[53] P3HT dissolved in pure DCB, a very good solvent, did not show any alignment and the sample would dry out before any fibers were formed. From microscopy experiments, it was evident that the spontaneous formation of fibers due to supersaturation was an essential element to achieve good alignment. Moreover, the quality of the aligned array was also strongly dependent on the P3HT concentration since this directly affected the rate of crystallization. Highly oriented and good quality arrays tended to form at lower P3HT concentrations. This is observed in Figure 3.10 where fibers are thinner and better aligned at lower concentrations. Figure 3.16 shows a schematic of the proposed process highlighting the interplay between DEP and crystallization rates.

The typical time scale of DEP force directed assembly can be estimated by equating the magnitude of viscous drag force based on Stokes' law to that of DEP force. For an 8 nm particle, it will take ~0.25 s for it to travel from the center of a 100 μm gap to the edge of one electrode. In comparison, the time scale of crystallization can vary a lot depending on the sample concentrations and solvent qualities[53]. The bulk crystallization time is on the order of 10 min to first observe evidence of

electrical and mechanical percolation as probed by rheology and dielectric spectroscopy.[51] However, by tuning supersaturation with temperature, concentration or solvent quality, the kinetics of fiber growth can be significantly slowed or accelerated. When the kinetics of crystallization is slow, but fibers are still being produced, nanofibers are effectively aligned and transported by DEP to regions of high field gradient. In contrast, at very high concentrations or in poor solvent conditions, the crystallization rate is so fast that fibers grow and branch much faster than they can be advected by DEP. This effect was demonstrated by either increasing P3HT concentration (Figure 3.3) or by changing solvent quality at a constant P3HT concentration (Figure 3.7). Moreover, previous work demonstrating electric field alignment of P3HT also relied on the use of xylene, which is a solvent of intermediate quality that readily leads to the formation of nanofibers.[44,50] When the solvent quality is very good, the polymer remains dissolved and it is too small to experience any significant DEP forces.

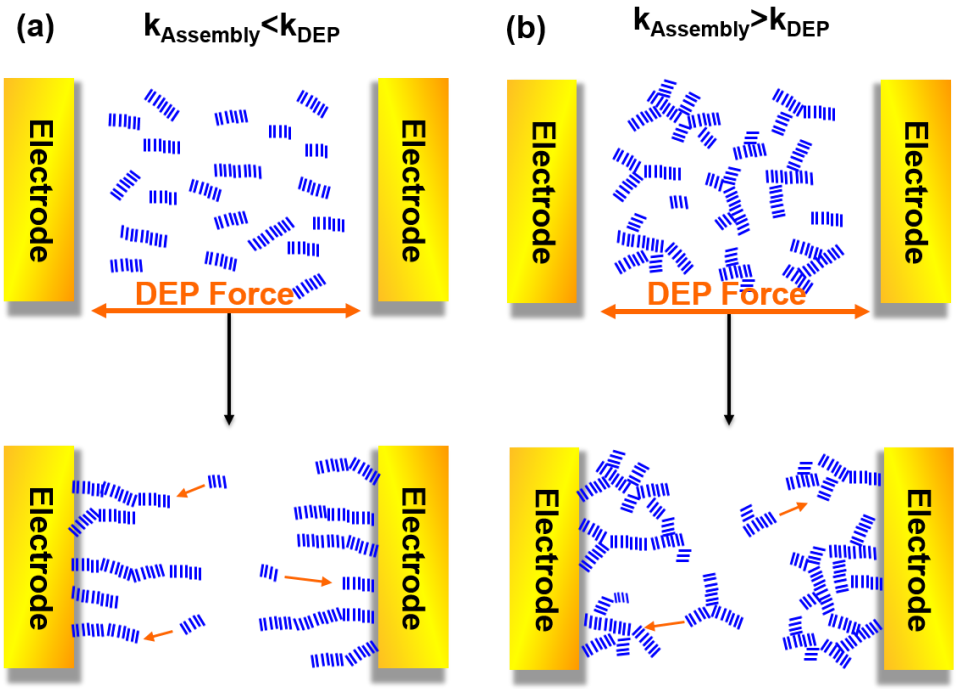

Figure 3.16. Schematic of the cases when one-dimensional crystallization rate is (a) slower and (b) faster than that of dielectrophoresis.

3.4.4 *Accelerated crystallization and molecular orientation*

An acceleration of crystallization under AC electric fields was also observed through both rheology (Figure 3.12) and SANS measurements (Figure 8.14). UV-Vis results also showed a higher fraction of fibers for samples aligned with AC fields over samples that were left to assemble without external fields. The accelerated crystallization rate under electric fields could potentially lead to more defects in the structure. This was indeed confirmed by a slightly lower exciton bandwidth value (W) obtained from UV-Vis (Figure 8.15).[70] Fits of SANS data to a parallelepiped model (Figure 3.17) also shows similar cross-sectional sizes for samples assembled with and without electric fields.[50–52] These results, together with the AFM images in Figure 3.8 and Figure

3.9, suggest that the thick fibers that are observed in optical microscopy are formed from bundles of smaller nanofibers.

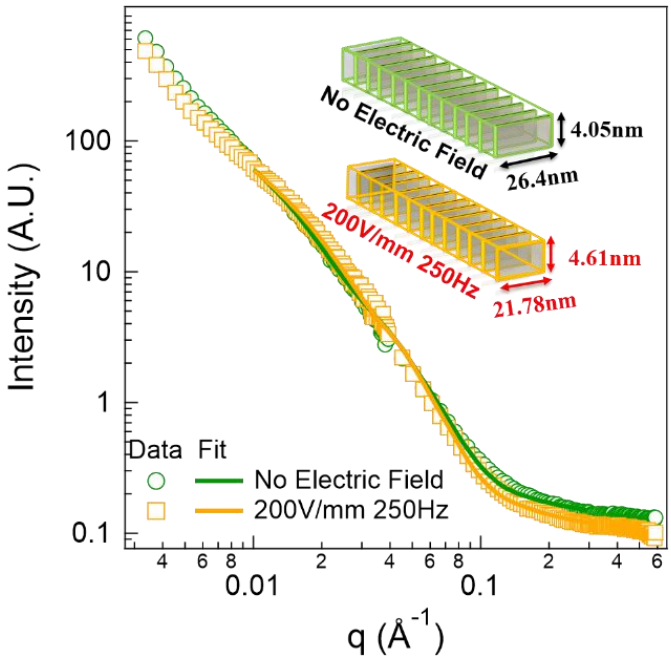

Figure 3.17. Combined model fitting of the scattering profiles at 2520s. The inset picture showed the dimensions of the cross-section from the fitting.

XRD measurements, which further confirmed the crystallinity of the aligned fibers, also demonstrated that the π-π stacking direction was oriented along the long fiber axis. Since transport along the π-π stacking direction is responsible for long-range charge transport, this fiber orientation increases the net electrical conductivity over randomly oriented polymer fibers. Movies online show that fibers grow until they eventually bridge and form a new electrical pathway between the electrodes. [57] Extended application of electric fields continues to thicken existing fibers or forms new fibers until all polymer is crystallized or the solvent dries out. Application of AC electric fields was also noted to increase the fraction of polymer in fibers as demonstrated with

UV-Vis spectroscopy (Figure 8.15). Therefore, the increased concentration of fibers also contributes to improved electrical conductivity.

3.4.5 *Changes to mechanical and electrical properties*

The alignment of P3HT also affected mechanical and electrical properties. Shear rheology demonstrated that alignment with AC fields could enhance the shear modulus (Figure 3.12). In contrast, DC fields reduced the modulus and produced weak organogels. Changes in electrical conductivity also correlated well with changes in mechanical properties, suggesting that there is a breakup of percolation for samples assembled under DC fields. In Figure 3.13(a), three separate relaxations were observed for samples assembled with and without AC electric fields. It is apparent from the Nyquist plot that the impedance for all relaxations was reduced after AC electric field alignment. The permittivity also showed significant differences between aligned (AC or DC) and unaligned samples (Figure 3.13(b)). At higher frequencies (>1 kHz), samples aligned with AC fields were found to be very similar to samples that were crystallized without an external field. In contrast, samples aligned with DC fields showed a much lower permittivity. In the low frequency range (<1 kHz) a significantly higher permittivity is observed for the sample aligned with the AC electric field in comparison to the DC and to unaligned samples (*i.e.* no field). Aligned fibers increase the low frequency permittivity due to improved percolation and conductivity. In contrast, samples formed with DC fields had the lowest permittivity due to a broken percolation pathway.

3.4.6 *Application of electric field alignment to other conjugated polymers*

Finally, in order to test the versatility of this method to align other systems, we also explored the effect using several other conjugated polymers. The resulting optical images and molecular structures are shown in Figure 3.18. The presence of unsubstituted (*i.e.* no side-chain) and fused rings in the backbone did not prevent alignment. Both PQT-12 and PBTT could be successfully aligned by an AC electric field. In contrast, side chain length and structure were found to be important considerations for determining alignment. P3ATs with very long (i.e. P3DDT) or branched (i.e. P3EHT) side-chains did not result in good alignment. Yet, P3ATs with side-chains that were composed of ten or fewer linear aliphatic carbons were all successfully aligned with AC electric fields. Regio-random P3HT was also impossible to align in electric fields, presumably this is because it remained in solution and could not crystallize into nanofibers.

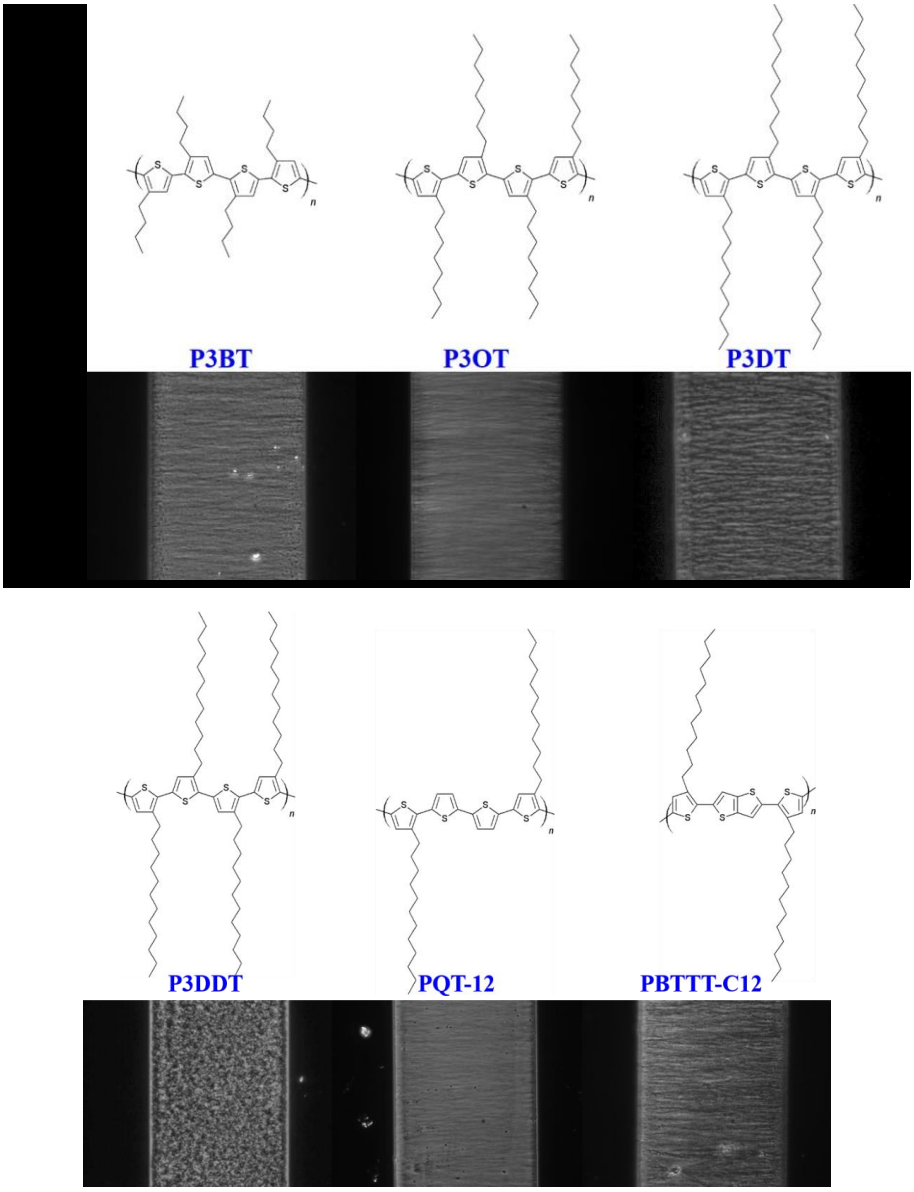

Figure 3.18. Molecular structure and the corresponding electric field alignment using 160 V/mm and 250 Hz of P3BT, P3OT, P3DT, P3DDT, PQT-12 and PBTTT-C12 dissolved in 25 wt% dodecane balanced with 75 wt% 1,2-dichlorobenzene.

3.5 SUMMARIES

It has been demonstrated that alternating electric fields can be used to effectively align poly(3-hexylthiophene) (P3HT) organogels over both micrometer and nanometer scales. This interesting phenomena is due to simultaneous dielectrophoresis (DEP) and electrophoresis in systems undergoing nanofiber crystallization. DEP, which dominated when AC fields were applied, would produce uniform and highly aligned fiber arrays. In contrast, when electrophoresis dominated in DC fields, this would produce non-uniformly aligned thick and branched fibers of very poor quality. An optimum frequency and amplitude under AC electric field alignment were found for alignment. Both mechanical and electrical properties were shown to be significantly enhanced in P3HT samples. XRD measurements further demonstrated that polymer fibers were crystalline and chains were aligned with the π-π stacking direction oriented along the fiber axis. Several conjugated polymers were successfully aligned by electric fields, but it was found that long and densely packed side chains could prevent some polymers from aligning.

Electric field alignment can be used to realize necessary performance improvements in organic electronic devices such as OFETs where aligned polymer fibers can effectively transport charges between source and drain electrodes. Moreover, aligned polymer arrays can also be transferred into elastomeric substrates and processed to generate flexible devices and sensors in future applications. Clearly, electric field alignment opens up new opportunities for engineering structures of conjugated polymer materials and it will be an important tool to further enhancing their unique properties.

3.6 REFERENCES

(1) Søndergaard, R.; Hösel, M.; Angmo, D.; Larsen-olsen, T. T.; Krebs, F. C. Roll-to-Roll Fabrication of Polymer Solar Cells As the Performance in Terms of Power Conversion Efficiency and Operational. *Mater. Today* **2012**, *15* (1–2), 36–49 DOI: 10.1016/S1369-7021(12)70019-6.

(2) Galagan, Y.; Fledderus, H.; Gorter, H.; Mannetje, H.; Shanmugam, S.; Mandamparambil, R.; Bosman, J. Roll-to-Roll Slot – Die Coated Organic Photovoltaic (OPV) Modules with High Geometrical Fill Factors. **2015**, 834–842 DOI: 10.1002/ente.201500150.

(3) Chou, H.; Nguyen, A.; Chortos, A.; To, J. W. F.; Lu, C.; Mei, J.; Kurosawa, T.; Bae, W.; Tok, J. B.; Bao, Z. Tactile Sensing. *Nat. Commun.* **2015**, *6*, 1–10 DOI: 10.1038/ncomms9011.

(4) Chortos, A.; Bao, Z. Skin-Inspired Electronic Devices. *Biochem. Pharmacol.* **2014**, *17* (7), 321–331 DOI: 10.1016/j.mattod.2014.05.006.

(5) Choi, M.; Kim, Y.; Ha, C. Polymers for Flexible Displays : From Material Selection to Device Applications. **2008**, *33*, 581–630 DOI: 10.1016/j.progpolymsci.2007.11.004.

(6) Luo, C.; Kyaw, A. K. K.; Perez, L. a.; Patel, S.; Wang, M.; Grimm, B.; Bazan, G. C.; Kramer, E. J.; Heeger, A. J. General Strategy for Self-Assembly of Highly Oriented Nanocrystalline Semiconducting Polymers with High Mobility. *Nano Lett.* **2014**, *14* (5), 2764–2771 DOI: 10.1021/nl500758w.

(7) He, Z.; Xiao, B.; Liu, F.; Wu, H.; Yang, Y.; Xiao, S.; Wang, C.; Russell, T. P.; Cao, Y. Single-Junction Polymer Solar Cells with High Efficiency and Photovoltage. *Nat. Photonics*

2015, *9* (3), 174–179 DOI: 10.1038/nphoton.2015.6.

(8) Dolev, M. MBE Growth of Ultra-Low Disorder 2DEG with Mobility Exceeding. **2009**, *311*, 1658–1661 DOI: 10.1016/j.jcrysgro.2008.09.151.

(9) Vidor, F. F.; Meyers, T.; Hilleringmann, U. Flexible Electronics: Integration Processes for Organic and Inorganic Semiconductor-Based Thin-Film Transistors. **2015**, 480–506 DOI: 10.3390/electronics4030480.

(10) Yu, D.; Yang, Y.; Chen, Z.; Tao, Y.; Liu, Y. Recent Progress on Thin- Fi Lm Encapsulation Technologies for Organic Electronic Devices. *Opt. Commun.* **2016**, *362*, 43–49 DOI: 10.1016/j.optcom.2015.08.021.

(11) Battaglia, C.; Cuevas, A.; Wolf, S. De. Environmental Science Status and Perspectives. *Energy Environ. Sci.* **2016**, *9*, 1552–1576 DOI: 10.1039/C5EE03380B.

(12) Coakley, B. K. M.; Srinivasan, B. S.; Ziebarth, J. M.; Goh, C.; Liu, Y.; Mcgehee, M. D. Enhanced Hole Mobility in Regioregular Polythiophene Infiltrated in Straight Nanopores **. **2005**, 1927–1932 DOI: 10.1002/adfm.200500364.

(13) Diao, Y.; Tee, B. C.-K.; Giri, G.; Xu, J.; Kim, D. H.; Becerril, H. a; Stoltenberg, R. M.; Lee, T. H.; Xue, G.; Mannsfeld, S. C. B.; Bao, Z. Solution Coating of Large-Area Organic Semiconductor Thin Films with Aligned Single-Crystalline Domains. *Nat. Mater.* **2013**, *12* (7), 665–671 DOI: 10.1038/nmat3650.

(14) Cao, Y.; Colaneri, N.; Heeger, a. J.; Smith, P. ‘“Plastic”’ Infrared Polarizers from Uniaxially Oriented Polyaniline Blends. *Appl. Phys. Lett.* **1994**, *65* (16), 2001 DOI: 10.1063/1.112843.

(15) Müller, C.; Garriga, M. Patterned Optical Anisotropy in Woven Conjugated Polymer Systems Patterned Optical Anisotropy in Woven Conjugated Polymer Systems. **2012**, *171907*, 1–5 DOI: 10.1063/1.4764518.

(16) Andersson, P.; Berggren, M.; Kugler, T. Switchable Optical Polarizer Based on Electrochromism in Stretch-Aligned Polyaniline. *Appl. Phys. Lett.* **2003**, *83* (7), 1307 DOI: 10.1063/1.1602556.

(17) Godbert, N.; Burn, P. L.; Gilmour, S.; Markham, J. P. J.; Samuel, I. D. W. Polarized Organic Electroluminescence: Ordering from the Top. *Appl. Phys. Lett.* **2003**, *83* (26), 5347 DOI: 10.1063/1.1632025.

(18) Whitehead, K. S.; Grell, M.; Bradley, D. D. C.; Jandke, M.; Strohriegl, P. Highly Polarized Blue Electroluminescence from Homogeneously Aligned Films of Poly(9,9-Dioctylfluorene). *Appl. Phys. Lett.* **2000**, *76* (20), 2946–2948 DOI: 10.1063/1.126525.

(19) Zhu, R.; Kumar, A.; Yang, Y. Polarizing Organic Photovoltaics. *Adv. Mater.* **2011**, *23* (36), 4193–4198 DOI: 10.1002/adma.201101514.

(20) Crossland, E. J. W.; Tremel, K.; Fischer, F.; Rahimi, K.; Reiter, G.; Steiner, U.; Ludwigs, S. Anisotropic Charge Transport in Spherulitic Poly(3-Hexylthiophene) Films. *Adv. Mater.* **2012**, *24* (6), 839–844 DOI: 10.1002/adma.201104284.

(21) Vohra, V.; Arrighetti, G.; Barba, L.; Higashimine, K.; Porzio, W.; Murata, H. Enhanced Vertical Concentration Gradient in Rubbed P3HT:PCBM Graded Bilayer Solar Cells. *J. Phys. Chem. Lett.* **2012**, *3* (13), 1820–1823 DOI: 10.1021/jz300710a.

(22) Brinkmann, M.; Aldakov, D.; Chandezon, F. Fabrication of Oriented and Periodic Hybrid

Nanostructures of Regioregular Poly(3-Hexylthiophene) and CdSe Nanocrystals by Directional Epitaxial Solidification. *Adv. Mater.* **2007**, *19* (22), 3819–3823 DOI: 10.1002/adma.200700311.

(23) Müller, C.; Aghamohammadi, M.; Himmelberger, S.; Sonar, P.; Garriga, M.; Salleo, A.; Campoy-Quiles, M. One-Step Macroscopic Alignment of Conjugated Polymer Systems by Epitaxial Crystallization during Spin-Coating. *Adv. Funct. Mater.* **2013**, *23* (19), 2368–2377 DOI: 10.1002/adfm.201202983.

(24) Alignment, N. I. C.; Defined, H. T. N.; Lithography, N. Nano-Confinement Induced Chain Alignment in Ordered P3HT Nanostructures Defined by Nanoimprint Lithography. **2009**, *3* (10), 3085–3090.

(25) Zheng, Z.; Yim, K. H.; Saifullah, M. S. M.; Welland, M. E.; Friend, R. H.; Kim, J. S.; Huck, W. T. S. Uniaxial Alignment of Liquid-Crystalline Conjugated Polymers by Nanoconfinement. *Nano Lett.* **2007**, *7*, 987–992 DOI: 10.1021/nl070022k.

(26) Hu, Z.; Muls, B.; Gence, L.; Serban, D. a.; Hofkens, J.; Melinte, S.; Nysten, B.; Demoustier-Champagne, S.; Jonas, A. M. High-Throughput Fabrication of Organic Nanowire Devices with Preferential Internal Alignment and Improved Performance. *Nano Lett.* **2007**, *7* (12), 3639–3644 DOI: 10.1021/nl071869j.

(27) Cimrová, V.; Remmers, M.; Neher, D.; Wegner, G. Polarized Light Emission from LEDs Prepared by the Langmuir-Blodgett Technique. *Adv. Mater.* **1996**, *8* (2), 146–149 DOI: 10.1002/adma.19960080209.

(28) Bhardwaj, N.; Kundu, S. C. Electrospinning : A Fascinating Fi Ber Fabrication Technique. **2010**, *28*, 325–347 DOI: 10.1016/j.biotechadv.2010.01.004.

(29) Beachley, V.; Wen, X. Effect of Electrospinning Parameters on the Nanofiber Diameter and Length. *Mater. Sci. Eng. C* **2009**, *29* (3), 663–668 DOI: 10.1016/j.msec.2008.10.037.

(30) Olszowka, V.; Hund, M.; Kuntermann, V.; Scherdel, S.; Tsarkova, L.; Böker, A. Electric Field Alignment of a Block Copolymer Nanopattern: Direct Observation of the Microscopic Mechanism. *ACS Nano* **2009**, *3* (5), 1091–1096 DOI: 10.1021/nn900081u.

(31) Xu, T.; Zhu, Y.; Gido, S. P.; Russel, T. P. Electric Field Alignment of Symmetric Diblock Copolymer Thin Films. *Macromolecules* **2004**, *37* (7), 2625–2629 DOI: 10.1007/978-1-4020-6330-5_6.

(32) Lin, C.-Y.; Schick, M. Self-Consistent Field Study of the Alignment by an Electric Field of a Cylindrical Phase of Block Copolymer. *J. Chem. Phys.* **2006**, *125* (3), 34902 DOI: 10.1063/1.2214718.

(33) Kaddami, H.; Raihane, M. Electric Field Alignment of Nano Fi Brillated Cellulose (NFC) in Silicone Oil: Impact on Electrical Properties. *ACS Appl. Mater. Interfaces* **2014**, *6* (12), 9418–9425.

(34) Oliva-Avilés, a I.; Avilés, F.; Sosa, V.; Oliva, a I.; Gamboa, F. Dynamics of Carbon Nanotube Alignment by Electric Fields. *Nanotechnology* **2012**, *23* (46), 465710 DOI: 10.1088/0957-4484/23/46/465710.

(35) Senthil Kumar, M.; Lee, S. H.; Kim, T. Y.; Kim, T. H.; Song, S. M.; Yang, J. W.; Nahm, K. S.; Suh, E. K. DC Electric Field Assisted Alignment of Carbon Nanotubes on Metal Electrodes. *Solid. State. Electron.* **2003**, *47* (11), 2075–2080 DOI: 10.1016/S0038-1101(03)00258-2.

(36) Ural, A.; Li, Y.; Dai, H. Electric-Field-Aligned Growth of Single-Walled Carbon Nanotubes on Surfaces. *Appl. Phys. Lett.* **2002**, *81* (18), 3464 DOI: 10.1063/1.1518773.

(37) Ahmed, W.; Kooij, E. S.; Van Silfhout, A.; Poelsema, B. Quantitative Analysis of Gold Nanorod Alignment after Electric Field-Assisted Deposition. *Nano Lett.* **2009**, *9* (11), 3786–3794 DOI: 10.1021/nl901968e.

(38) Smith, P. a.; Nordquist, C. D.; Jackson, T. N.; Mayer, T. S.; Martin, B. R.; Mbindyo, J.; Mallouk, T. E. Electric-Field Assisted Assembly and Alignment of Metallic Nanowires. *Appl. Phys. Lett.* **2000**, *77* (9), 1399–1401 DOI: 10.1063/1.1290272.

(39) Zijlstra, P.; van Stee, M.; Verhart, N.; Gu, Z.; Orrit, M. Rotational Diffusion and Alignment of Short Gold Nanorods in an External Electric Field. *Phys. Chem. Chem. Phys.* **2012**, *14* (13), 4584–4588 DOI: 10.1039/c2cp24092k.

(40) Geng, J.; Zhou, E.; Li, G.; Lam, J. W. Y.; Tang, B. Z. Electric-Field-Induced Molecular Alignment of Side-Chain Liquid-Crystalline Polyacetylenes Containing Biphenyl Mesogens. *J. Polym. Sci. Part B Polym. Phys.* **2004**, *42*, 1333–1341 DOI: 10.1002/polb.20021.

(41) Chang, W.-S.; Link, S.; Yethiraj, A.; Barbara, P. F. Single Molecule Spectroscopy of Conjugated Polymer Chains in an Electric Field-Aligned Liquid Crystal. *J. Phys. Chem. B* **2008**, *112*, 448–453 DOI: 10.1021/jp076345m.

(42) Marzouk, J.; Lucas, B.; Trigaud, T.; Pothier, A.; Bouclé, J.; Ratier, B. Simple Strategy to Tune the Charge Transport Properties of Conjugated Polymer/Carbon Nanotube Composites Using an Electric Field Assisted Deposition Technique. *Polym. Int.* **2014**, *63* (February), 1378–1386 DOI: 10.1002/pi.4686.

(43) Fischer, F. S. U.; Tremel, K.; Sommer, M.; Crossland, E. J. W.; Ludwigs, S. Directed Crystallization of Poly(3-Hexylthiophene) in Micrometre Channels under Confinement and in Electric Fields. *Nanoscale* **2012**, *4* (6), 2138–2144 DOI: 10.1039/c2nr12037b.

(44) Mas-Torrent, M.; Boer, D. Den; Durkut, M.; Hadley, P.; Schenning, a P. H. J. Field Effect Transistors Based on Poly(3-Hexylthiophene) at Different Length Scales. *Nanotechnology* **2004**, *15* (4), S265–S269 DOI: 10.1088/0957-4484/15/4/028.

(45) Pethig, R. Dielectrophoresis: Status of the Theory, Technology, and Applications. *Biomicrofluidics* **2010**, *4* (2), 022811 DOI: 10.1063/1.3456626.

(46) Molina-lopez, F.; Yan, H.; Gu, X.; Kim, Y.; Toney, M. F.; Bao, Z. Electric Field Tuning Molecular Packing and Electrical Properties of Solution-Shearing Coated Organic Semiconducting Thin Films. *Adv. Funct. Mater.* **2017** DOI: 10.1002/adfm.201605503.

(47) Velev, O. D.; Bhatt, K. H. On-Chip Micromanipulation and Assembly of Colloidal Particles by Electric Fields. *Soft Matter* **2006**, *2* (9), 738 DOI: 10.1039/b605052b.

(48) Jamshidi, A.; Pauzauskie, P. J.; Schuck, P. J.; Ohta, A. T.; Chiou, P.-Y.; Chou, J.; Yang, P.; Wu, M. C. Dynamic Manipulation and Separation of Individual Semiconducting and Metallic Nanowires. *Nat. Photonics* **2008**, *2*, 86–89 DOI: 10.1038/nphoton.2007.277.

(49) Jones, T. B. *Electromechanics of Particles*; Cambridge University Press, 1995.

(50) Newbloom, G. M.; Kim, F. S.; Jenekhe, S. a.; Pozzo, D. C. Mesoscale Morphology and Charge Transport in Colloidal Networks of Poly(3-Hexylthiophene). *Macromolecules* **2011**, *44* (10), 3801–3809 DOI: 10.1021/ma2000515.

(51) Newbloom, G. M.; Weigandt, K. M.; Pozzo, D. C. Electrical, Mechanical, and Structural

Characterization of Self-Assembly in Poly(3-Hexylthiophene) Organogel Networks. *Macromolecules* **2012**, *45*, 3452–3462 DOI: 10.1021/ma202564k.

(52) Newbloom, G. M.; Weigandt, K. M.; Pozzo, D. C. Structure and Property Development of Poly(3-Hexylthiophene) Organogels Probed with Combined Rheology, Conductivity and Small Angle Neutron Scattering. *Soft Matter* **2012**, *8* (34), 8854 DOI: 10.1039/c2sm26114f.

(53) Newbloom, G. M.; de la Iglesia, P.; Pozzo, L. D. Controlled Gelation of Poly(3-Alkylthiophene)s in Bulk and in Thin-Films Using Low Volatility Solvent/Poor-Solvent Mixtures. *Soft Matter* **2014**, *10* (44), 8945–8954 DOI: 10.1039/c4sm00960f.

(54) Schneider, C. a; Rasband, W. S.; Eliceiri, K. W. NIH Image to ImageJ: 25 Years of Image Analysis. *Nat. Methods* **2012**, *9* (7), 671–675 DOI: 10.1038/nmeth.2089.

(55) Kline, S. R. Reduction and Analysis of SANS and USANS Data Using IGOR Pro. *J. Appl. Crystallogr.* **2006**, *39* (6), 895–900 DOI: 10.1107/S0021889806035059.

(56) P. Butler, G. Alina, R. C. Hernandez, M. Doucet, A. Jackson, P. Kienzle, S. K. and J. Z. SASView for Small Angle Scattering Analysis http://www.sasview.org/.

(57) Xi, Y.; Pozzo, L. D. Electric Field Directed Formation of Aligned Conjugated Polymer Fibers. *Soft Matter* **2017**, *13*, 3894–3908 DOI: 10.1039/C7SM00485K.

(58) Iglesia, P. D. La; Pozzo, D. C. Effects of Supersaturation on the Structure and Properties of Poly(9,9-Dioctyl Fluorene) Organogels. *Soft Matter* **2013**, *9* (47), 11214 DOI: 10.1039/c3sm51753e.

(59) Gopinadhan, M.; Choo, Y.; Osuji, C. O. Strong Orientational Coupling of Block Copolymer Microdomains to Smectic Layering Revealed by Magnetic Field Alignment. **2016** DOI:

10.1021/acsmacrolett.5b00924.

(60) Trebbin, M.; Steinhauser, D.; Perlich, J.; Buffet, A.; Roth, S. V; Zimmermann, W. Anisotropic Particles Align Perpendicular to the Fl Ow Direction in Narrow Microchannels. **2013**, *110* (17) DOI: 10.1073/pnas.1219340110.

(61) Li, J.-L.; Yuan, B.; Liu, X.-Y.; Xu, H.-Y. Microengineering of Supramolecular Soft Materials by Design of the Crystalline Fiber Networks. *Cryst. Growth Des.* **2002**, *10* (6), 2699–2706 DOI: 10.1021/cg100188w.

(62) Liu, X. Y.; Sawant, P. D.; Tan, W. B.; Noor, I. B. M.; Pramesti, C.; Chen, B. H. Creating New Supramolecular Materials by Architecture of Three-Dimensional Nanocrystal Fiber Networks. *J. Am. Chem. Soc.* **2002**, *124* (50), 15055–15063 DOI: 10.1021/ja0206137.

(63) Liu, X. Y.; Sawant, P. D. Mechanism of the Formation of Self-Organized Microstructures in Soft Functional Materials. *Adv. Mater.* **2002**, *14* (6), 421–426 DOI: 10.1002/1521-4095(20020318)14:6<421::AID-ADMA421>3.0.CO;2-7.

(64) Hou, D.; Chang, H. Ac Field Enhanced Protein Crystallization. **2014**, 23–25 DOI: 10.1063/1.2938887.

(65) Jang, J.; Oh, J. Y.; Kim, S. K.; Choi, Y. J.; Yoon, S. Y.; Kim, C. O. No Title. *Nature* **1998**, *395* (6701), 481–483 DOI: 10.1038/26711.

(66) Yuryev, Y.; Wood-Adams, P. M. Crystallization of Poly(L-/D-Lactide) in the Presence of Electric Fields. *Macromol. Chem. Phys.* **2012**, *213* (6), 635–642 DOI: 10.1002/macp.201100448.

(67) Yan, J. Y.; Patey, G. N. Heterogeneous Ice Nucleation Induced by Electric Fields. *J. Phys.*

Chem. Lett. **2011**, *2* (20), 2555–2559 DOI: 10.1021/jz201113m.

(68) Burt, J. P. H.; Al-ameen, T. A. K.; Pethig, R. An Optical Dielectrophoresis Spectrometer for Low -Frequency Measurements on Colloidal Suspensions. *J. Phys. E Sci. Instrum.* **1989**, *22*, 952–957 DOI: 10.1088/0022-3735/22/11/011.

(69) Newbloom, G. M.; Hoffmann, S. M.; West, A. F.; Gile, M. C.; Sista, P.; Cheung, H. C.; Luscombe, C. K.; Pfaendtner, J.; Pozzo, L. D. Solvatochromism and Conformational Changes in Fully Dissolved Poly(3-Alkylthiophene)S. *Langmuir* **2015**, *31* (1), 458–468 DOI: 10.1021/la503666x.

(70) Clark, J.; Chang, J. F.; Spano, F. C.; Friend, R. H.; Silva, C. Determining Exciton Bandwidth and Film Microstructure in Polythiophene Films Using Linear Absorption Spectroscopy. *Appl. Phys. Lett.* **2009**, *94* (16), 2007–2010 DOI: 10.1063/1.3110904.

Chapter 4. Acoustic Wave directed assembly of conjugated polymers

4.1 INTRODUCTION AND MOTIVATION

Conjugated polymers (CPs) have been extensively pursued as candidate materials for use in organic photovoltaics (OPVs), organic light emitting diodes (OLEDs), and organic field-effect transistors (OFETs).[1–3] In addition to their (opto)electronic properties, properties such as flexibility, bio-compatibility, and highly tunable molecular design make them promising materials for novel sensors and bioelectronic devices.[4,5] Unfortunately, limited electrical conductivity is still a major hindrance for the effective application of CPs in many applications. Frequently, amorphous polymer structures lead to inefficient inter-chain charge hopping that limits charge transport. This is often corrected by initiating the formation of ordered polymer phases that are driven by stacking π-orbitals orthogonal to the polymer backbone. The resulting formation of large crystalline structures facilitates inter-chain charge propagation, which enables transport over much longer distances and improves charge-carrier mobility by several orders of magnitude.[6] Recently, much work has also been dedicated to further increasing conductivity by engineering polymer structures with external forces, including capillary,[7] shear,[8] gravitational,[9] and electrostatic forces.[10] In this work, the use of acoustic fields at ultrasound frequencies (>20kHz) is investigated as an effective method to assemble polymer chains into fibers with long-range order.

In colloid and polymer science, ultrasound is most frequently used in a destructive way to mechanically break up aggregates, disperse particles, emulsify oils, and even to break up whole cells in a process known as sonofragmentation.[11–14] However, and often counter-intuitively, in some cases ultrasound is also used to assemble molecules into highly ordered structures in a process known as sonocrystallization, where the wavelength of the acoustic wave (~cm) is several

orders larger than the size of the molecules. Successful demonstrations of sonocrystallization usually involve small molecules, such as adipic acid,[15] sulfamerazine,[16] and glucose.[17] In the above systems, ultrasound is typically applied to solutions with supersaturation to induce crystallization. Although the mechanism of crystallization under ultrasound is still ambiguous, it has been reported that ultrasound can effectively shorten the induction time (i.e. duration between achievement of supersaturation and appearance of detectable crystals). Recently, pioneering work provided evidence of the possibilities of inducing sonocrystallization on macromolecules including proteins[18–20] and conjugated polymers.[21–23] It was reported that poly(3-hexylthiophene) (P3HT) polymers chains can assemble into nanofibers that are micrometers long under ultrasound in chloroform or toluene.[21–23] Early investigations of P3HT sonication in 'good' solvents (i.e. chlorobenzene and 1,2-dichlorobenzene) did not observe nanofibers formation, but they revealed that the solution's specific viscosity decreased, which was hypothesized to correlate to a change in chain conformation. [23] The higher the concentration (namely supersaturation), the more obvious the changes are. Furthermore, the formation of nanofibers was demonstrated to enhance the charge carrier's mobility by up to one order of magnitude due to more efficient inter-chain transport.[21] On the other hand, spontaneous nanofiber formation in conjugated polymers is also routinely achieved by tuning solvent quality or changing temperature in the absence of any external fields.[24–27] Therefore, there are still important questions remaining on the specific effect of ultrasound on polymer chains and how this relates to spontaneous self-assembly that may occur due to variations in solubility in the absense of ultrasound.

We hypothesize that the role of ultrasound in sonocrystallization of conjugated polymers, from a thermodynamics point of view, follows the energy diagram shown in Figure 4.1. For ideal good solvents, the dissolved state is supposed to be a global energy minimum within the energy

landscape, which means once it is dissolved, it should stay in the thermodynamically favored dissolution state without assembly. However, in reality polymer chains that appear to be fully dissolved in ‘good’ solvents, are instead confined to a local energy minimum created by an energy barrrier. This prevents them from achieving crystallization, which is a more energetically favorable state, in a reasonable time frame. As the solvent quality increases, the energy necessary to cross this stabilizing barrier is larger. This is analogous to the kinetic stabilization of colloidal particles that can remain suspended for long periods of time due to electrostatic repulsion. Although these particles may appear to be in an energetically stable state, the global energy minima is in the aggregated state, but a significant energy barrier prevents them from achieving this state in a reasonable time frame.

In sonocrystallization, ultrasound provides enough energy to allow molecules and polymers to overcome the stabilizing barrier resulting in the formation of crystalline nuclei that facilitate further crystallization. Still, a persistent question is by what mechanism is ultrasound triggering the crystallization process. We hypothesize that cavitation induces sonocrystallization by modifying the conformation of polymer chains to facilitate the formation of crystal nuclei for continued growth. In this process, the formation of cavitation events is strongly dependent on the applied acoustic field frequency and pressure. In order to quantitatively relate the acoustic field to the nucleation process, to shed light on the mechanism of conjugated polymer sonocrystallization, it is essential to use well-characterized acoustic fields to probe the system.

To accurately describe an acoustic wave, its pressure and frequency are typically uitilized.[28] When the pressure of the acoustic wave is lower than ambient pressure (i.e. in the so called negative pressure phase), it exerts a tension on the surrounding liquid medium that could induce the formation of a cavity if its magnitude is above a certain threshold.[29] Cavitation is defined by

Neppiras as the creation of new surface or cavity within the liquid.[30] Cavitation thresholds depend on several factors including the frequency of the acoustic wave, the pressure amplitude, the surface tension, temperature and boiling point. At higher frequencies, larger pressure amplitudes are required to induce cavitation.[31,32] The formation of a cavity favors growth under acoustic waves because of rectified diffusion. During expansion (negative pressure), liquid molecules diffuse into vapor bubbles to form a larger gaseous phase. In contrast, vapors condense into the liquid in response to the compression force that is induced at the positive pressure stage of the wave.[31] Importantly, the transport into and out of the cavity is not balanced because the bubble surface area during the expansion stage is much larger than that during compression. This results in the growth of the cavity or bubble under continued insonation. When a bubble grows to a critical size, it will eventually resonate with the acoustic wave and this will lead to an abrupt collapse producing localized extreme conditions (i.e. temperature up to 5000 K and pressure up to 1000 atm) and ejecting high-speed jets (100-400 m/s) that mechanically act on the surrounding fluid and container.[33–35] Subsequently, rapid cooling (10^7-10^{10} K/s) occurs and shock waves are generated.[36] The extreme effects of thousands of these local cavitation events are largely responsible for the cleaning action and sample manipulation (e.g. emulsification) that makes ultrasound a valuable tool in the laboratory.

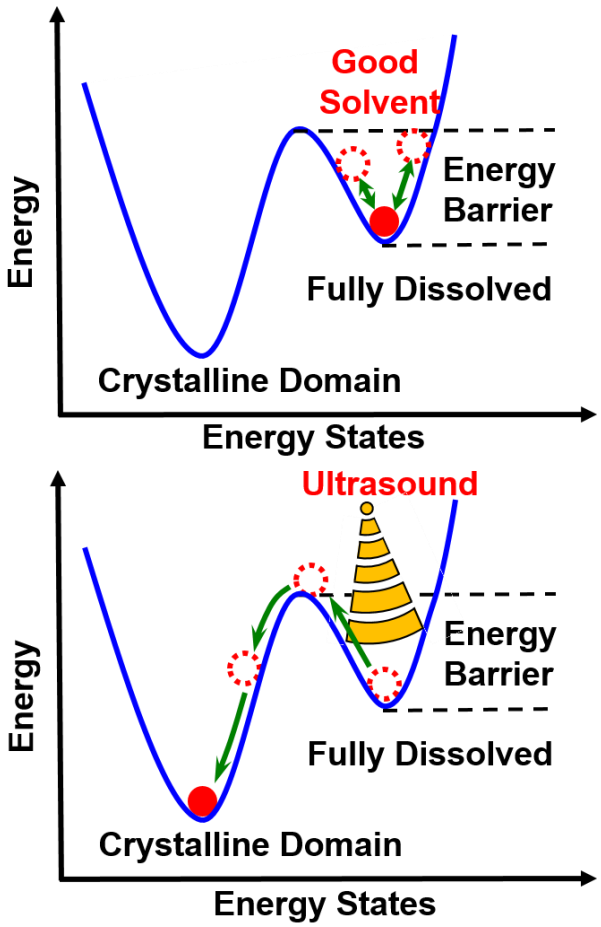

Figure 4.1. Schematic of energy diagram of the thermodynamic process from polymers in a fully dissolved state to the formation of crystalline structures under ultrasound.

In this work, we provide a detailed mechanistic and structural analysis of the processes involved in the formation of organized crystalline domains (i.e. nanofibers) during the ultrasound activation of conjugated polymers dissolved in what are considered to be 'good' solvents for these materials. We use carefully characterized acoustic waves and perform cavitation and structural analyses to properly inform the mechanisms of fiber formation.

4.2 EXPERIMENTAL

4.2.1 *Materials*

All chemicals were used as received. Poly(3-alkylthiophene) (P3AT), including regio-regular, regio-random poly(3-hexylthiophene) (P3HT), and Poly(3-dodecylthiophene) (P3DDT) were purchased from Rieke Metals (Lincoln, NE, USA). Poly(3,3’’’-didodecylquarterthiophene) (PQT-12) was purchased from Solaris Chem (Montreal, Quebec, Canada). Two lots of regio-regular P3HT with the same degree of polymerization, dispersity, and regioregularity were utilized: RMI-001E, lot# PTL14-85 and lot# BS 23-49 (Mw=69 k, $Đ$=2.3, and regioregularity=96%). Lot#14-85 was used to collect most of the data with the exception of samples analyzed with in-situ neutron scattering during ultrasound. The molecular weights and lot numbers of other conjugated polymers are summarized in Table 4.1. Hydrogenated solvents: chloroform (99.9%) and chlorobenzene were purchased from Fisher Scientific (Waltham, MA, USA). 1,2-dichlorobenzene (99%) were purchased from Sigma-Aldrich (St. louis, MO, USA). Deuterated solvents: d-chloroform (D, 99.8%), d5-chlorobenzene (D, 99%), d4-1,2-dichlorobenzene (D, 99%), and d5-bromobenzene (D, 99%) were purchased from Cambridge Isotope Laboratories (Cambridge, MA, USA).

Table 4.1. Summary of molecular weight and dispersities of polymers.

Polymers	Lot #	M_n	$Đ$
Regiorandom P3HT	BS20-92	26k	2.4
P3DDT	BS21-87	22k	1.8
PQT-12	DL158	24k	1.7

4.2.2 *Transmission Electron Microscopy*

An FEI (Tecnai G2 F20, FEI company, Hillsboro, OR, USA) transmission electron microscope (TEM) was used in scanning mode to take images of conjugated polymer samples. Before analysis, solutions were diluted by 20 times (chloroform) or 40 times (dichlorobenzene) in the same solvent as that was used for sample preparation. The polymer samples were drop-cast onto a pure carbon grid (200 mesh Cu, Ted Pella Inc., Redding, CA, USA) placed on top of a filter paper and dried for at least a day in air.

4.2.3 *UV-vis spectroscopy*

A Thermo (Evolution 300, Thermo Fisher Scientific Inc., Waltham, MA, USA) UV-Vis spectrometer was utilized to measure the absorbance spectra of polymer solutions between wavelength of 350 and 700 nm. A glass cuvette with a pathlength of 1 cm was used. After treatment with ultrasound, samples were diluted by ~ 500 times to measure time-dependent absorbance after aging over several days. The spectrum of reference samples that were not exposed to ultrasound were also recorded over the same aging time for comparison. All the spectra were normalized by concentration. The concentration was determined by using the absorption peak of the same polymer solution sample after re-heating and fully re-dissolving it.

4.2.4 *Small angle neutron scattering (SANS)*

Small angle neutron scattering (SANS) experiment were conducted at NIST center for Neutron Research (NCNR) on NGB 30. Three standard detector positions were used to cover a q-range of $0.003\ Å^{-1} < q < 0.45\ Å^{-1}$. Part of the scattering data was also collected in the GP-SANS instrument

at Oak Ridge national laboratories with a configuration achieving a similar q-range. Standard sample cells with quartz windows and a 1 mm pathlength were used for samples that were insonated outside of the neutron beam in Branson (3510, 40 kHz, 160W, Danbury, CT, USA) sonication bath. The SANS data was reduced by using standard Igor reduction protocols, [37] and SASView software was used to fit to appropriate models.[38]

4.2.5 *Ultra-small Angle X-ray Scattering (USAXS)*

Ultra-small angle x-ray scattering (USAXS) experiments were conducted at sector 9-ID-C beamline in Advanced Photon Source (APS) of Argonne National Laboratory.[39] Standard configuration was used to cover the range of 0.0001 $Å^{-1} < q < 0.3$ $Å^{-1}$. The energy of x-ray beam was 21 keV (λ=0.5904 Å). In-situ acoustic sample environment that allows in-situ scattering experiment under ultrasound is mounted along the beam path. The detailed description of the customized sample environment is described in the ultrasound insonation section below. The raw USAXS data was collected with Bonse-Hart camera and the Irena macro based on Igor Pro package was used to reduce the USAXS data. [40]

4.2.6 *Ultrasound Insonation*

Polymers were fully dissolved in good solvents at elevated temperatures (~ 60 °C for chloroform samples and above 80 °C for those in 1,2-dichlorobenzne) until a homogeneous orange solution was formed. The solutions were then allowed to cool down to room temperature before use. These solutions were then used in sequential characterization with either ex-situ or in-situ application of ultrasound.

For ex-situ experiment using a sonication bath, fully dissolved samples were then divided to explore different ultrasound conditions. This reduces any error that may be introduced by variations in concentration during preparations of different batches. Moreover, it ensures that aging conditions (i.e. time and temperature) for ultrasound treated and reference samples (i.e. without sonication) are the same. Data for samples in a sonication bath was collected with a Branson 5000 (40 kHz, 160W, Danbury, CT, USA) sonication bath.

For in-situ experiments, the polymer solutions were injected into a customized sample environment that allows simultaneous application of High Intensity Focused Ultrasound (HIFU)**.** The acoustic sample environment consisted of a central sample holder, two coaxially aligned transmitting focused transducers, and one broadband receiving transducer (Figure 4.2). Windows were formed from 100 µm thick Kapton films for both acoustic and neutron beam transmission. Two 1.24 MHz spherically focused transducers (H-102, 68 mm diameter, 63 mm focal length, f-number 0.95, Sonic-Concepts Inc., Bothell, WA, USA) coaxially aligned to the left and right of the sample environment were used to sonicate the sample under highly controlled fields in the absence of large reflections. The transducers, which were held in a degassed water chamber that was used as a coupling medium, were able to transmit up to 7.2 MPa of peak negative acoustic pressure. The transducer chambers were designed with angled walls to minimize shadowing of the scattered neutron beam while also accommodating the focusing beam geometry of the transducers. The transducer chamber dimensions ensured that the acoustic beam focus was within the sample holder. The bottom of the sample holder held a custom wide-band polyvinylidene difluoride (PVDF) transducer (28 µm thick) with a nearly constant bandwidth sensitivity at frequencies up to 40 MHz. Medical ultrasound gel was used to facilitate acoustic contact between all transducers and the sample environment.

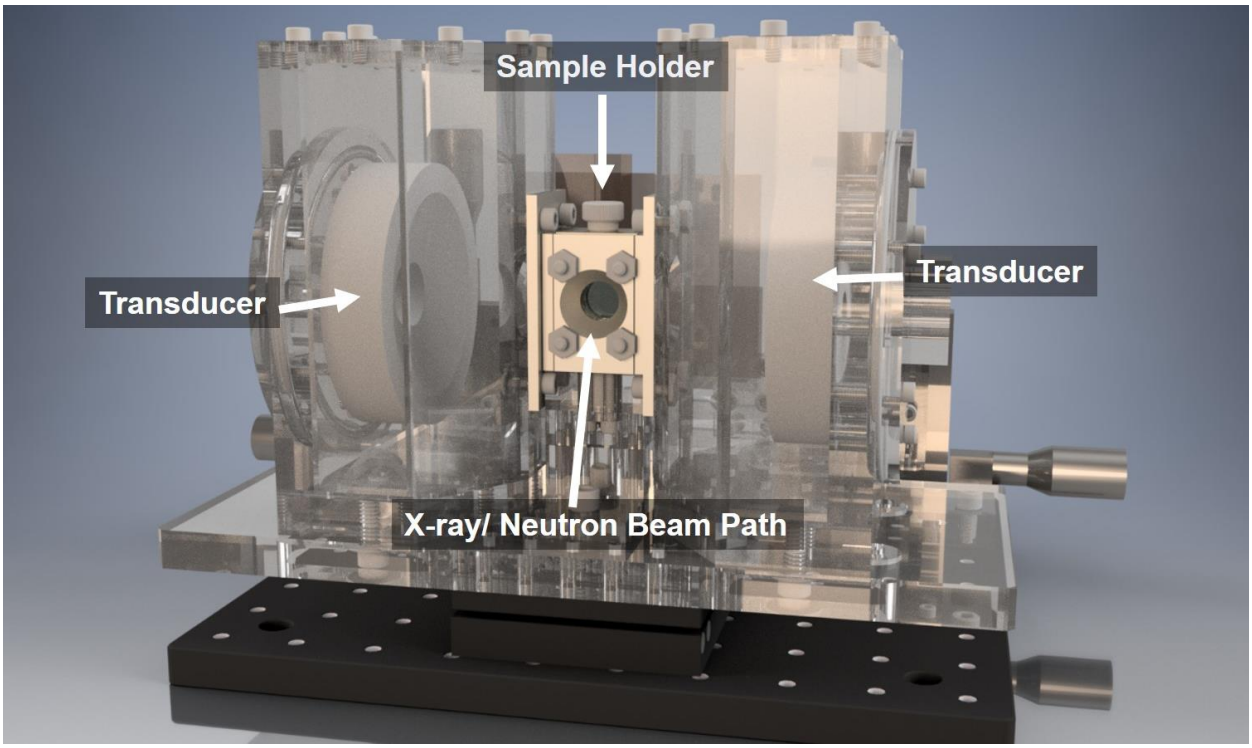

Figure 4.2. In-situ acoustic sample environment for simultaneous scattering measurement.

During SANS, the scattering volume was defined by cadmium slits to form a 1 mm by 8 mm rectangle that matched the focal volume of the HIFU transducers. For USAXS, slits were not necessary because the beam size (<1 mm) was smaller than the ultrasound focal volume. The ultrasound focal volume was approximately 1.6 mm in the radial direction and 13.2 mm in the axial direction. The beam profiles of the ultrasound transducers were obtained using a needle hydrophone (HNC-1000, Onda Corp., Sunnvale, CA, USA) while the pressure output was calibrated using a fiber optic hydrophone (FOPH 2000, RPI Acoustics, Germany).

A laptop was used to control and acquire acoustic data from the acoustic sample environment using MATLAB (Mathworks Inc., Watham, MA, USA). The transducers were driven using short N-cycle sine-wave bursts generated from a two-channel arbitrary waveform generator (4154, BK Precision) amplified by 55 dB through a power RF amplifier (A150, ENI). The transducers were

activated in an alternating configuration using a custom relay circuit, to avoid sonophoresis from a single transducer (i.e. sample depletion from acoustic radiation force) or sample enrichment at acoustic standing wave antinodes (i.e. during simultaneous transducer activation). The acoustic pressure amplitude, pulse duration, pulse repetition frequency, and transducer switching frequency could be controlled using the laptop through the arbitrary function generator. In general, the acoustic sample environment was driven using peak negative pressure amplitudes ranging from 0 to 7.2 MPa, a pulse duration of 40 cycles (32.3 μs pulse length), pulse repetition frequency of 6.2 KHz, and switching between each transducer at a rate of 1 Hz. The scattered acoustic data received from the PVDF transducer, which was used for cavitation detection, was preconditioned using a preamplifier (Precision Acoustics, Dorchester, UK). The cavitation signal was a differential ultrasound signal obtained by comparing the received signal to a background measurement. A 40 μs window starting from 43 μs after the transducer was fired, which was the one-way time of flight from transducer face to its focal point, was used for cavitation analysis. When the acoustic signal captured by the PVDF transducer was above a threshold value (in this study it is 9 times above the background noise), this was categorized as a cavitation event. The cavitation probability was then simply calculated from the total number of cavitation events that were generated from a given number of incident ultrasound pulses. This value is dependent on the solvent (lower boiling point solvents cavitate more readily) and also on the properties of the acoustic pulse (e.g. pressure, frequency). Information on which transducer was fired along with the acoustic waveforms were stored on the laptop for cavitation analysis through an oscilloscope (2190D, BK Precision). All acoustic data was time-stamped for possible co-registration with changes observed in scattering profiles.

Since ultrasound introduces energy into the system, the temperature of samples could also change depending on the ultrasound conditions and history. To control this, all experiments were conducted at room temperature and the duty cycle (on/off ratio) of the incident ultrasound was controlled to allow for heat dissipation to keep the temperature nearly constant. For samples sonicated in a water bath, the change in temperature is negligible due to the high heat capacity of water and the large volume of the bath. Increases in temperature of up to ~ 20 °C were observed towards the end of long experiments performed with the in-situ sample environment, which does not currently have active cooling capabilities, but these effects were minimized by controlling the duty cycle. Work is currently in progress to implement active cooling and temperature control schemes into the sample environment for future experiments.

4.3 RESULTS

Scanning transmission electron microscopy (sTEM) was used to directly visualize the structural change induced by acoustic wave after 1 day of aging time in Figure 4.3. Regio-regular poly (3-hexylthiophene) (RR-P3HT) was fully dissolved in commonly used good solvents: chloroform (CF) (Figure 4.3(a) and (b)), and 1,2-dichlorobenzene (DCB) (Figure 4.3(c) and (d)). Acoustic insonation was then applied by placing the polymer solution vials in a commercial sonication bath for 10 min for the sample in CF (Figure 4.3(a)) and 30 min for that in DCB (Figure 4.3(c)). Fibers are formed in both solutions after sonication. It is interesting to note that the sample prepared in CF (Figure 4.3(a)) showed relatively short fibril lengths (< 1 μm), whereas DCB produces fibers that are tens of micrometers long (Figure 4.3(c)). The inset images are taken with higher

magnification and the width of the nanofibers cross-sections are ~30 nm. In contrast, the sample without sonication does not show fiber formation (Figure 3(b)) in CF. In DCB, very different fibril structures with low contrast are observed for samples without ultrasound irradiation (Figure 3 (d)), which also appears faintly in the background of the sonicated samples (Figure 3 (c)). This effect could originate be from the slow drying process of DCB that is used for sample preparation. In contrast, samples without sonication do not show fiber formation (Figure 4.3(b) and (d)) in either solution. sTEM provides representative information on the nanofiber's shape. However, due to the limit in sTEM sample preparation procedure, it cannot determine the overall fraction of fibers formed in the polymer solution. Also, it could be possible that drying, which is required for sTEM, could also induce supersaturation and crystallization. Therefore, in-situ techniques that can directly characterize the fiber formation processes in solution would be highly complementary to sTEM.

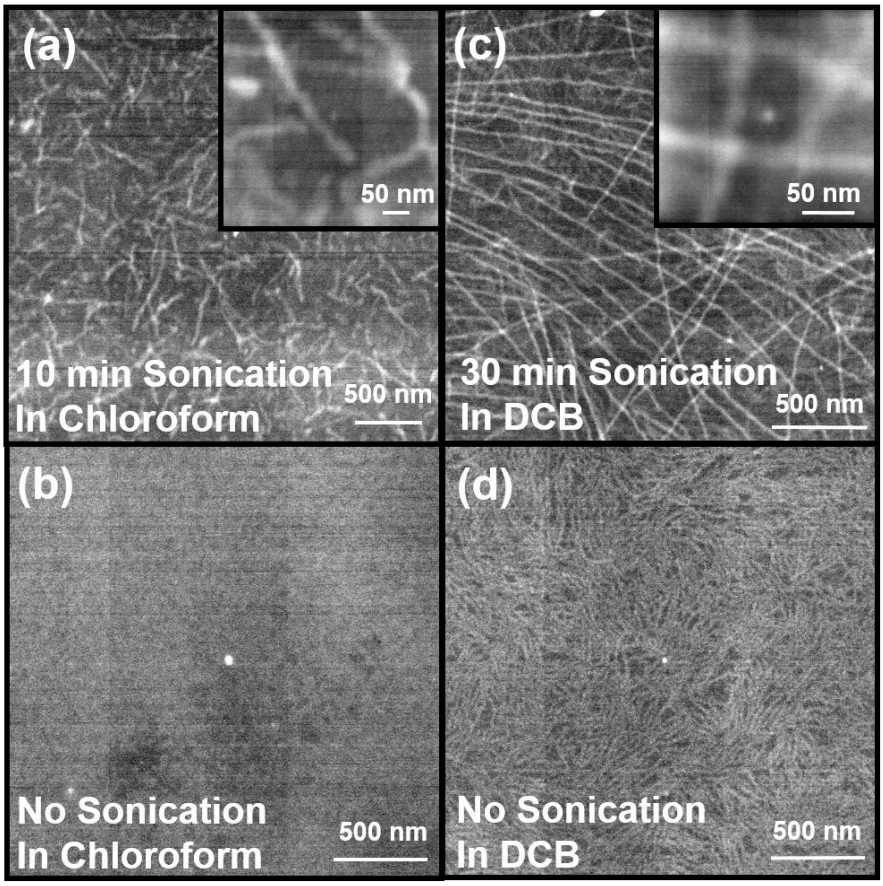

Figure 4.3. sTEM images of RR-P3HT samples with acoustic waves applied in the following conditions: 4 mg/ml in CF (a) sonicated for 10 min and (b) without sonication. 10 mg/ml in DCB (c) sonicated for 30 min and (d) without sonication. The inset figures are the same sample with higher magnification.

UV-vis spectroscopy was used to quantify the amount of RR-P3HT aggregates in solutions based on distinct absorption peaks of crystalline structures due to various vibrational states.[41] Visually, solutions of fully dissolved polymers show a transparent orange color. In contrast, the formation of even small numbers of aggregates results in a very dark solution. Figure 4.4 shows an example of ultrasound induced color change of RR-P3HT solutions. Spectra are recorded in Figure 4.5 as a function of aging time after sonication of polymer solutions in both CF and DCB. In Figure 4.5(a),

two new peaks at 566 and 618 nm start to emerge right after sonication in chloroform, which indicates formation of aggregates. The intensity of the two absorption peaks keeps increasing and they stay relatively constant after 6 hrs of aging. In contrast, the reference sample without acoustic treatment does not show aggregate formation even after 97 hrs of aging (Figure 4.5(b)). By switching solvent to DCB (Figure 4.5(c)), 10 min insonation does not result in any instantly observable change to the spectrum. Longer sonication time (30 min) induces a small peak at 607 nm for the initial spectrum after sonication (Figure 4.5(e)). Compared to CF, more absorption peaks emerge and more dramatic shifts in absorption peak positions are observed in DCB. Three distinct peaks at 512, 552, and 600 nm develop during this process. The major absorption peak also shows a red shift from 465 nm in the original spectra to 479 nm after 97 hrs of aging. Similar to samples in CF, RR-P3HT in DCB without ultrasound treatment does not exhibit any optical change due to aging (Figure 4.5(d)). Amorphous and aggregated peak absorption areas are used to convert the absorption spectrum to polymer aggregates fractions by considering the differences in extinction coefficient of fully dissolved polymers in those two forms. [41,42] The spectra after subtraction of the dissolved polymer fraction are shown in Figure 4.6, where the peaks of lowest energy 0-0 transition (A_{0-0}) and 0-1 first vibronic absorption transition (A_{0-1}) are labeled. The relative strength of A_{0-0} and A_{0-1} can be used to determine the type of aggregates. [41,43] It is interesting to note that polymers form J-like aggregates ($A_{0-0}/ A_{0-1}>1$) in CF, whereas H-like aggregates ($A_{0-0}/ A_{0-1}<1$) are produced in DCB. This implies that intrachain coupling is stronger in CF and interchain coupling signal dominates in DCB. The aggregate fraction is plotted as a function of aging time in Figure 4.5(f). It is clear that the polymer fraction that forms aggregates quickly reaches steady-state at 9% in CF. In contrast, no sign of the stabilization of aggregate concentrations is observed for DCB even after 97 hrs in solution. The fraction of polymer chains

in aggregates can be as high as ~ 17% with 30 min sonication time after 97 hrs of aging in DCB. Longer sonication time results in sharper increases of the polymer fiber fraction.

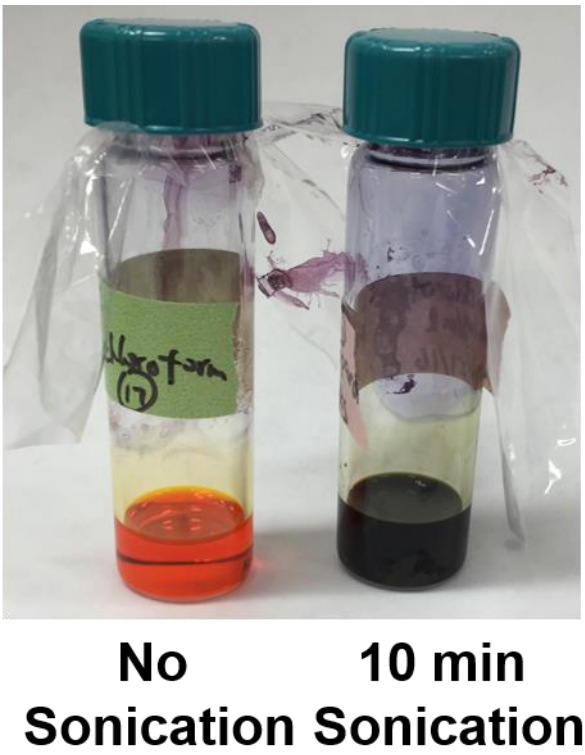

Figure 4.4. Photograph of 4 mg/ml P3HT solutions in chloroform with 10 min and without application of acoustic wave in sonication bath.

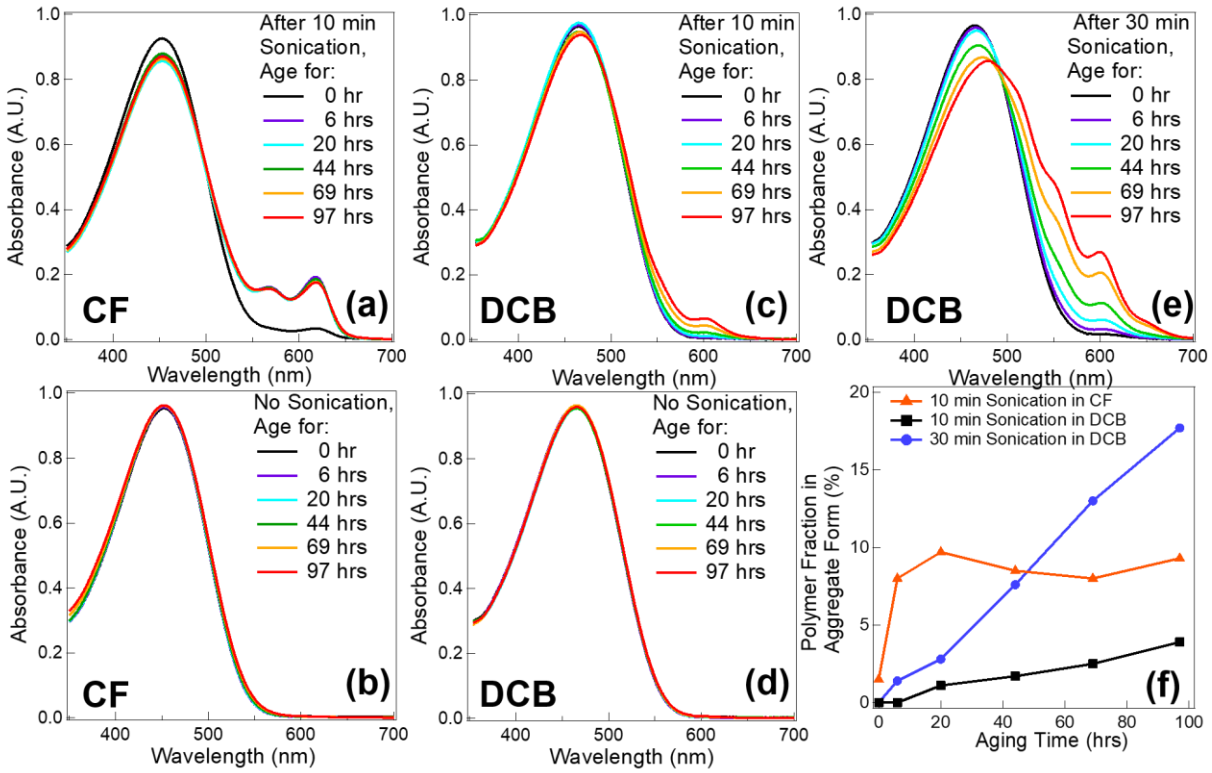

Figure 4.5. Evolution of UV-vis spectra of P3HT aging time with and without 10 min sonication in (a), (b) chloroform and in (c), (d) 1,2- dichlorobenzene, respectively. (e) shows the spectra of a sample under 30 min sonication time in 1,2-dichlorobenzene with various aging times. The corresponding aggregate fraction in different solvents under various sonication conditions is plotted in (f) as a function of aging time.

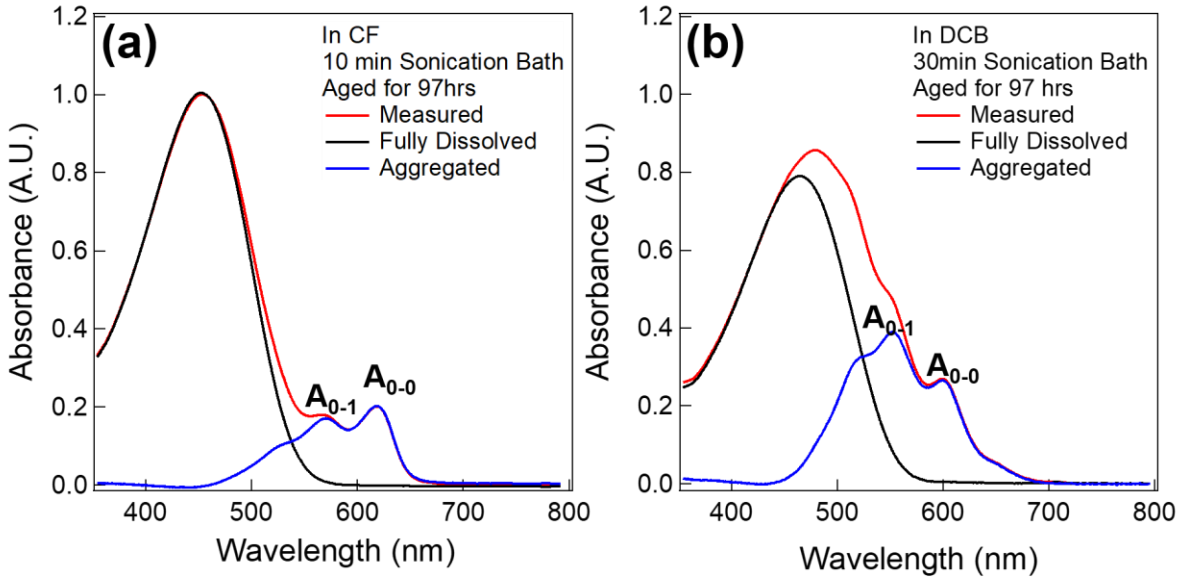

Figure 4.6. Measured absorption spectra of polymer solution aged 97 hrs after ultrasound application, completely dissolved P3HT solution, and subtracted absorption spectra of pure aggregates in (a) chloroform and (b) dichlorobenzene.

In addition to UV-vis measurements, small angle neutron scattering (SANS) was carried out to quantitatively analyze fiber formation in solution. Moreover, this is a sensitive technique that probes the system over multi-length scales and can provide information on the cross-sectional dimensions of these polymer fibers. It is important to note that fiber fractions from SANS resolves RR-P3HT portions in fibril form, whereas UV-vis probes total aggregate fraction that may or may not incorporate into fibers. Figure 4.7 shows the SANS profiles of RR-P3HT solution with various sonication times in both CF and DCB after approximately 1 day of aging. After ex-situ acoustic field irradiation, an increase in intensity at low-q range is observed in both solvents after sonication. In contrast, reference samples without ultrasonic treatment do not show fiber formation. The lack

of assembly is also observed in the sTEM images shown in Figure 3. Also, the longer the insonation time, the more significant the enhancement of the SANS intensity (Figure 5(b)). A combined model, equation (4.1), is utilized to fit the scattering profiles to extrapolate the fiber fractions and cross-sectional dimensions. This model was successfully demonstrated by our group for nanofiber system containing dissolved polymers.[26,27,44–46] Excluded volume effects ($P_{PExV}(q)$) are considered when describing the dissolved polymers. [47,48] Meanwhile, the nanofibers are modeled by a long parallelepiped form factor with a rectangular cross-section ($P_{PP}(q)$). [49,50] The first half of equation (4.1) describes the polymer nanofibers and the second half of the model represents dissolved polymers.

$$I\,(q) = \phi_v \varphi_f (\Delta\rho_{PP})^2 P_{PP}(q) + \phi_v (1-\varphi_f)(\Delta\rho_{PExV})^2 P_{PExV}(q) \qquad (4.1\ )$$

Where ϕ_v is the volume fraction of P3HT in solution, φ_f is the polymer fraction in fiber form, $\Delta\rho_{PP}$ is the SLD difference between solvent and nanofibers, and $\Delta\rho_{PExV}$ is the SLD difference between solvent and fully dissolved P3HT chains. The form factors of the parallelepiped ($P_{PP}(q)$) and polymer excluded volume model ($P_{PExV}(q)$) are given by equation (4.1) and equation (4.2) ~(4.5), respectively. In this model, only three parameters were allowed to change. These were fiber height (a), width (b), as well as polymer fractions in fiber form (φ_f). Other parameters were known or determined from fits at sonication time=0 (e.g. radius of the dissolved polymer) and kept fixed in fits at other sonication times.

$$P_{PP}(q) = \frac{2}{\pi}\int_0^{2\pi}\int_0^{2\pi}\left[\left(\frac{\sin(qA\sin\alpha\cos\beta)}{qA\sin\alpha\cos\beta}\right)\left(\frac{\sin(qB\sin\alpha\cos\beta)}{qB\sin\alpha\cos\beta}\right)\left(\frac{\sin(qC\cos\alpha)}{qC\cos\alpha}\right)\right]^2 \sin\alpha\, d\alpha d\beta \quad (4.2\ )$$

$$P_{PExV}(q) = \frac{1}{\nu U^{\frac{1}{2\nu}}}\gamma\left(\frac{1}{2\nu}, U\right) - \frac{1}{\nu U^{\frac{1}{\nu}}}\gamma\left(\frac{1}{\nu}, U\right) \qquad (4.3\ )$$

$$\gamma(x,U) = \int_0^U dt\, \exp(-t)t^{x-1} \quad (4.4)$$

$$U = \frac{q^2 R_g^2 (2\nu+1)(2\nu+2)}{6} \quad (4.5)$$

A schematic representation of the cross-sectional height (a), width (b), and fiber length (c) is illustrated in the inset schematic drawing of Figure 4.7(b). Both a and b are left as fitting variables while c is fixed at 1 μm, since it is outside of the q-range SANS is probing and cannot be determined accurately. However, this length can be justified by the fiber lengths observed from sTEM images (Figure 4.3). The fiber fraction for P3HT in chloroform after sonication is 2.79%, which is less than the fiber fractions obtained from UV-vis measurement (~ 9%). The difference could be due to the fact that UV-vis is probing the total number of aggregates but some of them may not be in fiber forms. For samples in DCB, the fiber percentages associated with each insonation periods are labeled in Figure 4.7(b). Longer exposure time to ultrasound leads to higher amounts of fiber formed. The fiber fractions after 10 min and 30 min ultrasound application time are 0.75% and 3.85%, respectively. The cross-sectional dimensions, 'a' and 'b', of the nanofibers formed in those two solvents, as extracted from SANS fits, are also listed in Table 4.2. The nanofiber formed in CF has a similar size to that in DCB, but may be a little thinner. The dimensions in both solutions are consistent with what is observed from sTEM images in Figure 4.3. They are also similar in size to P3HT fibers formed using poor solvent induced self-assembly.[26,44,46]

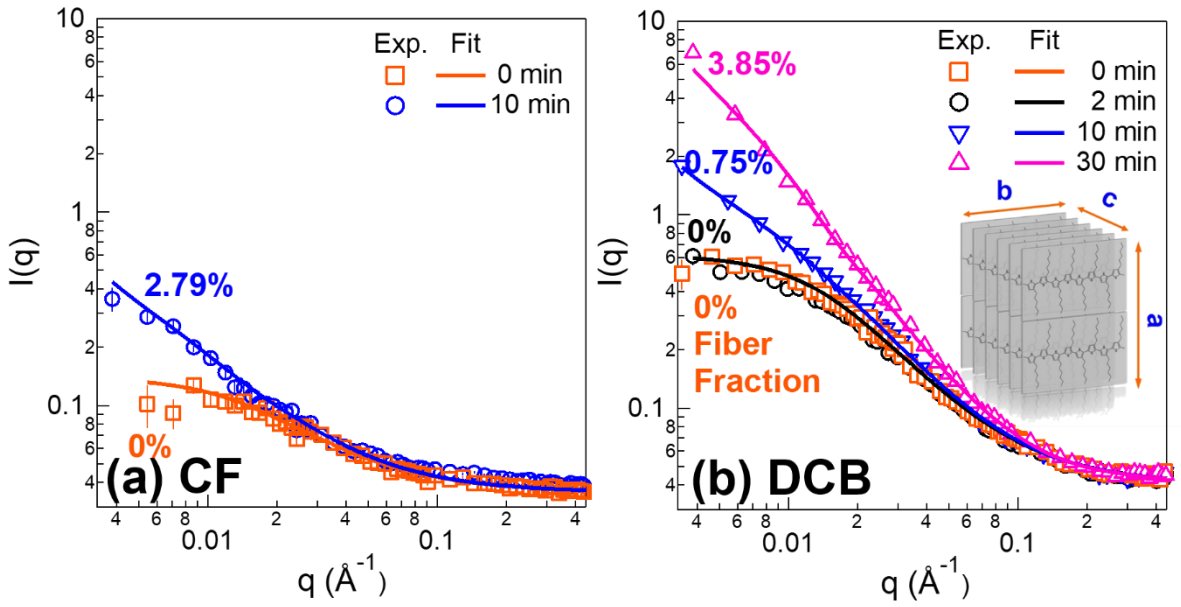

Figure 4.7. Small angle neutron scattering profiles of (a) 4 mg/ml P3HT in Chloroform with 0 and 10 min sonication durations (b) 10 mg/ml RR-P3HT in 1,2-dichlorobenzene after sonicating for 0, 2, 10, and 30min. The markers represent the experimental data and lines are the fittings based on combined model of parallelepiped and dissolved polymer model with excluded volume effect.

Table 4.2 The fixed parameters used in combined model. The dimensions of the parallelepiped model and polymer excluded volume model for chloroform, chlorobenzene, and 1,2-dichlorobenzene.

Parallelepiped			Dissolved Polymer	
Solvents	a (nm)	b (nm)	Porod Exponent	R_g (nm)
CF	1.4	38.0	1.37	9.1
DCB	2.7	38.4	1.55	9.7

Acoustic fields can also affect the assembly of other conjugated polymers with different molecular structures. Side chain engineering is an important strategy in conjugated polymers to tune their

solubility in solutions and molecular packing in films, which plays a critical role in affecting charge transport. It is also found that the final assembly structure is strongly dependent on side-chain arrangements. To gain insights into this, three polymers with variable regio-regularity, side chain length, and alkyl chain to thiophene ratio are chosen: regio-random P3HT (RRa-P3HT), P3DDT, and PQT-12. The molecular structures are depicted in the inset images in Figure 4.8. All the three polymers were dissolved in DCB at the same concentration (10 mg/ml). The samples are either not treated or exposed to 10 min ultrasound irradiation in the sonication bath.

The steep slope of the SANS profile in the low-q region of RRa P3HT in Figure 4.8(a) indicates the formation of large aggregates after the dissolution of the polymer. sTEM images in Figure 4.9 also clearly show spherical clusters with sizes of several hundred nanometers are formed. A combined model of spheres, [51] describing the aggregates, and dissolved polymer was used to quantify the polymer fractions in aggregated form (equation(4.6)). The form factor of sphere model is in equation (4.7) and dissolved polymer model with excluded volume effect is shown in equation (4.3)~ equation (4.5).

$$I\,(q) = \phi_v \varphi_f \left(\Delta\rho_{Sph}\right)^2 P_{Sph}(q) + \phi_v (1-\varphi_f)(\Delta\rho_{PExV})^2 P_{PExV}(q) \qquad (4.6)$$

$$P_{Sph}(q) = V \times \left[\frac{3(\sin(qr) - qr\,\cos(qr))}{(qr)^3}\right]^2 \qquad (4.7)$$

Where $\Delta\rho_{Sph}$ is the scattering length density difference between polymer and solution and P_{Sph} is the form factor of the sphere model, which is defined in (4.7). V is the volume of a single polymer chain and r is the radius of the sphere. All the rest of the parameters are the same as those defined in Equation (4.1). In this model, only the sphere radius and polymer fraction in sphere form are used as variables.

The model fitting was performed by varying the radius of the sphere and the fraction of the polymers that form the spherical structures, while fixing the total concentration of polymers. The results are tabulated in Table 4.3. Based on the fits, sonication can break these clusters down to smaller sizes from 441 nm to 57 nm while, at the same time, a little over six times more polymer chains are assembled into these aggregated clusters of RRa polymer. It is worth mentioning that a small fraction of the RRa P3HT polymers form aggregates in solution even before sonication. Considering that the fit has an estimated uncertainty of ± 0.01%, this value is still much smaller than the aggregated polymer fraction that results after ultrasound.

In comparison, by increasing the side chain length from 6 carbons to 12 carbons (P3DDT), the scattering profile remains unchanged after sonication (Figure 4.8(b)). This suggests that P3DDT may be closer to a thermodynamically stable solution in these solvents due to a higher solubility imposed by the longer chains. A simple model of dissolved polymer with excluded volume is used to fit this data. The radius of gyration (Rg) is found to be 5.8 nm with Porod exponent being 1.8.

In contrast, SANS profiles of PQT-12, which has the same side chain length as P3DDT but half the number of side chains per chain length, shows significant ultrasound effects (Figure 4.8(c)). Interestingly, sonication changes the scattering profile by increasing intensity at low-q. sTEM images were also utilized to visualize the final structure formed by PQT-12 (Figure 4.10). Without sonication, PQT-12 itself has a strong tendency to self-assemble into complex structures. They can form short fibers that are >100 nm long, or spherulites that can be up to several micro-meters in diameter. After sonication, longer fibers are observed and the large spherulitic particles become more branched on the perimeter. To quantify the fraction and cross-sectional sizes of the fibril

structure, the parallelepiped model combined with the dissolved polymer model was used once again. Since the spherulites are large in size, the SANS results in this q-range characterizes both the free-standing fibers and also the fibril shapes grouped radially within the spherulites. The fiber cross-sectional dimensions are similar in size, but the polymer fraction in fiber form is enhanced by about one order of magnitude from 0.03% to 0.3% after sonication. The fitting results are summarized in Table 4.4.

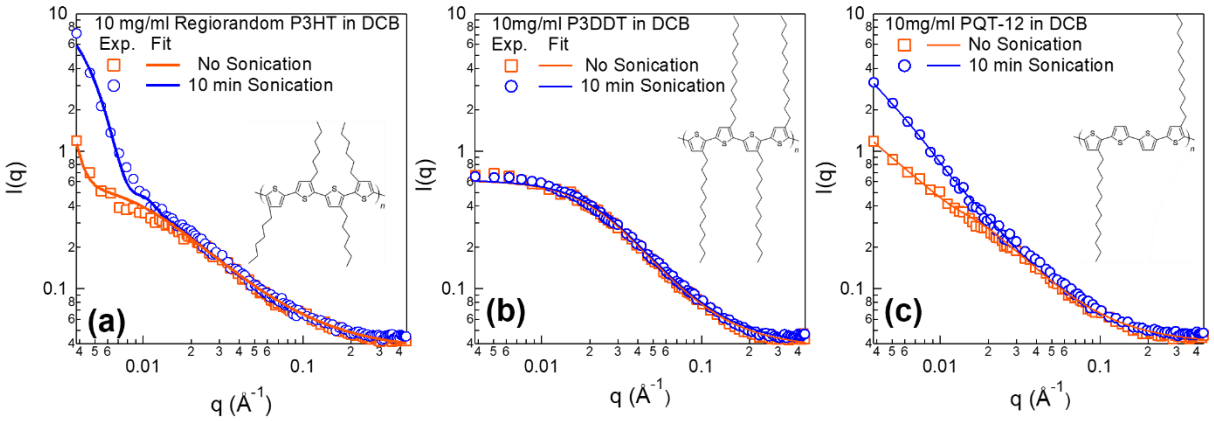

Figure 4.8. SANS profiles for 10 mg/ml (a) RRa P3HT, (b) P3DDT and (c) PQT-12 in 1,2-dichlorobenzene without and with 10 min sonication. The inset schematics show the molecular structure of each polymer. The models used for fitting the experimental data are the sphere model [51] combined with dissolved polymer with excluded volume for RRa P3HT and also a combined model of parallelepipeds [49,50] with dissolved polymer with excluded volume for PQT-12. The scattering profile of P3DDT is fit with just the dissolved polymer model with excluded volume. [47,48]

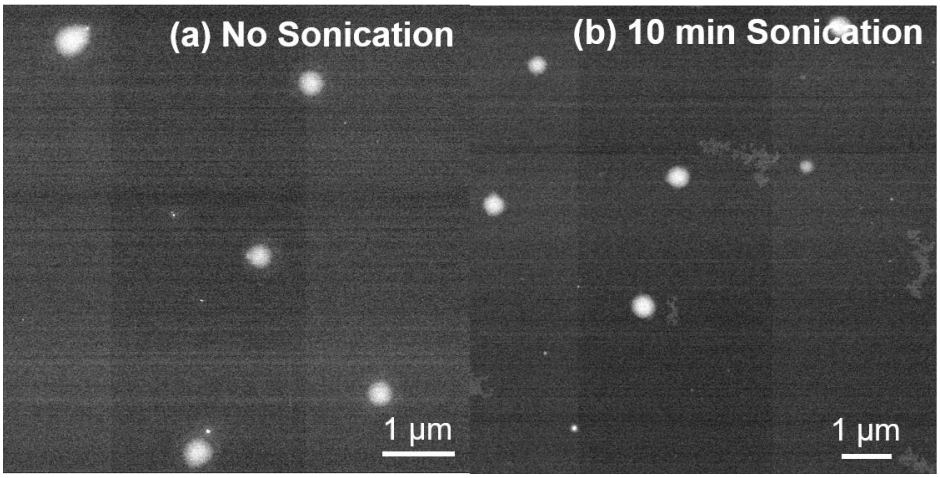

Figure 4.9. sTEM images of regio-random P3HT solution in 1,2-dichlorobenzene (a) without and (b) with 10 min sonication.

Table 4.3**.** The radius and fraction of spheres extrapolated from the scattering profile of regio-random P3HT by fitting into a combined model.

	r (nm)	φ_f(%)
No Sonication	440.7	0.02
10 min Sonication	57.4	0.13

Table 4.4**.** The cross-sectional sizes and polymer fractions in fiber form extrapolated from the scattering profile for 10 mg/ml PQT-12 in dichlorobenzene with and without sonication.

Parallelepiped				Dissolved Polymer	
	a (nm)	b (nm)	Polymer fraction in fiber form (%)	Porod Exponent	R_g (nm)
No Sonication	44.7	44.7	0.03	1.55	8.4
10 min Sonication	14.8	49.3	0.3		

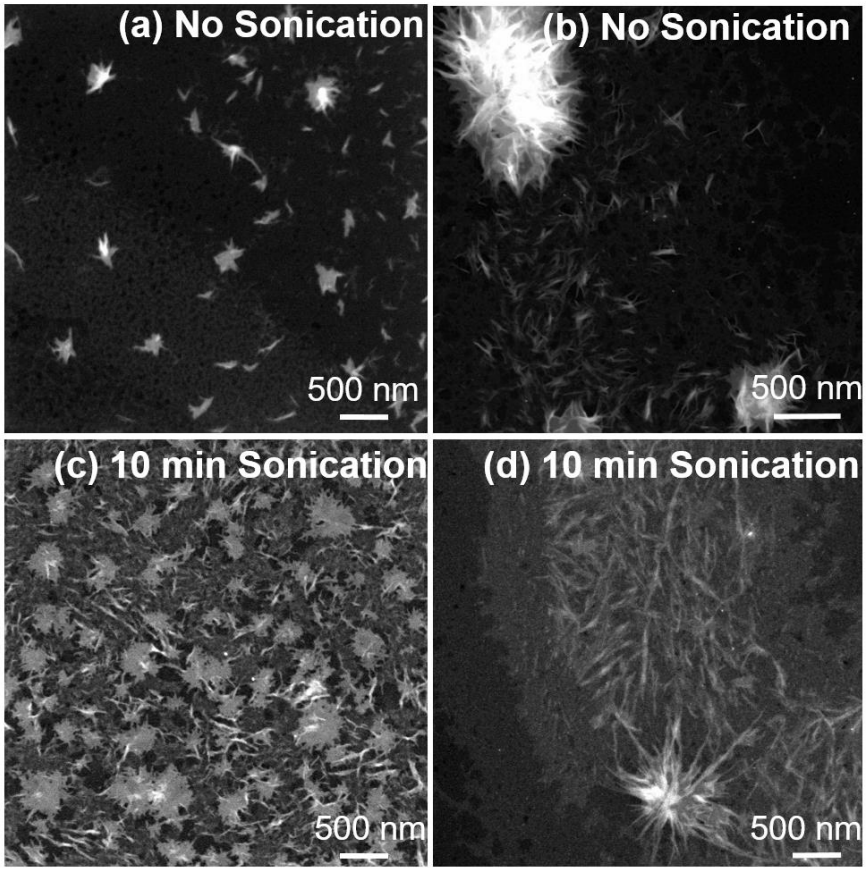

Figure 4.10. sTEM images of PQT-12 in 1,2-dichlorobenzene (a) (b) without and (c) (d) with 10 min sonication.

Well-characterized focused acoustic field experiments were also used to quantitatively draw mechanistic information. Typically, acoustic wave fields in laboratory sonication baths are chaotic and complex. This means that acoustic pressure distributions vary from place to place and may also change as a function of time. Moreover, sonication baths only operate at low frequencies (20-40 kHz) where cavitation is always present and also have poor power level control to sweep over acoustic pressures. In order to better control the incident acoustic field that is applied to the polymer solution, spherically focused transducers were utilized to systematically vary the applied

acoustic pressures at the focal point and to reduce the influence of acoustic reflections. Samples in this setup were also characterized during ultrasound application to more effectively correlate the process of fiber formation to the acoustic field. Since polymer solutions in chloroform show instantaneous color change right after ultrasound application (Figure 4.5), UV-vis measurement was also used to calculate the aggregate fraction. The normalized UV-vis spectra are plotted in Figure 4.11. The cavitation probability, which is defined as the probability of detecting a cavitation event from each acoustic pulse, for pure chloroform is shown in Figure 4.12 as a function of peak negative pressure. The threshold pressure for cavitation is at ~ 4 MPa, above which the cavitation dominates. Below this pressure, the sample is still exposed to the acoustic field and its effects, but not to the violent temperature and flow fluctuations that are induced by bubble cavitation.

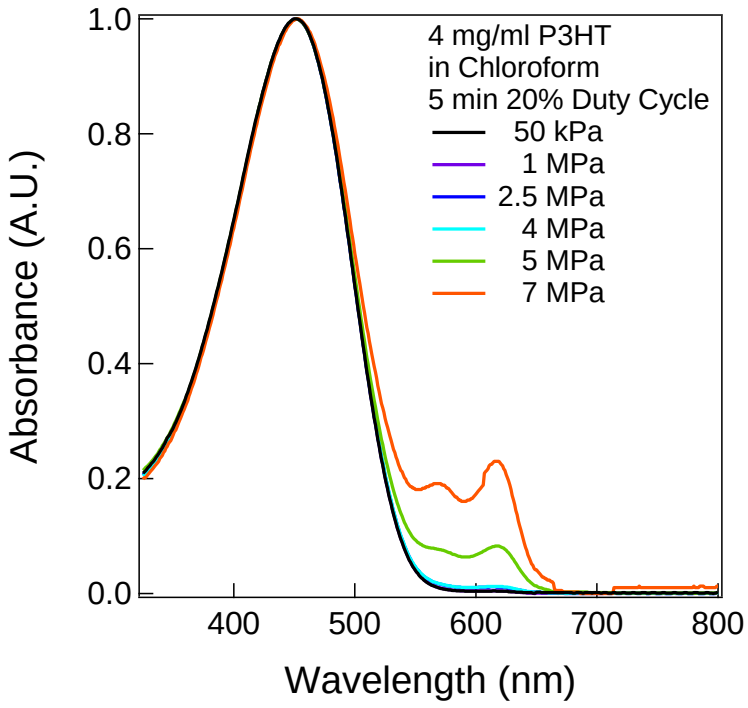

Figure 4.11. Normalized UV-vis spectra of P3HT solutions in chloroform after acoustic wave applied with varied peak negative pressures with pulse on for 5 min.

Results (Figure 4.12) show that the cavitation pressure is closely related to the onset for fiber formation, below which the polymers stay fully dissolved. When the system is exposed to a pressure above threshold, the longer the irradiation time, the higher the amount of fibers formed. Figure 4.13 shows a series of UV-vis spectra collected under 7.2 MPa over different ultrasound durations. This shows that ~100 s of insonation is enough to induce fiber formation. On the other hand, 1500 s of sonication more than doubled the amount of fibers compared to that obtained with just 100 s. In contrast, if the peak negative pressure is below the threshold, 3 MPa for example, even four times longer ultrasound application time (6000 s) is not enough to result in any observable optical change (Figure 4.14).

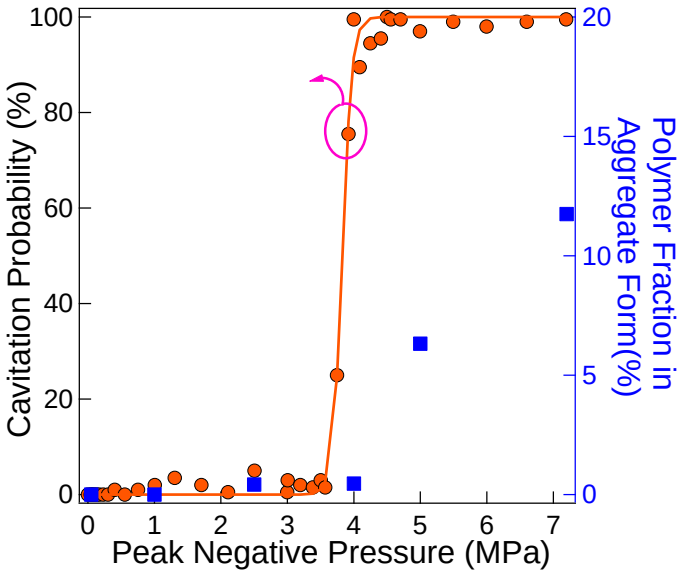

Figure 4.12. Cavitation probability curve of pure chloroform and aggregate percentage of 4 mg/ml P3HT in chloroform calculated from UV-vis measurements right after ultrasound application as a function of peak negative pressure.

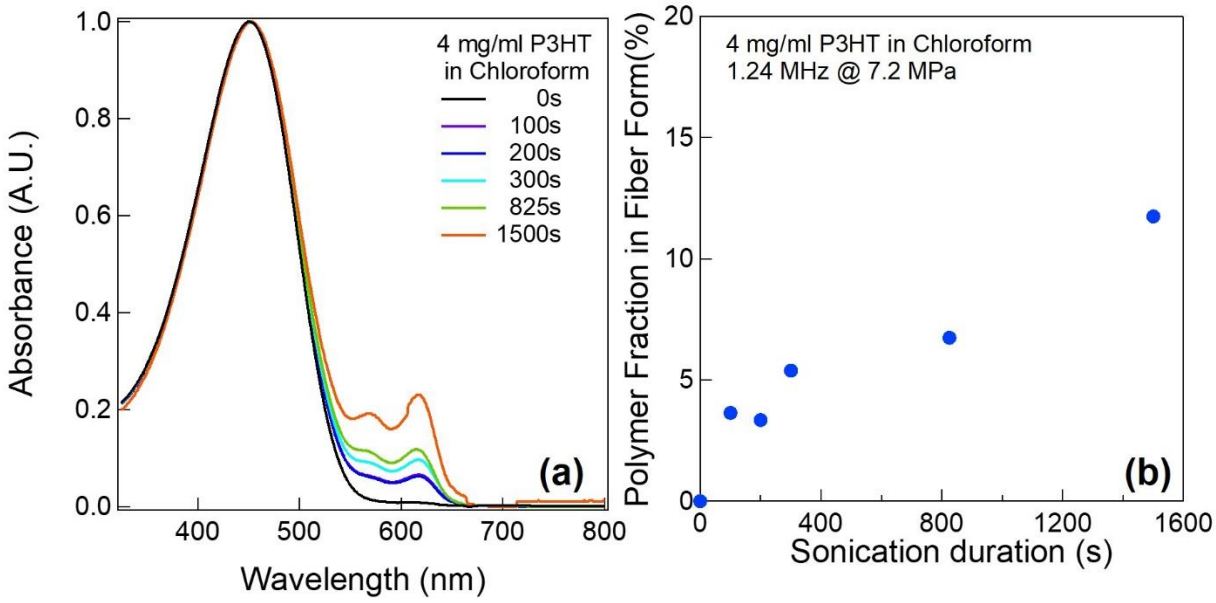

Figure 4.13. (a) Normalized UV-vis spectra of P3HT solutions in chloroform after acoustic wave applied with varied amount of time at 7.2 MPa peak negative pressure. (b) Fiber fraction calculated from UV-vis measurement as a function of sonication time.

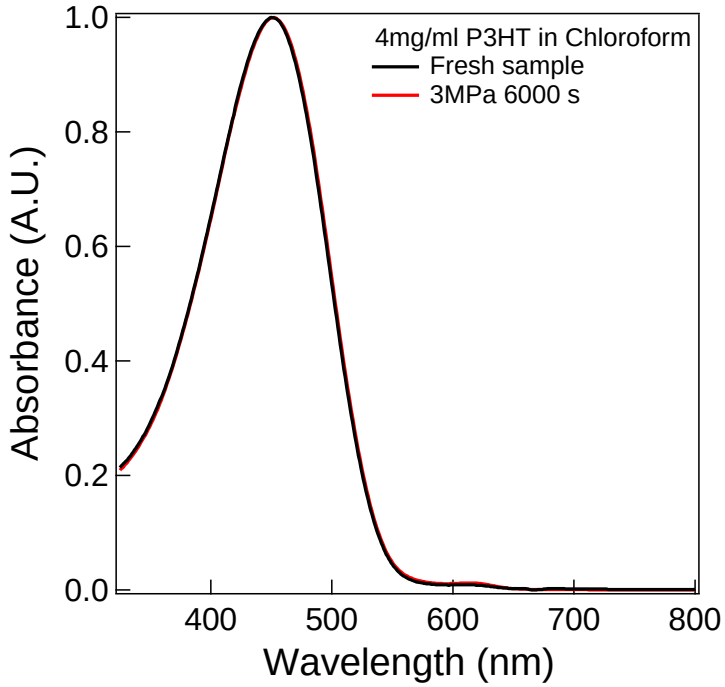

Figure 4.14. Normalized UV-vis spectra of P3HT solutions in chloroform with and without 3 MPa pressure for 6000 s. The duty cycle of the acoustic wave is 20%.

Compared to solutions in chloroform, the optical change right after ultrasound application in DCB is not as obvious (Figure 4.5). In order to probe the instantaneous structural change under ultrasound, a new sample environment was built to allow for in-situ characterization using scattering techniques (i.e. SANS, SAXS, USAXS). Figure 4.2 shows a schematic view of the setup. The sample holder is sandwiched between two identical transducers that operate alternatively to prevent accumulation of materials on either side of the container via sonophoresis. Thin Kapton films are used as front and back windows of the sample cell to provide transparent pathways for the x-ray or neutron beam. Figure 4.15(a) shows scattering profiles obtained from a combination of USAXS and SANS of RR-P3HT in DCB during sonication. Similar to ex-situ SANS results for samples exposed to ultrasound in a sonication bath (Figure 4.7), an increase in intensity is observed at the low-q range (< 0.01 $Å^{-1}$) of the data after exposure to acoustic waves at 7.2 MPa, demonstrating the formation of fiber structures. USAXS allows probing of a much lower q-range (0.0001 $Å^{-1}$ < q < 0.001 $Å^{-1}$) and it was used to track simultaneous structural changes for polymer solutions under ultrasound as a function of insonation time. Figure 4.15(a) shows a substantial increase of USAXS (i.e. low q) intensity after just 5 min of ultrasound application. The extension in sonication time lead to increased scattering intensities and decreased slopes. A power law model (equation (3.1)) is used to fit the USAXS data from 0.00014 to 0.0006 $Å^{-1}$, where both the scale factor (B) and power-law exponents (A) are left as variables for fitting.

$$I(q) = B \cdot q^{-A} \qquad (4.8)$$

Figure 4.15(b) shows the fit results corresponding to both of the parameters in equation (3.1) as a function of sonication time. The power-law exponent starts at ~3.3 and steadily decreased to ~2.3 at 17 min. It then plateaus with increased sonication time. The scale factor (B) is proportional to the fiber volume and the total amount of polymer that is forming assembled structures. This parameter increases and reaches steady state at the same time as the power-law exponents plateau. By fitting the SANS data at low-q range (0.003 to 0.01 $Å^{-1}$), a similar power-law exponent (2.39) and scale factor (6.96×10^{-6}) as in the USAXS data are obtained showing consistency in the results. All fit results are plotted with the corresponding scattering profile in Figure 8.16.

Consistent with what is observed in P3HT samples in DCB that are insonated with sonication baths, no optical shift was observed when aging for a short time (10 hrs) (Figure 4.16 (a)), in spite of the obvious changes in the scattering profiles. After an extended time aging (108 days), crystallization is observed for polymer solutions with and without ultrasound treatment based on new absorption peak formation of UV-vis spectra (Figure 4.16(b)). sTEM images also confirm that nanofibers are formed in both samples that were aged for 108 days. However, without ultrasound treatment the fibers are thick and short (typically under 500 nm) while nanofibers formed on sonicated samples are several micro-meters long.

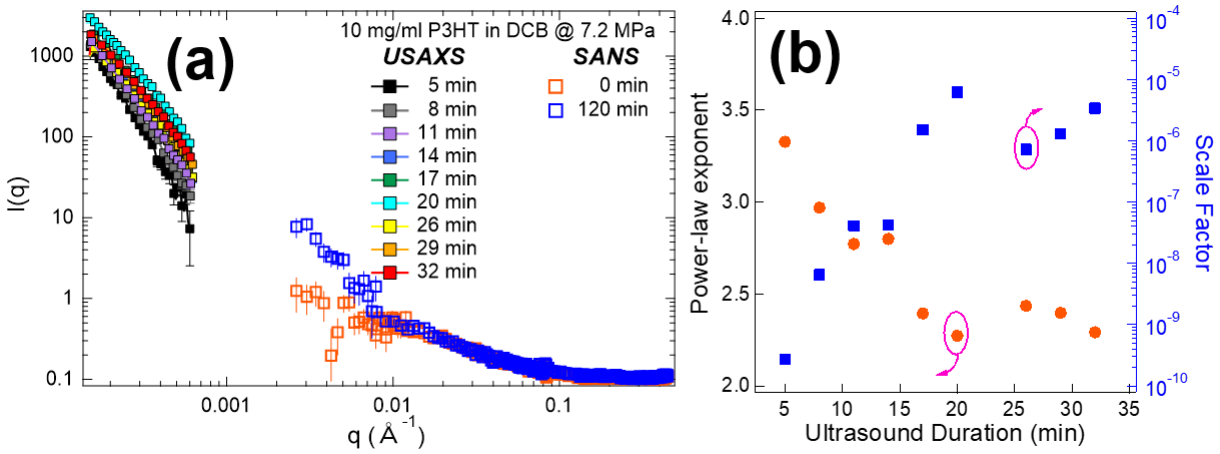

Figure 4.15. (a) In-situ characterization of assembled structures in DCB under ultrasound using USAXS and SANS for different q-ranges. The legend indicates the integrated sonication time corresponding to each scattering profile. (b) The power-law exponents and scale factors extrapolated by power law fitting as a function of ultrasound application time.

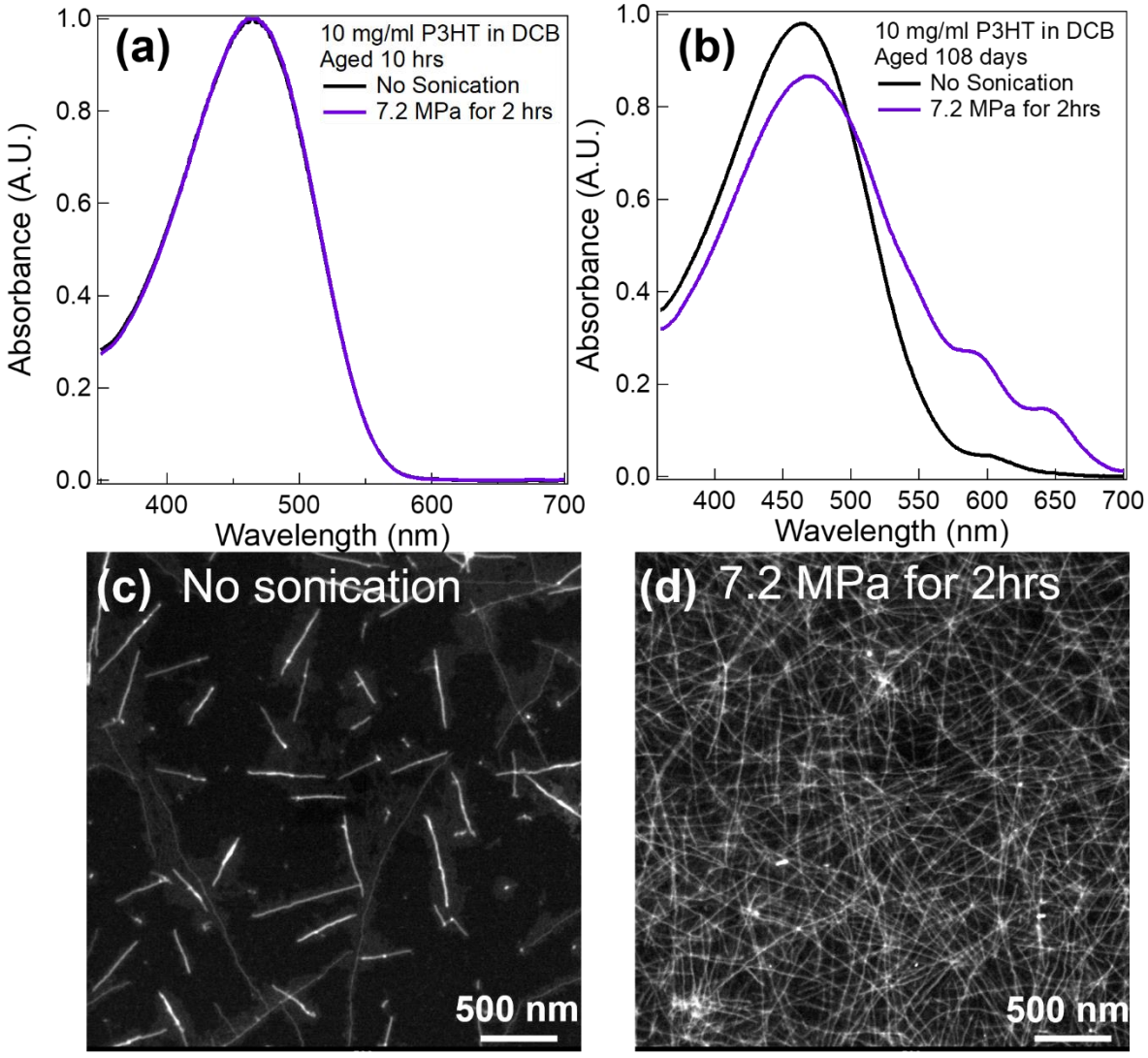

Figure 4.16. UV-vis measurement of 10 mg/ml P3HT in DCB (a) aged for 10 hrs and (b) aged for 180 days with and without ultrasound application in in-situ cell. sTEM image of (c) sample solution without ultrasound treatment and (d) 2hrs application of 7.2 MPa ultrasound after aging for 108 days.

A question still remains as to whether ultrasound can provide enough energy to induce crystallization for samples dissolved in even better solvents. To do this we used bromobenzene, which is a much better solvent for P3HT. Bromobenzene has more than five times higher solubility

than DCB and to the best of our knowledge is currently the best known solvent for P3HT. [52] In addition, deuterated bromobenzene also provides good neutron scattering contrast for P3HT. The polymer concentration and insonation time are kept the same as samples in DCB. Figure 4.17 (a) shows SANS profiles of RR-P3HT in bromobenzene before and after ultrasound of 7.2 MPa treated for 2 hrs. Ultrasound induced an increase in scattering profile in low-q range, indicating the formation of large structures. In contrast, a lower peak negative pressure of 4 MPa, Figure 4.17 (b), does not show any detectable change by SANS.

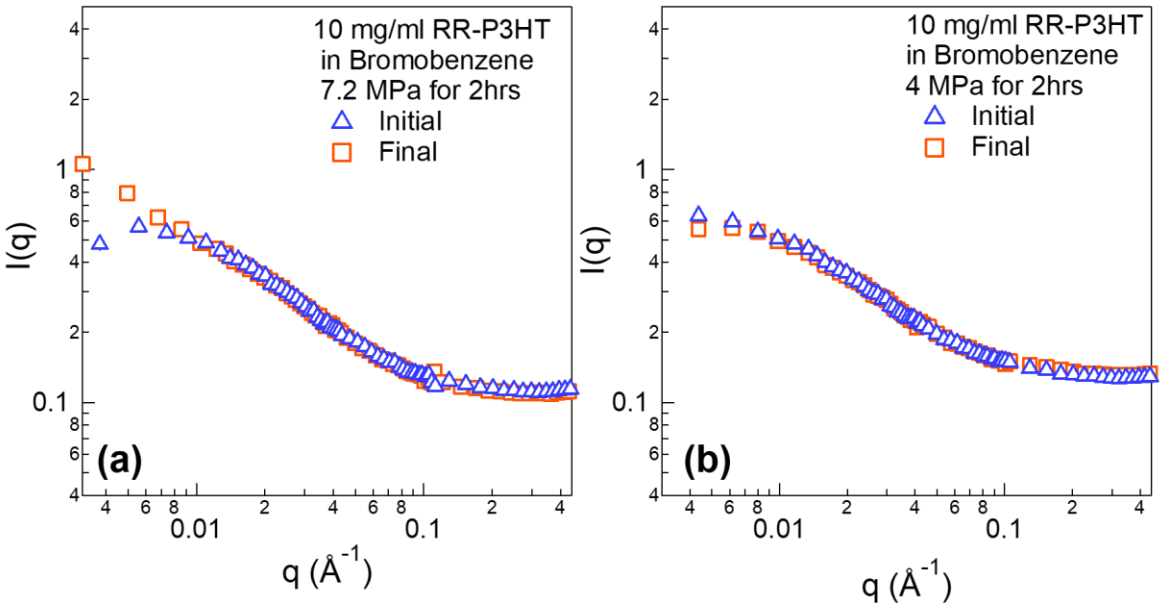

Figure 4.17. (a) SANS profiles of 10 mg/ml RR-P3HT in bromobenzene before and right after application of 7.2 MPa ultrasound for 2 hrs. (b) The same concentration of polymer solution before and right after application of 4 MPa ultrasound for 2 hrs.

4.4 Discussion

Figure 4.18 summarizes the proposed mechanism of nanofiber formation resulting from cavitation events based on homogeneous nucleation. Polymers are in a coil conformation after they are fully dissolved at higher temperatures. [53,54] When the applied acoustic wave exceeds the cavitation

threshold pressure for the solvent, bubbles form. Due to rectified diffusion into and out of the bubbles, ultrasound oscillation favors bubble growth until the bubbles grow large enough to resonate with the field and collapse under the positive pressure phase of acoustic waves.[29] The large pressures generated during the bubble collapse process alters the polymer chains to induce a more planar configuration that is more favorable for π-π stacking. This is evidenced by the UV-vis data in Figure 4.5 (a) that improved intrachain coupling is observed right after sonication in CF. It is possible that strong shear fields, which are produced by ultrasound induced cavitation, are able to stretch the chains allowing them to form extended conformations. If two extended polymers get close to each other, they could form larger structures that serve as nucleation sites for further crystallization into nanofibers. Another possibility is that the formation of a new bubble-liquid interface may also trigger the assembly of conjugated polymer nanofibers. When cavitation is generated, polymer chains can accumulate at the interface by adsorption. Since bubbles undergo a large volume expansion, they sweep through a large region of the solvent. This increases the opportunity for polymer chains to assemble when the bubble collapses and they are brought close to each other. Unfortunately, our current data is insufficient to unequivocally determine the dominating effect.

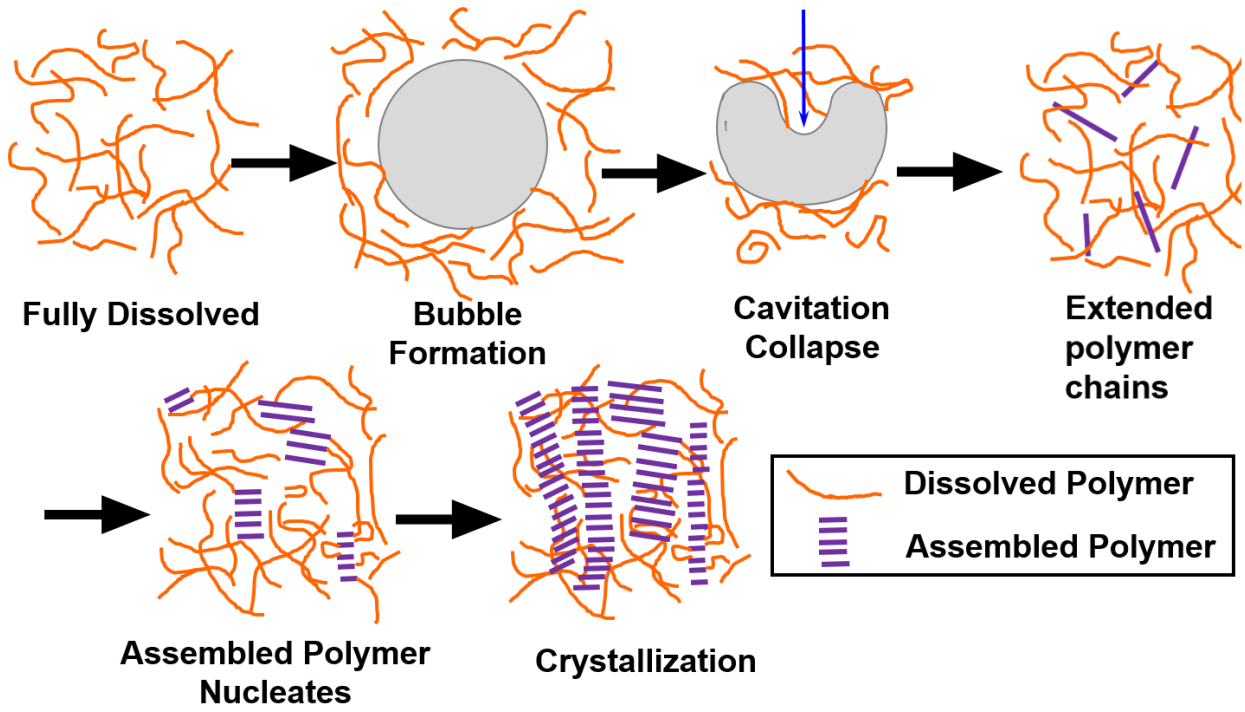

Figure 4.18. Possible mechanism of nucleation sites formation based on bubble collapse under acoustic field. Nucleation sites serve as seeds for long fiber formation.

To provide evidence of nuclei formation under ultrasound at early stages, in-situ scattering characterization experiments were performed. USAXS data in Figure 4.15 (a) shows that nucleation sites are formed after very short time of sonication (within 5 min). The high power-law exponents at the beginning of the sonication process in Figure 4.15 (b) indicates that the initial structures are highly branched. Those fractal dimensions are typical values that are also observed in P3HT colloidal and gel system.[10,44] The decrease of the power-law exponents can be attributed to the favored growth of fibril structure due to one-dimensional sonocrystallization (Figure 4.18) or the breakup of the large aggregates into small anisotropic fibrils. At the same time, the scale factor of the power law model increased with longer time of sonication. The scale factor is proportional to the volume fraction of fibers in solution and the increase can be explained by the

integrated energy that is placed into the system by continued ultrasound insonation. An equilibrium is eventually established at around 17 min of sonication, which could be a steady-state process involving the growth of new fibers induced by ultrasound, the mechanical fracture of larger fibers and the re-dissolution of fibers through dissipated heat. In a much better solvent, such as in bromobenzene (Figure 4.17), the initial nucleation is also observed with ultrasound but it is not as obvious as in 1,2-dichlorobenzene. This could be due to a larger energy barrier for inducing sonocrystallization. Since bromobenzene is a better solvent, it should be easier to re-dissolve the nucleation sites and limit the equilibrium concentration of nucleation sites. During the scattering experiment, the energy input from ultrasound could also potentially raise the sample temperature and affect the crystallization. However, an increase in temperature would act in reverse to the process of assembly since it would further increase the solubility of the polymer in the solvent. Therefore, it is conclusive that the nucleation of fibers that is observed in scattering experiments originates from ultrasound induced cavitation.

In all the 'good' solvents that were investigated in this work, nucleation and growth of fibers still resulted from application of ultrasound. It is important to note that this suggests that none of the samples were 'good' solvents in a thermodynamic sense (i.e. where the solvated state is a minimum free energy configuration). Indeed, the crystalline nanofiber state represented a minimum energy configuration and the polymer samples were only kinetically stabilized (Figure 4.1). This argument is further supported by the formation of nanofibers from fully dissolved RR-P3HT in DCB after aging for 108 days (Figure 4.16 (c)). When the temperature is raised, polymers fully dissolve in a thermodynamic sense but, as the temperature is lowered to room temperature, the polymer chains are kinetically trapped in a local energy minimum and crystallization is slowed down. Ultrasound

only accelerates the crystallization process by providing very high energy locally and in a short time to enable polymers to achieve other configurations.

Based on the above mechanism, ultrasound serves as the driving force for polymers to assemble into nucleation sites. At the same time, the high mechanical energy is also likely to break up larger structures (i.e. sonofragmentation). It is important to note that ultrasound does not break apart covalent bonds and cause polymer chain scission. This is proved by gel permeation chromatography (GPC) measurement that no obvious change is observed on P3HT samples before and after ultrasound application (Table 4.5). The unaffected molecular weight by ultrasound is also reported by Amassian's group. [25] For large structures, it has been demonstrated by kinetics experiment that the primary mechanism for sonofragmentation is based on shock waves. [55] The shock wave generated during cavitation collapse can break assembled nanofibers preventing them from growing too long. In systems with violent cavitation events, such as chloroform (i.e. low cavitation threshold) under high peak negative pressures, defects can be generated that are detrimental for producing high quality nanofibers. UV-vis results in chloroform show that very small amounts of fibers formed right after sonication (Figure 4.5) but growth continued after sonication was halted.

Table 4.5. Summary of molecular weight and polydispersity index (PDI) of P3HT (Lot # BS23-49) before and after sonication. The GPC measurements used polystyrene standard and performed by dissolving P3HT in chlorobenzene.

Polymers	M_w	*Đ*
No Treatment (Rieke Value)	69k	2.3
No Treatment (Measured)	74k	2.2
30 min Sonication bath in chloroform	74k	2.3
2 hrs 7.2 MPa with 20% duty cycle in o-DCB	66k	2.6

SANS data of RRa P3HT (Figure 4.7(a)) also reveals that large aggregates are broken into smaller sizes after sonication while at the same time the total fraction of polymers in aggregate form increased (Table 4.3). The decreased size can be attributed to sonofragmentation and the increased volume fraction of aggregates is due to sonocrystallization. For PQT-12 (Figure 4.7 (c)), SANS also confirms that ultrasound assembles the polymer chains into fibers. On the other hand, sTEM results in Figure 4.10 (c) and (d) suggest that smaller fibers are fragments produced by ultrasound breakup of branched spherulites. Although both processes are observed in polymer systems and caused by the ultrasound field, sonocrystallization is the desirable effect for improving charge transport by producing nanofibers for electronic applications. Thus, it is important to understand the underlying physics of both processes.

In sonocrystallization, after nucleation sites are initially formed, an aging process without any additional ultrasound produces larger fibers without an acoustic field to break the fibers (Figure 4.3). In chloroform, although fiber formation is observed by UV-vis right after sonication, the majority of the fibers (~ 4 times more) come from aging after cessation of ultrasound. In Figure 4.5 (f), the quick establishment of a steady-state aggregate concentration in chloroform is due to the low cavitation threshold of the solvent (Figure 4.19), which results in more cavitation events and nucleation sites at a given acoustic input.

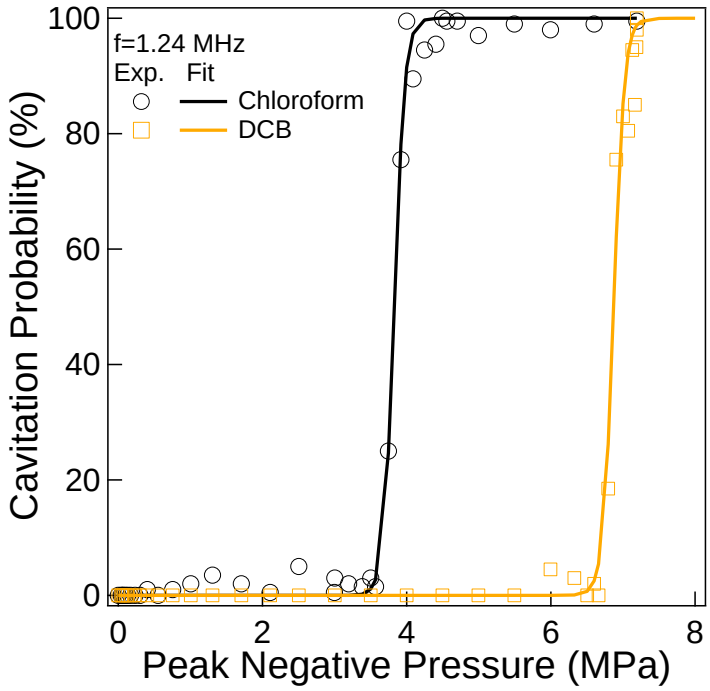

Figure 4.19. Cavitation probability of solvents as a function of peak negative pressure for chloroform and dichlorobenzene.

In contrast, P3HT in DCB has a higher cavitation threshold (Figure 4.19) and a larger energy barrier to confine polymers in the fully dissolved local minimum, creating fewer nucleation sites. Therefore, it does not form enough crystallites to cause optical shifts in UV-vis measurement right

after ultrasound application without aging. This also results in a slower crystallization process, which produces longer fibers (Figure 4.3(c)). A longer sonication time in DCB also results in faster fiber growth because more energy input produces more crystalline nuclei. For this reason, both the UV-vis and SANS data show that longer sonication times creates more fibers (Figure 4.5(f) and Figure 4.7).

It is worth mentioning that the capability of tuning the excitonic coupling could be useful for changing the population of different spin states, thus controlling the photophysics. [41] For example, J-like aggregates have been shown to promote triplet formation that leads to stronger photoluminescence (PL) quenching as compared to H-like aggregates. [41] Not many reports exist on methods to form J-like aggregates. They are often formed in toluene and it requires polymers to have high regioregularity or low dispersity. [43,56,57] This work provides an alternative and simple method to reliably generate J-like aggregates from commercially available P3HT in chloroform. The aggregate type can also be tuned using different solvents. In Figure 4.5 (a), polymers exhibit stronger intrachain coupling in CF (J-like aggregates), which indicates that π-π stacking is weaker than when compared to fibers formed in DCB (H-like aggregates). The stronger intrachain coupling in CF could also explain why the fiber length is shorter in CF as compared to DCB.

During the crystallization process, the interactions between polymer chains can alter the final assembled structures. This can be achieved by changing the polymer molecular structure, such as the side chains as shown in Figure 4.8. RRa-P3HT (Figure 4.8(a)) is known not to crystallize because of the steric hindrance imposed by randomly oriented side chains. Still, ultrasound promotes polymer chains to form aggregates (Table 4.3 and Figure 4.9). In contrast, RR polythiophenes with longer side-chains (i.e. 12 carbons in P3DDT) achieve a high solubility at room temperature so that ultrasound fields are unable to produce any fiber crystallization or

induced-assembly. Interestingly, assembled structures can still be induced by ultrasound for PQT-12, which also has long side-chains (12 carbons) but fewer chains-per-monomer resulting in a lower solubility when compared to P3DDT. Therefore, the capacity to sonocrystallize a conjugated polymer seems to correlate best with its solubility.

4.5 SUMMARIES

In summary, it is demonstrated that P3HT can be assembled into nanofibers under ultrasound in solvents that are commonly believed to be 'good' solvents in a thermodynamic sense. Our results suggest that the dissolved state of these polymers is not a global minimum in the free-energy landscape. The formation of fiber in solution was quantified by both UV-vis and SANS measurements with consistent results. Ultrasound was determined to induce the formation of nucleation sites in the system and continued aging without acoustic insonation is crucial to achieve high fiber fractions. The molecular structure of the conjugated polymers was also found to be critical for ultrasound-directed polymer assembly. It was also shown via in-situ experiments that polymer assembly is strongly correlated to solvent cavitation. The mechanism of sonocrystallization is proposed to be based on nucleation-and-growth.

4.6 REFERENCES

(1) Cho, J. H.; Lee, J.; Xia, Y.; Kim, B.; He, Y.; Renn, M. J.; Lodge, T. P.; Daniel Frisbie, C. Printable Ion-Gel Gate Dielectrics for Low-Voltage Polymer Thin-Film Transistors on Plastic. *Nat. Mater.* **2008**, *7* (11), 900–906 DOI: 10.1038/nmat2291.

(2) Wu, C.-H.; Chueh, C.-C.; Xi, Y.-Y.; Zhong, H.-L.; Gao, G.-P.; Wang, Z.-H.; Pozzo, L. D.; Wen, T.-C.; Jen, A. K.-Y. Influence of Molecular Geometry of Perylene Diimide Dimers

and Polymers on Bulk Heterojunction Morphology Toward High-Performance Nonfullerene Polymer Solar Cells. *Adv. Funct. Mater.* **2015**, *25* (33), 5326–5332 DOI: 10.1002/adfm.201501971.

(3) Sekine, C.; Tsubata, Y.; Yamada, T.; Kitano, M.; Doi, S. Recent Progress of High Performance Polymer OLED and OPV Materials for Organic Printed Electronics. *Sci. Technol. Adv. Mater.* **2014**, *15* (3), 034203 DOI: 10.1088/1468-6996/15/3/034203.

(4) Löffler, S.; Libberton, B.; Richter-Dahlfors, A. Organic Bioelectronic Tools for Biomedical Applications. *Electronics* **2015**, *4* (4), 879–908 DOI: 10.3390/electronics4040879.

(5) Oh, J. Y.; Rondeau-Gagné, S.; Chiu, Y.-C.; Chortos, A.; Lissel, F.; Wang, G.-J. N.; Schroeder, B. C.; Kurosawa, T.; Lopez, J.; Katsumata, T.; Xu, J.; Zhu, C.; Gu, X.; Bae, W.-G.; Kim, Y.; Jin, L.; Chung, J. W.; Tok, J. B.-H.; Bao, Z. Intrinsically Stretchable and Healable Semiconducting Polymer for Organic Transistors. *Nature* **2016**, *539* (7629), 411–415 DOI: 10.1038/nature20102.

(6) Noriega, R.; Rivnay, J.; Vandewal, K.; Koch, F. P. V.; Stingelin, N.; Smith, P.; Toney, M. F.; Salleo, A. A General Relationship between Disorder, Aggregation and Charge Transport in Conjugated Polymers. *Nat. Mater.* **2013**, *12* (11), 1038–1044 DOI: 10.1038/nmat3722.

(7) Luo, C.; Kyaw, A. K. K.; Perez, L. a.; Patel, S.; Wang, M.; Grimm, B.; Bazan, G. C.; Kramer, E. J.; Heeger, A. J. General Strategy for Self-Assembly of Highly Oriented Nanocrystalline Semiconducting Polymers with High Mobility. *Nano Lett.* **2014**, *14* (5), 2764–2771 DOI: 10.1021/nl500758w.

(8) Diao, Y.; Tee, B. C.-K.; Giri, G.; Xu, J.; Kim, D. H.; Becerril, H. a; Stoltenberg, R. M.; Lee, T. H.; Xue, G.; Mannsfeld, S. C. B.; Bao, Z. Solution Coating of Large-Area Organic

Semiconductor Thin Films with Aligned Single-Crystalline Domains. *Nat. Mater.* **2013**, *12* (7), 665–671 DOI: 10.1038/nmat3650.

(9) Li, J.-H.; Xi, Y.; Pozzo, L. D.; Xu, J.-T.; Luscombe, C. K. Macroscopically Aligned Nanowire Arrays of π-Conjugated Polymers via Shear-Enhanced Crystallization. *J. Mater. Chem. C* **2017** DOI: 10.1039/C7TC01419H.

(10) Xi, Y.; Pozzo, L. D. Electric Field Directed Formation of Aligned Conjugated Polymer Fibers. *Soft Matter* **2017**, *13*, 3894–3908 DOI: 10.1039/C7SM00485K.

(11) Cheng, Q.; Gregan, E.; Byrne, H. Ultrasound-Assisted SWNTs Dispersion : Effects of Sonication Parameters and Solvent Properties Ultrasound-Assisted SWNTs Dispersion : Effects of Sonication Parameters and Solvent Properties. *J. Phys. Chem. C* **2010**, *114* (19), 8821–8827.

(12) Gaikwad, S. G.; Pandit, A. B. Ultrasound Emulsification: Effect of Ultrasonic and Physicochemical Properties on Dispersed Phase Volume and Droplet Size. *Ultrason. Sonochem.* **2008**, *15* (4), 554–563 DOI: 10.1016/j.ultsonch.2007.06.011.

(13) Brown, R. B.; Audet, J. Current Techniques for Single-Cell Lysis. *J. R. Soc. Interface* **2008**, *5* (Suppl_2), S131–S138 DOI: 10.1098/rsif.2008.0009.focus.

(14) Czechowska-Biskup, R.; Rokita, B.; Lotfy, S.; Ulanski, P.; Rosiak, J. M. Degradation of Chitosan and Starch by 360-KHz Ultrasound. *Carbohydr. Polym.* **2005**, *60* (2), 175–184 DOI: 10.1016/j.carbpol.2004.12.001.

(15) Rossi, D.; Jamshidi, R.; Saffari, N.; Kuhn, S.; Gavriilidis, A.; Mazzei, L. Continuous-Flow Sonocrystallization in Droplet-Based Microfluidics. *Cryst. Growth Des.* **2015**, *15* (11),

5519–5529 DOI: 10.1021/acs.cgd.5b01153.

(16) Kurotani, M.; Hirasawa, I. Polymorph Control of Sulfamerazine by Ultrasonic Irradiation. *J. Cryst. Growth* **2008**, *310* (21), 4576–4580 DOI: 10.1016/j.jcrysgro.2008.08.002.

(17) Ruecroft, G.; Hipkiss, D.; Ly, T.; Maxted, N.; Cains, P. W. Sonocrystallization:? The Use of Ultrasound for Improved Industrial Crystallization. *Org. Process Res. Dev.* **2005**, *9* (6), 923–932 DOI: 10.1021/op050109x.

(18) Zhang, C. Y.; Wang, Y.; Schubert, R.; Liu, Y.; Wang, M. Y.; Chen, D.; Guo, Y. Z.; Dong, C.; Lu, H. M.; Liu, Y. M.; Wu, Z. Q.; Betzel, C.; Yin, D. C. Effect of Audible Sound on Protein Crystallization. *Cryst. Growth Des.* **2016**, *16* (2), 705–713 DOI: 10.1021/acs.cgd.5b01268.

(19) Crespo, R.; Martins, P. M.; Gales, L.; Rocha, F.; Damas, A. M. Potential Use of Ultrasound to Promote Protein Crystallization. *J. Appl. Crystallogr.* **2010**, *43* (6), 1419–1425 DOI: 10.1107/S0021889810040951.

(20) Kitayama, H.; Yoshimura, Y.; So, M.; Sakurai, K.; Yagi, H.; Goto, Y. A Common Mechanism Underlying Amyloid Fibrillation and Protein Crystallization Revealed by the Effects of Ultrasonication. *Biochim. Biophys. Acta - Proteins Proteomics* **2013**, *1834* (12), 2640–2646 DOI: 10.1016/j.bbapap.2013.09.016.

(21) Lee, M.; Jeon, H.; Jang, M.; Yang, H. A Physicochemical Approach Toward Extending Conjugation and the Ordering of Solution-Processable Semiconducting Polymers. *ACS Appl. Mater. Interfaces* **2016**, *8* (7), 4819–4827 DOI: 10.1021/acsami.5b12552.

(22) Kleinhenz, N.; Persson, N.; Xue, Z.; Chu, P. H.; Wang, G.; Yuan, Z.; McBride, M. A.; Choi,

D.; Grover, M. A.; Reichmanis, E. Ordering of Poly(3-Hexylthiophene) in Solutions and Films: Effects of Fiber Length and Grain Boundaries on Anisotropy and Mobility. *Chem. Mater.* **2016**, *28* (11), 3905–3913 DOI: 10.1021/acs.chemmater.6b01163.

(23) Hu, H.; Zhao, K.; Fernandes, N.; Boufflet, P.; Bannock, J. H.; Yu, L.; de Mello, J. C.; Stingelin, N.; Heeney, M.; Giannelis, E. P.; Amassian, A. Entanglements in Marginal Solutions: A Means of Tuning Pre-Aggregation of Conjugated Polymers with Positive Implications for Charge Transport. *J. Mater. Chem. C* **2015**, *3* (28), 7394–7404 DOI: 10.1039/C5TC01425E.

(24) Lim, J. A.; Liu, F.; Ferdous, S.; Muthukumar, M.; Briseno, A. L. Polymer Semiconductor Crystals. *Mater. Today* **2010**, *13* (5), 14–24 DOI: 10.1016/S1369-7021(10)70080-8.

(25) Zhao, K.; Khan, H. U.; Li, R.; Su, Y.; Amassian, A. Entanglement of Conjugated Polymer Chains Influences Molecular Self-Assembly and Carrier Transport. *Adv. Funct. Mater.* **2013**, *23* (48), 6024–6035 DOI: 10.1002/adfm.201301007.

(26) Newbloom, G. M.; de la Iglesia, P.; Pozzo, L. D. Controlled Gelation of Poly(3-Alkylthiophene)s in Bulk and in Thin-Films Using Low Volatility Solvent/Poor-Solvent Mixtures. *Soft Matter* **2014**, *10* (44), 8945–8954 DOI: 10.1039/c4sm00960f.

(27) Iglesia, P. D. La; Pozzo, D. C. Effects of Supersaturation on the Structure and Properties of Poly(9,9-Dioctyl Fluorene) Organogels. *Soft Matter* **2013**, *9* (47), 11214 DOI: 10.1039/c3sm51753e.

(28) T. G. Leighton. *The Acoustic Bubble*; Academic Press, 1997.

(29) Caupin, F.; Herbert, E. Cavitation in Water: A Review. *Comptes Rendus Phys.* **2006**, *7* (9–

10), 1000–1017 DOI: 10.1016/j.crhy.2006.10.015.

(30) Neppiras, E. A. Acoustic Cavitation Series: Part One. Acoustic Cavitation: An Introduction. *Ultrasonics* **2017**, *22* (1), 3894–3908 DOI: 10.1016/0041-624X(84)90057-X.

(31) Ahmadi, F.; McLoughlin, I. V.; Chauhan, S.; Ter-Haar, G. Bio-Effects and Safety of Low Intensity, Low Frequency Ultrasonic Exposure. *Prog. Biophys. Mol. Biol.* **2012** DOI: 10.1016/j.pbiomolbio.2012.01.004.

(32) Sponer, J. Dependence of the Cavitation Threshold on the Ultrasonic Frequency. *Czechoslov. J. Phys.* **1990**, *40* (10), 1123–1132 DOI: 10.1007/BF01597973.

(33) Dear, J. P.; Field, J. E. A Study of the Collapse of Arrays of Cavities. *J. Fluid Mech.* **1988**, *190* (1), 409 DOI: 10.1017/S0022112088001387.

(34) Tomita, Y.; Shima, A. Mechanisms of Impulsive Pressure Generation and Damage Pit Formation by Bubble Collapse. *J. Fluid Mech.* **1986**, *169* (1), 535 DOI: 10.1017/S0022112086000745.

(35) Suslick, K. S.; Didenko, Y.; Fang, M. M.; Hyeon, T.; Kolbeck, K. J.; McNamara III, W. B.; Mdleleni, M. M.; Wong, M. Acoustic Cavitation and Its Consequences. *Philos. Trans. R. Soc. A* **1999**, *357* (1927), 335–353 DOI: 10.1098/rsta.1999.0330.

(36) Ruecroft, G.; others. Sonocrystallization: The Use of Ultrasound for Improved Industrial Crystallization. *Org.Proc.Res.Dev.* **2005**, *9* (6), 923–932.

(37) Kline, S. R. Reduction and Analysis of SANS and USANS Data Using IGOR Pro. *J. Appl. Crystallogr.* **2006**, *39* (6), 895–900 DOI: 10.1107/S0021889806035059.

(38) P. Butler, G. Alina, R. C. Hernandez, M. Doucet, A. Jackson, P. Kienzle, S. K. and J. Z.

SASView for Small Angle Scattering Analysis http://www.sasview.org/.

(39) Ilavsky, J.; Jemian, P. R.; Allen, A. J.; Zhang, F.; Levine, L. E.; Long, G. G. Ultra-Small-Angle X-Ray Scattering at the Advanced Photon Source. *J. Appl. Crystallogr.* **2009**, *42* (3), 469–479 DOI: 10.1107/S0021889809008802.

(40) Ilavsky, J.; Jemian, P. R. Irena: Tool Suite for Modeling and Analysis of Small-Angle Scattering. *J. Appl. Crystallogr.* **2009**, *42* (2), 347–353 DOI: 10.1107/S0021889809002222.

(41) Clark, J.; Chang, J. F.; Spano, F. C.; Friend, R. H.; Silva, C. Determining Exciton Bandwidth and Film Microstructure in Polythiophene Films Using Linear Absorption Spectroscopy. *Appl. Phys. Lett.* **2009**, *94* (16), 2007–2010 DOI: 10.1063/1.3110904.

(42) Scharsich, C.; Lohwasser, R. H.; Sommer, M.; Asawapirom, U.; Scherf, U.; Thelakkat, M.; Neher, D.; Köhler, A. Control of Aggregate Formation in Poly(3-Hexylthiophene) by Solvent, Molecular Weight, and Synthetic Method. *J. Polym. Sci. Part B Polym. Phys.* **2012**, *50* (6), 442–453 DOI: 10.1002/polb.23022.

(43) Mazzio, K. A.; Rice, A. H.; Durban, M. M.; Luscombe, C. K. Effect of Regioregularity on Charge Transport and Structural and Excitonic Coherence in Poly(3-Hexylthiophene) Nanowires. *J. Phys. Chem. C* **2015**, *119* (27), 14911–14918 DOI: 10.1021/acs.jpcc.5b02914.

(44) Newbloom, G. M.; Kim, F. S.; Jenekhe, S. a.; Pozzo, D. C. Mesoscale Morphology and Charge Transport in Colloidal Networks of Poly(3-Hexylthiophene). *Macromolecules* **2011**, *44* (10), 3801–3809 DOI: 10.1021/ma2000515.

(45) Newbloom, G. M.; Weigandt, K. M.; Pozzo, D. C. Electrical, Mechanical, and Structural Characterization of Self-Assembly in Poly(3-Hexylthiophene) Organogel Networks.

Macromolecules **2012**, *45*, 3452–3462 DOI: 10.1021/ma202564k.

(46) Newbloom, G. M.; Weigandt, K. M.; Pozzo, D. C. Structure and Property Development of Poly(3-Hexylthiophene) Organogels Probed with Combined Rheology, Conductivity and Small Angle Neutron Scattering. *Soft Matter* **2012**, *8* (34), 8854 DOI: 10.1039/c2sm26114f.

(47) Hammouda, B. SANS from Homogeneous Polymer Mixtures - A Unified Overview. *Adv. Polym. Sci.* **1993**, *106*, 87–133.

(48) H. Benoit. La Diffusion de La Lumiere Par Des Macromolecules En Chaines En Solution Dans Un Bon Solvant. *Comptes Rendus* **1957**, *245*, 2244–2247.

(49) Roman Nayuk, K. H. Formfactors of Hollow and Massive Rectangular Parallelepipeds at Variable Degree of Anisometry. *Zeitschrift für Phys. Chemie* **2012**, *226*, 837–854.

(50) P. Mittelbach, G. P. X-Ray Low-Angle Scattering by Dilute Scattering Colloidal Systems. The Calculation of Scattering Curves of Parallelepipeds. *Acta Phys. Austriaca* **1961**, *14*, 185–211.

(51) A Guinier, G. F. *Small-Angle Scattering of X-Rays*; John Wiley & Sons, Inc., 1955.

(52) Machui, F.; Langner, S.; Zhu, X.; Abbott, S.; Brabec, C. J. Determination of the P3HT:PCBM Solubility Parameters via a Binary Solvent Gradient Method: Impact of Solubility on the Photovoltaic Performance. *Sol. Energy Mater. Sol. Cells* **2012**, *100*, 138–146 DOI: 10.1016/j.solmat.2012.01.005.

(53) Newbloom, G. M.; Hoffmann, S. M.; West, A. F.; Gile, M. C.; Sista, P.; Cheung, H. C.; Luscombe, C. K.; Pfaendtner, J.; Pozzo, L. D. Solvatochromism and Conformational Changes in Fully Dissolved Poly(3-Alkylthiophene)S. *Langmuir* **2015**, *31* (1), 458–468

DOI: 10.1021/la503666x.

(54) McCulloch, B.; Ho, V.; Hoarfrost, M.; Stanley, C.; Do, C.; Heller, W. T.; Segalman, R. A. Polymer Chain Shape of Poly(3-Alkylthiophenes) in Solution Using Small-Angle Neutron Scattering. *Macromolecules* **2013**, *46* (5), 1899–1907 DOI: 10.1021/ma302463d.

(55) Zeiger, B.; Suslick, K. Sonofragmentation of Molecular Crystals: Observations and Modeling. *Proc. Meet. Acoust.* **2013**, *19*, 045089 DOI: 10.1121/1.4800930.

(56) Thomas, A. K.; Garcia, J. A.; Ulibarri-Sanchez, J.; Gao, J.; Grey, J. K. High Intrachain Order Promotes Triplet Formation from Recombination of Long-Lived Polarons in Poly(3-Hexylthiophene) J-Aggregate Nanofibers. *ACS Nano* **2014**, *8* (10), 10559–10568 DOI: 10.1021/nn5040026.

(57) Niles, E. T.; Roehling, J. D.; Yamagata, H.; Wise, A. J.; Spano, F. C.; Moulé, A. J.; Grey, J. K. J-Aggregate Behavior in Poly-3-Hexylthiophene Nanofibers. *J. Phys. Chem. Lett.* **2012**, *3* (2), 259–263 DOI: 10.1021/jz201509h.

Chapter 5. Self-assembly of Donor-acceptor Conjugated Polymers Induced by Miscible Poor Solvents

5.1 INTRODUCTION AND MOTIVATION

Conjugated polymers (CPs) have gained interests due to their potential to be used in electronic devices, such as flexible and stretchable electronic skin, light weight and economic organic photovoltaics (OPVs), electrically controllable and scalable smart windows, and biocompatible electronics mimicking neural systems. [1–4] However, limited charge transport is still a major hindrance for most CP devices in comparison to inorganic counterparts.

Thanks to effective molecular design, donor-acceptor CPs (DACPs) with alternating electron-rich units (donor) and electron-deficient units (acceptor) covalently bonded within the same chain are emerging as excellent candidates to realize high mobilities (>10 cm^2/V-s). [5,6] Examples are poly[4-(4,4-dihexadecyl-4H-cyclopenta[1,2-b:5,4-b′]dithiophen-2-yl)-alt-[1,2,5]- thiadiazolo[3,4-c]pyridine] (PCDTPT) with 21.3 cm^2/V-s and poly[2,5-(2-octyldodecyl)-3,6-diketopyrrolopyrrole-alt-5,5-(2,5-di(thien-2-yl)thieno [3,2b]thiophene (DPPDTT) of 19.5 cm^2/V-s. [6,7,5] Besides excellent electrical performance, light harvesting efficiency of OPVs also benefits from this type of polymer because of a lower bandgap.[8] It is worth mentioning that the demonstrated high electrical performance often involves carefully controlled processing of the polymers. [6,5] This is because conjugated polymers have multiple degrees of freedom and may form structures that interrupt charge transport. [9] Forming long and well-organized chain packing, for example by interchain π-π stacking, is an effective way to enhance the conductivity. [10] Therefore, inducing the formation of such structures is of great interest for high performance organic electronic devices. [11–15]

Solution-based whisker self-assembly is one of the most widely used methods to induce the formation structures with long range order in homo-polymer CPs (e.g. Poly(3-hexylthiophene) (P3HT)). By tuning the quality of solvents, either by decreasing temperature or by introducing poor solvents to effectively reduce the solubility, nanofibers or nanoribbons can be formed. [16–18] The shape of the assembled structure depends on the solvent, the kinetics of self-assembly and the polymer concentration among other parameters. [16–18] Previous work in our group has systematically investigated the effect of solvent choice on the assembled nanostructures of homopolymers P3HT and poly(9,9-dioctylfluorene) (PFO)) using small angle neutron scattering (SANS). [13,19] Small angle neutron scattering was successfully utilized to determine the cross-sectional size, fiber fractions, and fractal dimensions. [11,13,14,20] External electric and acoustic fields were utilized to control the assembly in our group, which can either align conjugated polymers or induce nanofiber formation with long range order. [14,21]

The self-assembly of DACPs, however, is challenging due to the complex molecular structure of the polymer backbone. Very few works have been reported the formation of whiskers from DACPs in solution. Still, Chen et al. discovered that hole mobility could be further enhanced by about 1.5 times after mixing 30v% methanol into polymer solutions. [22] They ascribe this result to reduced π-π stacking distance and a more favorable in-plane orientation in the substrate. Zheng et al. reported the formation of 1-D rod-like structures in good solvents and a 2-D lamellar structure in poor solvents. Using solvent mixtures leads to an enhancement of both crystallinity and interconnectivity, resulting in electron mobility improvements from 1.8 cm^2/V-s to 3.2 cm^2/V-s. [23] Moreover, polar co-solvents, in comparison to nonpolar counterparts, are reported to achieve almost one order of magnitude in enhancement of power conversion efficiency (PCE) due to the formation of small aggregate sizes. [24]

Here we present a systematic investigation of the effect of poor co-solvents on self-assembled structures of DACPs to provide insights into structure engineering for these solution-based processes. DPPDTT is chosen as a model system for this study because it has a high mobility and because it exhibits extraordinary stability at ambient environmental conditions, which is often deficient in many CPs. No degradation is observed for this polymer based OFETs after switching on and off for more than 3500 cycles and its high electrical performance can be maintained over a year in air. [6,15]

5.2 EXPERIMENTAL

5.2.1 *Materials*

DPPDTT was purchased from ossila (Sheffield, UK). PCDTPT and Poly[(5-fluoro-2,1,3-benzothiadiazole-4,7-diyl)(4,4-dihexadecyl-4H- cyclopenta[2,1-b:3,4- b']dithiophene-2,6-diyl)(6-fluoro-2,1,3-benzothiadiazole-4,7-diyl)(4,4-dihexadecyl-4H cyclopenta [2,1-b:3,4-b']dithiophene-2,6-diyl)] (PFT-100) were obtained from 1-Material (Quebec, Canada). Poly[N-9′-heptadecanyl-2,7-carbazole-alt-5,5-(4′,7′-di-2-thienyl-2′,1′,3′ benzothiadiazole)] (PCDTBT) was acquired from Sigma-Aldrich (St. Louis, MO, USA). Detailed information of the polymers, including batch numbers, molecular weight (Mw) and dispersity (*Đ*) is listed in Table 5.1. Trichloro(decyl)silane (DTS) was purchased from Gelest (Morrisville, PA, USA). Hydrogenated solvents: chloroform, methanol, dimethyl sulfoxide (DMSO), isopropanol (IPA), n-hexane, and acetonitrile (ACN) were purchased from Sigma-Aldrich. Acetone and toluene was obtained from Fisher Scientific (Hampton, NH, USA). Deuterated solvents: d-chloroform, d4-methanol, d6-dimethyl sulfoxide, and d3-acetonitrile were purchased from Cambridge Isotope Laboratories (Tewksbury, MA, USA). All chemicals were used as received without further purification.

Mechanical grade silicon wafers were obtained from University Wafer (South Boston, MA, USA). Heavily n-doped silicon wafers with 200 nm thermally grown oxide were acquired from WRS Materials (Vancouver, WA, USA). Chromium rods and gold pellets used for evaporation were purchased from RD Mathis company (Long Beach, CA, USA).

Table 5.1. Summary of lot number, molecular weight and dispersities of polymers.

Polymers	Lot #	M_w	$Đ$
DPPDTT	M315	279 k	3.65
PCDTPT	YY9100 & YY11066	76 k	2.5
PFT-100	YY8224P1	50 k	3
PCDTBT	MKBJ8073V	65 k	19.1

5.2.2 *Sample Preparation*

DPPDTT, PCDTBT, and PFT-100 were first dissolved in chloroform at 60 °C, which is a good solvent for all polymers. The initial polymer concentration in chloroform was adjusted accordingly for all samples to keep the final concentration at 1.6 mg/ml after mixing with the co-solvents at variable ratios. All of the solvent ratios that are stated in this work correspond to volume percentage. Due to the high solubility of PCDTPT, its final concentration was adjusted to 3.2 mg/ml in order to induce self-assembly. After full dissolution in chloroform, a specific co-solvent (i.e. methanol, n-hexane, dimethyl sulfoxide (DMSO), acetonitrile (ACN), isopropanol, or acetone) was slowly added to the polymer solution. Large aggregates form instantaneously at the vicinity

of the poor solvent. To make a dispersible solution, samples were immersed for 5 min in a sonication bath (Branson 5000, 40 kHz, 160W, Danbury, CT, USA).

5.2.3 *Scanning Transmission Electron Microscopy (sTEM):*

An FEI (Tecnai G2 F20, FEI company, Hillsboro, OR, USA) transmission electron microscope (TEM) was used to characterize the structures the polymer formed in various solvent mixtures. Due to the relatively low contrast for polymer samples, scanning mode was utilized to capture high resolution images. The solutions were diluted by 10 times in a solvent mixture with the same solvent ratio before characterization. A volume of ~5 μl of the samples were drop-cast onto a pure carbon grid (200 mesh Cu, Ted Pella Inc., Redding, CA, USA) that was placed on top of filter paper to wick the excess solvent. The grid was left in a well-ventilated chemical hood to dry at least one day in air.

5.2.4 *Atomic Force Microscopy (AFM)*

A Bruker Dimension Icon-PT atomic force microscope (AFM) was used to characterize the surface morphology of all polymer films in peak force tapping mode. The samples were prepared by spin coating polymer solution onto a precut glass slide or SiO_2 surface that is thermally grown on a silicon wafer. A scan size of 2.5 μm by 2.5 μm was used for each image.

5.2.5 *Grazing-Incidence small angle x-ray scattering (GISAXS)*

GISAXS experiments were performed at beamline 8-ID-E of the Advanced Photon Source at Argonne National Laboratory. [25] The polymer samples were prepared by drop casting ~100 μl of

solution on a silicon substrate that was sequentially cleaned using acetone, IPA, and DI water in a sonication bath. The samples were dried in air for at least overnight. A beam size of 200 μm by 20 μm was used with an energy of 10.92 keV. The substrates were aligned with a tilt angle of 0.14˚ so that the x-ray beam would penetrate through the polymer layer and be reflected off from the polymer/silicon interface. A total of two frames were recorded with a vertical detector offset to form a full image. The two frames were combined together using GIXSGUI software to remove dark stripes from the x-ray detector. [26] Each frame was exposed for 10 s for every sample. GIXSGUI was also used to reduce the 2-D pattern to a 1-D scattering profile in both out-of-plane and in-plane directions. [26]

5.2.6 *Small Angle Neutron Scattering (SANS)*

SANS experiment was conducted at NIST center for neutron research (NCNR, Gaithersburg, Maryland). Both NG7 and NGB-30 were used for characterization of polymer solutions. Standard configurations with three detector positions were used and the 1-D profiles were stitched together to cover a q range of 0.0033 $Å^{-1}$< q <0.45 $Å^{-1}$. The experiments utilized sample cells with either 1 mm path length (NG7) or 2 mm path length (NG3) without any influence on the results. Quartz windows were held together by the titanium cells and sealed by PTFE coated o-rings. All the samples were prepared fresh on-site and the scattering experiment was performed within the same day of preparation. Scattering profiles for quartz windows were recorded for every sample to account for the scattering of the empty cell and to subtract the background precisely. The Igor (WaveMetrics, Inc., Lake Oswego, OR, USA) reduction macros were used to reduce the SANS data. [27] SASview software was then utilized to fit the data to an appropriate model. [28]

5.2.7 *Organic Field Effect Transistor (OFETs) fabrication*

OFETs devices were fabricated in a bottom gate bottom contact configuration. Standard photolithography processes were used to define a device active region of Lg=100 μm and Wg=1000 μm. Two layers of metal (10 nm Cr and 50 nm Au) were deposited over a wafer having a dielectric layer of 200 nm SiO_2 thermally grown on heavily n-doped silicon. The substrates were diced into chips 0.9 cm by 1 cm in size by a Disco dicing saw (DAD321, Tokyo, Japan) after coating a thin layer of photoresist for surface protection. The pre-patterned substrates were cleaned sequentially with acetone, IPA and DI water and blow dried in air. Then the surface was further cleaned by UV/ozone treatment for 20 min right before silane treatment to passivate the surface. Afterwards, the substrates were submerged in a solution of 1 v% of DTS in toluene at 60 ˚C for 30 min. Then they were rinsed with toluene and blow dried in air. The polymer solution was spin coated at 1500 rpm for 30s and dried in a nitrogen filled glovebox. In order to characterize the structures as formed in solution, no annealing was used after spin coating. The electrical characterization was conducted in a nitrogen filled glove box with a Signatone probe station (Gilroy, CA, USA). Hewlett-Packard (Palo Alto, CA, USA) 4145B semiconductor parameter analyzer was utilized to record the current voltage curve.

5.3 RESULTS

DPPDTT was fully dissolved in chloroform at ~60 ˚C, and methanol was slowly added into the polymer solutions to induce assembly while keeping the final polymer concentration constant. Figure 5.1 shows the AFM and sTEM images of polymer samples with varying ratios of methanol,

which is a poor solvent for DPPDTT. Compared to the morphology of samples processed from pure chloroform, the addition of 10v% methanol increases the domain size. Starting at a higher ratio of 15 v% methanol, assembly into fibril structures is observed in both AFM and sTEM images. Further increasing methanol concentration to 20 v% produces wider and longer nanoribbons that appear to be flexible and superimposed over each other. The width of the nanoribbon varies from ~20 nm to above ~100 nm. It is important to note that uniform polymer films can only be prepared from spin coating at low methanol concentrations. Above 15 v%, the large aggregates formed in solution results in discrete islands on the substrate during spin coating. All the samples shown in Figure 5.1 are prepared within a couple hours after mixing the poor solvent. The structures formed in solution at longer aging times for methanol concentrations of 20 v% (ribbons) and 10v% (no ribbons) are shown in Table 5.2. For 10 v% methanol, no observable nanoribbons were formed even after 12 days of aging. In contrast, for 20 v% methanol concentration, the initially formed nanoribbons gradually grow larger in size and can be above 100 nm in width after 12 days aging in solution.

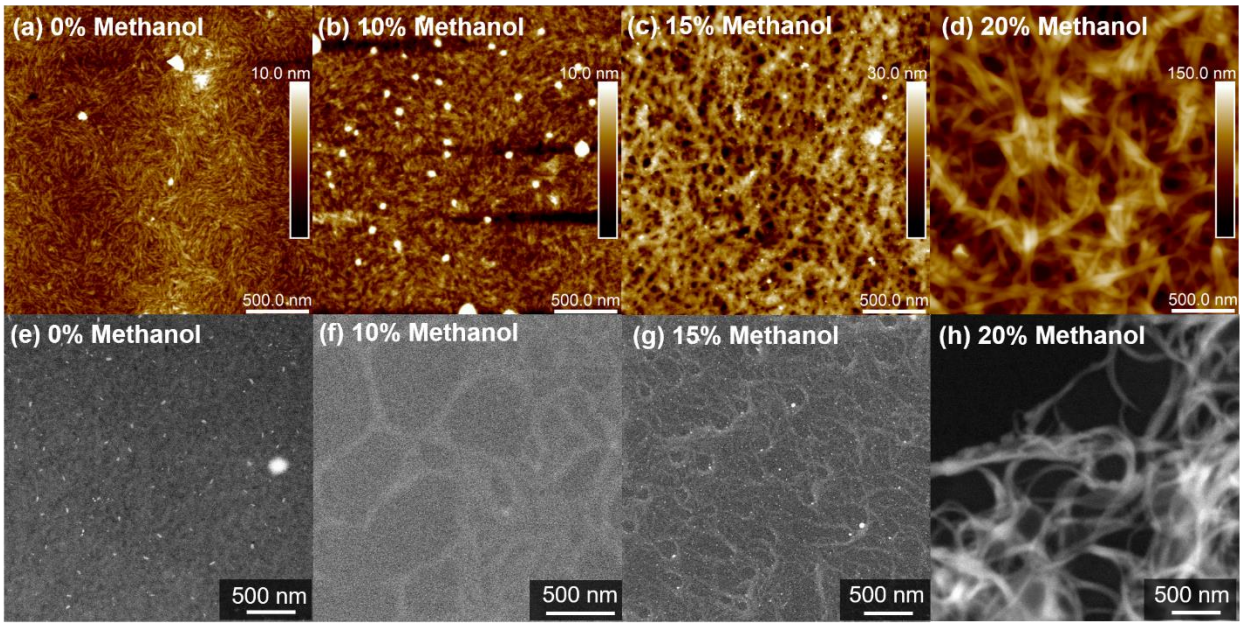

Figure 5.1. (a)~(d) AFM and (e)~(h) sTEM images of 1.6 mg/ml DPPDTT in chloroform mixed with (a) (e) 0 v% (b) (f)10 v% (c) (g) 15 v% and (d) (h) 20 v% Methanol.

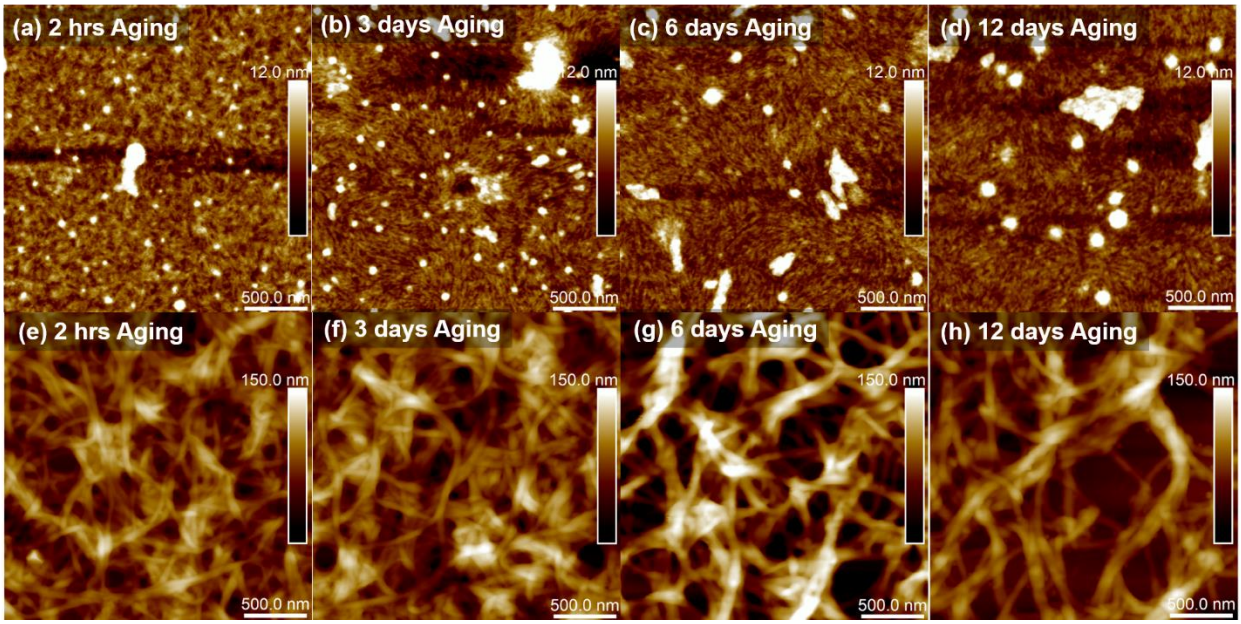

Figure 5.2. AFM images of 1.6 mg/ml DPPDTT in chloroform mixed with (a) (b) (c) (d) 10 v% methanol and (e) (f) (g) (h) 20 v% methanol after aging for (a) (e) 2 hrs, (b) (f) 3 days, (c) (g) 6 days, (d) (h) 12 days.

Nanoribbons are clearly visible in solid films probed by microscopy techniques. A more quantitative way of characterizing polymer conformations, as well as nanostructures, in solution is also important to eliminate artifacts that may occur from coating and drying. Figure 5.3 shows SANS profiles for the DPPDTT polymer in solvent mixtures of chloroform and methanol at various concentrations. The scattering profiles never show a plateau at low-q, indicating a large size and very rigid conformation in solution, even before inducing self-assembly. This is due to both the long polymer chain (i.e. high molecular weight) and the stiff and planar molecular structures of the DACP backbones. At low methanol ratios (below 10 v%), the scattering profiles overlap on top of each other, which suggests that no solution assembly occurs. At methanol concentrations higher than 15 v%, the scattering intensity increases in the low q-region and a clear hump develops at methanol concentrations of 20 v%, which correlates to the formation of

nanoribbons. A semi-flexible cylinder model is used to fit the dissolved polymer chains in solution before they assemble into nanoribbons. [29,30] In this model, the contour length, Kuhn length and cylinder radius were left as adjustable variables. The length of each rigid rod was called persistent length (l_p). Kuhn length (b) was defined as two times of persistent length, which reflected the rigidity of a polymer chain. The scattering intensity using flexible cylinder form factor can be modeled with concentration (c), SLD difference ($\Delta\rho$), and molecular weight (M) as shown in equation (5.1). [6,7] The scattering functions of single semiflexible chain ($S(q,L,b)$) considering polydispersity of contour length and cross section of a rigid rod ($P(q,r)$) were defined from equation (5.2)to equation (5.13).

$$I(q,L,b,r) = c\Delta\rho^2 M < S(q,L,b) >_{SZ} P(q,r) + bkg \tag{5.1}$$

$$P(q,r) = [\frac{2J_1(qr)}{qr}]^2 \tag{5.2}$$

$$< S(q,L,b) >_{SZ} = \frac{\int N_{SZ}(L)L^2 S(q,L,b)dL}{\int N_{SZ}(L)L^2 dL} \tag{5.3}$$

$$N_{SZ}(L) = \frac{L^z}{z!}(\frac{z+1}{<L>})^{z+1}\exp[\frac{-L(z+1)}{<L>}] \tag{5.4}$$

$$S(q,L,b) = [1 - w(qR_G)S_{Debye}(q,L,b) + w(qR_G)\left[1.22(qR_G)^{-\frac{1}{0.585}} + 0.4288(qR_G)^{-\frac{2}{0.585}} + 1.651(qR_G)^{-\frac{3}{0.585}}\right] + \frac{C(n_b)}{n_b}\{\frac{4}{15} + \frac{7}{15u} - (\frac{11}{15} + \frac{7}{15u}) \times \exp[-u(q,L,b)]\} \tag{5.5}$$

$$S_{Debye}(q,L,b) = \frac{2}{u(q,L,b)}\{\exp[-u(q,L,b)] + u(q,L,b) - 1\} \tag{5.6}$$

$$u(q,L,b) = \frac{Lb}{6}\{1 - \frac{3}{2n_b} + \frac{3}{2n_b^2} - \frac{3}{4n_b^3}[1 - \exp(-2n_b)]\}q^2 \tag{5.7}$$

$$n_b = \frac{L}{b} \tag{5.8}$$

$$w(x) = \frac{\{1+\tanh[(x-1.523)/0.1477]\}}{2} \quad (5.9)$$

$$< R_G^2 >= \alpha(n_b)^2 \frac{bL}{6} \quad (5.10)$$

$$u(q, L, b) = \alpha(n_b)^2 q^2 \frac{bL}{6} \quad (5.11)$$

$$\alpha(x) = \sqrt{[1 + \left(\frac{x}{3.12}\right)^2 + (\frac{x}{8.67})^3]^{0.176/3}} \quad (5.12)$$

$$C(n_b) = \begin{matrix} 3.06 n_b^{-0.44} & for\ L > 10b \\ 1 & for\ L \leq 10b \end{matrix} \quad (5.13)$$

Using the size of the repeat units and the molecular weight measured from gel permeation chromatography (GPC), the contour length of the polymer is estimated to be ~141 nm. [31] Still, the contour length was left as a variable because it is possible that polymer chains could assemble along the chain length direction and effectively increase the length probed by SANS. Figure 5.3 (b) compares the fit parameters as obtained from the SANS data. The contour length stays roughly at around 120 nm until methanol concentrations of 10 v%. At 15 v% methanol, an abrupt increase in the length to almost three times is observed, indicating the onset of self-assembly to larger structures. Similar trends apply to the radius since gradual addition of methanol induces an increase in the cross-sectional size of the cylinder. The Kuhn length is roughly constant with small amounts of added methanol but it decreases abruptly when polymers start to form larger structures.

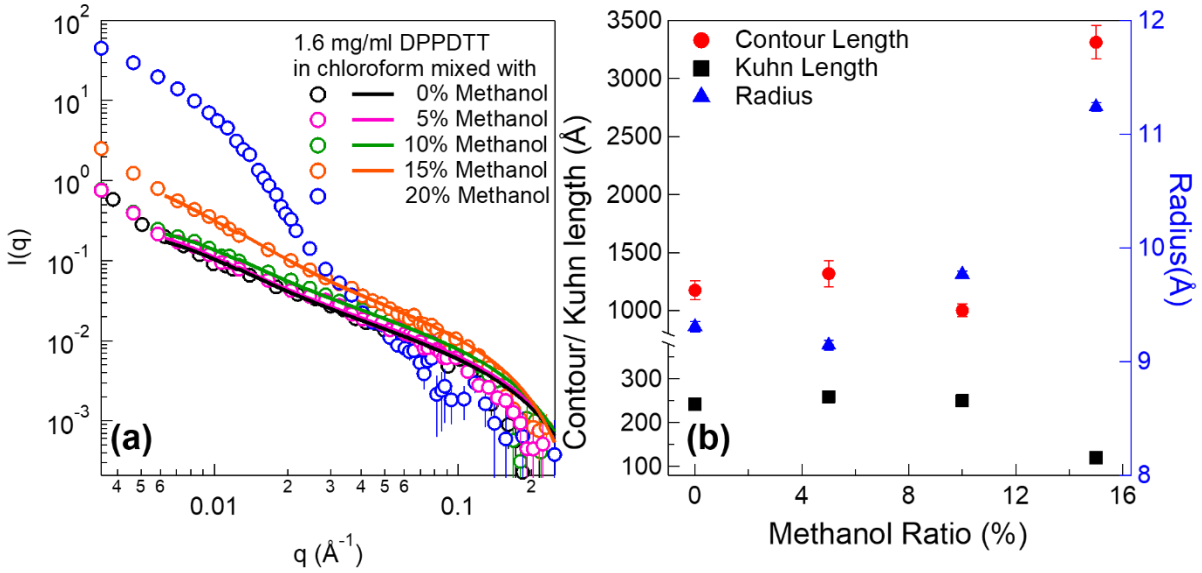

Figure 5.3. (a) SANS profiles for 1.6 mg/ml DPPDTT in chloroform mixed with various amounts of methanol. The data for samples with 0 v% to 15 v% methanol is fit using a semi-flexible cylinder model. (b) The contour length, Kuhn length, and radius of the cylinder as a function of methanol concentration.

In sharp contrast, the addition of the non-polar solvent n-hexane (ε=2), which is also a poor solvent for DPPDTT, does not lead to nanoribbon formation. Figure 5.4 (a) shows AFM images of the resulting films after addition of 20 v% n-hexane. No nanoribbons formed even after the addition of up to 50 v% n-hexane. Instead, the addition of non-polar poor solvents results in large aggregates with amorphous shapes. The diameter of the aggregates increases with the hexane content in the solvent, which ranges from tens of nanometers to a few hundred nanometers. In contrast, the addition of hexane would promote the formation of nanofibers for P3HT. [17]

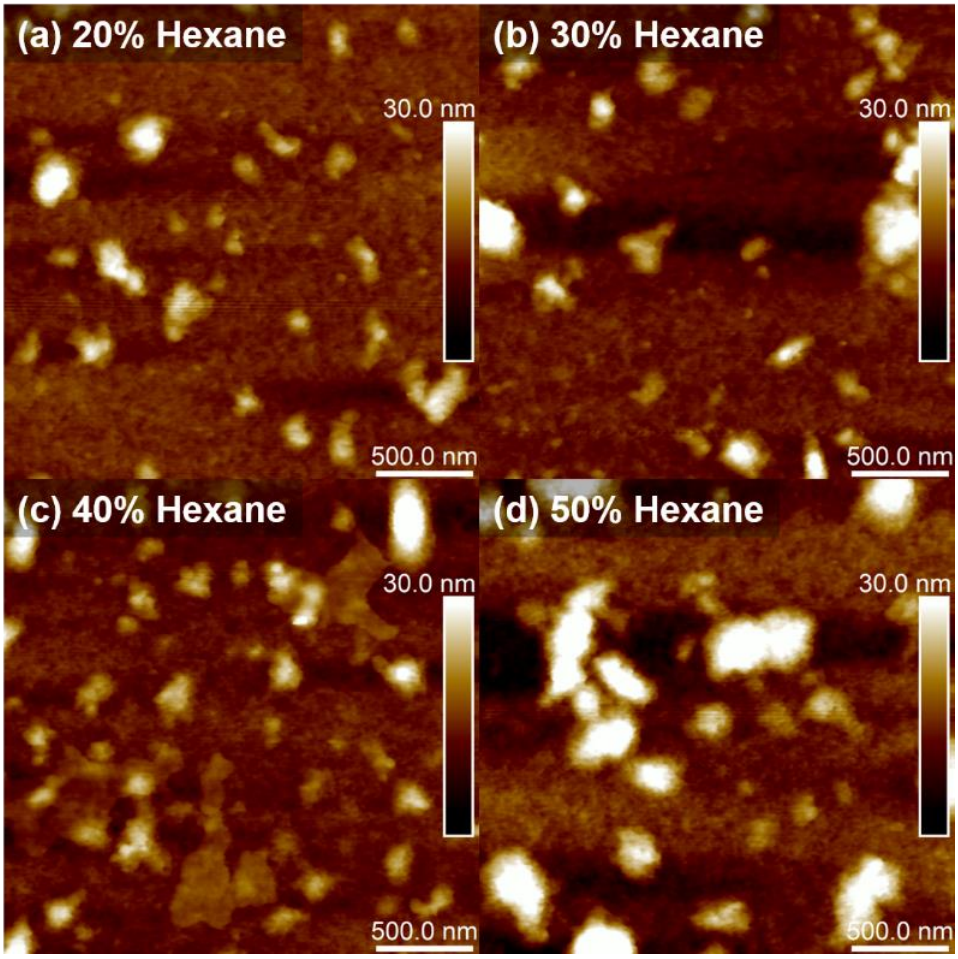

Figure 5.4. AFM images of spin coated films of 1.6 mg/ml DPPDTT in chloroform mixed (a) 20 v% (b) 30 v% (c) 40 v% and (d) 50 v% n-hexane.

While the formation of nanofibers and/or nanoribbons is typically indicative of a well-ordered chain arrangement, it is still important to analyze the crystalline structure and polymer packing using higher resolution methods. Grazing-incidence small angle x-ray scattering (GISAXS) was utilized to probe polymer samples prepared from chloroform mixtures with methanol (polar) and n-hexane (non-polar) poor solvents in Figure 5.5. The polymer chain orientation with respect to the substrate can be characterized by the azimuthal intensity distribution for crystalline peaks along different angles from the 2-D profiles. The intensity distribution of the π-π stacking peak at 1.7 $Å^{-}$

[1] shows that the face-on orientation was favorable in pure chloroform samples. In contrast, the addition of 20 v% n-hexane increased the edge-on orientation while still maintaining a fairly strong scattering signal at the out-of-plane direction. This indicated the coexistence of both chain orientations (i.e. face-on and edge-on) as shown in Figure 5.5 (b). For pure chloroform and 20 v% n-hexane samples, the edge-on π-π stacking peaks are better defined in the in-plane direction (horizontal) as compared to out-of-plane direction (vertical).

In sharp contrast, samples with 20 v% methanol (Figure 5.5 (c)) showed a nearly uniform distribution of the intensity of the π-π stacking peak along all azimuthal angles. This is attributed to the formation of nanoribbons since the interconnected stiff structure leads to a random isotropic distribution of fiber orientations with π-π stacking peaks oriented in nearly all directions. By integrating along both out-of-plane (Figure 5.5 (d)) and in-plane (Figure 5.5 (e)) directions, the peak positions and relative peak intensities were also compared. In Figure 5.5 (d), the intensity of the peak at 1.37 $Å^{-1}$ was greatly enhanced as compared to the π-π stacking peak at 1.7 $Å^{-1}$ when n-hexane was used. The intensities of those two peaks were comparable to each other for both pure chloroform and for samples with 20 v% methanol. The peak at 1.37 $Å^{-1}$ was found to be strongly correlated to the distance between two interdigitated side chains by comparing to molecular dynamics simulation. [32] This means that the addition of n-hexane affected the side chain packing. Another obvious change is the emergence of two new scattering peaks at 2.2 $Å^{-1}$ and 3.2 $Å^{-1}$ for the sample with 20 v% methanol, while they do not show up in either pure chloroform or 20 v% n-hexane. The emergence of those peaks is the result of at least one new repeat distance in real space. It is worth mentioning also that these peaks do not originate from the substrate. The tilt angle of the substrate for each sample is carefully aligned so that no x-ray beam penetrates the substrate. In addition, The diffraction peaks of both silicon and silicon dioxide are located at

different q positions. [33,34] The time-dependence of the two new diffraction peaks after aging in solution can be found in Figure 5.6 (e) ~(h). The new crystalline features show up right after the sample is prepared but longer aging time enhances the peak intensity. Moreover, the peaks are already visible for samples formed in 10 v% methanol, which is before large nanoribbons are formed (Figure 5.6 (a) ~(d)). The new peaks at high-q are also isotropic in all azimuthal angle directions Figure 5.5 (c). Three sharp peaks, 2.1 $Å^{-1}$, 2.54 $Å^{-1}$, and 2.84 $Å^{-1}$, show up at the high-q region for both chloroform and n-hexane samples in the in-plane direction. However, those peaks were barely visible for methanol induced nanostructures. This suggests that methanol induces a different crystal structure in the polymer, whereas n-hexane maintains the same structure as in pure chloroform.

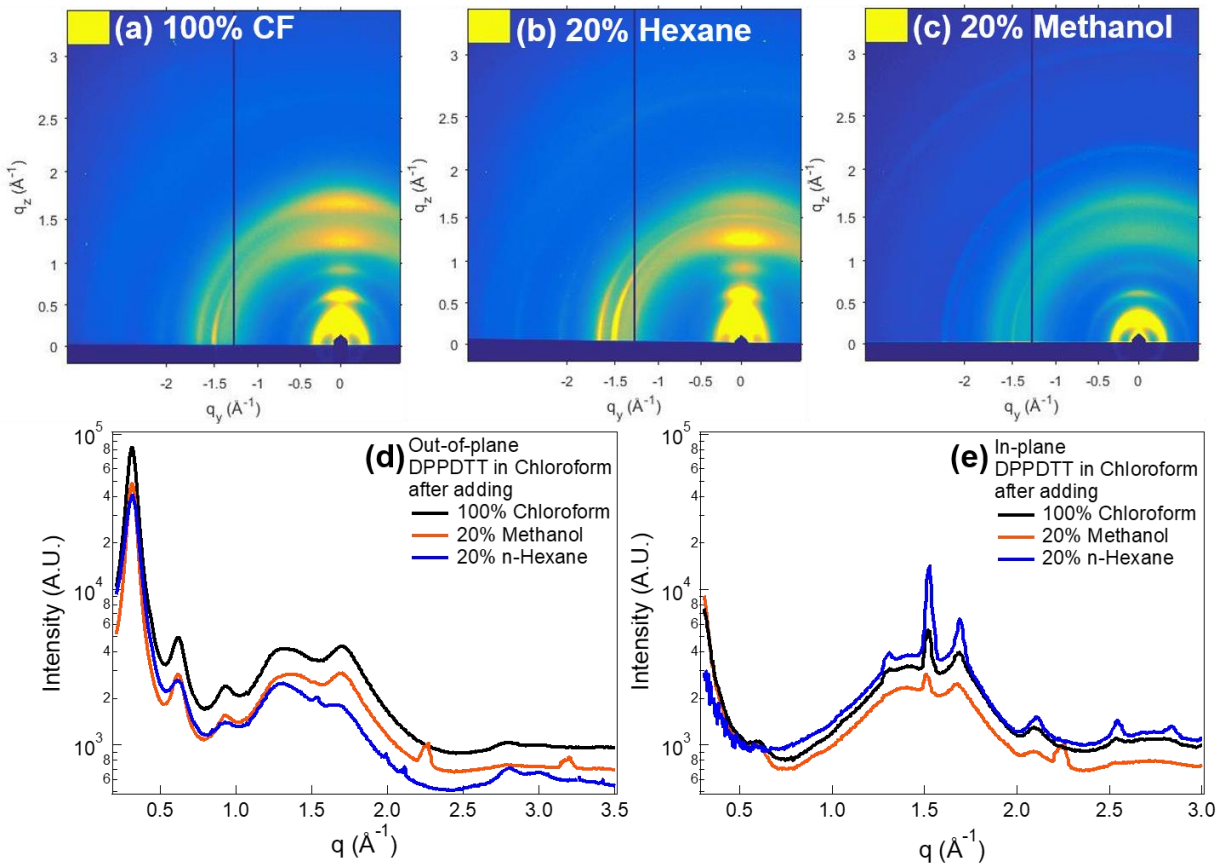

Figure 5.5. 2-D GISAXS pattern of film drop casted from 1.6 mg/ml DPPDTT in (a) pure chloroform and with (b) 20v% methanol (polar) and (c) 20v% n-hexane (non-polar) poor solvent addition. 1-D (d) out-of-plane (φ=105°) and (e) in-plane (φ=175°) line cut for the three samples with a 5˚ integration angle.

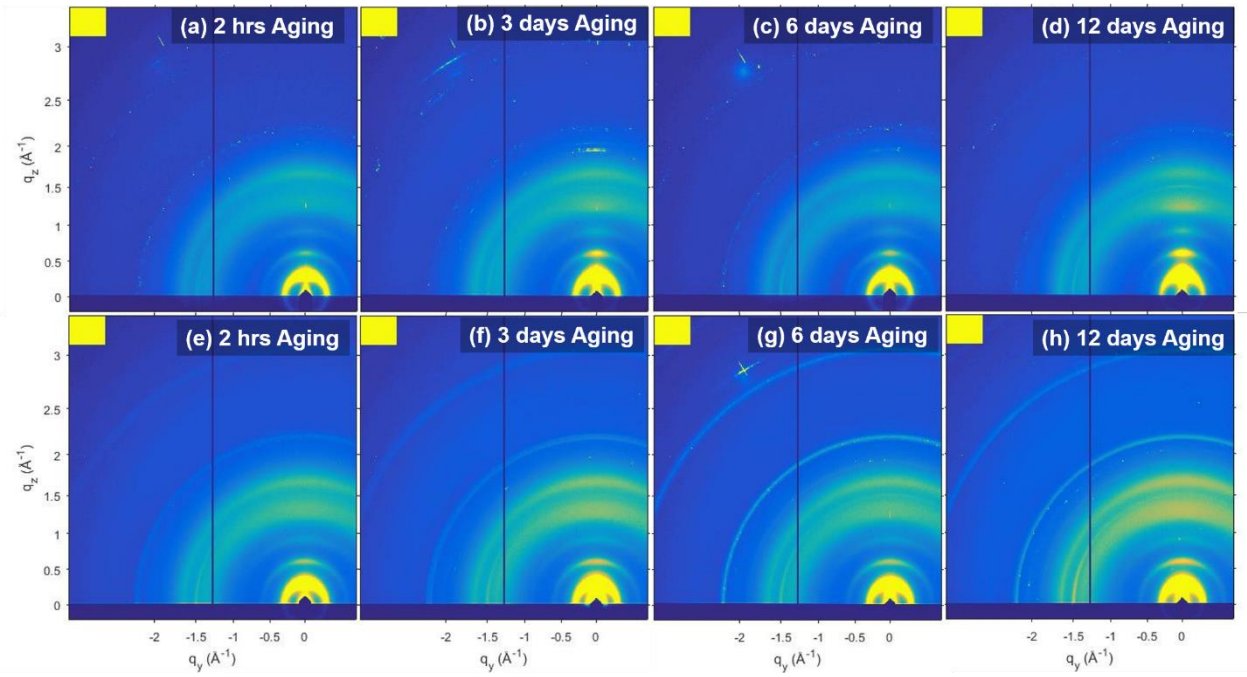

Figure 5.6. The corresponding 2-D GISAXS pattern of the samples in Figure S1 of 1.6 mg/ml DPPDTT in chloroform mixed with (a) (b) (c) (d) 10 v% methanol and (e) (f) (g) (h) 20 v% methanol after aging for (a) (e) 2 hrs, (b) (f) 3 days, (c) (g) 6 days, (d) (h) 12 days.

The differences in both nanostructure and polymer packing that is caused by methanol motivated the exploration of other commonly used polar poor solvents, including DMSO (ε=47), ACN (ε=37.5), acetone (ε=20), and IPA (ε=17). The measured dielectric constant of different poor solvents with various ratios are shown in Figure 5.8. Nanoribbon formation can be clearly observed in samples containing DMSO and ACN after 10 days of aging in Figure 5.7 (a) and (b). The samples without aging are shown in Figure 5.9, which also presented nanoribbon formation with polar poor solvents. The cross-sectional size of these nanoribbons is tens of nanometers and the length can extend to a few micrometers. Compared to the above two solvents, IPA and acetone did not show clear signs of nanoribbon formation. In order to ensure enough supersaturation was induced by the addition of IPA and acetone, higher solvent ratios were also prepared and their

AFM images are shown in Figure 5.10. With 30 v% of IPA, nanoribbons were also generated. However, samples with acetone did not produce nanoribbons even at concentrations of up to 40 v%.

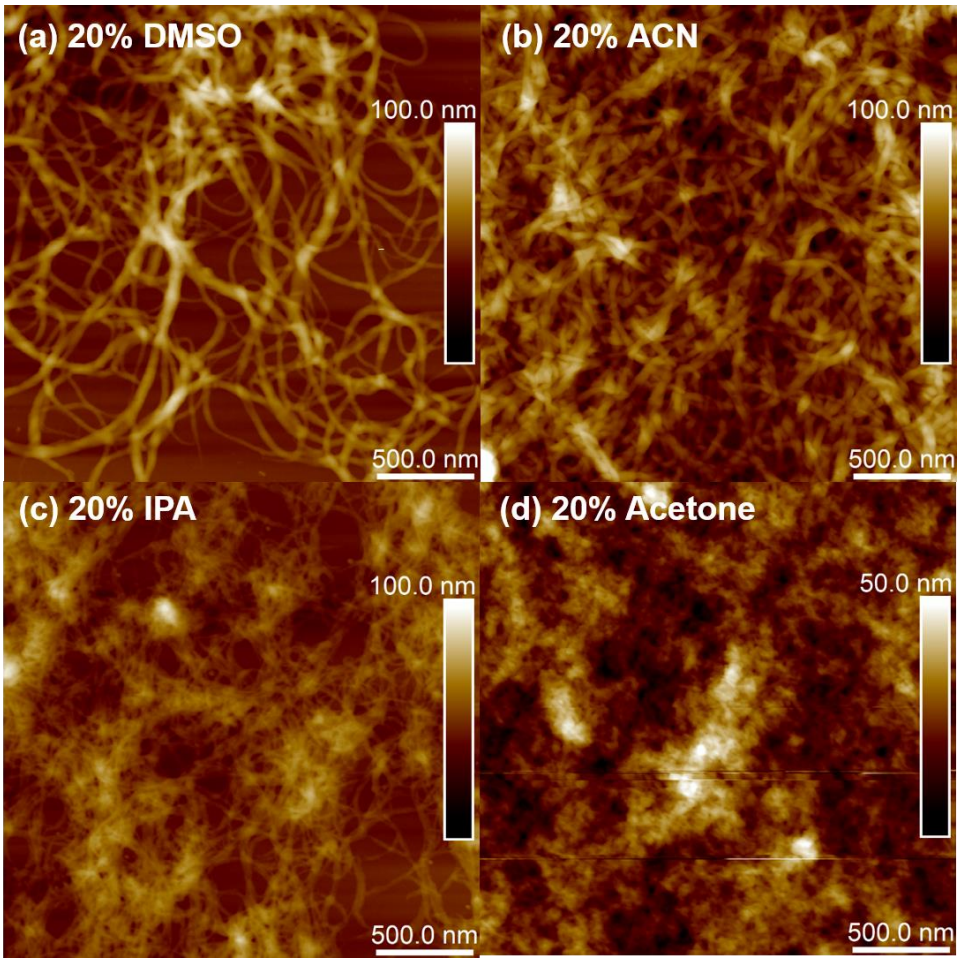

Figure 5.7. AFM images of 1.6 mg/ml DPPDTT in chloroform mixed with 20 v% (a) DMSO (b) Acetonitrile (ACN) (c) IPA (d) Acetone. The samples were casted after aging for 10 days in solution.

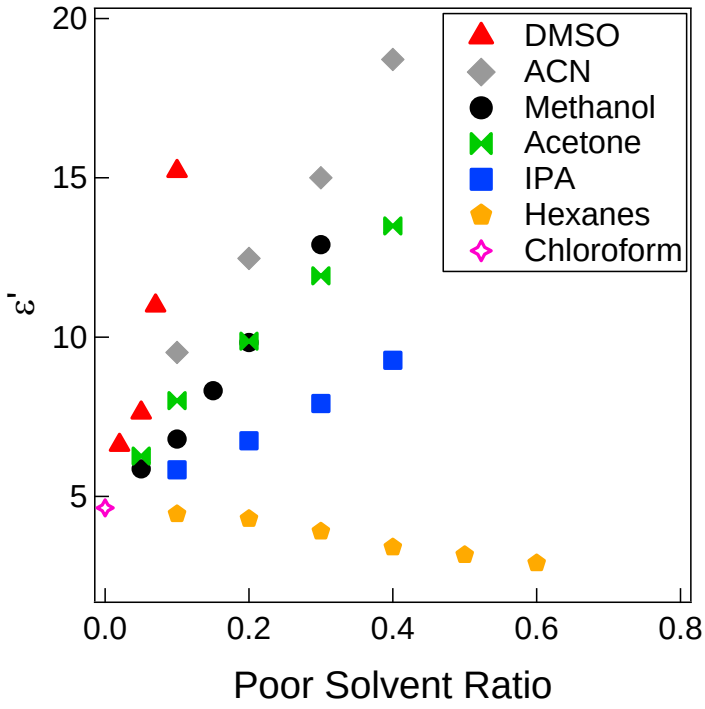

Figure 5.8. Measured dielectric constant of chloroform mixture with various poor solvents of different ratios.

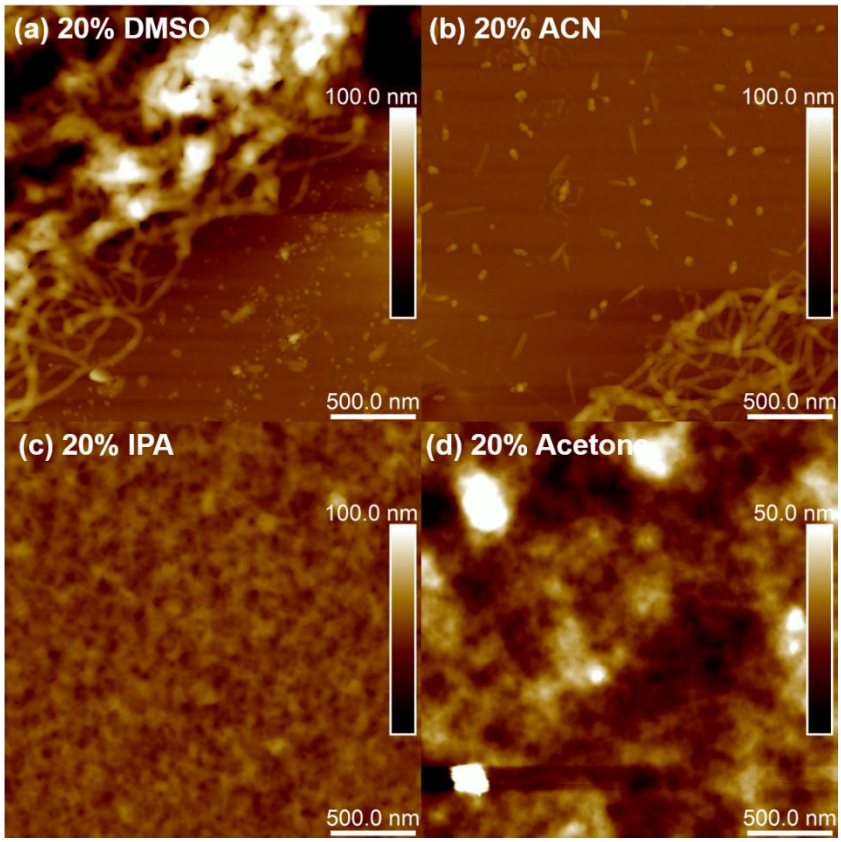

Figure 5.9. AFM images of 1.6 mg/ml DPPDTT in chloroform mixed with 20 v% (a) DMSO (b) Acetonitrile (ACN) (c) IPA (d) Acetone. The samples were casted after preparation without aging.

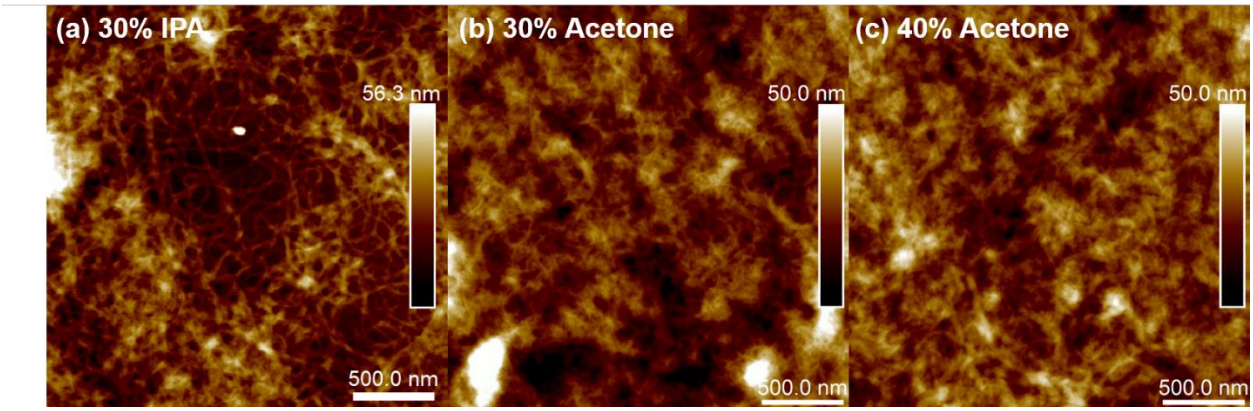

Figure 5.10. AFM images of films spin coated from1.6 mg/ml DPPDTT mixed with (a) 30 v% IPA, (b) 30 v% acetone and (c) 40 v% acetone. The samples are casted within a day after preparation.

To further quantify the size of nanoribbons, SANS was also used on other polar poor solvents (i.e. ACN, and DMSO) that also formed these structures. The scattering profiles are shown in Figure 5.11 along with reference samples that were prepared in pure chloroform. A combined model of long parallelepiped fibers [35,36] and dissolved polymers [37,38] was used to fit the data and to obtain the cross-sectional dimensions and the total amount of polymers that formed nanoribbons in the solvent mixtures. This model was previously implemented to characterize the size of P3HT nanofibers in solutions. [11,14,21] The fraction of parallelepiped model (φ_f) indicates the amount of polymers that form nanoribbons. The form factor of the combined model is depicted in equation (5.14).

$$I\,(q) = \phi_v \varphi_f (\Delta\rho)^2 P_{PP}(q) + \phi_v (1-\varphi_f)(\Delta\rho)^2 P_{PExV}(q) \qquad (5.14\ )$$

Where the total volume fraction of conjugated polymers in solution is denoted by ϕ_v, $\Delta\rho$ is the scattering length density (SLD) difference between solvent and polymer chains. $P_{PP}(q)$ represents the form factor of the parallelepiped model and $P_{PExV}(q)$ is that of dissolved polymers with excluded volume effect. Both of the form factors are defined in equation (5.15)~(5.18).

$$P_{PP}(q) = \frac{2}{\pi}\int_0^{2\pi}\int_0^{2\pi}\left[\left(\frac{\sin(qA\sin\alpha\cos\beta)}{qA\sin\alpha\cos\beta}\right)\left(\frac{\sin(qB\sin\alpha\cos\beta)}{qB\sin\alpha\cos\beta}\right)\left(\frac{\sin(qC\cos\alpha)}{qC\cos\alpha}\right)\right]^2 \sin\alpha\, d\alpha d\beta \quad (5.15)$$

$$P_{PExV}(q) = \frac{1}{\nu U^{\frac{1}{2\nu}}}\gamma\left(\frac{1}{2\nu}, U\right) - \frac{1}{\nu U^{\frac{1}{\nu}}}\gamma\left(\frac{1}{\nu}, U\right) \quad (5.16)$$

$$\gamma(x, U) = \int_0^U dt\, \exp(-t)t^{x-1} \quad (5.17)$$

$$U = \frac{q^2 R_g^2 (2\nu+1)(2\nu+2)}{6} \quad (5.18)$$

Where a and b are the width and height of the parallelepiped, and c denotes the length of the nanoribbons. As the length of the nanoribbon is over one micrometer, which is outside of the windown that SANS is probing. The length c of the model is fixed at 1 μm for all the samples. R_g is the radius of gyration of fully dissolved polymers and ν represents excluded volume paramter, which is the inverse of Porod exponent.

The width and thickness of nanoribbons, as well as the fraction of the total polymer that was forming nanoribbons were the only fit variables. The rest of the parameters are constrained with known values. The fit results are summarized in Table 5.2. The nanoribbons formed in ACN and DMSO were very similar in size, with cross-sectional thickness (parameter 'a') of ~10 nm and width (parameter 'b') of ~25 nm. In contrast, the nanoribbons formed in methanol were substantially larger with both dimensions almost doubled. This result was further corroborated by

comparing AFM images of Figure 5.1 (d) with Figure 5.7 (a) and (b). Even though nanoribbons were generated in different polar solvents, the size of those induced by methanol was different from the others. Besides the cross-sectional size of the nanoribbons, the fraction of polymers that assembled into nanoribbons varied from solvent to solvent. This fraction correlated well with the polarity of the poor solvents. Almost 80% of polymers formed nanoribbons in DMSO (ε=47) and ~ 66% of polymer chains assembled into ribbons upon addition of ACN (ε=37.5). Methanol, with the lowest dielectric constant of the three (ε=32), caused the assembly of the lowest amount of polymer into nanoribbons.

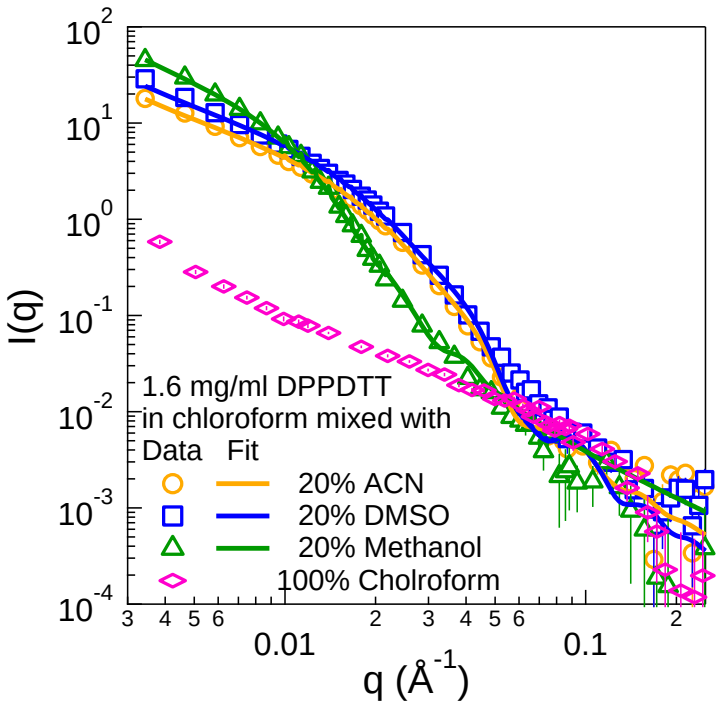

Figure 5.11. 1-D SANS profiles of nanoribbons formed with 20 v% ACN, DMSO, and methanol mixed in polymer solutions in chloroform. The data is fitted with a combined model of parallelepiped and dissolved polymer with excluded volume effect.

Table 5.2. The cross-sectional sizes of parallelepiped extrapolated from fitting, as well as polymer fractions in nanoribbons.

Poor solvent Ratio	a (nm)	b (nm)	Dielectric Constant (ε)	Polymer Fraction in Nanoribbons (%)
20% DMSO	9.8	25.2	47	78.9
20% ACN	10.1	23.5	37.5	66.7
20% Methanol	22.5	40.9	32	40.2

GISAXS was again used to characterize the chain packing for samples from these other poor solvents. The 2D scattering patterns and 1D integration profiles are shown in Figure 5.12. Similar to that of methanol samples in Figure 5.5, the π-π stacking peaks at 1.7 Å-1 are uniformly distributed across the azimuthal angles when the polymers form nanoribbons (i.e. DMSO and ACN samples), which is consistent with a random orientation of the ribbons with respect to the substrate. A comparison of the 1D integration profiles over in-plane and out-of-plane directions is shown in Figure 5.12 (e) and (f). In the out-of-plane direction, the π-π stacking peaks (q=1.7 Å-1) showed weaker scattering intensities compared to the peaks at q=1.37 Å-1 for less polar solvents, IPA and acetone. This is also observed for samples mixed with n-hexane in Figure 5.5 (d). In contrast, the relative intensity of the two peaks was similar for both DMSO and ACN samples. Additionally, the position of one of these peaks shifts from ~1.37 Å-1 to 1.29 Å-1 in less polar solvents, indicating a larger distance between side chains. In both Figure 5.12 (e) and (f), the scattering profiles of samples with 20 vv% methanol and 20 vv% n-hexane are plotted as dashed lines for

comparison. The two new peaks that appeared in methanol samples (q=2.2 Å-1 and q=3.2 Å-1) were not observed in other poor solvents, except for very faint peaks in DMSO and ACN.

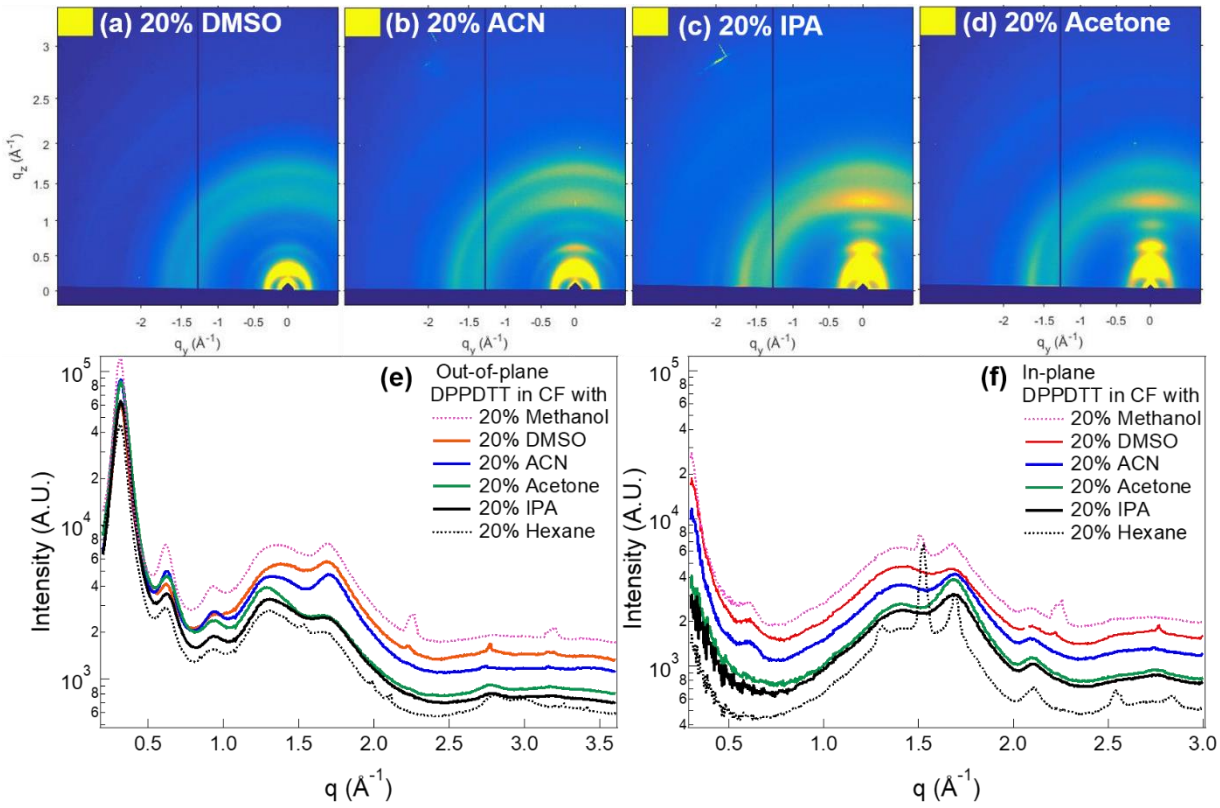

Figure 5.12. 2-D GISAXS pattern of films drop casted from 1.6 mg/ml DPPDTT in chloroform mixed with 20 v% (a) DMSO (b) Acetonitrile (ACN) (c) IPA (d) Acetone. (e) and (f) show the 1-D integration in the out-of-plane (φ=105°) and in-plane (φ=175°) directions with a 5˚ integration angle, respectively. The dashed lines in each figure are the corresponding integration of methanol and hexane samples.

The electrical properties of nanoribbons was also investigated for methanol samples. Unfortunately, after the polymers were fully assembled into nanoribbons, it was difficult to form a uniform film with spin coating due to the increased viscosity and elasticity. This was also documented for nanofibers formed from P3HT. [11] In order to gain insights into changes to the

electrical properties of these structures, a high methanol ratio (15 v%) was used to induce partial assembly but kept low to achieve an adequate film quality for OFET fabrication. Based on SANS results in Figure 5.3, self-assembly starts to become evident at this solvent concentration. No annealing was used during the fabrication process to ensure that the solution structure was maintained in the devices. The performance of these materials was characterized by bottom gate bottom contact OFETs in Figure 5.13 (a). After self-assembly, the drain current increased by a factor of almost two at the same gate voltage when the channel is fully 'on'. A larger hysteresis was observed for devices processed from pure chloroform but not in devices made with nanoribbons This indicated that defects were effectively reduced with self-assembly in solution. To calculate the saturation mobility from the transfer curves, the curves were replotted to the square root of the current as a function of gate voltage (Figure 5.13 (b)). Double slopes were observed for both conditions, which is very common for this type of conjugated polymers. [6,7,5,39] Significant efforts have been devoted to understanding the origin of this phenomena and it was recently proposed that reducing the contact resistance or using polymeric dielectric layers could help alleviate this effect. [40] It was also reported that this would be resolved when a very small gate length (5 μm) was used. [7] However, many of the literature-reported mobilities for DPPDTT have been extracted from analysis of the largest slope that is adjacent to the threshold voltage. This was recently considered to be an overestimation of the true mobility. [41]

In order to compare with published literature values and also to more accurately estimate the real mobility, we used two different methods to calculate the mobility. The first consists of an analysis of the largest slope as has been done routinely in the literature for DPPDTT (dark dashed line in Figure 5.13 (b)). In addition, we also follow recent suggestions to calculate mobilities at high gate voltages (pink dashed line in Figure 5.13 (b)). [41] The results from both methods are summarized

in Figure 5.13 (c) and an enhancement of mobilities for nanoribbons was observed in both analyses. 'High' represents the mobility obtained from fitting the largest slope of the curve close to threshold voltage and 'Low' means the conservative estimation of the mobility from the high voltage slope shown as the dashed pink line. The averaged mobility of 10 devices, as estimated from the 'High' model fit, improves about 5 times after self-assembly was induced. The averaged value of the methanol 15 vv% sample was ~3 $cm^2v^{-1}s^{-1}$ and highest mobility for one device was above 5 $cm^2v^{-1}s^{-1}$. Those values are comparable to the reported performance in recently published work for the same polymer but without any kind of annealing process.[42] Mobilities in that work were also calculated using the highest slope of the I-V curve. With the more conservative estimate, the average mobility was about 0.13 $cm^2v^{-1}s^{-1}$, which was slightly improved from those of samples processed from pure chloroform. The output curves of devices in Figure 5.13 (d) showed significant enhancements in the drain current after self-assembly is induced by methanol.

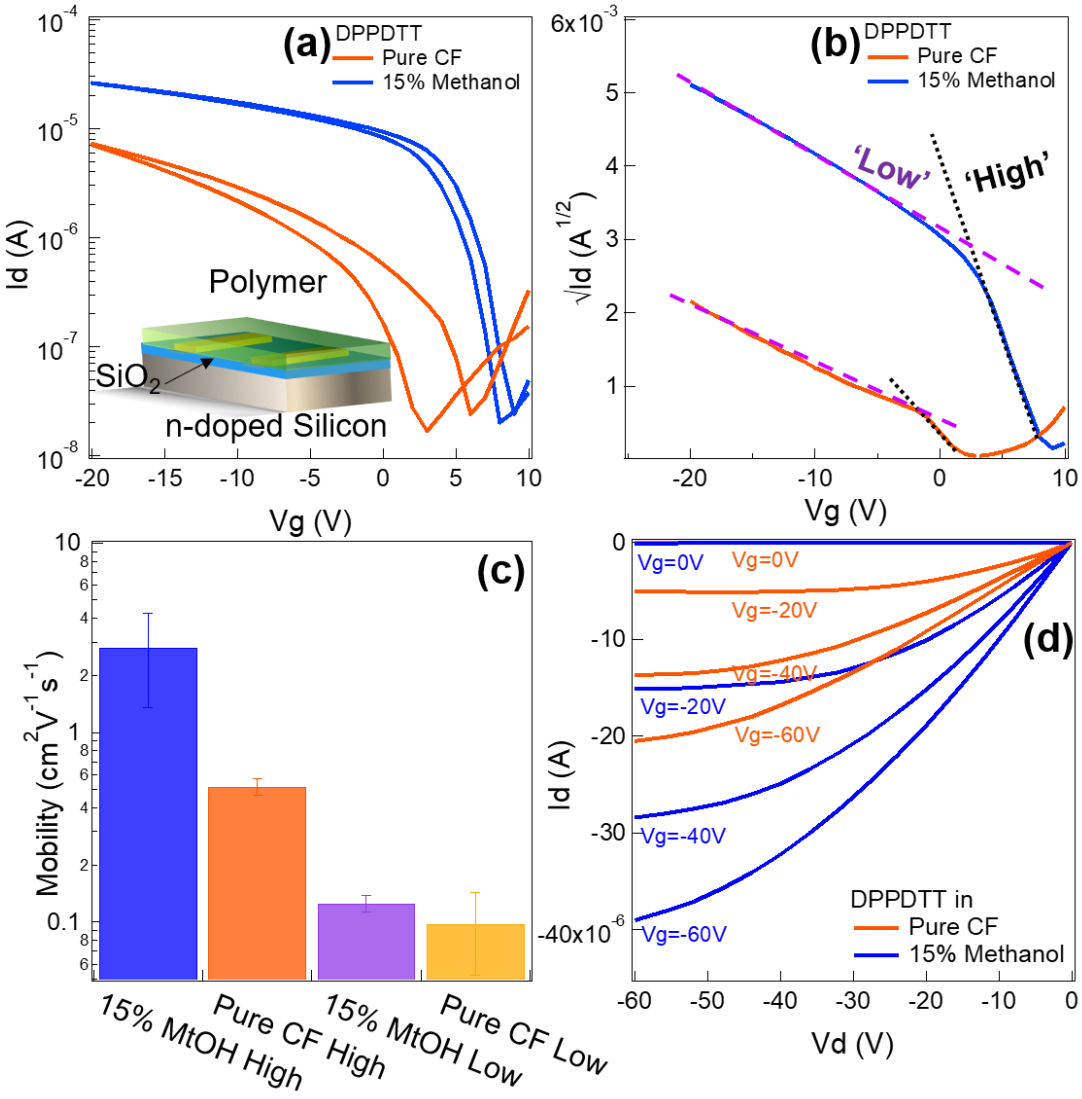

Figure 5.13. (a) Transfer curves for bottom-gate bottom-contact OFETs fabricated from DPPDTT dissolved in pure chloroform and with 15 v% methanol. The inset figure shows the device geometry. (b) Square root of current v.s. gate voltage for two representative devices. The dashed lines represent the two fits ('High' and 'Low') that were used to obtain the mobility values.[41] (c) The average mobilities as estimated from the two different methods. The mobility was averaged from more than 10 devices for each condition. (d) Comparison of output curves from fully dissolved and self-assembled (15 v% methanol) polymers.

We also explored other donor-acceptor conjugated polymers in order to see if the same poor solvent polarity dependence of self-assembly was observed. This analysis included PCDTBT, PCDTPT, and PFT-100, where the molecular structures are depicted together with DPPDTT in Figure 5.14. The surface morphology of films formed after addition of methanol and n-hexane were also characterized with AFM and are shown in Figure 5.15. With the addition of n-hexane, the films are relatively flat and uniform. In comparison, the same amount of methanol (polar) shows clear signs of induced self-assembly into large aggregates. For samples composed of PFT-100, short nanoribbons were formed that are micrometers long and less than 50 nm in width. It is important to note that the polymer structures of PCDTPT and PFT-100 are very similar and only differ in the areas shown in dashed circles in Figure 9. Therefore, a small change in composition within the polymer drastically affected the nanostructures.

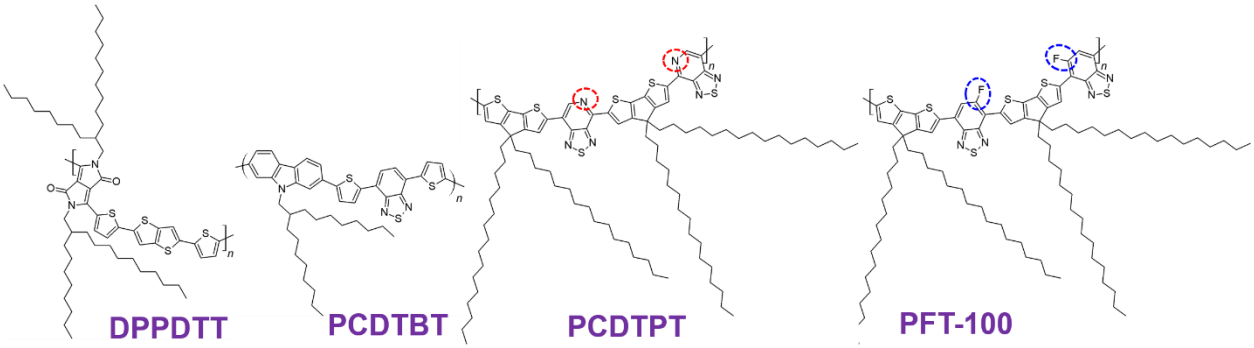

Figure 5.14. The schematic drawing of molecular structures of DPPDTT, PCDTPT, PFT-100, and PCDTBT.

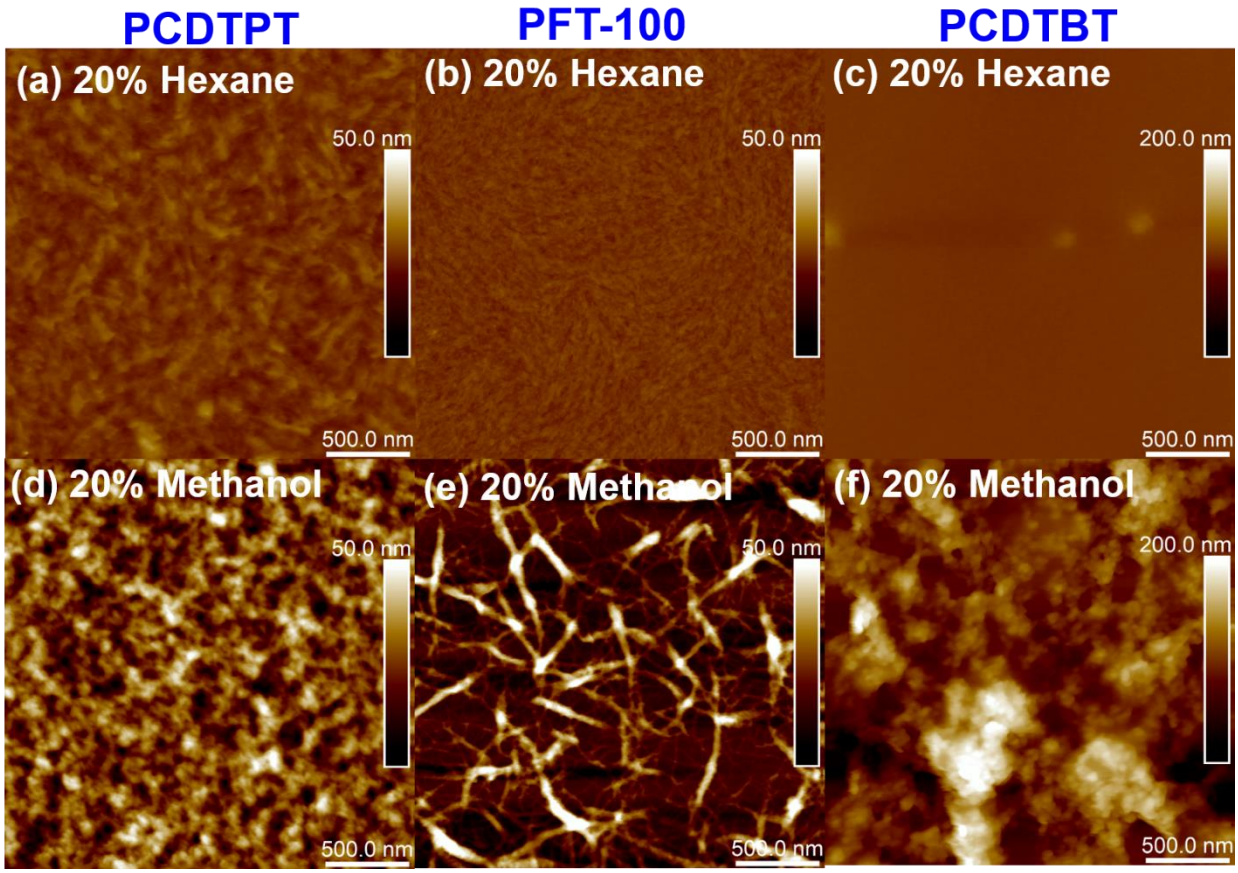

Figure 5.15. AFM images of structure formed from three different donor-acceptor conjugated polymers by mixing 20 v% (a) (b) (c) hexane and (d) (e) (f) methanol.

The corresponding polymer chain packings were also investigated with GISAXS for the different polymers upon addition of polar non-solvents. The 1D profiles along both out-of-plane and in-plane directions are shown in Figure 5.16. The corresponding 2D scattering patterns are also presented in Figure 5.17. Polymers did not show strong orientation of π-π stacking peaks except for PCDTBT that showed a face-on orientation when processed from 20 v% hexane. In the 1D scattering profiles, the lamellar peaks of the three conjugated polymers all shift towards lower-q when methanol is added as compared to samples with n-hexane and pure chloroform. This indicates that a larger lamellar packing distance emerges for samples mixed with polar poor

solvents. The 100 lamellar peak positions are summarized in Table 5.3. The largest change in the lamellar distance is observed in PCDTBT samples. A small peak at ~ 1.98 $Å^{-1}$ in the out-of-plane direction of PCDTBT sample disappeared when 20 v% methanol was used to induce assembly. This peak was also observed in samples prepared from 100 v% chloroform, which is shown in Figure 5.17. It is intriguing to see that two new peaks, which appeared in methanol-assembled DPPDTT (i.e. q=2.2 $Å^{-1}$ and q= 3.2 $Å^{-1}$), also appear in all the other DACPs when nanostructures are induced by methanol. Moreover, the peaks appear to be in the same location for polymers with different molecular structures suggesting that it is a conserved feature for these samples. In the in-plane direction (Figure 5.16 (b)), all the samples showed weaker lamellar scattering peaks as compared to those in the out-of-plane direction. This suggests a preferred lamellar orientation that is parallel to the substrate.

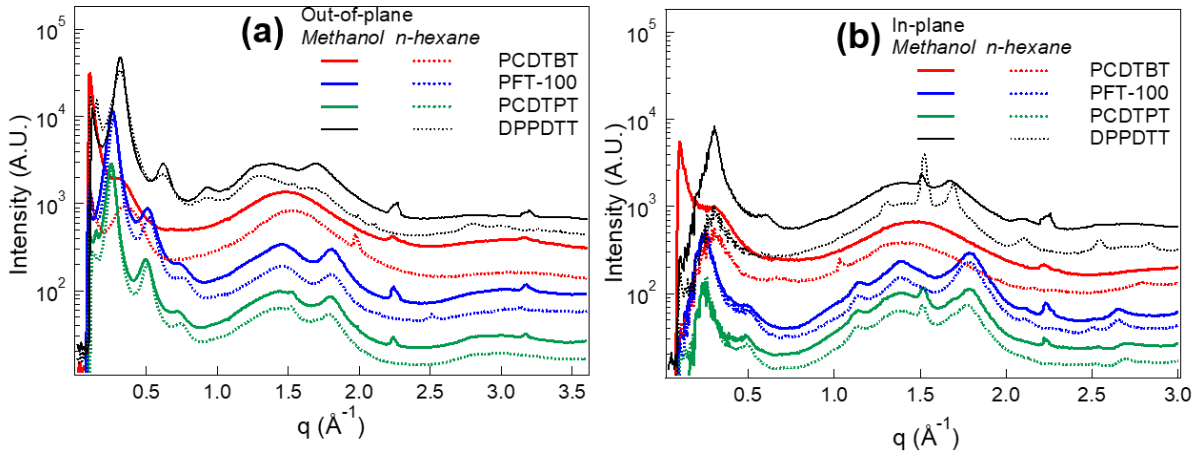

Figure 5.16. 1-D integration in the (a) out-of-plane (φ=105°) and (b) in-plane (φ=175°) directions with a 5˚ integration angle of PCDTPT, PFT-100, and PCDTBT using 20% n-hexane (dashed lines) and 20 v% methanol (solid lines).

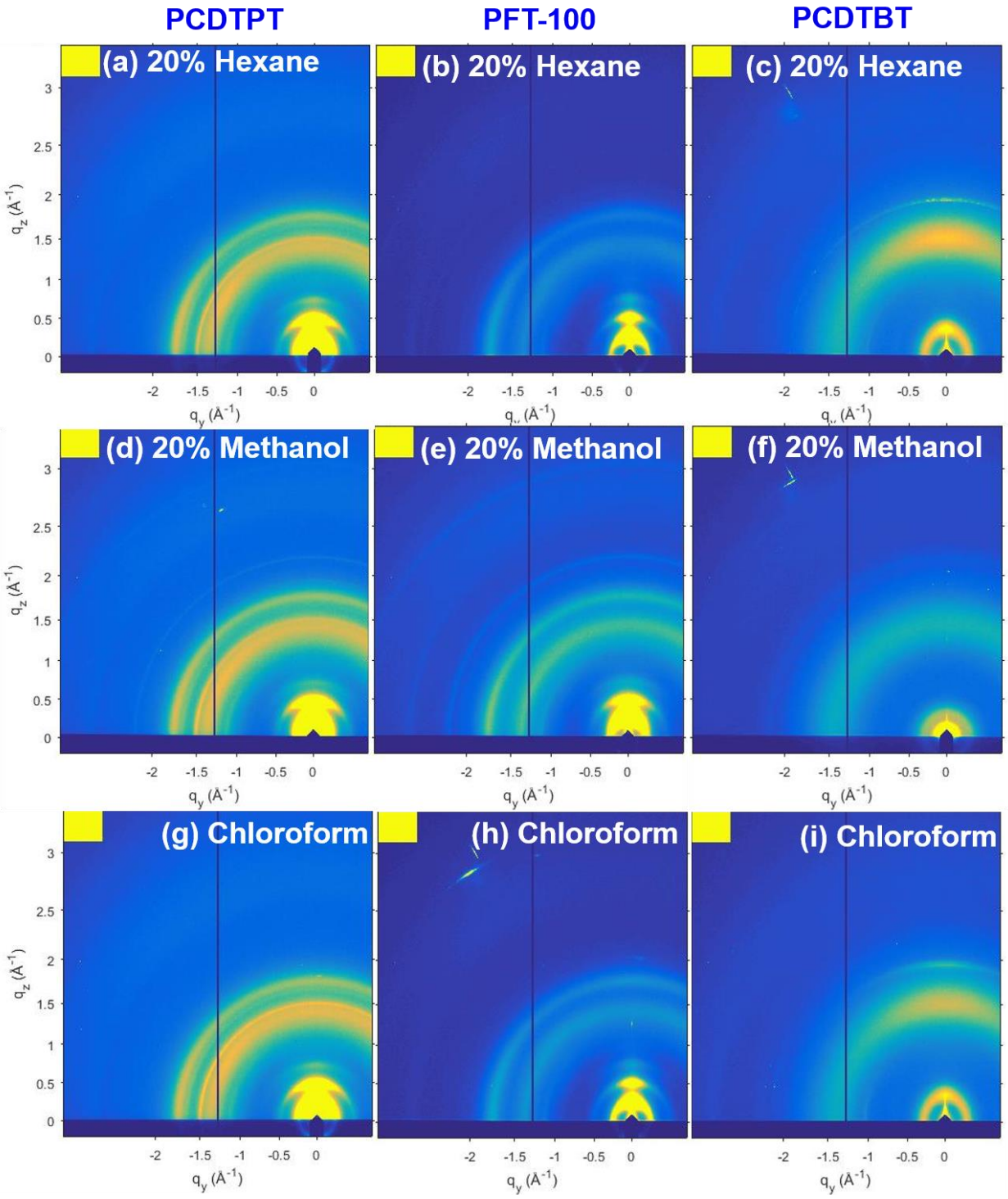

Figure 5.17. 2-D GISAXS patterns of PCDTPT, PFT-100, and PCDTBT using 20 v% n-hexane, 20 v% methanol, and 100 v% chloroform.

Table 5.3. 100 lamellar peak position in the polymer films after treating with 20% methanol, 20% n-hexane and pure chloroform of the three conjugated polymers in the out-of-plane direction.

Conjugated Polymers	20% Methanol ($Å^{-1}$)	20% n-Hexane ($Å^{-1}$)	100% Chloroform ($Å^{-1}$)
PCDTBT	0.318	0.361	0.361
PFT-100	0.261	0.268	0.268
PCDTPT	0.254	0.261	0.261

5.4 DISCUSSION

Donor-acceptor conjugated polymers (DACPs) were shown to form ordered nanoribbons by mixing polar poor solvents into stable solutions in good solvents. It is hypothesized that addition of poor solvents effectively reduces the solubility of polymers and induces aggregation in solution. However, solvents may also alter the solvent-polymer interactions and in this way affect the structure of the resulting aggregates. When polar poor solvents are added, the dipole within the solvent molecules may interact with the backbone of the polymer that has electron rich and electron deficient subunits. Therefore, these dipole-dipole interactions may play a role in helping align polymers to facilitate the formation of π-π stacking interactions in solution, which is not easily achieved for DACPs due to their complex backbone structure. Furthermore, continued crystallization and growth due to this lower solubility leads to the formation of nanoribbons over long distances (Figure 5.1, Figure 5.4, and Figure 5.7). In contrast, non-polar poor solvents (e.g. hexane) would likely interact with the aliphatic side chains and do not lead to a preferred

orientation for assembly. Therefore, aggregates were observed to have amorphous shapes Figure 3.

The addition of poor solvents also leads to conformational changes of polymers before they fully assemble, which is evidenced by the SANS data in Figure 5.3. The Kuhn length, which is a measure of the rigidity of the polymer chains in solution, increased slightly from 24.2 nm to 25.9 nm with 5 v% methanol addition. At 10 v% methanol the Kuhn length was still larger than that in chloroform and radius started to also increase indicating that assembly started to occur. Further addition of methanol to 15 v% ratio formed much larger structures. The increased stiffness of the polymer chains and initial assembly were also observed with addition of the non-polar solvent n-hexane. The SANS profiles and the corresponding fits are summarized in Figure 5.19. This suggests that a change in polymer conformation is not directly correlated to the formation of nanoribbons. Similar conformation changes were observed with PCDTPT, which had a much shorter chain as compared to the DPPDTT samples. A cylinder model was used to fit the SANS data shown in Figure 5.18. With 10 v% methanol, the chain radius remained constant but the length of the polymer increased by ~ 3 nm (Table 5.4). This could be rationalized as a slight extension of the polymer chains with methanol addition. A larger structure was observed with even higher methanol concentrations. All in all, the addition of methanol changed the conformation of DACPs for self-assembly to occur. This explanation is further supported by recent reports stating that the incorporation of small amounts of ionic liquids (polar) in DPPDTT hindered side-chain torsion, making it easier for the polymer chains to form ordered stacks. [6] In addition, non-polar poor solvents also increased polymer rigidity, but did not result in ordered structures.

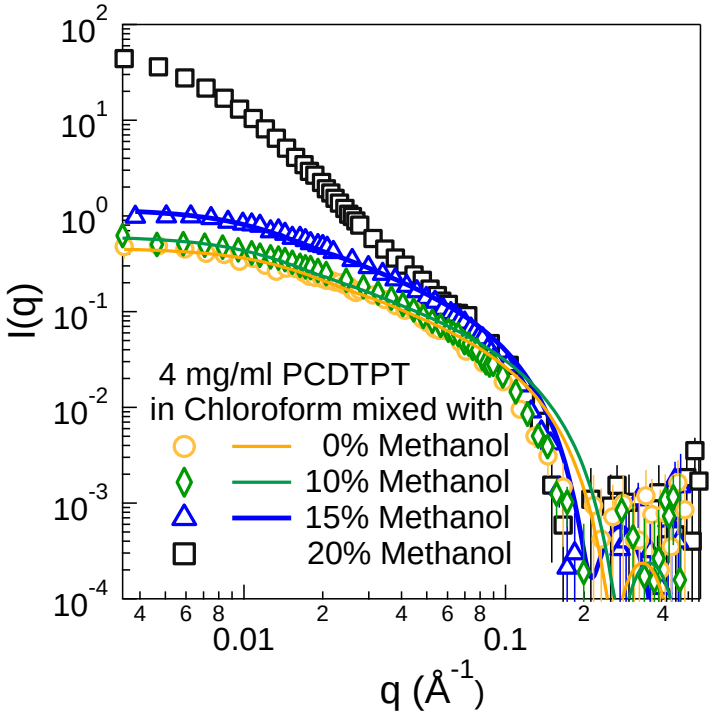

Figure 5.18. 1-D SANS scattering profile of 4 mg/ml PCDTPT in chloroform mixed with varied methanol concentrations. A cylinder model is used to fit the SANS profile at low methanol concentrations.

Table 5.4. Extrapolated fitting parameters for PCDTPT samples from a cylinder model.

Methanol Ratio	Radius (nm)	Length (nm)
0%	1.6	24.8
10%	1.6	27.9
15%	1.9	32.6

It is also worth mentioning that the solvent-polymer interactions are not limited to dipole-dipole interactions. Hydrogen bonding may also play a role in forming these ordered structures. Compared to nanostructures formed in other polar poor solvents, methanol induced nanoribbons with a substantially wider cross-section, which was shown by both AFM in Figure 5.1 and SANS in Figure 5.11.

The chain packing within the nanostructures was also very different for samples assembled from methanol mixtures and other co-solvents. Additional peaks emerged at high-q in the GISAXS scattering profiles as shown in Figure 5.5 for sample with methanol. These peaks were either totally suppressed or significantly reduced for other polar poor solvents. This was also observed for several other DACPs at similar q values as shown in Figure 5.16.

In contrast to polar solvents, non-polar poor solvents such as n-hexane affect the polymer structures in different ways. Unlike whiskers formed in P3HT and other homopolymers, nanoribbons were not observed by addition of n-hexane for any DA polymer. Instead, large aggregates were formed that could be observed in AFM images for all polymers investigated in Figure 5.4 and Figure 5.15. Therefore, the solubility of a DACP cannot be the only parameter that determines the final structure. In sharp contrast, by reducing the solubility of P3HT using nonpolar solvent (e.g. dodecane) fiber formation is easily achieved. [13]

GISAXS results showed that the scattering peaks were the same for samples containing hexane as those for samples coated from pure chloroform (Figure 5.5). This indicated that non-polar poor solvent did not change the crystal structure of the polymers in coated films. Since hexane may be considered a good solvent for alkyl side chains, [17] it could affect the packing of these side-chains in the crystals. This was verified by slightly smaller lamellar packing distances (higher q values in

Table 5.3) and an enhanced scattering peak at q= 1.37 $Å^{-1}$ that is shifted towards low-q directions, which represents a larger interdigitated side-chain distance (Figure 5.12). [32]

The interactions between poor solvent and good solvent molecules may also important in affecting the formation of nanostructures from DACPs. Neither methanol nor n-hexane form completely miscible mixtures with chloroform. This can be observed in SANS scattering profiles for solvent mixtures (i.e. no polymer) in Figure 5.20. A 'hump' is observed at very high-q after methanol or hexane addition to chloroform. Fits to spherical form factors revealed a radius of ~ 4 Å of methanol and ~ 3 Å dispersed in chloroform. It is possible that the new crystal structure that appears upon methanol addition is due to methanol-chloroform and/or methanol-polymer interactions. To determine this, molecular dynamics simulations may be useful to understand how solvent-polymer interactions evolve in mixed solvents. In contrast, DMSO and ACN are completely miscible with chloroform and only showed a fully flat background at high q values.

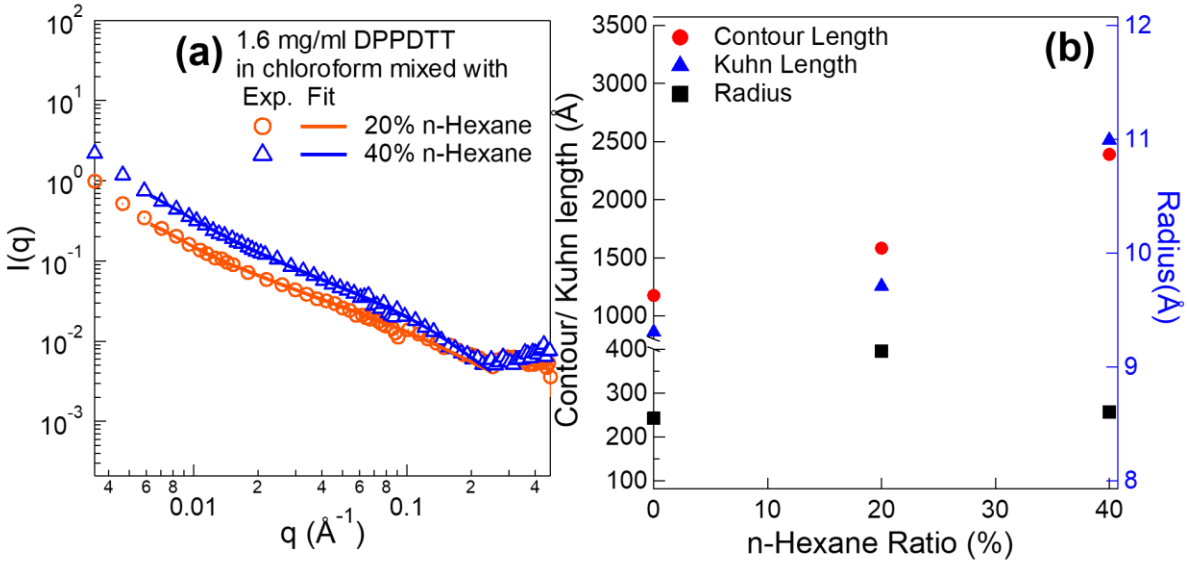

Figure 5.19. (a) SANS profiles of DPPDTT with 20 v% and 40 v% n-Hexane. The profiles are fitted with flexible cylinder model. (b) The extrapolated contour length, Kuhn Length, and radius from the model.

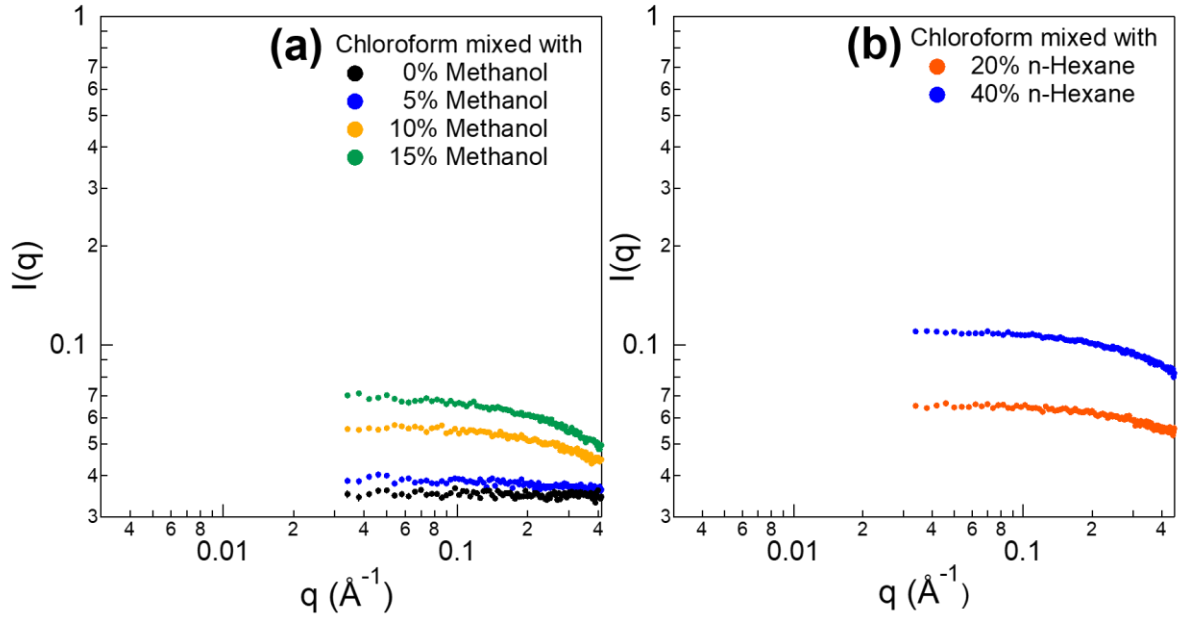

Figure 5.20. 1-D SANS scattering profiles of d-chloroform mixed with (a) d4-methanol and (b) d14-n-hexane with different ratios.

5.5 SUMMARIES

The self-assembly of donor-acceptor conjugated polymers into nanoribbons was easily induced by addition of certain miscible polar poor solvents. The polarity of the poor solvent additive was found to be important for this self-assembly process to occur. The use of non-polar solvent to induce aggregation resulted in particles with amorphous shapes in solution. The interactions between poor solvent molecules and polymers, as well as poor solvent and good solvent molecules were both important in determining the resulting structure and chain packing conformation. Of all poor solvents that were investigated, methanol facilitates the formation of unique crystalline peaks that appear at high q values. This indicated the formation of a different crystal polymorph from the same polymer. An enhancement of hole mobility in OFETs resulted from the formation of nanostructures upon addition of methanol. Self-assembly of DACPs by addition of polar poor solvents into mixtures with good solvents was found to be a general and powerful method to further improve the performance of these promising materials.

5.6 REFERENCES

(1) Shin, H.; Seo, S.; Park, C.; Na, J.; Han, M.; Kim, E. Energy Saving Electrochromic Windows from Bistable Low-HOMO Level Conjugated Polymers. *Energy Environ. Sci.* 2016, *9* (1), 117–122 DOI: 10.1039/C5EE03160E.

(2) Simon, D. T.; Gabrielsson, E. O.; Tybrandt, K.; Berggren, M. Organic Bioelectronics: Bridging the Signaling Gap between Biology and Technology. *Chem. Rev.* 2016, *116* (21), 13009–13041 DOI: 10.1021/acs.chemrev.6b00146.

(3) Chortos, A.; Liu, J.; Bao, Z. Pursuing Prosthetic Electronic Skin. *Nat. Mater.* 2016, No.

July, 1–14 DOI: 10.1038/nmat4671.

(4) Wu, C.-H.; Chueh, C.-C.; Xi, Y.-Y.; Zhong, H.-L.; Gao, G.-P.; Wang, Z.-H.; Pozzo, L. D.; Wen, T.-C.; Jen, A. K.-Y. Influence of Molecular Geometry of Perylene Diimide Dimers and Polymers on Bulk Heterojunction Morphology Toward High-Performance Nonfullerene Polymer Solar Cells. *Adv. Funct. Mater.* 2015, *25* (33), 5326–5332 DOI: 10.1002/adfm.201501971.

(5) Luo, H.; Yu, C.; Liu, Z.; Zhang, G.; Geng, H.; Yi, Y.; Broch, K.; Hu, Y.; Sadhanala, A.; Jiang, L.; Qi, P.; Cai, Z.; Sirringhaus, H.; Zhang, D. Remarkable Enhancement of Charge Carrier Mobility of Conjugated Polymer Field-Effect Transistors upon Incorporating an Ionic Additive. *Sci. Adv.* 2016, *2* (May), e1600076 DOI: 10.1126/sciadv.1600076.

(6) Li, J.; Zhao, Y.; Tan, H. S.; Guo, Y.; Di, C.-A.; Yu, G.; Liu, Y.; Lin, M.; Lim, S. H.; Zhou, Y.; Su, H.; Ong, B. S. A Stable Solution-Processed Polymer Semiconductor with Record High-Mobility for Printed Transistors. *Sci. Rep.* 2012, *2*, 754 DOI: 10.1038/srep00754.

(7) Luo, C.; Kyaw, K. K.; Perez, L. a; Patel, S.; Wang, M.; Grimm, B.; Bazan, G. C.; Kramer, E. J.; Heeger, A. J. General Strategy for Self-Assembly of Highly Oriented Nanocrystalline Semiconducting Polymers with High Mobility. *Nano Lett.* 2014, *14*, 2764 DOI: 10.1021/nl500758w.

(8) Müllen, K.; Pisula, W. Donor–Acceptor Polymers. *J. Am. Chem. Soc.* 2015, *137* (30), 9503–9505 DOI: 10.1021/jacs.5b07015.

(9) Noriega, R.; Rivnay, J.; Vandewal, K.; Koch, F. P. V.; Stingelin, N.; Smith, P.; Toney, M. F.; Salleo, A. A General Relationship between Disorder, Aggregation and Charge Transport in Conjugated Polymers. *Nat. Mater.* 2013, *12* (11), 1038–1044 DOI: 10.1038/nmat3722.

(10) Street, R. A. Unraveling Charge Transport in Conjugated Polymers. *Science (80-.).* 2013, *341* (6150), 1072–1073 DOI: 10.1126/science.1242935.

(11) Newbloom, G. M.; Kim, F. S.; Jenekhe, S. a.; Pozzo, D. C. Mesoscale Morphology and Charge Transport in Colloidal Networks of Poly(3-Hexylthiophene). *Macromolecules* 2011, *44* (10), 3801–3809 DOI: 10.1021/ma2000515.

(12) Newbloom, G. M.; Weigandt, K. M.; Pozzo, D. C. Electrical, Mechanical, and Structural Characterization of Self-Assembly in Poly(3-Hexylthiophene) Organogel Networks. *Macromolecules* 2012, *45*, 3452–3462 DOI: 10.1021/ma202564k.

(13) Newbloom, G. M.; de la Iglesia, P.; Pozzo, L. D. Controlled Gelation of Poly(3-Alkylthiophene)s in Bulk and in Thin-Films Using Low Volatility Solvent/Poor-Solvent Mixtures. *Soft Matter* 2014, *10* (44), 8945–8954 DOI: 10.1039/c4sm00960f.

(14) Xi, Y.; Pozzo, L. D. Electric Field Directed Formation of Aligned Conjugated Polymer Fibers. *Soft Matter* 2017, *13*, 3894–3908 DOI: 10.1039/C7SM00485K.

(15) Li, J.-H.; Xi, Y.; Pozzo, L. D.; Xu, J.-T.; Luscombe, C. K. Macroscopically Aligned Nanowire Arrays of π-Conjugated Polymers via Shear-Enhanced Crystallization. *J. Mater. Chem. C* 2017 DOI: 10.1039/C7TC01419H.

(16) Zheng, Y.-Q.; Yao, Z.-F.; Lei, T.; Dou, J.-H.; Yang, C.-Y.; Zou, L.; Meng, X.; Ma, W.; Wang, J.-Y.; Pei, J. Unraveling the Solution-State Supramolecular Structures of Donor-Acceptor Polymers and Their Influence on Solid-State Morphology and Charge-Transport Properties. *Adv. Mater.* 2017, *1701072*, 1701072 DOI: 10.1002/adma.201701072.

(17) Liu, J.; Arif, M.; Zou, J.; Khondaker, S. I.; Zhai, L. Controlling Poly(3-Hexylthiophene)

Crystal Dimension: Nanowhiskers and Nanoribbons. *Macromolecules* 2009, *42* (24), 9390–9393 DOI: 10.1021/ma901955c.

(18) Kiriy, N.; Jähne, E.; Adler, H. J.; Schneider, M.; Kiriy, A.; Gorodyska, G.; Minko, S.; Jehnichen, D.; Simon, P.; Fokin, A. A.; Stamm, M. One-Dimensional Aggregation of Regioregular Polyalkylthiophenes. *Nano Lett.* 2003, *3* (6), 707–712 DOI: 10.1021/nl0341032.

(19) Han, Y.; Guo, Y.; Chang, Y.; Geng, Y.; Su, Z. Chain Folding in Poly(3-Hexylthiophene) Crystals. *Macromolecules* 2014, *47* (11), 3708–3712 DOI: 10.1021/ma5006149.

(20) Iglesia, P. D. La; Pozzo, D. C. Effects of Supersaturation on the Structure and Properties of Poly(9,9-Dioctyl Fluorene) Organogels. *Soft Matter* 2013, *9* (47), 11214 DOI: 10.1039/c3sm51753e.

(21) Treat, N. D.; Nekuda Malik, J. A.; Reid, O.; Yu, L.; Shuttle, C. G.; Rumbles, G.; Hawker, C. J.; Chabinyc, M. L.; Smith, P.; Stingelin, N. Microstructure Formation in Molecular and Polymer Semiconductors Assisted by Nucleation Agents. *Nat. Mater.* 2013, *12* (7), 628–633 DOI: 10.1038/nmat3655.

(22) Lei, Y.; Deng, P.; Li, J.; Lin, M.; Zhu, F.; Ng, T.; Lee, C.; Ong, B. S. Solution-Processed Donor-Acceptor Polymer Nanowire Network Semiconductors For High-Performance Field-Effect Transistors. *Sci. Rep.* 2016, *6* (1), 24476 DOI: 10.1038/srep24476.

(23) Chen, M. S.; Lee, O. P.; Niskala, J. R.; Yiu, A. T.; Tassone, C. J.; Schmidt, K.; Beaujuge, P. M.; Onishi, S. S.; Toney, M. F.; Zettl, A.; Fréchet, J. M. J. Enhanced Solid-State Order and Field-Effect Hole Mobility through Control of Nanoscale Polymer Aggregation. *J. Am. Chem. Soc.* 2013, *135* (51), 19229–19236 DOI: 10.1021/ja4088665.

(24) Hu, Z.; Willard, A. P.; Ono, R. J.; Bielawski, C. W.; Rossky, P. J.; Vanden Bout, D. A. An Insight into Non-Emissive Excited States in Conjugated Polymers. *Nat. Commun.* 2015, *6*, 1–9 DOI: 10.1038/ncomms9246.

(25) Ferdous, S.; Liu, F.; Wang, D.; Russell, T. P. Solvent-Polarity-Induced Active Layer Morphology Control in Crystalline Diketopyrrolopyrrole-Based Low Band Gap Polymer Photovoltaics. *Adv. Energy Mater.* 2014, *4* (2), 1–10 DOI: 10.1002/aenm.201300834.

(26) Jiang, Z.; Li, X.; Strzalka, J.; Sprung, M.; Sun, T.; Sandy, A. R.; Narayanan, S.; Lee, D. R.; Wang, J. The Dedicated High-Resolution Grazing-Incidence X-Ray Scattering Beamline 8-ID-E at the Advanced Photon Source. *J. Synchrotron Radiat.* 2012, *19* (4), 627–636 DOI: 10.1107/S0909049512022017.

(27) Jiang, Z. GIXSGUI : A MATLAB Toolbox for Grazing-Incidence X-Ray Scattering Data Visualization and Reduction, and Indexing of Buried Three-Dimensional Periodic Nanostructured Films. *J. Appl. Crystallogr.* 2015, *48* (3), 917–926 DOI: 10.1107/S1600576715004434.

(28) Kline, S. R. Reduction and Analysis of SANS and USANS Data Using IGOR Pro. *J. Appl. Crystallogr.* 2006, *39* (6), 895–900 DOI: 10.1107/S0021889806035059.

(29) P. Butler, G. Alina, R. C. Hernandez, M. Doucet, A. Jackson, P. Kienzle, S. K. and J. Z. SASView for Small Angle Scattering Analysis http://www.sasview.org/.

(30) Kim, D. H.; Han, J. T.; Park, Y. D.; Jang, Y.; Cho, J. H.; Hwang, M.; Cho, K. Single-Crystal Polythiophene Microwires Grown by Self-Assembly. *Adv. Mater.* 2006, *18* (6), 719–723 DOI: 10.1002/adma.200502442.

(31) Chen, W.-R.; Butler, P. D.; Magid, L. J. Incorporating Intermicellar Interactions in the Fitting of SANS Data from Cationic Wormlike Micelles. *Langmuir* 2006, *22* (15), 6539–6548 DOI: 10.1021/la0530440.

(32) Pedersen, J. S.; Schurtenberger, P. Scattering Functions of Semiflexible Polymers with and without Excluded Volume Effects. *Macromolecules* 1996, *29* (23), 7602–7612 DOI: 10.1021/ma9607630.

(33) Chaudhari, S. R.; Griffin, J. M.; Broch, K.; Lesage, A.; Lemaur, V.; Dudenko, D.; Olivier, Y.; Sirringhaus, H.; Emsley, L.; Grey, C. P. Donor–acceptor Stacking Arrangements in Bulk and Thin-Film High-Mobility Conjugated Polymers Characterized Using Molecular Modelling and MAS and Surface-Enhanced Solid-State NMR Spectroscopy. *Chem. Sci.* 2017, *8* (4), 3126–3136 DOI: 10.1039/C7SC00053G.

(34) Niedzialek, D.; Lemaur, V.; Dudenko, D.; Shu, J.; Hansen, M. R.; Andreasen, J. W.; Pisula, W.; Müllen, K.; Cornil, J.; Beljonne, D. Probing the Relation between Charge Transport and Supramolecular Organization down to Ångström Resolution in a Benzothiadiazole-Cyclopentadithiophene Copolymer. *Adv. Mater.* 2013, *25* (13), 1939–1947 DOI: 10.1002/adma.201201058.

(35) P. Mittelbach, G. P. X-Ray Low-Angle Scattering by Dilute Scattering Colloidal Systems. The Calculation of Scattering Curves of Parallelepipeds. *Acta Phys. Austriaca* 1961, *14*, 185–211.

(36) Roman Nayuk, K. H. Formfactors of Hollow and Massive Rectangular Parallelepipeds at Variable Degree of Anisometry. *Zeitschrift für Phys. Chemie* 2012, *226*, 837–854.

(37) H. Benoit. La Diffusion de La Lumiere Par Des Macromolecules En Chaines En Solution

Dans Un Bon Solvant. *Comptes Rendus* 1957, *245*, 2244–2247.

(38) Hammouda, B. SANS from Homogeneous Polymer Mixtures - A Unified Overview. *Adv. Polym. Sci.* 1993, *106*, 87–133.

(39) Phan, H.; Ford, M. J.; Lill, A. T.; Wang, M.; Bazan, G. C.; Nguyen, T.-Q. Electrical Double-Slope Nonideality in Organic Field-Effect Transistors. *Adv. Funct. Mater.* 2018, *28* (17), 1707221 DOI: 10.1002/adfm.201707221.

(40) Lei, Y.; Deng, P.; Zhang, Q.; Xiong, Z.; Li, Q.; Mai, J.; Lu, X.; Zhu, X.; Ong, B. S. Hydrocarbons-Driven Crystallization of Polymer Semiconductors for Low-Temperature Fabrication of High-Performance Organic Field-Effect Transistors. *Adv. Funct. Mater.* 2018, *28* (15), 1–9 DOI: 10.1002/adfm.201706372.

(41) Vaz, P. D.; Nolasco, M. M.; Gil, F. P. S. C.; Ribeiro-Claro, P. J. A.; Tomkinson, J. Hydrogen-Bond Dynamics of C□H···O Interactions: The Chloroform···Acetone Case. *Chem. - A Eur. J.* 2010, *16* (30), 9010–9017 DOI: 10.1002/chem.201000479.

Chapter 6. Organic Electrode materials for printable battery applications

6.1 INTRODUCTION AND MOTIVATION

Recently, organic electronic devices have gained tremendous attention, since they are promising candidates for making wearable devices that are flexible and stretchable. At the same time, the solution processable materials can be easily scaled up for roll-to-roll process. Due to those reasons, various flexible electronics have been demonstrated, such as organic field effect transistors (OFETs) [1], photovoltaics (OPVs) [2–4], and light emitting diodes (OLEDs) [5]. On top of those basic building blocks of electronic devices, novel wearable devices within the framework of bioelectronics are emerging as a hot topic, such as organic electrochemical transistors (OECTs) to mimic neural interface [6], and electronic skins to convert contact and touch to electrical signal [7]. Currently, however, the device testing requires bulky power supplies that restricts their flexibility as an operating unit [8]. Therefore, it is important to explore energy storage materials with wearable mechanical properties to power bioelectronics and could potentially remove the form factor constraint from the power supplies. [9]

An important factor to consider for electrode materials is the cost of processing. Nowadays, most batteries are fabricated in a batch mode that requires grinding and high temperature annealing, which is costly and difficult to be scaled up. [10,11] Printing is a great technique that is suitable for large scale production and it has been demonstrated in OPVs and OLEDs fabrication. [12,13] This technique has already been applied to battery fabrication to lower the cost, especially inorganic electrode materials, including Zn/MnO_2, Zn/Ag, Zn/Ag_2O, $Li_4Ti_5O_{12}/LiFePO_4$, and $LiCoO_2/Li_4Ti_5O_{12}$. [8,14–17] The charge capacity for the printed battery $LiCoO_2/Li_4Ti_5O_{12}$ can be 120 mAh/g. [8] For those material, the preparation of a homogeneous ink is critical for printing. The ink

is a multi-component system that includes electrochemically active materials, polymers, binder, and solvents. A tremendous amount of effort is needed to achieve well dispersed paint or slurry. Typically, ultrasonication and strong mechanical shaking are necessary for paint preparation. [14] Sometimes, a careful separation of particles based on their sizes using centrifugation are required as well. [15] All the extra steps add complexity to the processing, which calls for new materials that can be easily dispersed into solvent to prepare the ink. Additionally, there is a strong need to eliminate the use of water as solvent to ensure the quality of batteries. In order to achieve this, very careful steps are taken during battery assembly process to remove absorbed water in chemicals from atmosphere, which may not be suitable for mass production in industry.[18] Instead of using water, materials that can be readily dispersed into organic solvents are desirable for electronic device fabrication. [19]

Conductive polymers are good candidates for solution processable redox active materials. Compared to inorganic particles, it is relatively easy to form dissolved state or dispersion of conductive polymers. [19] Two methods are generally used to stabilize polymer chains to decrease the strong polymer-polymer interaction, which includes utilizing electrostatically bonded large counterions, such as PEDOT:PSS, or covalently bonded side chains to the backbone, P3HT for example. [19] The electrostatically bonded conjugated polymers can be potentially used for active materials of battery electrodes, since the process of gaining and releasing the dopants is associated with the formation of positive and negative polarons, [20] which provides the electrochemistry of charge and discharge. Another benefit of conjugated polymers is that their structures can be tuned by many factors, such as solvents, monomer molecular structures, and dopants, which offers itself a large freedom to control the final structures for enhanced performance. What is more, conjugated polymers are electrically conductive, which is beneficial for energy storage devices as they provide

more charge transport paths. In fact, they have been shown to replace the insulating binder material (polyvinylidene fluoride) and increased the capacity. [21,22] The incorporation of conjugated polymers as a binder also improves the quality of the film.

Some pioneer work has been done to apply conjugated polymers into batteries as electrode materials. Polyaniline, PEDOT, polypyrrole, and polythiophene have all been characterized as electrode materials. [20] Polyaniline shows a very high theoretical charge capacity (294 mAh/g) and has been demonstrated a practical charge capacity of 120 mAh/g. [23] For polypyrrole and PEDOT, the experimental capacity were around 80 mAh/g. [20]

Organometallic complex, on the other hand, can also be used as electrode materials for printable batteries. Instead of forming polarons in a conjugated polymer backbone, utilizing multi-valent metallic ions is another way to achieve redox active electrochemistry. Different ways have been reported to disperse metallic ions into organic solvents. It has been reported that polymers can be synthesized to covalently bonded to metallic radicals, such that polymer backbone was used to carry the redox active species. [24] Charged metallic cations can also be dispersed into organic solvents (apolar) by forming reverse micelles with surfactant counterions as well. [25,26] The advantage of using surfactant chains for dispersing is that it is a simple, economical, and versatile method that works for almost all multi-valent cations. In this study, electrochemistry of organometallic complex that can be dispersed into organic solvent is investigated.

6.2 EXPERIMENTAL

6.2.1 *Materials*

Sodium dodecyl sulfate (SDS, 98%), Dioctyl sulfosuccinate sodium salt (AOT, 97%), Sodium dodecylbenzenesulfonate (SDBS, technical grade), iron (III) chloride (97%), aluminum chloride hexahydrate, vanadium (III) chloride (97%), cobalt (II) chloride (97%), pyrrole (98%), 3,4-ethylenedioxythiophene (EDOT, 97%), tetrabutylammonium tetrafluoroborate (TBATFB, 99%), ferrocene (Fc, 98%), potassium sulfate (99%), and propylene carbonate (PC, 99.7%) were purchased from Sigma Aldrich (St Louis, MO). Cerium (III) chloride (99.9%) was obtained from Alfa Aesar (Tewksbury, MA). Sodium chloride was purchased from Fisher Scientific (Pittsburgh, PA). All chemicals were used as received without any further purification. Lithium disks, battery separators and cases for packaging were bought from MTI corporation (Richmond, CA). 1M lithium hexafluorophosphate solution in ethylene carbonate and dimethyl carbonate (EC/DMC=50/50(v/v)) was purchased from Sigma Aldrich and used as electrolyte.

6.2.2 *Scanning Electron Microscopy*

SEM images were taken by an FEI XL830 dual beam scanning electron microscope. Sample solutions were drop casted on a piece of silicon wafer. After they were completely dried, a thin layer of ~8 nm gold/palladium was sputtered onto the sample surface. This extra step right before imaging was to prevent charging during imaging, since conjugated polymer themselves were not conductive enough to completely eliminate charging effects.

6.2.3 *Organometallic salt complex, PEDOT, and Ppy synthesis*

The general synthesis procedure was following the method reported by de la Iglesia et al. [26,27] Surfactants were dissolved in DI water and stirred for at least a few hours before they completely dissolve. AOT sample required a much longer time for dissolution, which was typically stirred overnight before use. Metallic chloride was dissolved in DI water. They were then added to surfactant solutions while stirring until organometallic salt complex aggregated and precipitated. Extra metallic chloride solutions were added to ensure the consumption of all surfactant groups. The precipitate was filtered and dried in a watch glass under vacuum at room temperature for at least 24 hours. To synthesize conjugated polymers doped with surfactant chains, the dried iron (III) salt complex was dissolved in toluene first at a concentration of 30 mg/ml and either monomer 3,4-Ethylenedioxythiophene (EDOT) or pyrrole (Py) was added to salt complex solution at a ratio of monomer/Iron complex=1:1. The solutions were left polymerizing for a few weeks to ensure complete polymerization. The resulted polymer solution was washed for at least three times using ultrafiltration to remove the excess surfactant chains and reacted iron (II) complex until the filtrate color become clear. Then the polymer solutions were dried in chemical hood before use.

6.2.4 *Small Angle Neutron and x-ray Scattering (SANS and SAXS)*

Small angle neutron scattering experiments were performed at the NIST Center for Neutron Research (NCNR) (Gaithersburg, MD). Standard configuration with four detector positions, including lens, was used to cover a q-range of $0.002<q(Å^{-1})<0.4$ of NGB 30. For detector position with lens, neutron beam with 8.4 Å wavelength was used and 6 Å neutron was utilized for the rest of the detector positions. Ultra-small angle neutron scattering (USANS) was performed on BT5 at

NCNR. [28] The obtained data was stitched with SANS profile to extend the low q range to 3×10^{-5} $Å^{-1}$. The SANS and USANS experiments were conducted on the exact same sample. The polymer samples were dispersed into d-chloroform at a concentration of 15 mg/ml. Tip sonicator was utilized assist polymers to form a stable dispersion. Titanium cell with 1 mm path length was used and the samples were loaded between two quartz windows. The scattering profile was corrected using the empty cell scattering from two quartz windows and background scattering signal with blocked beam. The intensity was normalized to absolute scale by measuring the open beam flux. [29] Igor reduction macro [29] was followed to reduce the SANS data.

The solid sample was characterized by small angle x-ray scattering (SAXS) using a SAXSESS instrument from Anton Paar (Graz, Austria). X-ray beam with 1.54 Å wavelength was utilized. 2-D scattering patterns was collected using an image plate and the data is reduced by SAXSQuant software. For powder samples, a 75 μm thin glasses were used to sandwich the organometallic salt complex in a static cell. The scattering profile was collected for glass and subtracted from the sample intensity. For printed films, the polymer solution was spray coated on the thin glass before use.

6.2.5 *Brunauer-Emmet-Teller (BET) measurement*

A FlowSorb surface area analyzer (MicroMeritics Corp., Norcross, GA) is used to characterize the surface area of the polymers. Before each measurement, the weight of the sample was measured and recorded. The samples were purged with dry nitrogen flow for overnight to remove water or solvent molecules that were trapped within the materials that could potentially affect the results. A gas mixture of helium (70%) and nitrogen (30%) was used for the experiment. Helium served as carrier gas and nitrogen was used as adsorbate. The system was calibrated by injecting 1 ml

pure nitrogen into the system until 2.84 m^2 reading was obtained. Liquid nitrogen was used to cool down the system and to induce gas adsorption. The surface area was extrapolated by measuring the thermal conductivity difference after nitrogen adsorption.

6.2.6 *Cyclic Voltammetry*

A Gamry potentiostat (Reference 600, Warminster, PA) was used to conduct cyclic voltammetry experiments. Working electrode (glassy carbon), counter electrode (platinum wire), as well as Ag/AgCl reference electrodes were purchased from BASi (West Lafayette, IN). The 3-electrode characterization in solution was followed by purging of argon gas with C-3 cell stand (BASi). The solid salt CV was conducted by dissolving them in methanol and then was drop casted onto working electrode repeatedly. They were dried in a chemical hood before measurement. Electrolytes were dissolved in water before measurement. The cell stand was also served as a faraday cage to minimize the electrical interference for the signal. The cyclic charge and discharge testing for coin battery was also performed with Gamry potentiostat.

6.2.7 *Battery assembly and characterization*

The battery schematic was shown in Figure 6.5. The electrode materials were coated on aluminum foil and dried in vacuum chamber before use. If carbon black (Super P, Timcal Graphite & Carbon) is used, it is mixed with active materials in 1:4 ratio. 1M $LiPF_6$ in a mixture of ethylene carbonate and dimethyl carbonate with 1:1 ratio was used as electrolyte. The separator film (Celgard 2400) was soaked in electrolyte before assembly. The assembly of the coin battery (CR2016) was achieved by using a hydraulic crimping machine (MSK-110, MTI, Richmond CA) in an argon

filled glovebox to ensure complete seal. The battery cyclic charge and discharge testing was performed using a Gamry potentiostat with a global software license. The voltage range was chosen between 1.5 V and 5 V (v.s. Li/Li^+).

6.3 Results & Discussions

The general synthesis method of organometallic salt complex enables customized production of various metallic ions and surfactant chains, which can be finely adjusted to accommodate different applications. The electrostatic interaction between metal ions and surfactant head groups results in a relatively stable complex that is not soluble in water. Figure 6.1 (a) shows photo images of several examples of organometallic salt complexes. The molecular structure of the three surfactants are drawn in Figure 6.1 (b). The materials can be designed in different ways for different purposes. Simply switching the metallic chloride and the surfactants can result in a new material. The color of the salt complexes varies greatly with the choice of metal ions. Aluminum and Cerium metal ions usually have a white color, while cobalt, iron, and vanadium samples are more colorful. Changing the surfactant groups can also tune the colors. Of the same metal ion, AOT and SDBS have a relatively dark color and SDS shows a lighter color. In addition, the physical forms of the samples are also determined by the molecular structures of the complexes. The SDS samples are often in powder form. In comparison, SDBS and AOT samples tend to form gels. Generally speaking, the yield of divalent organometallic (cobalt) salt complex is much lower than their counterparts with trivalent metal ions. This is because the divalent salt complexes are electrostatically bonded to two surfactant chains at most. Thus, they remain dispersed and are relatively difficult to precipitate out from aqueous solutions.

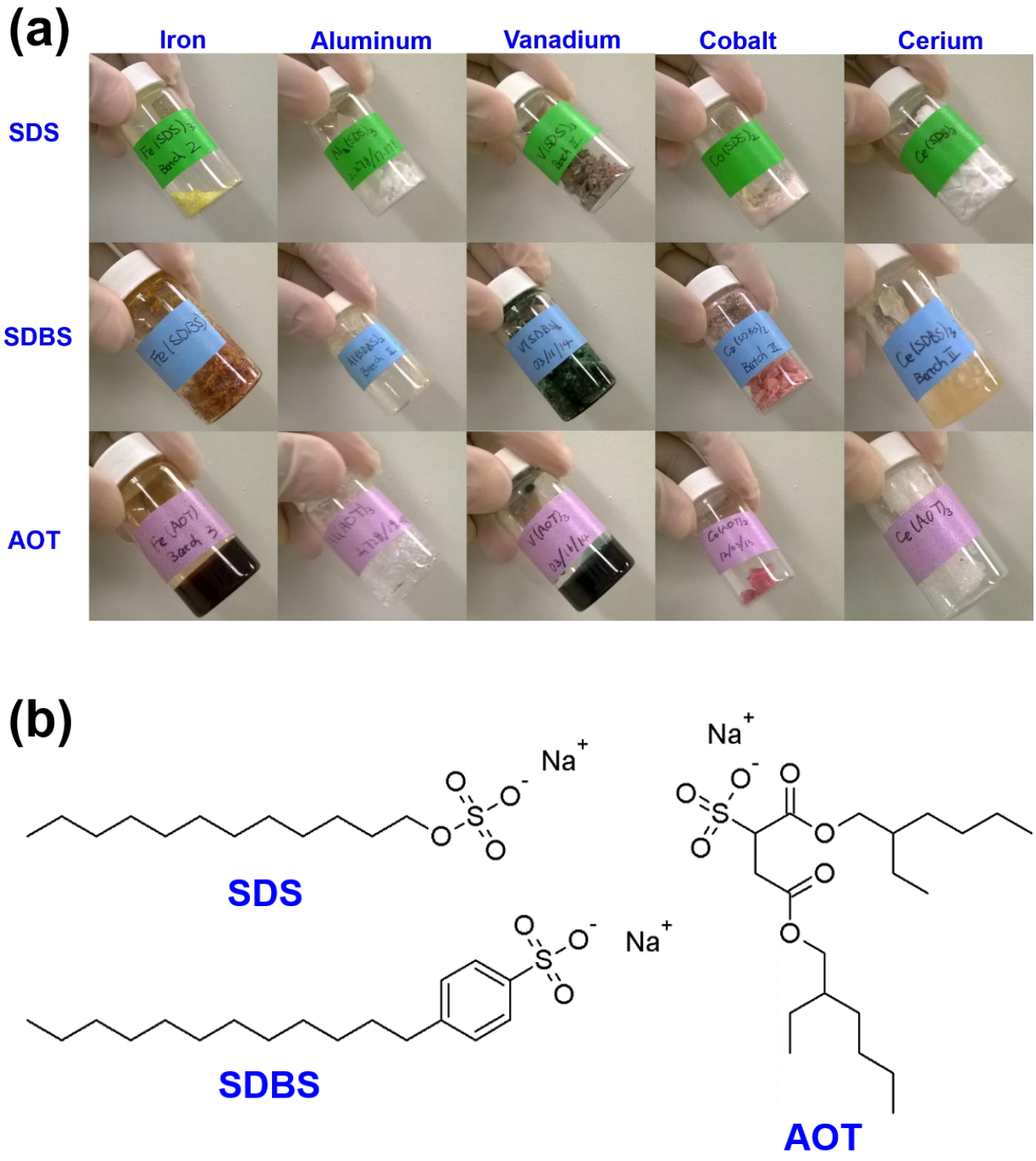

Figure 6.1. (a) Optical photographs of the synthesized salt complex using various metal ions (columns) and different surfactant groups (rows). (b) Molecular structures of surfactants SDS, SDBS, and AOT.

A closer look into the organometallic salt complex from the molecular scale could provide more insights into the physical difference of the complexes using different metal ions and surfactant chains. The molecular packing of the complex is highly dependent on the surfactant chains. For example, SDS, a relatively short linear chain surfactant, leads to a very crystalline form of the salt complex. The SAXS patterns of iron and aluminum complexes are shown in Figure 6.2. For both metal ions, SDS samples exhibit multiple well-defined peaks at relative high q region, indicating high crystallinity in the samples. At low q-region, both iron and aluminum samples with SDS show steepest slopes of all three surfactants. Power law fitting to the low-q region of SDS reveals a slope of ~-2. This could be due to the formation of fractal structures with a fractal dimension of 2. It is also possible that part of SDS doped metal complex may form larger structures, leading to an increase in low-q region. It is interesting to note that simply changing the metal ions does not affect the major peak positions between 0.2 and 0.3 $Å^{-1}$ for DBS and AOT salts. This indicates that those peaks may result from the scattering of the surfactant chains.

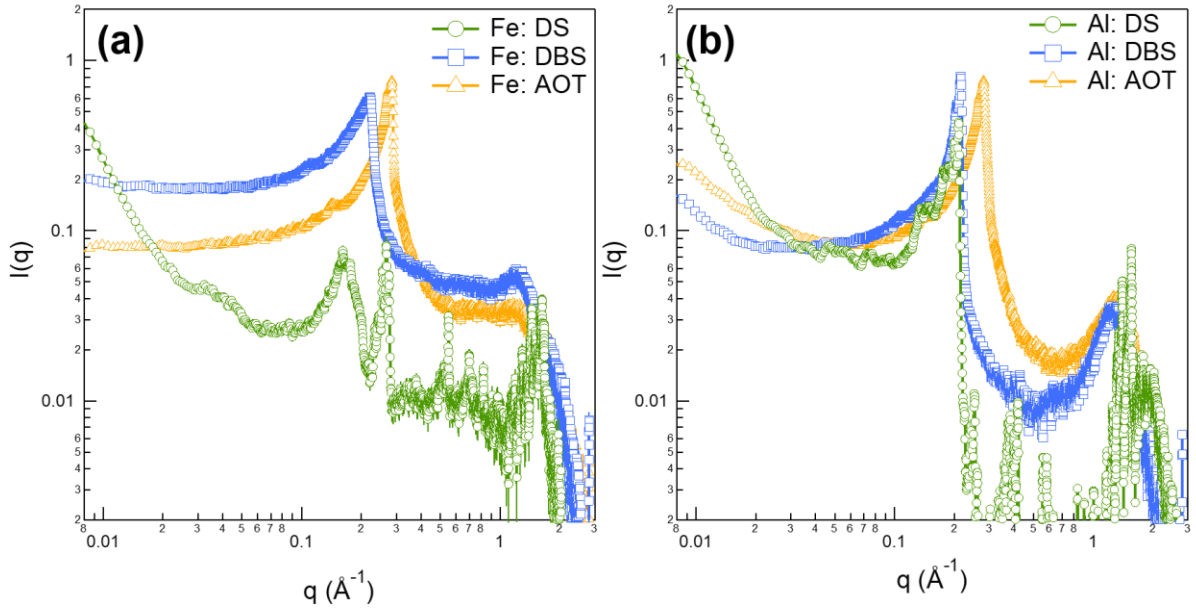

Figure 6.2. 1-D SAXS scattering profiles of (a) iron and (b) aluminum salt complexes with the three surfactant chains: SDS, SDBS, and AOT. The measurement was conducted on samples in a solid form.

The electrochemical behavior of iron salt complexes is investigated by cyclic voltammetry (CV) in Figure 6.3. After coating the salt on electrodes, the iron salt complexes are systematically tested with multiple sweeps. It is obvious that the iron salt complex is redox active no matter what electrolyte solution is used. This redox active specie is attributed to Fe^{3+}/Fe^{2+} couples, which are closely related to the losing and obtaining one surfactant group, depending on the formed species. Different surfactant groups can slightly tune the location of oxidation and reduction peaks. This could be related to the different mass transfer rates of the surfactant groups while iron ions are oxidized or reduced. It is also possible that the varied molecular structure and moiety within the surfactant chains could affect their bonding strength with metal ions. In 1M NaCl solution, $Fe(DS)_3$ shows both the closest oxidation and reduction peak, which indicates that it is the most quasi-

reversible reaction of the three. [30] The distance between oxidation and reduction peak for $Fe(DBS)_3$ are very large, which could probably due to the electron withdrawing benzene group in the surfactant chain. Pealing problem exists for all the three iron surfactant complexes in all electrolyte solutions. The more the sample has been cycled through, the less material remains on the electrodes. $Fe(DBS)_3$ shows the least peeling problem during the cycle, which is attributed to its physical gel form.

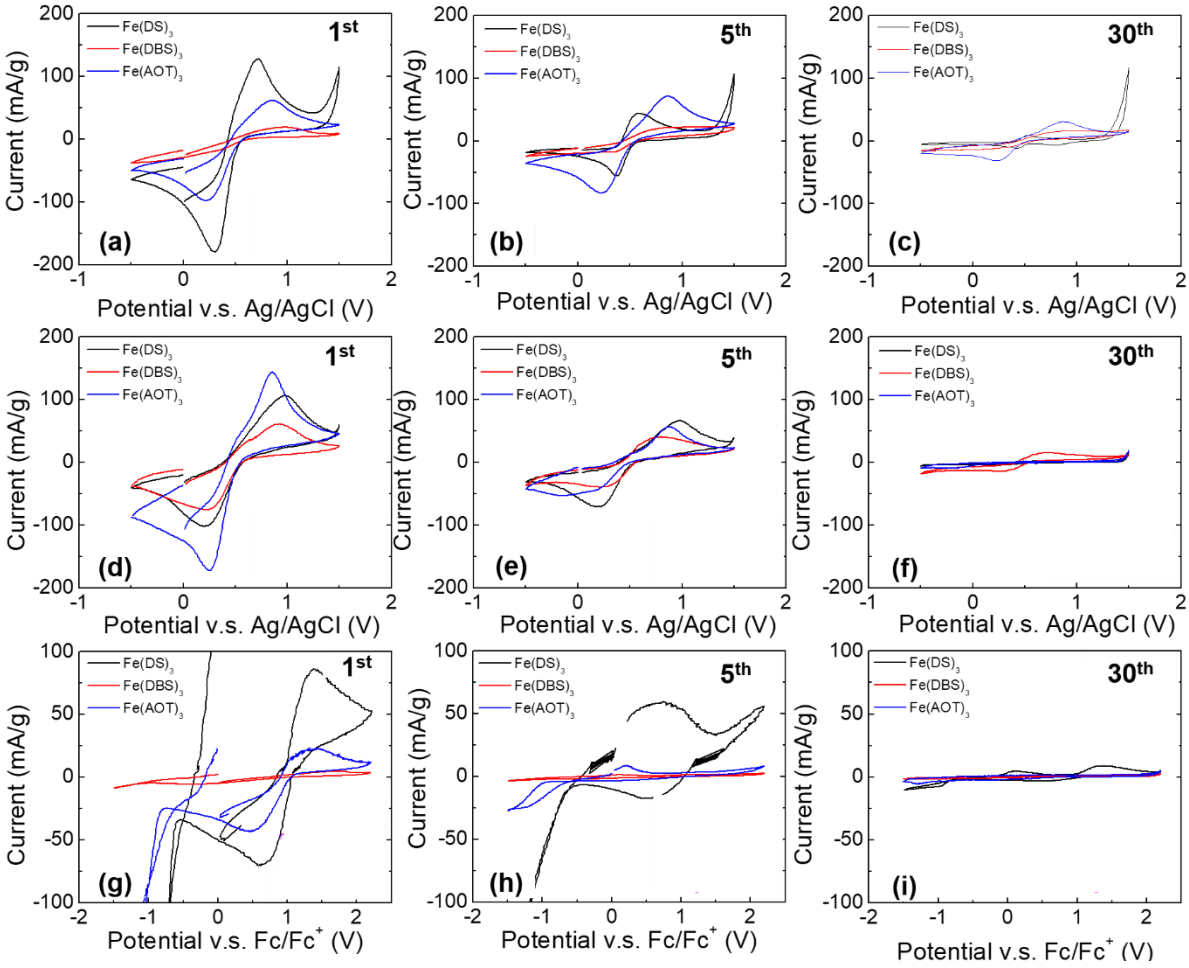

Figure 6.3. Cyclic voltammetry measurement of iron complexes with three surfactant groups in various electrolytes. (a) ~(c) are in 1M NaCl aqueous solution. (d)~(f) are in 0.4M K_2SO_4 aqueous solution. (g)~(i) are in 0.1 M TBATFB in propylene carbonate. The columns from left to right indicates the 1st, 5th, and 30th cycles. The salt complexes were dissolved in methanol and drop casted on the working electrode before use. The scan rate was fixed at 100 mV/s.

Not only are iron salt complexes redox active, other metal complexes also exhibit potential to be used as battery electrode materials. Vanadium, cerium, and cobalt metal complex are synthesized and their CV curves are recorded in Figure 6.4. Vanadium complexes show the highest

electrochemical activity. Linear surfactant chains (i.e. DS and DBS) show clearer redox behavior compared with branched surfactant chains (AOT). This could be due to the better accessibility because of less steric hindrance of the linear chain. The first oxidation peak appears between 0V to 1V and the second oxidation peak is at close to 2V. A tiny reduction peak is observed for $V(DBS)_3$ between 0V and 1V and a well-defined one at ~-1V. In addition, the moiety in the surfactant group can shift the redox potential of the peaks. By comparing $V(DBS)_3$ with $V(DS)_3$, shifts towards negative potential are observed for all the peaks, which could be explained by the electron pulling from the benzene ring in DBS group. In contrast, complexes with cerium and cobalt as cations do not exhibit reproducible redox peaks. It is interesting to note that those ones that do have oxidation peaks for both metal ions are with DS surfactant groups.

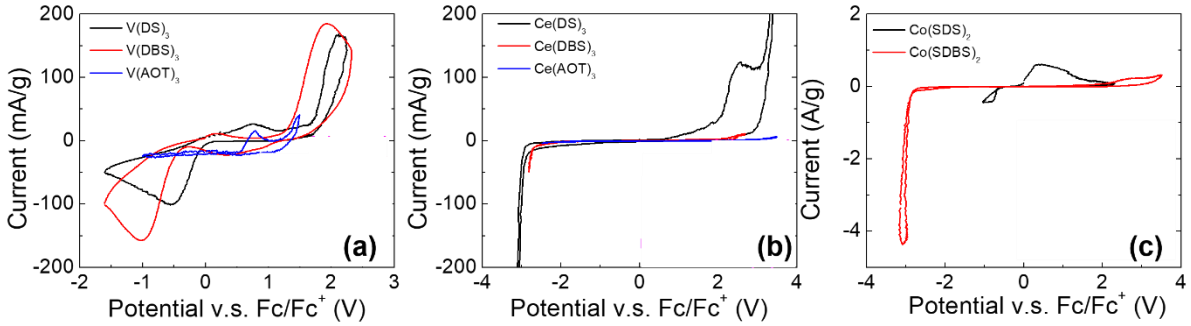

Figure 6.4. Cyclic voltammetry of (a) vanadium (b) cerium (c) cobalt salt complex with DS, DBS, and AOT. Ferrocene is used as reference electrode. The measurement was conducted in propylene carbonate with 0.1 M TBATFB as supporting electrolyte. The scan rate is fixed at 100 mV/s. All the curves are recorded after repeatedly sweeping for four cycles.

After the initial cyclic voltammetry test, the organometallic salt complexes are prepared into a coin battery cell as cathode to measure the storage capacity. The schematic drawing is shown in Figure 6.5 (a). Lithium metal is used anode. Different salt complexes are characterized and CV results are

shown in Figure 6.5 (b). Five cycles are recorded to show the repeatability. Both vanadium and iron salt complexes show redox active curves. Iron complex has one oxidation peak (4V v.s. Li/Li^+) and one reduction peak (2.8V v.s. Li/Li^+). Vanadium exhibites two reduction and oxidation peaks, which is consistent to what is shown in the CV measurement in solution in Figure 6.4. The mild oxidation peak at 4.3V v.s. Li/Li^+ and reduction peak at 2.2 V v.s. Li/Li^+ indicate that vanadium could have irreversible chemical reactions with lithium metal. [11] Interestingly, when organometallic salts are assembled into coin batteries, the dissolution problem disappears. The curves are all reproducible even if several cycles were measured. This could be due to the confined space defined by the separator in the lithium ion battery cell, which avoids the mass transport issue one the DBS group is dissolved in the electrolytes during a reduction cycle. Similar to what are observed in Figure 6.4 (b) and (c), cerium and cobalt complexes do not show redox behavior.

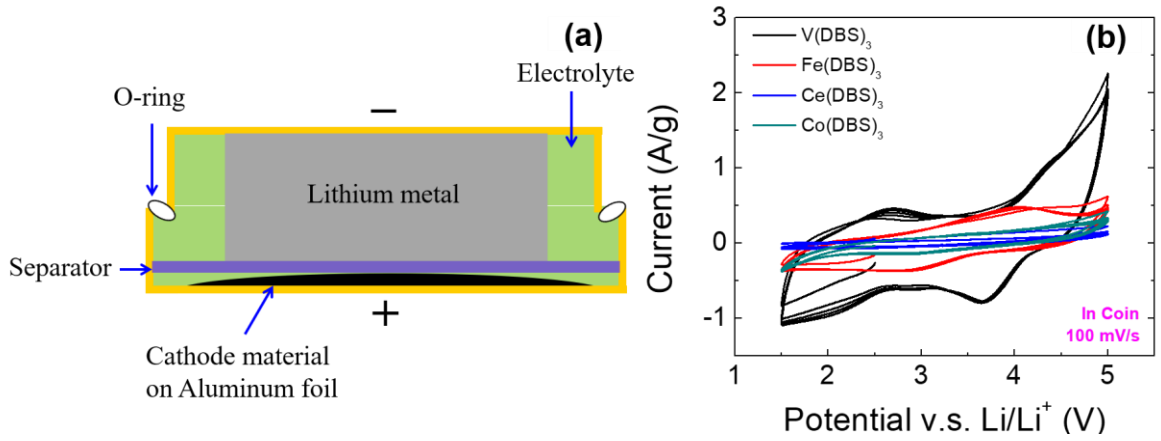

Figure 6.5. (a) Schematic drawing of a coin battery. The electrode materials were coated to aluminum foil to be used as cathode. (b) Cyclic voltammetry measurement of DBS salt complexes with different metal ions. The scan rates were fixed at 100 mV/s.

The charge and discharge rate performances are characterized for the two metal complexes that have shown redox behavior in CV measurements (i.e. $Fe(DBS)_3$ and $V(DBS)_3$). Not much decay is observed for both batteries. Vanadium battery show a slightly higher capacity (~7 mAh/g) at a current density of 26 mA/h compared to its iron counterpart (~2 mAh/g). At all the current density tested, vanadium battery exhibits higher capacity. After charging at high current density, the capacity retains for iron battery when a lower current density is switched back on. In comparison, vanadium salt battery shows decay in capacity at a lower current density. This is consistent with the CV measurement in Figure 6.5 (b) that mild oxidation and reduction peaks are observed. The capacity for bother batteries are relatively low. This is probably due to the low conductivity of the metal salt complexes, since the metal core is associated with insulation layers of surfactant tails. Figure 6.6 (b) and (d) are the first several charge and discharge curves of iron and vanadium batteries. The first discharge cycle for vanadium show a capacity of 35 mAh/g, however, the second cycle show about 60% decrease charge capacity. This is probably due to the chemical reaction of vanadium with lithium mentioned before.

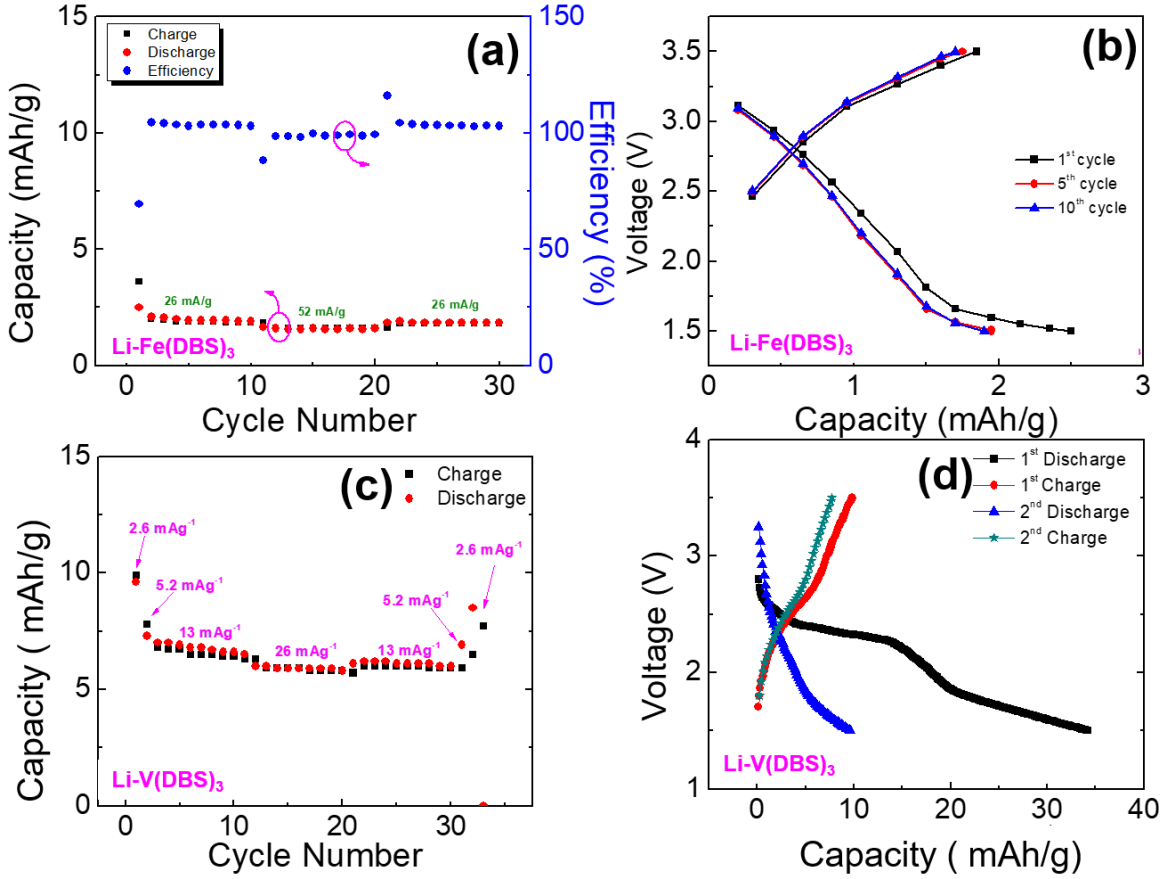

Figure 6.6. Cyclic performance of battery capacities under different current density, as well as charge discharge curves for (a) (b) Fe $(DBS)_3$ and (c) (d) $V(DBS)_3$.

Due to the redox activity of the salt complex, the salt can also be used as an oxidant to polymerize conductive polymers, such as poly (3,4-ethylenedioxythiophene) (PEDOT) and polypyrrole (Ppy). The polymerization follows a reactivation chain polymerization mechanism. [31,32] In the initiation step, iron surfactant complex, in our case, serves as the oxidant and catalyst of the reaction. The loss of one electron of each EDOT monomer enables them to attack another EDOT monomer to form a dimer. The propagation step requires the re-oxidation of the dimer. Therefore, the molar ratio of iron salt to EDOT monomer is an important parameter that determines the final chain

length and doping density, which closely correlates with the conductivity of the synthesized polymer. This general method can be applied to many conjugated polymer systems to synthesize different kinds of polymers that are dispersible in organic solvent by just simply changing the monomer used. For example, by using a pyrrole monomer, organic solvent dispersible Ppy can be synthesized. Figure 6.7 shows multi-scale images of a series of doped polypyrrole. They exhibited similar spherical shape superimposing on each other as PEDOT reported by Charba et al..[19] The size of the individual sphere varies for different dopants. DS and DBS doped PEDOT exhibited a diameter between 100 and 200 nm, whereas the AOT doped PEDOT has a much larger size of ~500 nm in diameter. This change is attributed to the molecular structure of the dopants, since AOT is a branched chain that occupies larger space.

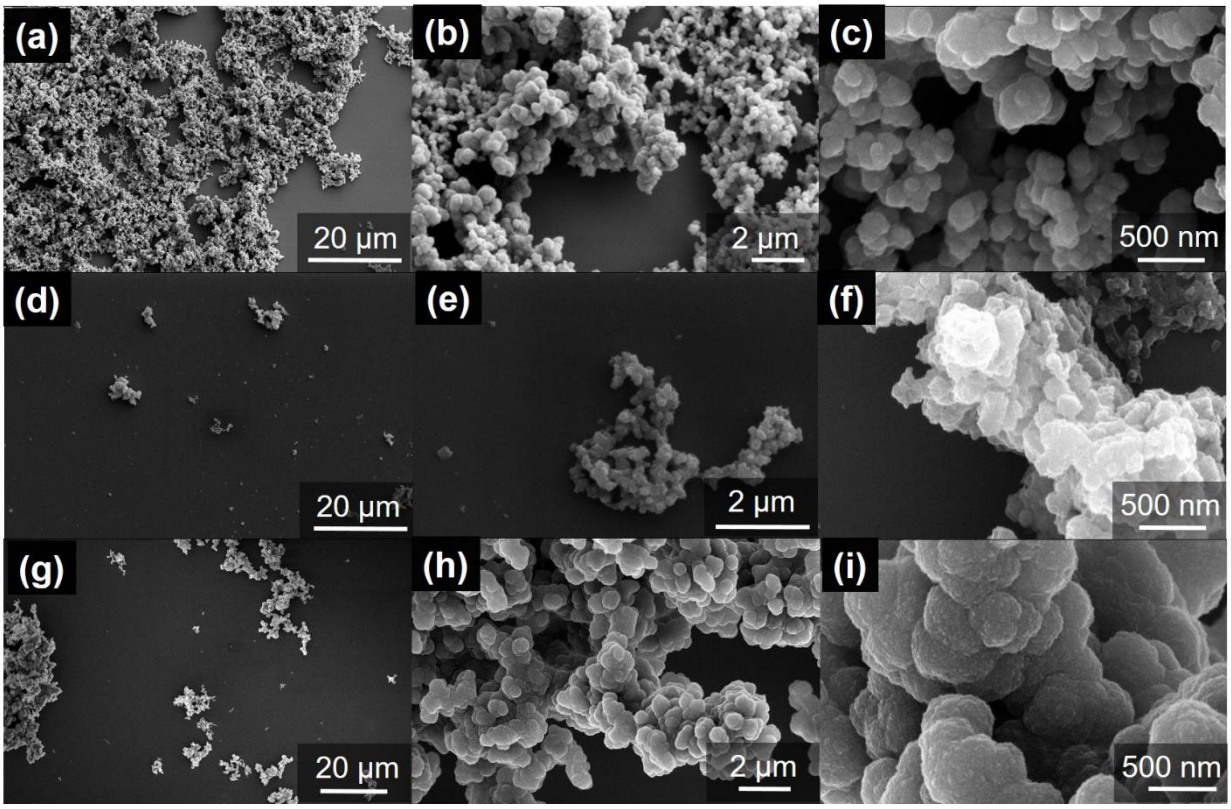

Figure 6.7. Scanning electron microscopy of polypyrrole doped with (a) (b) (c) dodecyl sulfate (98%), (d) (e) (f) Dioctyl sulfosuccinate, and (g) (h) (i) dodecylbenzenesulfonate.

It is important to note that the size of the spheres observed in the SEM images are critical to electrode material for the battery applications, since it determines the specific surface area. To gain more insights into this, polypyrrole samples doped with different surfactant groups are characterized with SANS and USANS in chloroform, shown in Figure 6.8 (a). Similar scattering profiles are observed for polypyrrole doped with all surfactant chains with a slope of ~-4 in the low q region of SANS, indicating a very smooth surface. The SANS profiles can be further transformed into Porod plot in Figure 6.8 (b), which can be used to calculate the specific surface area of the samples using Porod equation as below.

$$\lim_{q\to\infty}[I(q)\cdot q^4] = 2\pi(\Delta\rho)^2\Sigma \qquad (6.1)$$

Where $\Delta\rho$ is the scattering length density between polymer and solvents and Σ is surface area per volume [m^{-1}], which can be converted to specific surface area, S_v, [m^2/g] by knowing density ρ_m and volume fraction φ of polymer particles.

$$S_v = \frac{\Sigma}{\rho_m \cdot \varphi} \qquad (6.2)$$

Surface area directly reflects the area of sites that are available for electrochemical reactions. High surface area is desirable for high storage capacity devices. It is clear in the Porod plot that surface area for AOT is smaller than those of DS and DBS doped polymers. This is consistent with what was observed in the SEM images in Figure 6.7 that smaller particles result in larger surface areas.

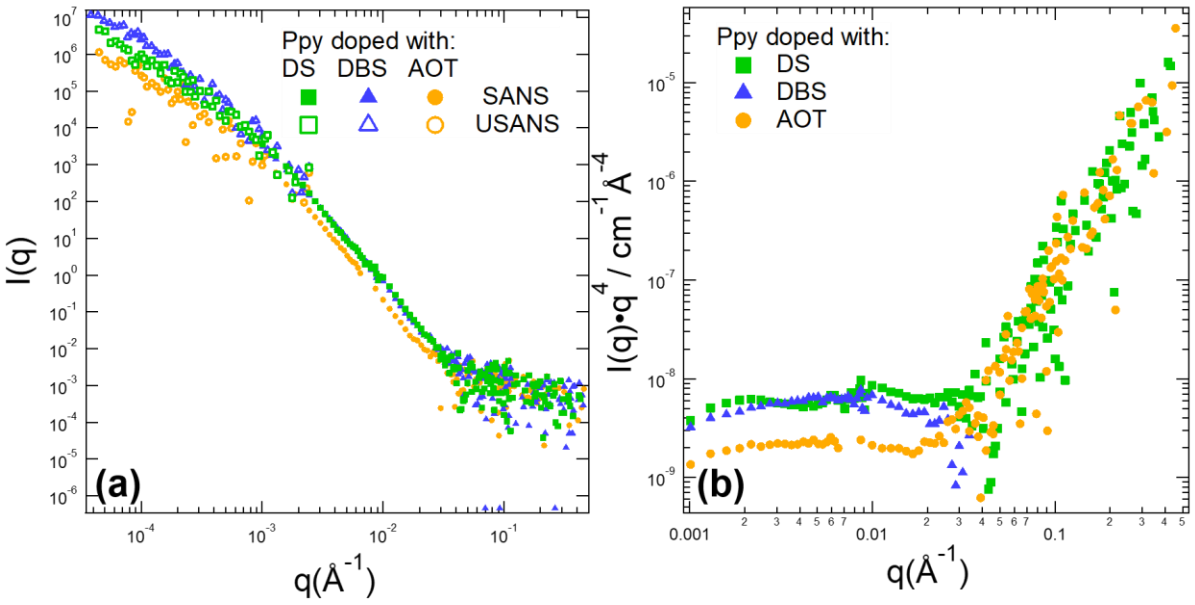

Figure 6.8. (a) 1-D SANS and USANS profiles of polypyrrole doped with different surfactant groups. (b) Corresponding Porod plot of the SANS profile to extrapolate specific surface area.

Another alternative way to obtain surface area is using BET measurement. The polymers are dried and purged overnight with nitrogen to remove the residue water and solvent molecules that are

trapped in small pores within the polymer particles. The surface areas obtained from BET is smaller those from SANS.

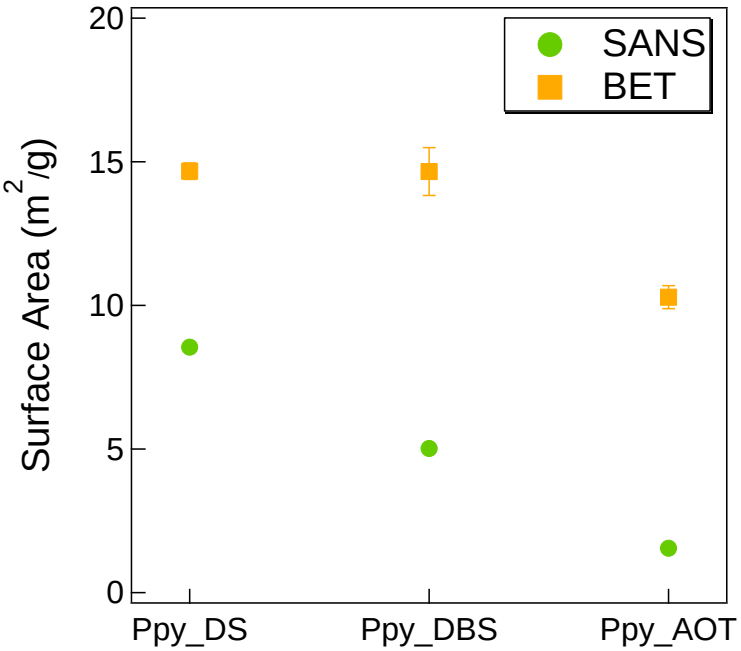

Figure 6.9. Comparison of specific surface areas obtained from BET measurement and Porod plot of SANS profile. Three measurements are conducted for each polymer sample to calculate the standard deviation.

Small angle x-ray scattering is also used to characterize polypyrrole and PDEOT powder doped with different surfactant groups, shown in Figure 6.10. The dried powder could remove the incoherent background caused by deuterated solvents, since it has been observed that the PEDOT samples prepared in the same manner show crystalline peaks at high q region.[27] It is important to note that the contrast of SANS comes from the hydrogen in the side chain groups of the dopants, whereas SAXS is more sensitive to the head groups in the dopant. Another important distinction between those two measurements is that SANS is measuring the polymer dispersion in organic solutions, whereas SAXS probes the solid-state phase in our experiment. A smaller slope (~-2) is

observed in DBS doped Ppy, whereas the slopes for AOT and DS doped polymer exhibit slope of -3. This could be because the DBS doped polymer has a 2-D fractal structure. In contrast, DS and AOT doped polymers have more branched 3-D structures. In other words, this indicates that the powder formed by AOT and DS doped Ppy are more densely packed. In comparison, all the PEDOT samples exhibit similar slopes at low q as that of Ppy: DBS. The difference is that a hump is observed for all PEDOT samples at ~ 0.2 $Å^{-1}$. Those peaks are at similar locations as that of the metallic salt complex in Figure 6.2 (b). Those peaks probably come from the surfactant dopant on the polymer backbone. This indicates that the dopant in the PEDOT samples possess a stronger interaction with the backbone. They can be easily associated with the polymer, but hard to lose during the iron salt wash step. At the high q region, DS and DBS doped PEDOT samples show well defined peaks, whereas AOT samples exhibit a broad peak at the same position. This phenomena has been observed and reported by de la Iglesia et al..[27] The differences in the peak shape and sharpness are probably coming from the variation in the batch synthesis. The peaks at high q are attributed to the stacking of polymer chains, which probably form lamellar structure. The large size and branched shape of AOT group may provide steric hindrance of effective packing of polymer chains.

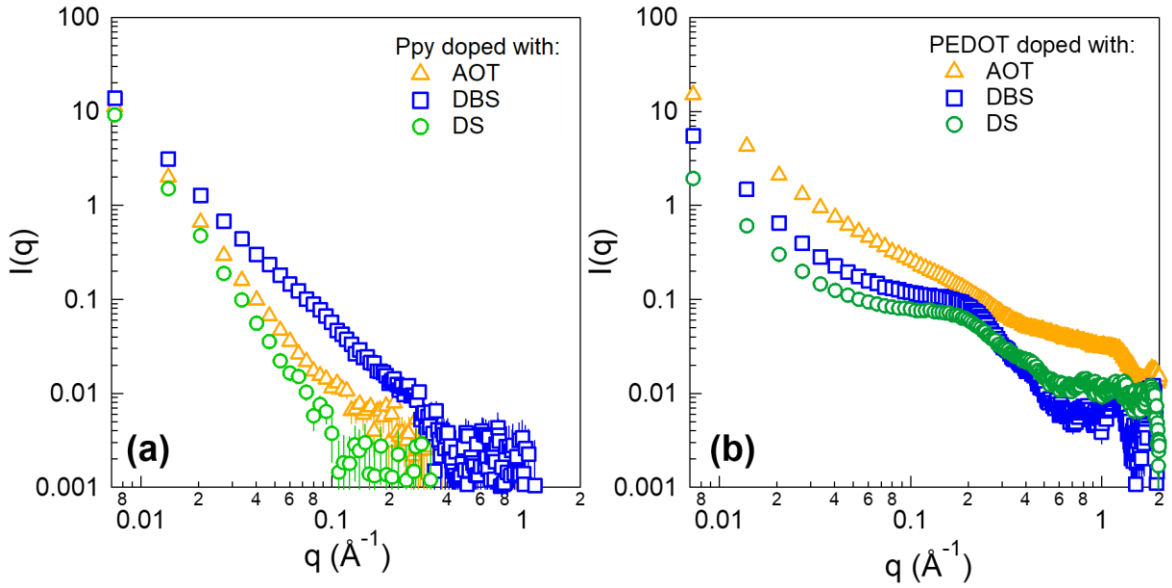

Figure 6.10. SAXS profile of (a) Polypyrrole and (b) PEDOT doped with different surfactant groups. The samples are solid powder films.

The above microscopy and scattering characterizations provide insights into the shape, packing, as well as the surface areas of the polymers. It is still important to explore the electrochemical properties in order to be used for battery applications. Figure 6.11 shows the CV curves of both PEDOT and polypyrrole doped with different surfactant groups. Compare to Ppy, PEDOT has better defined oxidation and reduction peaks. The potential difference between oxidation and reduction peaks are small, indicating the redox couple are quasi-reversible. Two oxidation and reduction peaks are observed for all three conjugated polymers with different dopants. DS and AOT doped PEDOT have well defined redox peaks and closer located oxidation and reduction peaks. By tuning the dopant used, the electrochemical properties can be changed. In contrast, Ppy shows well defined reduction peaks, however, DS and AOT doped polymers do not exhibit

oxidation peaks. It is important to note that the polymer samples do not exhibit as much dissolution issue into electrolytes as compared to organometallic salt samples, which can be attributed to both the better adhesion on substrates of polymers and stable oxidation and reduction species that is insoluble in propylene carbonate.

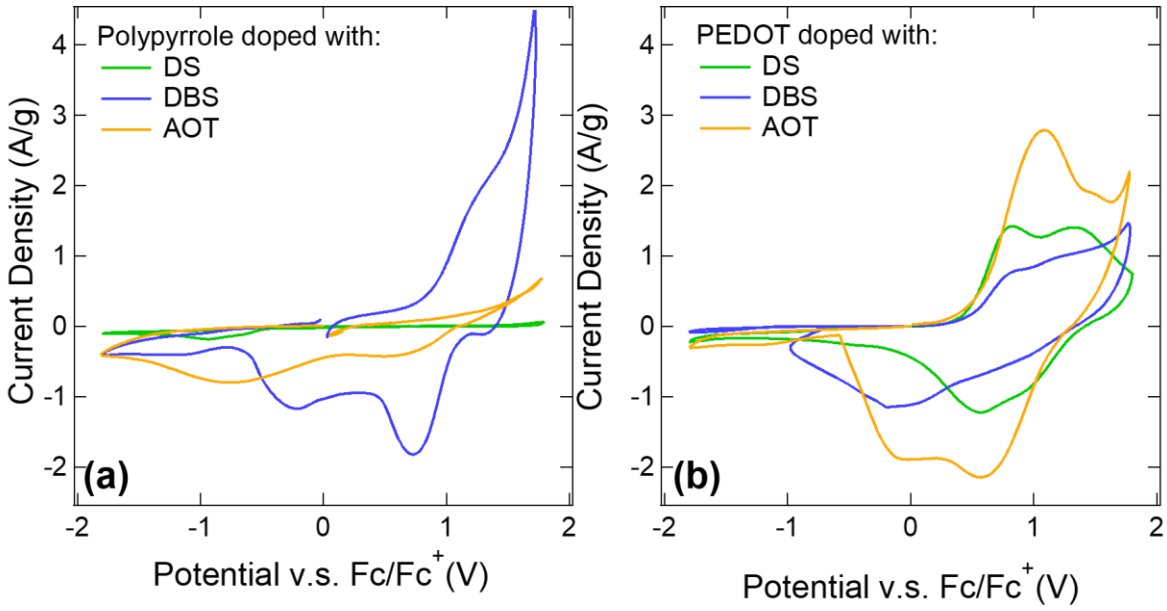

Figure 6.11. Cyclic voltammetry of DS, DBS, and AOT doped (a) polypyrrole and (b) PEDOT conjugated polymers in propylene carbonate solutions. The curves were taken after five sweeps.

Another advantage of conjugated polymer samples is that they are much more conductive than organometallic salts per unit mass (Figure 6.1). This is one of the general merits of polymers that they are both conductive and light weight. As a result, they have a strong potential to be used as batteries with large specific capacity. Due to the conductive and redox active nature, as well as the high stability, it is possible to use conjugated polymers to replace carbon black and binder in a battery. PEDOT: DBS was mixed with $V(DBS)_3$ at 1:1 mass ratio for cyclic voltammetry measurement in Figure 6.12 (a) and (d). The measurements were conducted for 30 cycles to test

the repeatability and stability. For vanadium salt complex, the CV curves finally disappeared due to irreversible chemical reactions or dissolution of certain oxidation state. DBSA was added into the electrolyte solution to enhance the diffusion of DBS chains to the vicinity of the electrode, thus lower the energy barrier for reforming organometallic complexes during oxidation. The increase in concentration of DBS does not solve the dissolution problem, even with up to 0.5 M concentration (Figure 6.12 (b) and (c)). The potential difference between reduction and oxidation peak become smaller after adding DBSA into electrolyte. At 0.5 M DBSA concentration, the current density is dramatically decreased. After mixing with PEDOT the current density is increased, however, the redox curve eventually disappears after the initial five cycles for electrolytes without DBSA (Figure 6.12 (d)). By adding 0.1 M and 0.5 M DBSA into electrolytes, the oxidation and reduction peaks still preserved even after 30 cycles of sweep (Figure 6.12 (e) and (f)). Two well defined oxidation peaks and two reduction peaks exist for the polymer/organometallic salt composite. By comparing the shape to PEDOT samples in Figure 6.11 (b) and Figure 6.12 (a), the double oxidation/reduction peaks are likely due to the vanadium complex. By introducing the conjugated polymer into the system, the potential for each reduction and oxidation was greatly changed. The potential difference also becomes smaller, which is probably due to the more accessibility of DBS chains.

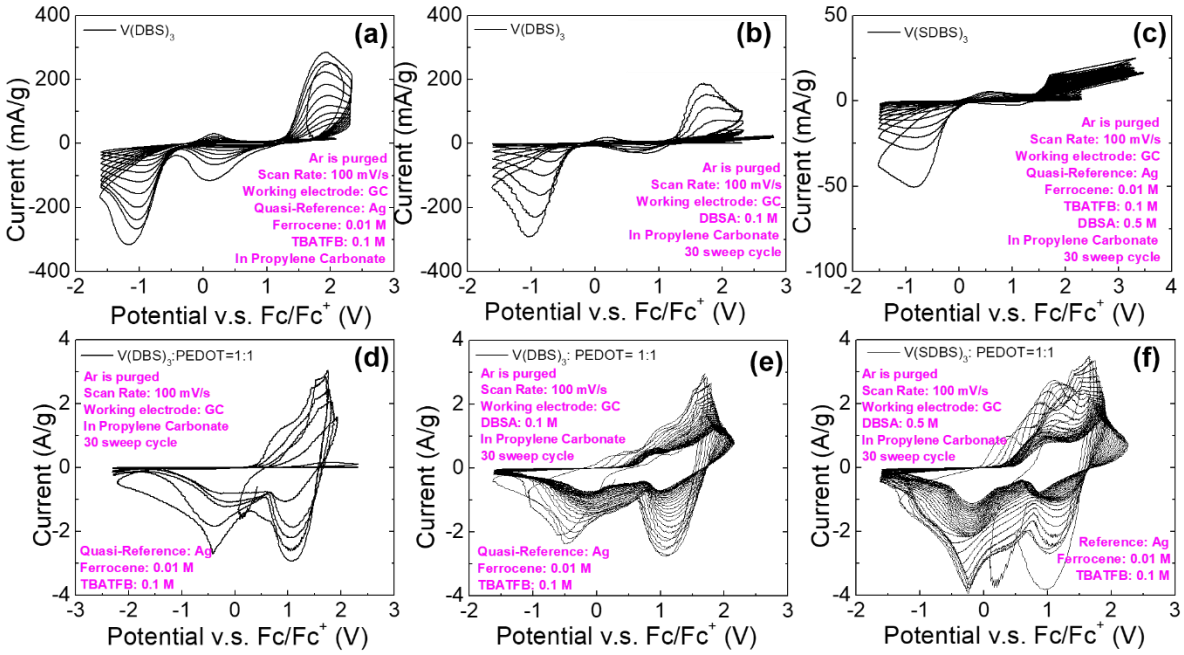

Figure 6.12. (a) (b) (c) are cyclic voltammetry measurements of vanadium salt complex doped with DBS. (d) (e) (f) are vanadium salt complex mixed with PEDOT: DBS with 1:1 mass ratio. (a) and (d) are measured in 0.1 M TBATFB in PC electrolyte. (b) and (e) are with 0.1 M DBSA and 0.1 M TBATFB. (c) and (f) are with increased DBSA concentration (0.5 M) and 0.1 M TBATFB.

After investigating the polymer structure and electrochemical properties, it is important to directly utilize those polymer materials as electrode material of a battery. The mass ratio of polymer to carbon black of 4:1 is used for the cathode formulation. Lithium metal was used as anode material. Figure 6.13 shows the charge and discharge characteristics of Ppy and PEDOT doped with different surfactant groups. The surfactant counterions play a huge role in changing the charge capacity of the electrode materials. This could be the result of a combination of several factors, including surface area, conductivity, interaction strength of dopants and doping concentrations. For both Ppy and PEDOT, the capacity could be above 100 mAh/g. It is interesting to note that the effect of the surfactant group on different polymers varies, which could come from the interactions

between polymer backbone and dopants. Ppy: AOT shows an initial charge capacity of 190 mAh/g and then started to decrease after the third cycle of the process. After five cycles, the capacity was reduced by almost 50% to ~100 mAh/g. The charge and discharge capacity become almost comparable after four cycles. For PEDOT: DS samples, the degradation was also observed, but to a smaller extent. It also starts with a capacity close to 200 mAh/g. After five cycles, the capacity reduces to ~ 150 mAh/g. Other than those two combinations for Ppy and PEDOT, other surfactant groups exhibit relatively low capacity of at ~ 50 mAh/g. However, for those low capacity materials, the cycling performance was better. No obvious degradation shows for 5 cycles. Although there are some problems associated with Ppy and PEDOT electrodes, those materials do show very promising results to be as electrodes. Compared to other published work of using conjugated polymers as electrodes, the capacity demonstrated here is among the high end of those polymers, which is typically at around 80 mAh/g. [20,33,34]

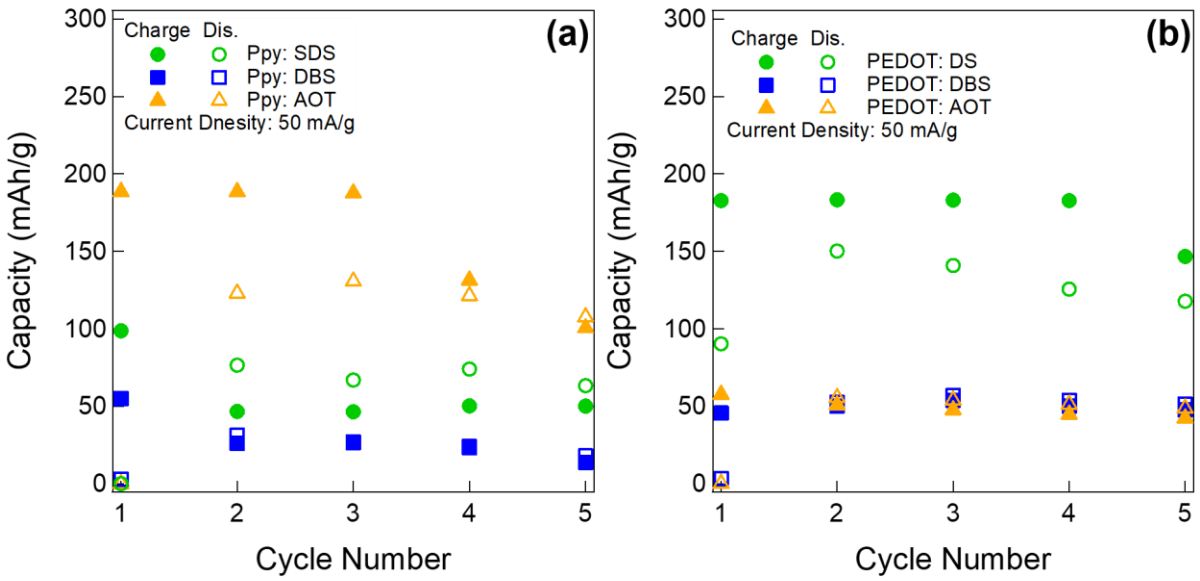

Figure 6.13. Charge-Discharge characteristics of (a) PEDOT and (b) Ppy doped with different surfactant chains measured in half battery cell by using Lithium metal as anodes for five cycles. 50 mA/g was used as the current density for charge and discharge the battery.

PEDOT and Ppy are promising as electrode materials for their high charge storage capacity and large tuning freedom. However, all the batteries above were prepared in a conventional way that is hard to scale up. In order to further take advantage of the solvent processability of polymers, the possibility of using them for printable battery applications is explored. Figure 6.14 (a) and (b) show the well dispersed polymer solutions in chloroform. The polymer concentrations are 15 mg/ml and can be readily dispersed into solutions under a short period of sonication. The solution can be spray coated on virtually all substrates. Aluminum, typically used as a current collector, is utilized as an example in Figure 6.14 (c) and (d). Uniform films can be prepared by spray printing of the film without inducing visible cracks on the films.

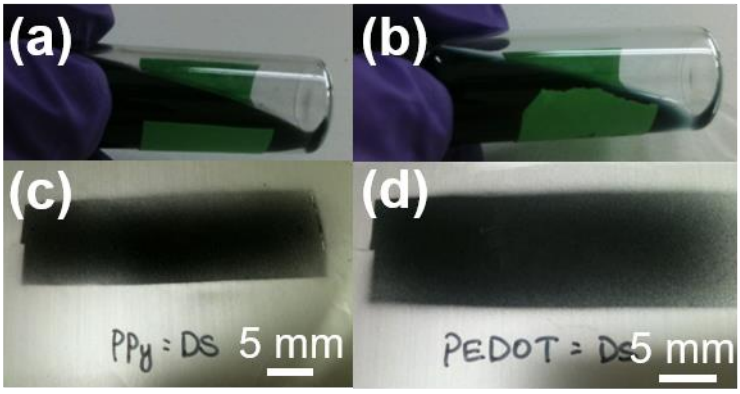

Figure 6.14. Optical microscopic images of 15 mg/ml (a) Ppy: DS and (b) PEDOT: DS dispersed in chloroform. (c) Ppy: DS and (d) PEDOT: DS films spray coated on to aluminum foil substrates.

The printed PEDOT film on aluminum foil is then assembled into a coin battery with lithium metal as anode. Based on the data shown in Figure 6.13, PEDOT: DS shows the highest capacity of all the three dopants, which was chosed as the model system for printed films. When PEDOT: DS was used as the only electrode material, a very low capacity was observed (less than 10 mAh/g in Figure 6.15 (a) and (d)). It was postulated that the low capacity was because of the low conductivity in the electrodes. Consequently, 20% mass ratio of carbon black was mixed with PEDOT: DS to form a stable dispersion before coating them into film. In Figure 6.15 (b) and (e), a dramatic enhancement to above 40 mAh/g was observed with the addition of carbon black. Five batteries were averaged to obtain the error bars. To validate that the improvement is purely due to the charge storage of PEDOT polymers, pure carbon black was spray coated onto aluminum substrate and the battery performance was shown in Figure 6.15 (c) and (f). The carbon black only sample shows a capacity below 10 mAh/g. It is clear that the improvement of capacity was because of more charge transport paths and the improved capacity was from PEDOT: DS. It is important to admit that

compared to the polymers prepared in the traditional way, the spray coated film exhibits lower capacity for the same material. Further engineering of the spray coating process can be controlled to improve the charge capacity. Also, it is necessary to investigate the polymers doped with different surfactant groups using spray coating to obtain a full spectrum of how the polymer films perform.

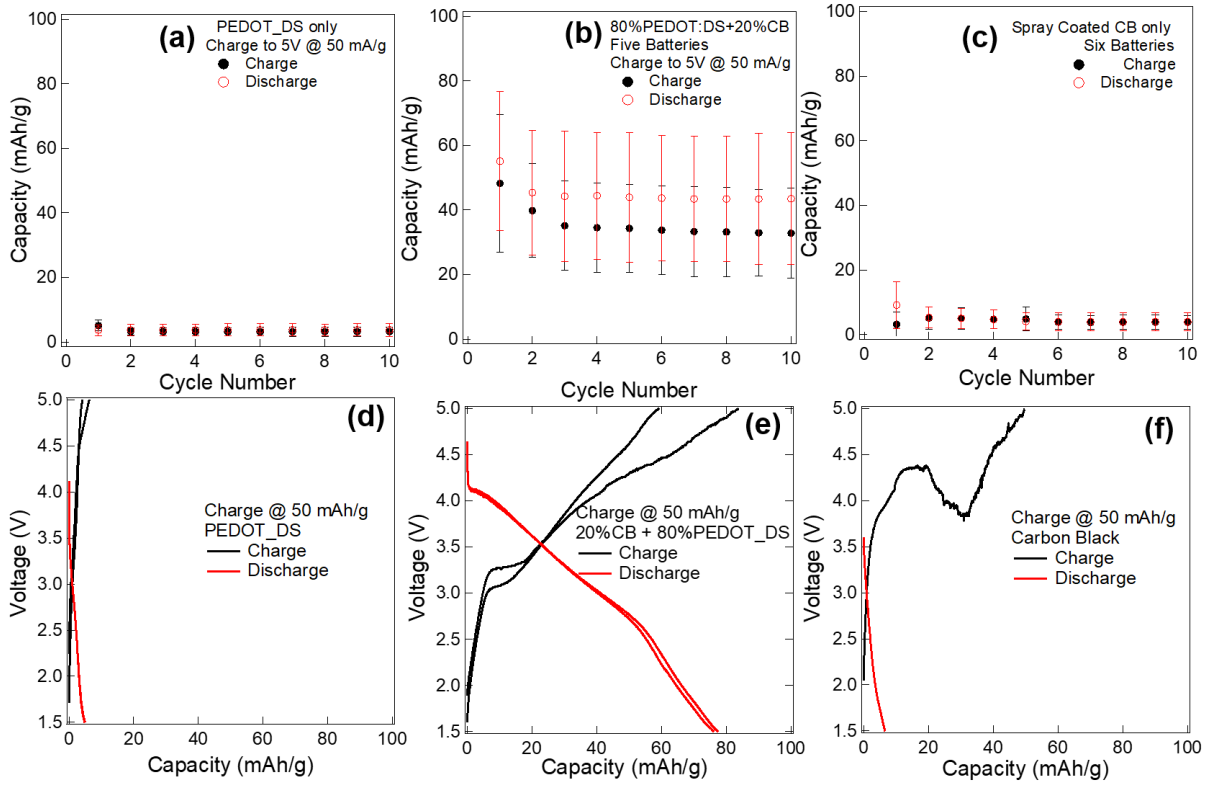

Figure 6.15. (a) (b) (c) Battery cyclic performance and (d) (e) (f) charge discharge curves of batteries prepared from spray coating film. (a) and (d) are films with only PEDOT: DS. (b) and (e) correspond to carbon black spray coated films. (c) and (f) are mixing PEDOT: DS with carbon black at 4: 1 mass ratio. The error bars in the battery cyclic performance curves come from the number of batteries specify in the legend of each condition.

To gain more insights of the differences between spray coated and powder films. Small angle x-ray scattering was utilized as tool to probe the chain packings by using a transmission mode. The powder films were sandwiched between two pieces of thin glass (75 μm thick) in a static cell. The spray coated films were directly coated on the thin glass. The glass background was subtracted from the sample scattering intensity. For DS and AOT doped Ppy, not much difference was observed of the spray coated film v.s. the powder films. A slight difference exists for Ppy: DBS films. At mid-q region (0.03 ~0.2 $Å^{-1}$), a broad hump appears for spray coated film. Same conclusion can be made that the DBS doped polymer has a shallower slope compare to the other two polymers, indicating a less densely packed film.

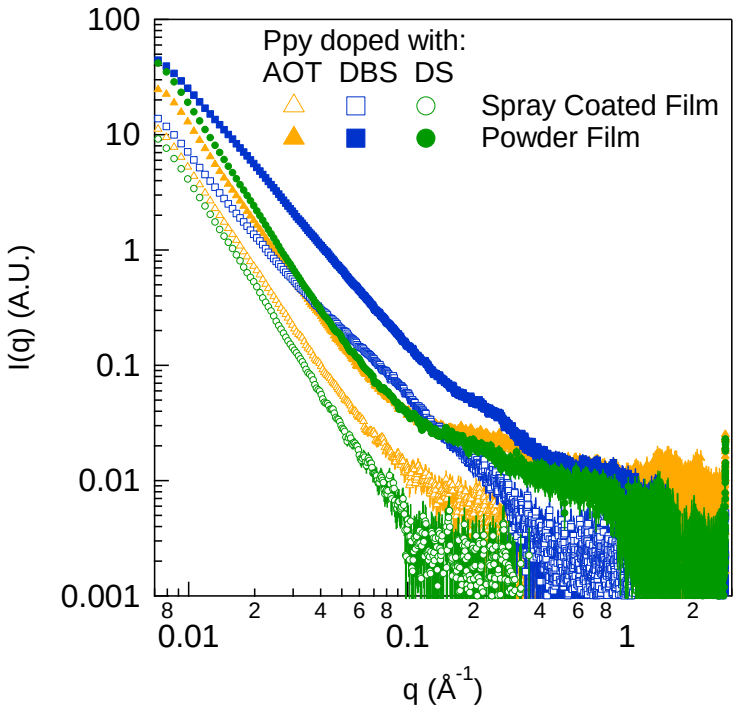

Figure 6.16. Small angle x-ray scattering of films prepared in powder form and spray coated form for the three surfactant groups doped Ppy conjugated polymers. The intensities were not normalized to absolute scale. They remain arbitrary units.

6.4 CONCLUSION AND OUTLOOK

In conclusion, both organometallic salt complex and surfactant group doped conjugated polymers that can be dispersed into organic solvents have been synthesized. The general method has the potential to be used for packing metal ions or polymer chains into apolar solvents. Various metal ions and polymers have been explored as electrode materials for printable battery applications. By simply changing the dopant to the polymer backbone, the surface area and redox behavior can be changed. Their structures were characterized by various techniques, including SEM, SANS, SAXS, and BET measurement. Cyclic voltammetry and coin battery was used to probe the film electrochemical properties. The polymers generally exhibit a specific area of ~ 10 m^2/g and the charge capacity can be up to 150 mAh/g, which is higher than most of the reported polymers of the same kind. It is demonstrated that conjugated polymer synthesized through reactivation chain polymerization has a strong potential to be used as printable battery electrodes.

To further enhance the charge capacity, the synthesis method could be modified to improve the conductivity and eliminate side reactions. It has been reported that using larger amount of oxidant (iron to monomer ratio) could result in enhanced conductivity. [19] Similar trend has also been observed in the PEDOT polymer we synthesized (Figure 6.17) that oxidant to monomer ratio above 2 leads to an increase in the conductivity. During the polymerization step, the organic side chains are doped on the polymer backbone. The dopant is necessary for achieving high conductivity, at the same time, they help polymers to disperse well in organic solvents. Another important factor that could lead to a better quality of the synthesized polymer is that the synthesize can be conducted in a glove box to remove water and oxygen that may lead to side product or terminate the activation sites during polymerization. What is more, the iron salt complex can also be changed to stronger

oxidant. Richards et al. and coworkers utilized sodium persulfate as oxidant and iron salt as catalyst, a DC conductivity of 100 S/m was obtained. [28]

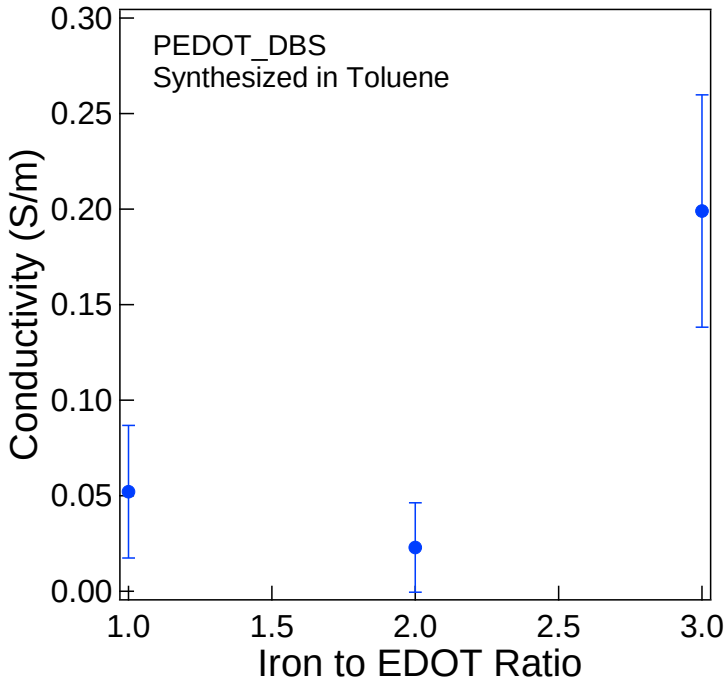

Figure 6.17. Conductivity of $Fe(DBS)_3$ salt complex synthesized under different iron to EDOT

Other than revising the synthesis procedure, other monomers could be selected for electrode materials, which could provide more choices for redox potential or charge capacity. For example, polyaniline shows a theoretical capacity of close to 300 mAh/g, which also follows a reactivation chain polymerization mechanism. [20,31,35] What is more interesting is that polyaniline film can be doped with the counterions from different acids, thus changing the redox states. [36] Thus the doping could be achieved either during the polymerization, as what was shown for Ppy and PEDOT, or after the polymerization when then form a film. Since the surfactant chains has their corresponding

acid form (DBSA is the acid form of SDBS), it would be interesting to explore how the acid change the redox states of polyaniline that can be dispersed into organic solvents.

6.5 REFERENCES

(1) Muccini, M. A Bright Future for Organic Field-Effect Transistors. *Nat. Mater.* **2006**, *5* (8), 605–613 DOI: 10.1038/nmat1699.

(2) Kaltenbrunner, M.; White, M. S.; Głowacki, E. D.; Sekitani, T.; Someya, T.; Sariciftci, N. S.; Bauer, S. Ultrathin and Lightweight Organic Solar Cells with High Flexibility. *Nat. Commun.* **2012**, *3* (1), 770 DOI: 10.1038/ncomms1772.

(3) Jose da Silva, W.; Kim, H. P.; Rashid bin Mohd Yusoff, A.; Jang, J. Transparent Flexible Organic Solar Cells with 6.87% Efficiency Manufactured by an All-Solution Process. *Nanoscale* **2013**, *5* (19), 9324 DOI: 10.1039/c3nr03011c.

(4) Lipomi, D. J.; Bao, Z. Stretchable, Elastic Materials and Devices for Solar Energy Conversion. *Energy Environ. Sci.* **2011**, *4* (9), 3314 DOI: 10.1039/c1ee01881g.

(5) Hu, L.; Li, J.; Liu, J.; Grüner, G.; Marks, T. Flexible Organic Light-Emitting Diodes with Transparent Carbon Nanotube Electrodes: Problems and Solutions. *Nanotechnology* **2010**, *21* (15), 155202 DOI: 10.1088/0957-4484/21/15/155202.

(6) Simon, D. T.; Gabrielsson, E. O.; Tybrandt, K.; Berggren, M. Organic Bioelectronics: Bridging the Signaling Gap between Biology and Technology. *Chem. Rev.* **2016**, *116* (21), 13009–13041 DOI: 10.1021/acs.chemrev.6b00146.

(7) Zou, Z.; Zhu, C.; Li, Y.; Lei, X.; Zhang, W.; Xiao, J. Rehealable, Fully Recyclable, and Malleable Electronic Skin Enabled by Dynamic Covalent Thermoset Nanocomposite. *Sci.*

Adv. **2018**, *4* (2), eaaq0508 DOI: 10.1126/sciadv.aaq0508.

(8) Singh, N.; Galande, C.; Miranda, A.; Mathkar, A.; Gao, W.; Reddy, A. L. M.; Vlad, A.; Ajayan, P. M. Paintable Battery. *Sci. Rep.* **2012**, *2*, 6–10 DOI: 10.1038/srep00481.

(9) Zamarayeva, A. M.; Ostfeld, A. E.; Wang, M.; Duey, J. K.; Deckman, I.; Lechêne, B. P.; Davies, G.; Steingart, D. A.; Arias, A. C. Flexible and Stretchable Power Sources for Wearable Electronics. *Sci. Adv.* **2017**, *3* (6), e1602051 DOI: 10.1126/sciadv.1602051.

(10) Lee, M.; Hong, J.; Lopez, J.; Sun, Y.; Feng, D.; Lim, K.; Chueh, W. C.; Toney, M. F.; Cui, Y.; Bao, Z. High-Performance Sodium-Organic Battery by Realizing Four-Sodium Storage in Disodium Rhodizonate. *Nat. Energy* **2017**, *2* (11), 861–868 DOI: 10.1038/s41560-017-0014-y.

(11) Li, S.; Xu, Q.; Uchaker, E.; Cao, X.; Cao, G. Comparison of Amorphous, Pseudohexagonal and Orthorhombic Nb_2O_5 for High-Rate Lithium Ion Insertion. *CrystEngComm* **2016**, *18* (14), 2532–2540 DOI: 10.1039/C5CE02069G.

(12) Abbel, R.; De Vries, I.; Langen, A.; Kirchner, G.; T'Mannetje, H.; Gorter, H.; Wilson, J.; Groen, P. Toward High Volume Solution Based Roll-to-Roll Processing of OLEDs. *J. Mater. Res.* **2017**, *32* (12), 2219–2229 DOI: 10.1557/jmr.2017.204.

(13) Søndergaard, R.; Hösel, M.; Angmo, D.; Larsen-olsen, T. T.; Krebs, F. C. Roll-to-Roll Fabrication of Polymer Solar Cells As the Performance in Terms of Power Conversion Efficiency and Operational. *Mater. Today* **2012**, *15* (1–2), 36–49 DOI: 10.1016/S1369-7021(12)70019-6.

(14) Ho, C. C.; Evans, J. W.; Wright, P. K. Direct Write Dispenser Printing of a Zinc

Microbattery with an Ionic Liquid Gel Electrolyte. *J. Micromechanics Microengineering* **2010**, *20* (10), 104009 DOI: 10.1088/0960-1317/20/10/104009.

(15) Kumar, R.; Shin, J.; Yin, L.; You, J.-M.; Meng, Y. S.; Wang, J. All-Printed, Stretchable Zn-Ag 2 O Rechargeable Battery via Hyperelastic Binder for Self-Powering Wearable Electronics. *Adv. Energy Mater.* **2017**, *7* (8), 1602096 DOI: 10.1002/aenm.201602096.

(16) Gaikwad, A. M.; Steingart, D. A.; Nga Ng, T.; Schwartz, D. E.; Whiting, G. L. A Flexible High Potential Printed Battery for Powering Printed Electronics. *Appl. Phys. Lett.* **2013**, *102* (23) DOI: 10.1063/1.4810974.

(17) Sun, K.; Wei, T. S.; Ahn, B. Y.; Seo, J. Y.; Dillon, S. J.; Lewis, J. A. 3D Printing of Interdigitated Li-Ion Microbattery Architectures. *Adv. Mater.* **2013**, *25* (33), 4539–4543 DOI: 10.1002/adma.201301036.

(18) Lin, M. C.; Gong, M.; Lu, B.; Wu, Y.; Wang, D. Y.; Guan, M.; Angell, M.; Chen, C.; Yang, J.; Hwang, B. J.; Dai, H. An Ultrafast Rechargeable Aluminium-Ion Battery. *Nature* **2015**, *520* (7547), 325–328 DOI: 10.1038/nature14340.

(19) Charba, A.; Mumtaz, M.; Brochon, C.; Cramail, H.; Hadziioannou, G.; Cloutet, E. Preparation of Water-Free PEDOT Dispersions in the Presence of Reactive Polyisoprene Stabilizers. *Langmuir* **2014**, *30* (42), 12474–12482 DOI: 10.1021/la502480r.

(20) Mike, J. F.; Lutkenhaus, J. L. Recent Advances in Conjugated Polymer Energy Storage. *J. Polym. Sci. Part B Polym. Phys.* **2013**, *51* (7), 468–480 DOI: 10.1002/polb.23256.

(21) Kim, J.; Park, H.-S.; Kim, T.-H.; Yeol Kim, S.; Song, H.-K. An Inter-Tangled Network of Redox-Active and Conducting Polymers as a Cathode for Ultrafast Rechargeable Batteries.

Phys. Chem. Chem. Phys. **2014**, *16* (11), 5295 DOI: 10.1039/c3cp54624a.

(22) Das, P. R.; Komsiyska, L.; Osters, O.; Wittstock, G. PEDOT: PSS as a Functional Binder for Cathodes in Lithium Ion Batteries. *J. Electrochem. Soc.* **2015**, *162* (4), A674–A678 DOI: 10.1149/2.0581504jes.

(23) Shao, L.; Jeon, J. W.; Lutkenhaus, J. L. Polyaniline/Vanadium Pentoxide Layer-by-Layer Electrodes for Energy Storage. *Chem. Mater.* **2012**, *24* (1), 181–189 DOI: 10.1021/cm202774n.

(24) Tamura, K.; Akutagawa, N.; Satoh, M.; Wada, J.; Masuda, T. Charge/Discharge Properties of Organometallic Batteries Fabricated with Ferrocene-Containing Polymers. *Macromol. Rapid Commun.* **2008**, *29* (24), 1944–1949 DOI: 10.1002/marc.200800526.

(25) Michor, E. L.; Berg, J. C. The Particle Charging Behavior of Ion-Exchanged Surfactants in Apolar Media. *Colloids Surfaces A Physicochem. Eng. Asp.* **2017**, *512*, 1–6 DOI: 10.1016/j.colsurfa.2016.10.032.

(26) De La Iglesia, P.; Jaeger, V. W.; Xi, Y.; Pfaendtner, J.; Pozzo, L. D. Structure Characterization and Properties of Metal-Surfactant Complexes Dispersed in Organic Solvents. *Langmuir* **2015**, *31* (33), 9006–9016 DOI: 10.1021/acs.langmuir.5b02071.

(27) Pablo, de la I. Structure-Property Relationships of SelfAssembled Conjugated Polymers, University of Washington, 2015.

(28) Richards, J. J.; Scherbarth, A. D.; Wagner, N. J.; Butler, P. D. Mixed Ionic/Electronic Conducting Surface Layers Adsorbed on Colloidal Silica for Flow Battery Applications. *ACS Appl. Mater. Interfaces* **2016**, *8* (36), 24089–24096 DOI: 10.1021/acsami.6b07372.

(29) Kline, S. R. Reduction and Analysis of SANS and USANS Data Using IGOR Pro. *J. Appl. Crystallogr.* **2006**, *39* (6), 895–900 DOI: 10.1107/S0021889806035059.

(30) Dale A. C. Brownson, C. E. B. *The Handbook of Graphene Electrochemistry*; 2014.

(31) George, O. *Principles of Polymerization*; John Wiley & Sons, Inc., 2004.

(32) Bhattacharyya, D.; Howden, R. M.; Borrelli, D. C.; Gleason, K. K. Vapor Phase Oxidative Synthesis of Conjugated Polymers and Applications. *J. Polym. Sci. Part B Polym. Phys.* **2012**, *50* (19), 1329–1351 DOI: 10.1002/polb.23138.

(33) Qie, L.; Yuan, L.-X.; Zhang, W.-X.; Chen, W.-M.; Huang, Y.-H. Revisit of Polypyrrole as Cathode Material for Lithium-Ion Battery. *J. Electrochem. Soc.* **2012**, *159* (10), A1624–A1629 DOI: 10.1149/2.042210jes.

(34) Song, H. K.; Palmore, G. T. R. Redox-Active Polypyrrole: Toward Polymer-Based Batteries. *Adv. Mater.* **2006**, *18* (13), 1764–1768 DOI: 10.1002/adma.200600375.

(35) Song, Z.; Zhou, H. Towards Sustainable and Versatile Energy Storage Devices: An Overview of Organic Electrode Materials. *Energy Environ. Sci.* **2013**, *6* (8), 2280 DOI: 10.1039/c3ee40709h.

(36) Hatchett, D. W.; Josowicz, M.; Janata, J. Acid Doping of Polyaniline: Spectroscopic and Electrochemical Studies. *J. Phys. Chem. B* **1999**, *103* (50), 10992–10998 DOI: 10.1021/jp991110z.

Chapter 7. Redox active materials for flow battery applications

7.1 INTRODUCTION AND MOTIVATION

Nowadays, climate change caused by harmful greenhouse gases (GHGs) emission has drew increased attention from all over the globe. [1] A lot of evidences are shown during this rapid change in the past century, including sea level rising because of the melting of glaciers, temperature increase, and water acidification due to the dissolution of the emitted carbon dioxide. [1] Those changes have been linked to the fossil fuel production and consumption, which accounts for 90% use of all the energy sources. [1,2] In order to mitigate the environmental problem and achieve sustainable development, renewable energy sources, such as solar energy, wind, biomass, and hydropower have spurred a lot research to convert all energy sources to electricity in order to face climate change. [2] However, the harvesting of renewable energy sources are often lack of consistency, which cannot be used as a reliable source for consumption. [3] On the other hand, the energy demand during the day is largely dependent on the time. Because of this variation, the peak time of energy generation may not necessarily match with that of the energy consumption. It is, therefore, important to develop energy storage systems that can collect the intermittent energy sources and serve as stable output to users. [4]

Redox flow battery is a great candidate that can be used to store electricity in a large scale. It consists of two tanks of redox active materials in liquid and is separated by a membrane that only allow certain ions or charges passing through. Its capacity depends on the amount of active species stored in the tank and can be easily scaled up to lower the cost. Redox flow battery has been considered as a promising candidate to achieve the target set by Department of Energy (DoE) to reduce the cost of energy to \$100 $(kWh)^{-1}$ by 2023. [4] So far, many redox active species have been

recognized, including organometallic ions that can be dispersed in organic solvents and small organic molecules that are economical. In this work, both the organometallic salt complex synthesized by the method described in Chapter 6 and small molecular species will be presented as candidates for redox flow batteries.

The major advantage of flow battery in organic solutions is that a wider potential window can be achieved compared to aqueous flow batteries. It can also work at elevated temperatures and possess high energy and power density. [5] Many metal ion species have been found to be dispersible and redox active in organic solvent, such as iron, vanadium, chromium, cobalt, and cerium. [3–8] Typically, those metal ions are packed into organic solvents by forming organometallic complex with organic chains to help metal ions forming stable dispersion. Due to the high potential window, a cell open circuit potential of above 2V can be achieved. Liu et al. demonstrated an open cell potential of 3.4V for vanadium battery. [4,5] In most of the papers, a relatively polar solvent (acetonitrile) is usually used to disperse the organometallic complex. It is important to note that by changing the organic side chains of the complex, or the solvent it is used, the structure of the dispersed structures can be tuned. [9,10] The complexes can form rod-like structures or micelles, which are important for flow batteries applications, since the active species are the metal core and the shell of organic chains are electrically insulating.

7.2 EXPERIMENTAL

7.2.1 *Materials*

All chemicals and solvents were used as received. Sodium dodecyl sulfate (98%), Dioctyl sulfosuccinate sodium salt (AOT, 97%), Sodium dodecylbenzenesulfonate (SDBS, technical

grade), iron (III) chloride (97%), aluminum chloride hexahydrate, vanadium (III) chloride (97%), and cobalt (II) chloride (97%) were obtained from Sigma Aldrich (St Louis, MO). Toluene (99.9%), chloroform (99.9%), acetone (99.7%), methanol (99.9%), propylene carbonate (99.7%), and 2-proponal (99.9%) were purchased from Fisher Scientific (Hampton, NH). Ferrocene (Fc) and tetrahexylammonium bromide (THABr) were purchased from Sigma Aldrich and used as received.

7.2.2 *Cyclic voltammetry*

The Cyclic voltammetry (CV) measurement is performed on Gamry potentiostat (Reference 600, Warminster, PA). Glassy carbon is used as working electrode and a platinum wire is used as counter electrode. A quasi reference electrode is assembled by immerging silver wire into a solution that dissolves 0.1 M ferrocene and 0.1 M supporting electrolytes (THABr). The same solvent that dissolves the analytes is used prepare the quasi reference electrode, unless otherwise mentioned. All the electrodes are purchased from BASi (West Lafayette, IN). The characterization is performed using 3-electrode mode with a C-3 cell stand (BASi) that is capable of stirring and purge argon gas into the solution, as well as screening out signal noise originates from electrical interference with a Faraday cage.

7.3 RESULTS & DISCUSSIONS

Dispersing metal ions into organic solvents can not only benefit electronic device fabrication, since water is eliminated from the process, it is also very useful in obtaining active materials that can be used in flow batteries. This is because the organic solvents usually provide a wide potential window for the batteries to operate, [11] which potentially enhances the charge capacity. At the same time, however, it remains difficult to disperse large amount of metal ions into organic solvent. As a result, the organometallic salt complexes that are previous described as active materials for solid-

sate batteries, are once again explored as candidates for use in organic flow batteries. The cyclic voltammetry measurement was used as a major characterization tool to measure the electrochemical activity. The salt complexes were dispersed in methanol and the CV characteristics are shown in Figure 7.1. All the measurements were repeated for ten cycles to demonstrate reversibility. Three different metal ions, including vanadium, iron, and cobalt, doped with different surfactants are all tested. In methanol, all the metal complexes are electrochemically active. The vanadium complexes show two oxidation peaks (~0.2V and ~1.5V) and two reduction peaks (~0V and ~-1V). By changing the type of the doped surfactant groups, the peak position will be shifted. The shape and current for oxidation and reduction peaks between 0V and 1V are affected the most. This is probably due to the accessibility of metal ions, since they are coated with a shell of insulating surfactants that form spherical micelles. Also, the bonding strength of the metal ions to different surfactant groups can vary. Clear oxidation and reduction peaks are observed in iron complexes as well. Similar to vanadium complexes, the measured redox potentials are affected by the choice of surfactant chains. Their oxidation peaks are located between 0.7 V and 1 V and the reduction peaks are in the range of 0 V and 0.5 V. For both vanadium and iron ions, their DBS doped complexes exhibit the lowest current density, which is probably due to the difference in electrostatic bonding exerted by additional benzene ring in the surfactant chains. The least active complex is cobalt (II) complex, which is shown in Figure 7.1 (c). For the two surfactant groups that are tested, only one oxidation peak is observed between 0 V and 0.5 V. No clear reduction peak presents, which indicates that the oxidation reactions are electrochemically irreversible.

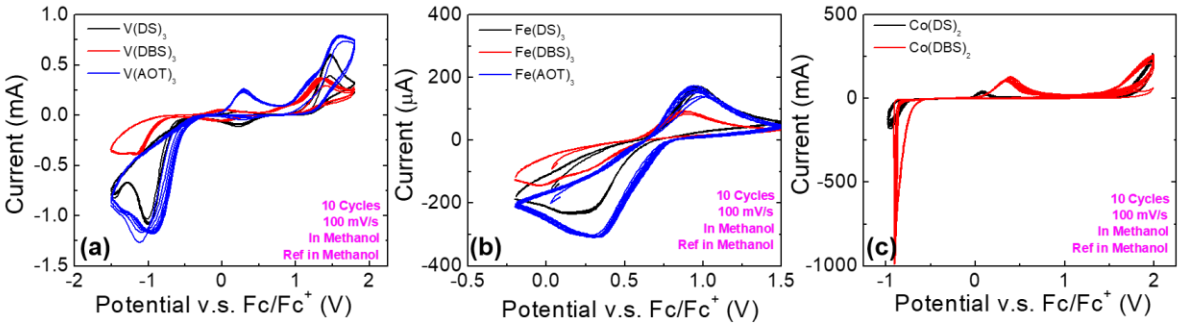

Figure 7.1. Cyclic voltammetry measurement in methanol of (a) vanadium (b) iron and (c) cobalt complex doped with different surfactant chains. A fixed concentration of 50 mM salt complexes is used.

It is found that that it is important to specify the solvent used to prepare quasi reference electrode because it shifts the potential of the measured potential. Figure 7.2 shows the CV curves of the same species at the same concentration, but using quasi electrodes prepared in PC, instead of methanol. Methanol is still the solvent used to disperse organometallic complex. It is clear that for quasi reference electrode prepared using PC as solvent, the electrochemical potential shifts towards higher potential values compared to reference electrodes in methanol. The difference also depends on redox active species and can vary between 0.2 V and 0.5 V.

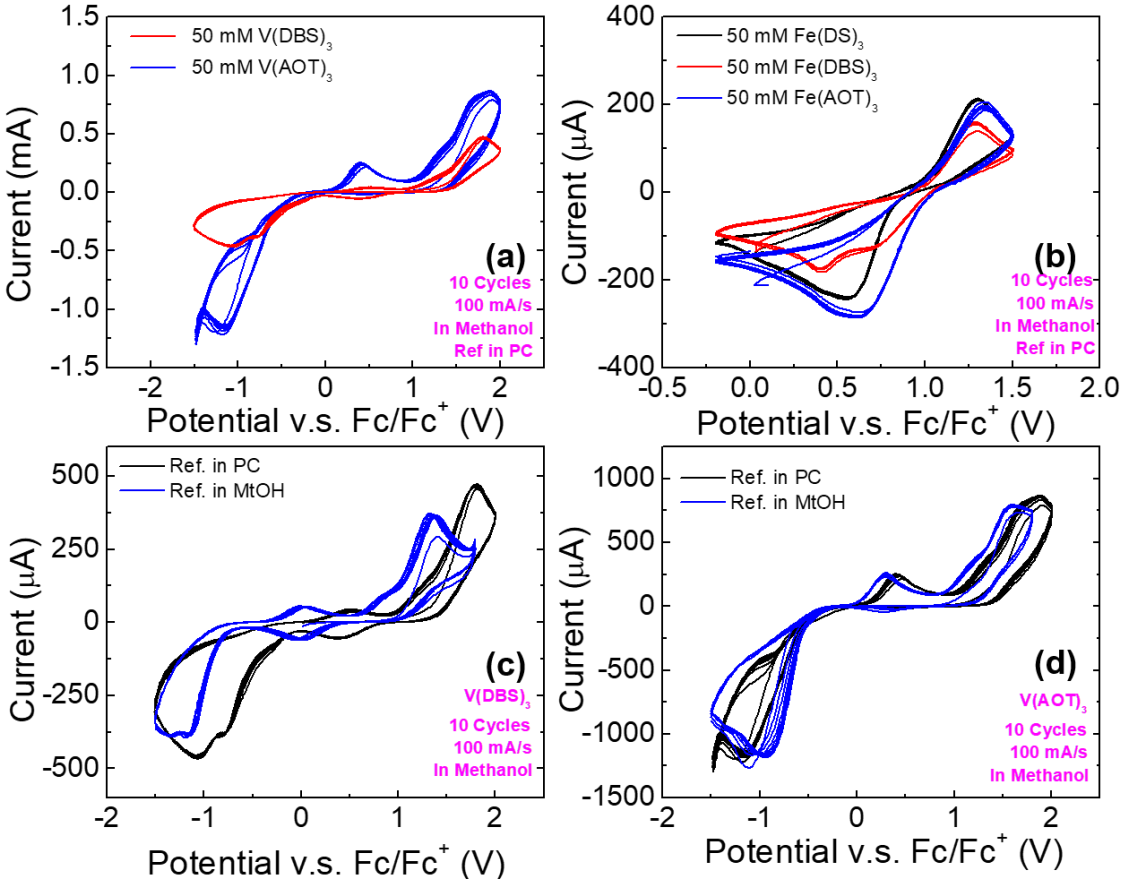

Figure 7.2. Cyclic voltammetry of (a) vanadium and (b) iron salt complexes doped with different surfactants using quasi reference electrodes prepared in propylene carbonate. The comparison of CV curves of (c) vanadium $(DBS)_3$ and (d) vanadium $(AOT)_3$ using reference electrodes prepared in different solvents.

The changing of the solvent can tune the potential window that the batteries are operating. In addition, the structures of the metallic organometallic complexes vary from solvent to solvent. [9,10] it is also important to explore the redox activity of metallic salt complexes in another solvent. Toluene, an apolar solvent, was chosen, which is more difficult to disperse metallic complexes in a large concentration. Figure 7.3 shows CV curves of both vanadium and iron organometallic complex that are dispersed at 50 mM in toluene. One reduction peak is observed for vanadium

complex and no oxidation shows up. In contrast, both oxidation and reduction peaks are presented for iron salt complex, but the oxidation peak is ill-defined. For DBS doped complex, a lower current density and worse redox behavior are observed. Compared to CV curves obtained in methanol, the same species exhibit much less current density and redox potential peaks are not as well-defined. This is probably due to the much larger metal ion core formed in toluene compared to methanol, which makes it difficult to access metal ions by the working electrodes, since more metal ions are clustered in the center that is shielded by insulating surfactant chains. [10]

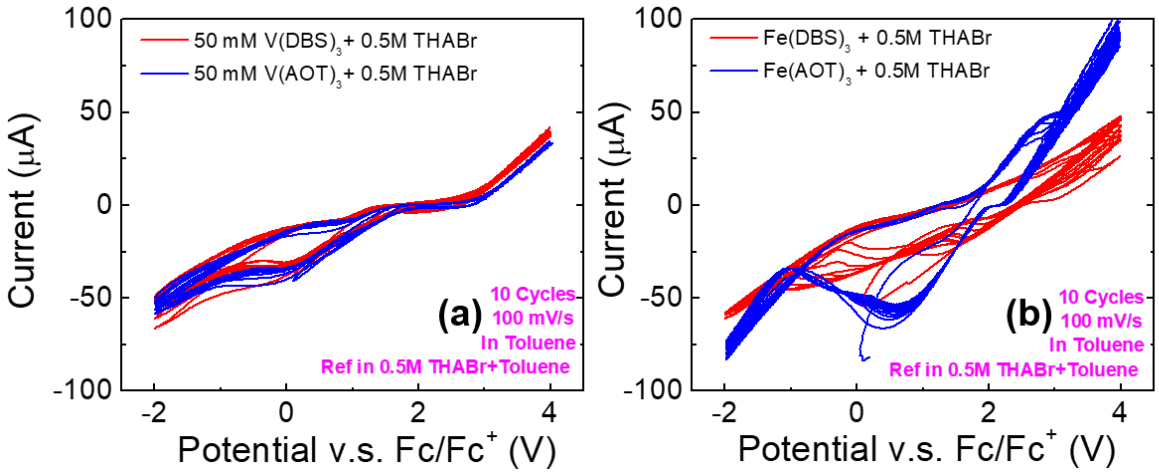

Figure 7.3. CV measurement of (a) iron and (b) vanadium complexes doped with DBS and AOT surfactant chains dispersed in toluene. The quasi reference electrodes are prepared in toluene as well. The concentration of all the organometallic complexes is fixed at 50 mM.

In order to enhance the accessibility of the redox active metal ions, a higher concentration of organometallic complexes, 300 mM, are dispersed into toluene, which is shown in Figure 7.4. No new redox peak appears for vanadium organometallic complexes. The existing peaks remains broad and ill-defined. For iron complexes, especially Fe $(AOT)_3$, however, the increased concentration does help to improve the redox reaction, indicated by better defined peaks. Two

reduction peaks become apparent at a higher concentration. The CV curves do not show good reversibility and they deviate from each other as it is swept more and more cycles. To further improve the redox behavior, a slower scan rate is used. A sweep of 10 mV/s is used in Figure 7.4 (b). This slow scan rate leads to much better reversible peaks. It is possible that kinetics of charge transport to the metal active sites may play a role in affecting the reversibility. As the micelles formed in toluene is covered with insulating shell consisting of surfactant chains,[10] the charge transport from the electrode to the center of the micelle takes a relatively longer time. This is because the micelles formed in toluene are elliptical in shape and the metal core is large in size when compared to the methanol case where metal cores are much smaller and well dispersed.

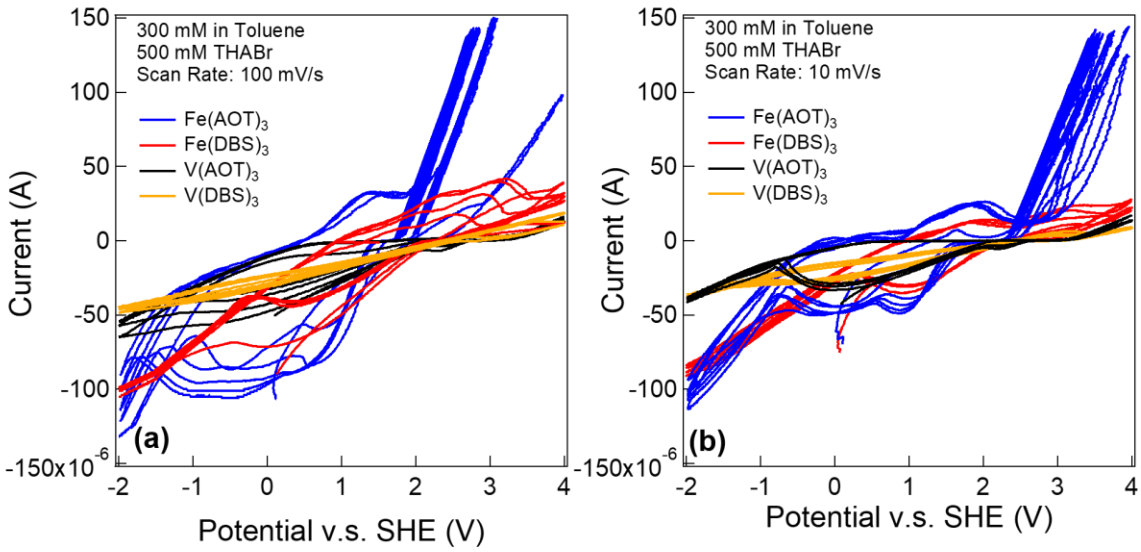

Figure 7.4. Cyclic voltammetry measurement of iron and vanadium complexes dispersed in toluene at 300 mM concentration and sweep with (a) 100 mV/s and (b) 10 mV/s.

7.4 CONCLUSIONS

It has been demonstrated that the simple, economical, yet versatile method of synthesizing metal complexes that can be used to disperse redox active metal ions into organic solvent, even in

nonpolar solvent, such as toluene, is promising for applications in flow batteries. Vanadium and iron complexes are used as model system to demonstrate the redox active behavior using cyclic voltammetry. Both methanol and toluene have been used to disperse the organometallic complexes. Excellent redox activity is shown in methanol and irons are electrochemically active in toluene. Future work of forming smaller micelles by implementing different chemistry in synthesizing metal complexes or methods to assist formation of smaller micelles are largely needed for organic flow batteries in apolar solvents.

7.5 REFERENCES

1 Z. A. Elum and A. S. Momodu, *Renew. Sustain. Energy Rev.*, 2017, **76**, 72–80.

2 J. Mohtasham, *Energy Procedia*, 2015, **74**, 1289–1297.

3 Z. Xie, Q. Liu, Z. Chang and X. Zhang, *Electrochim. Acta*, 2013, **90**, 695–704.

4 P. Leung, A. A. Shah, L. Sanz, C. Flox, J. R. Morante, Q. Xu, M. R. Mohamed, C. Ponce de León and F. C. Walsh, *J. Power Sources*, 2017, **360**, 243–283.

5 Q. Liu, A. A. Shinkle, Y. Li, C. W. Monroe, L. T. Thompson and A. E. S. Sleightholme, *Electrochem. commun.*, 2010, **12**, 1634–1637.

6 W. Wang, Q. Luo, B. Li, X. Wei, L. Li and Z. Yang, *Adv. Funct. Mater.*, 2013, **23**, 970–986.

7 A. A. Shinkle, A. E. S. Sleightholme, L. D. Griffith, L. T. Thompson and C. W. Monroe, *J. Power Sources*, 2012, **206**, 490–496.

8 D. Zhang, H. Lan and Y. Li, *J. Power Sources*, 2012, **217**, 199–203.

9 E. L. Michor and J. C. Berg, *Colloids Surfaces A Physicochem. Eng. Asp.*, 2017, **512**, 1–6.

10 P. De La Iglesia, V. W. Jaeger, Y. Xi, J. Pfaendtner and L. D. Pozzo, *Langmuir*, 2015, **31**, 9006–9016.

11 M. C. Buzzeo, C. Hardacre and R. G. Compton, *ChemPhysChem*, 2006, **7**, 176–180.

Chapter 8. Appendix

8.1 Sample environment for in-situ electric field alignment using neutron scattering technique

As discussed in Chapter 3, electric filed can be used to align the polymers chains to form anisotropic structures and enhance the charge transport. For the aligned fibers, scattering techniques can be used to quantify the degree of alignment. A simple laser engraved quartz slide is sandwiched between two metal plates was used to quantify the alignment at different electric fields. To continue that project, efforts have been put to improve the sample environment that is compatible with scattering techniques and allows characterization of degree of alignment without sacrificing the illumination area. The exploded and assembled schematic drawing with all parts are shown in Figure 8.1 (a) and (b), respectively. The sample environment consists of a rubber gasket sandwiched between two quartz plates that have lithography pattered silver wires to apply electric field. It is important to note that the baking time for patterning photoresist on quartz are drastically different from the recipe typically used for silicon processing, since the quartz are usually thicker (1 mm) than a silicon wafer and its heat conduction is worse. Roughly 3 times baking time of that of silicon is used for quartz slides. Another issue during the photoresist patterning is that quartz slide is transparent. If anything underneath the slide is a light reflector (such as a screw), even a mirror like dark surface would create an unwanted pattern of the reflective subject on the quartz slide or cause overexposure, which, otherwise, is never an issue for opaque silicon wafers. To solve this problem, a sand paper roughened dark acrylic piece was used under the quartz slide to absorb the UV light passing through the quartz slide. A thin layer of chromium (5 nm) is used before silver layer to improve the adhesion. 100 nm silver metal is deposited onto photoresist patterned quartz slide in a metal evaporator, followed by metal lift-off in a developer

solution. The drawing of the metal wires pattern and the aligned fibers formed on top of the quartz plates are shown in (c) and (d). This cell can dramatically reduce the path length for the neutron beam, which could reduce the chance of having multiple scattering if that ever becomes an issue. The path length is defined by the thickness of gaskets and can be easily tuned by changing different gaskets. Chemical solvent resistant Viton sheets are laser engraved into gaskets to ensuring well sealing of the cell. Another advantage of this cell is that the reduced distance between two electrodes can effectively reduce the applied electric potential for a given field. This way, very high frequency electric field can be easily achieved by using a function generator, which reduces the hazards of having electrical shock. In addition, the increased area of electrode edge compared to the initial design in Chapter 3 can align polymers more effectively. What is more, the cell is more practical to check for leaking or perform in-situ optical measurement, if the structure change can induce a color change, because of the transparent quartz windows. Figure 8.1 (e) is a 2-D scattering patterns of a demonstration of the sample environment aligning P3HT under electric field. The 1-D cut the 2-D scattering in both horizontal and vertical directions is presented in (f). Clearly, the alignment in nano-meter scale is observed using this sample environment and the alignment persist to micro-meter scale, which is shown in the optical image in the inset figure. This sample environment can be used to characterize alignment of various polymers over a wide length scale. [10] Less than 1 ml of the solution is used for the sample.

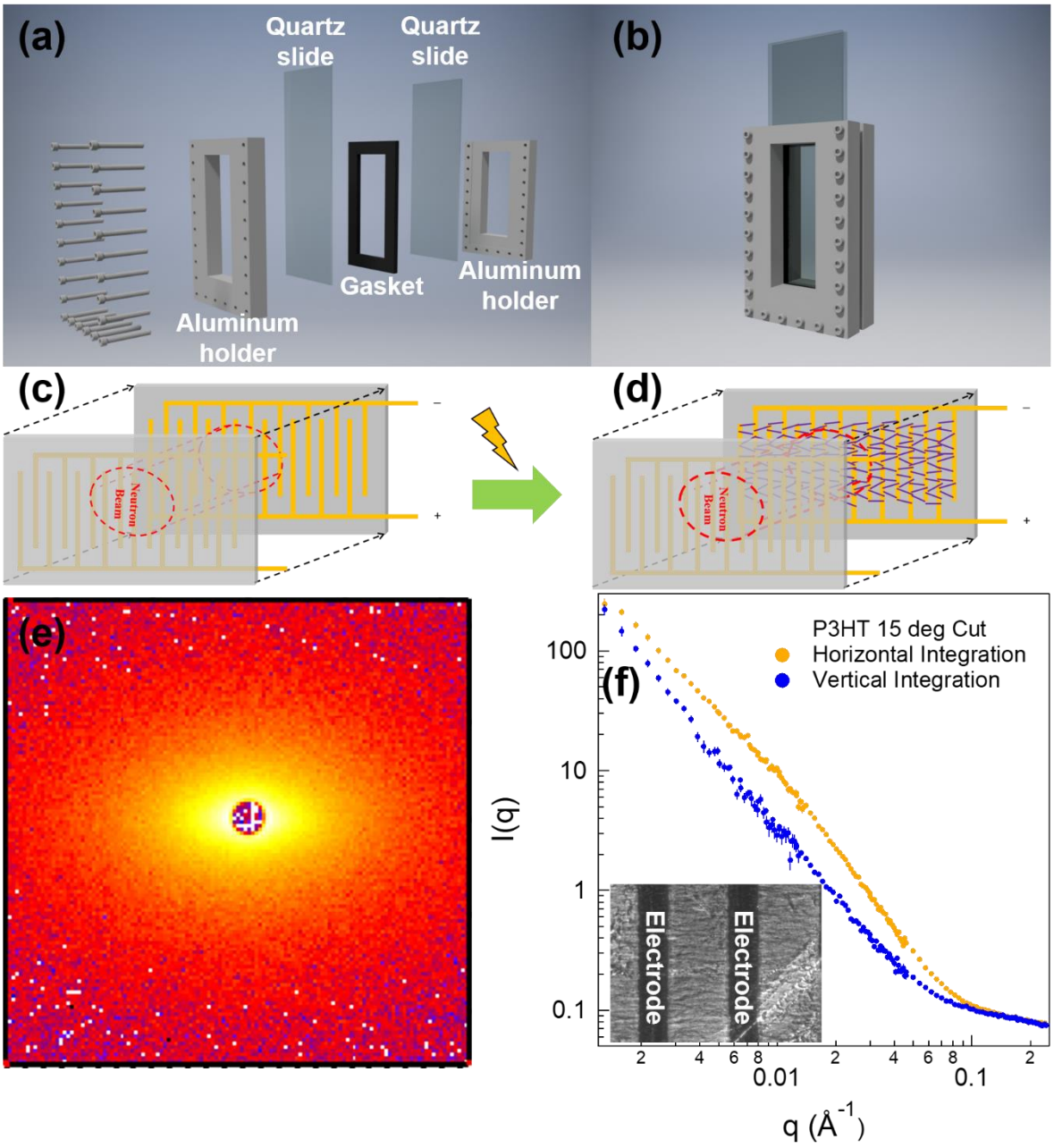

Figure 8.1. (a) Exploded view of the sample environment that enables in-situ application of electric field during scattering experiment. (b) Assembled view of (a). (c) Schematic of electrode lines patterned on quartz through photolithography (d) Schematic of aligned polymers under electric field. (e) 2-D SANS scattering profile of 3 mg/ml P3HT in a solvent mixture of 75% d4-dichlorobenzene and 25% d26-dodecane aligned with this sample environment (f) Reduced 1-D profile of aligned P3HT integrated along horizontal and vertical direction. The inset figures in (f)

is an optical microscopic image of the aligned fibers that resulted in scattering in (f). (a) and (b) are designed by Dr. David S. Li.

8.2 Supporting Information For Chapter 3

8.2.1 *Electrode Polarization*

In order to exclude the electrode polarization effect due to ions in the solvents, the following experiments were performed. If ions contribute to the measurement, the origins of ions may come from either the solvents or from impurities in the dissolved polymers. To test this while preventing the formation of nanofibers, regiorandom P3HT was used since it will not crystallize into nanofibers due to its random side chain configuration. Consequently, two sets of samples were prepared: solvent mixtures of dodecane and 1,2-dichlorobenzene and the same samples containing 30 mg/ml regiorandom P3HT. The configuration was identical to the parallel plates geometry described in the main text. Moreover, if any of the above samples induce electrode polarization, changes in permittivity should be observed as a function of electrode separation distance. Therefore, both sets of samples were measured at 0.5mm and 0.25 mm distances to compare the results.

From the result in Figure 8.2 below, solvent and regiorandom P3HT samples are almost identical to each other at all of the different gap distances. Moreover, the value of ε' is much lower than that found for electric field aligned P3HT fibers. Therefore, the high permittivity at low frequency should be attributed to the assembled P3HT structure. Impedance spectroscopy measurement carried out by other groups on solid P3HT films, also show a uptake of permittivity at low frequency. [11–13]

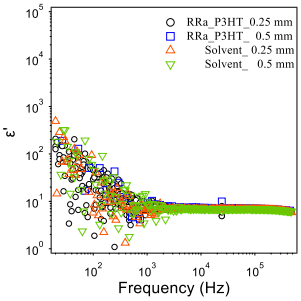

Figure 8.2. Permittivity of 30 mg/ml regiorandom P3HT in 25 wt% dodecane and 75 wt% 1,2-dichlorobenzene mixture and its solvent as a function of frequency. Both samples were conducted at two different gap distances: 0.25 and 0.5 mm, respectively. The experiment was performed in the same way as the dielectric spectroscopy measurement described in the main text. The voltage amplitudes used were 20 mV.

8.2.2 *FFT Transformation*

FFT transformation of model images was also used in order to better understand the meaning of features that were observed. Figure 8.3 shows FFTs performed on artificially generated images that were treated identically to the experimental images. Clearly, horizontal alignment results in the formation of vertical features of high intensity in the FFT. Interestingly, when lines are spaced with a repeating distance (Figure 8.3), the intensity concentrates in two high intensity ‘points’ similar to a diffraction pattern. When randomness is introduced in the separation distance, the

'points' diffuse and lead to a high intensity 'stripe'. In FFT from experimental images, we observe features that are characteristic of both of these cases.

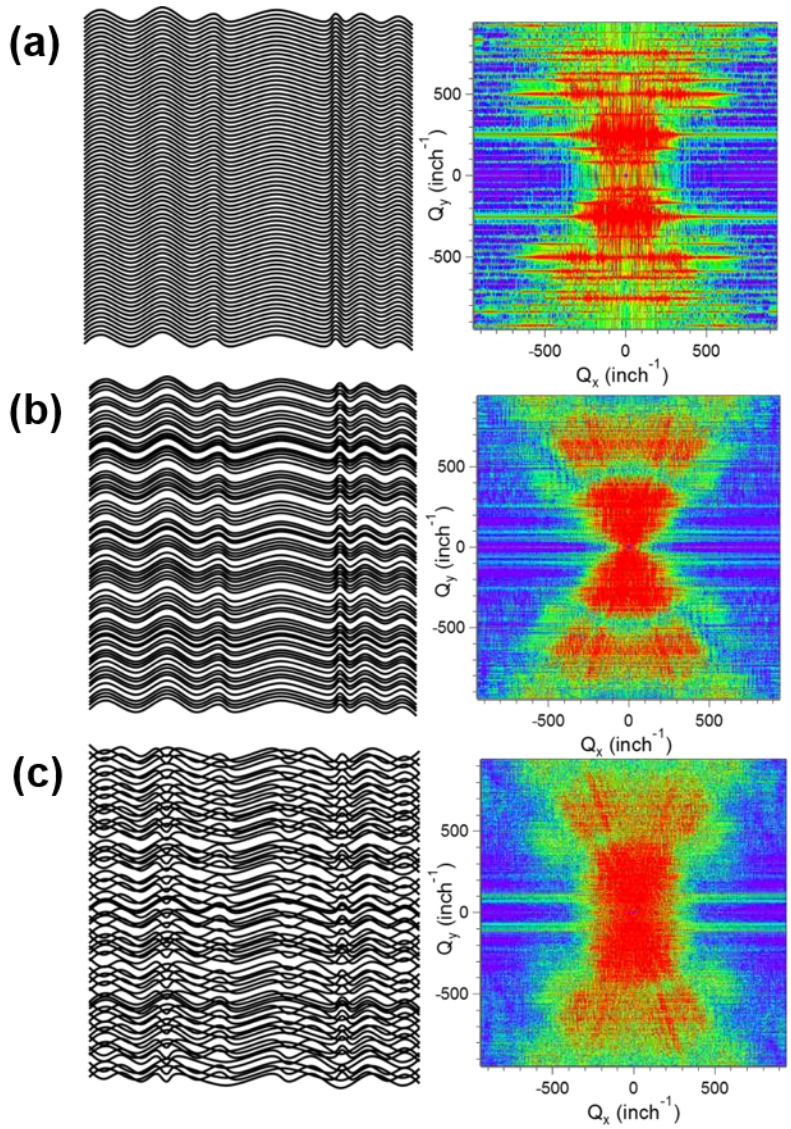

Figure 8.3. Raw images of artificially generated lines and corresponding FFT transform of (a) equally spaced (b) randomly spaced and (c) entangled fibers. Two dots appear in the FFT image if the fibers are well aligned and with equal distance as in (a). In contrast, the loss of alignment in (c) shows a vertical stripe for entangled fibers.

8.2.3 *SANS Fitting*

In order to extract more quantitative information from SANS experiments, direct 2-D fitting was performed using an aligned cylinder model at two electric field conditions that resulted in alignment: 200 V/mm and 400 V/mm at 250Hz. The SANS results and the corresponding fits are shown in Figure 8.4. The fitting was performed by keeping three parameters as variables: cylinder radius (r), length (l), and standard deviation of tilt angle θ with respect to the electric field direction (i.e. horizontal). An explanation is shown in Figure 8.5 (a). In perfectly aligned samples without deviations, the value of θ is 0°. During fitting, the mean value of the distribution was fixed at 0°and the standard deviation of the distribution was fit. The fit results are shown in a table in Figure 8.5 (b). It is noteworthy that higher electric field amplitudes resulted in fibers with smaller standard deviation of θ. This is consistent with our proposed mechanism that higher amplitude resulted in larger DEP force, which can transport smaller fibers and improve orientation along the electric field direction. The angular distribution is also plotted in Figure 8.5 (c)

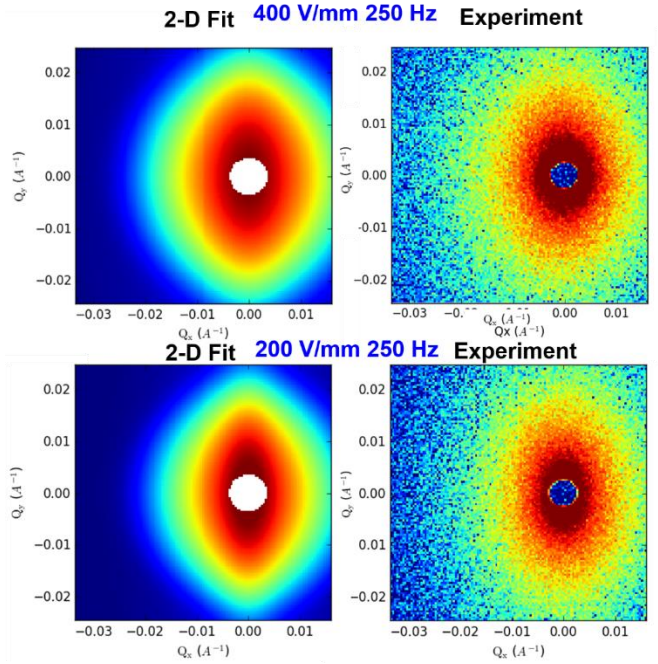

Figure 8.4. 2-D fitting of the SANS data based on cylinder model for 200V/mm at 250Hz and 400 V/mm at 250Hz electric field alignment conditions, respectively.

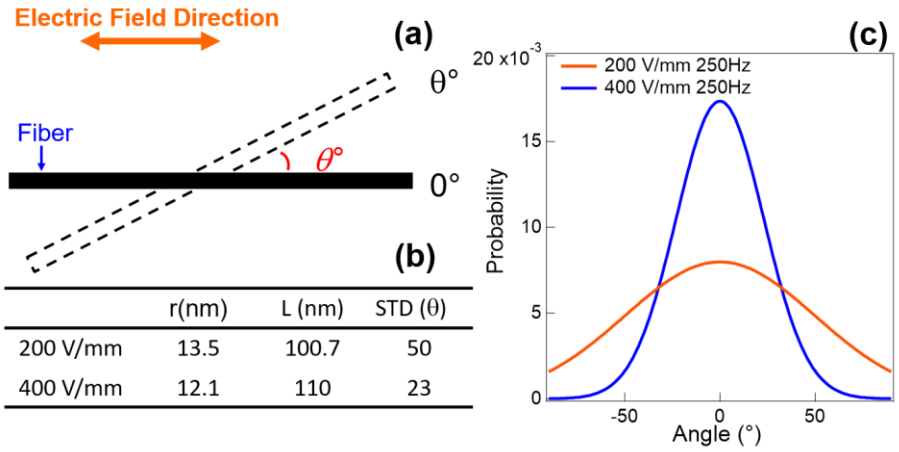

	r(nm)	L (nm)	STD (θ)
200 V/mm	13.5	100.7	50
400 V/mm	12.1	110	23

Figure 8.5. (a) Schematic of a perfectly aligned fiber (θ = 0°) and a fiber with a finite angle θ relative to horizontal direction. (b) Cylinder radius (r), cylinder length (l) and standard deviation of θ (mean was fixed at θ = 0°) obtained from 2-D fitting. (c) Angular distributions from 2D SANS fits for 200 and 400 V/mm.

8.2.4 *Rheology*

The repeatability of the rheology measurement in the main text is plotted in semi-log scale and shown in Figure 8.6. It is clear that the application of the AC field strengthens the gel while the application of DC fields results in a weaker gel.

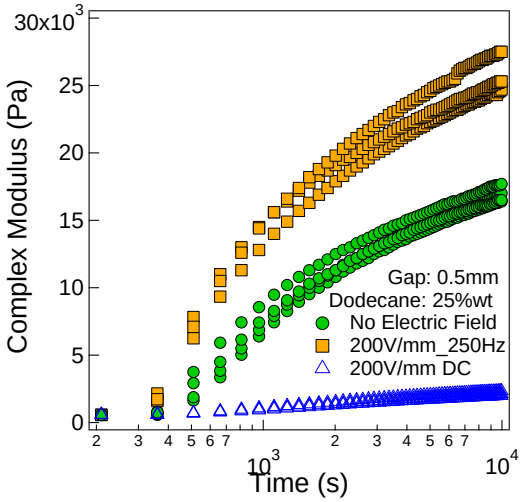

Figure 8.6. Complex modulus for 30 mg/ml P3HT samples in 25 wt% dodecane mixed with DCB formed with 0, 200 V/mm 250Hz and 200 V/mm DC electric fields as a function of time. Three samples were repeated and shown for each condition.

8.2.5 *Fractal dimensions obtained from rheology and SANS*

Linear fit of rheology kinetics based on Liu's model and power law fit of the SANS data at low q range to extrapolate fractal dimensions in Figure 8.7 and Figure 8.8.

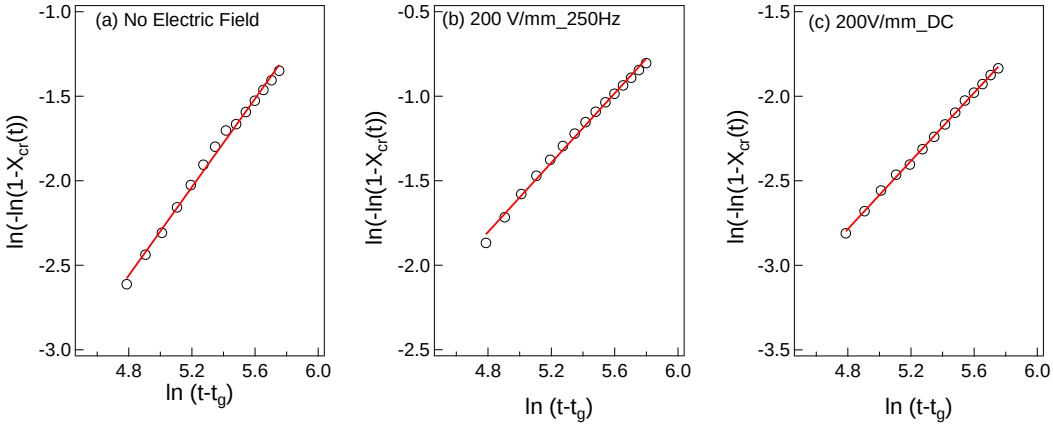

Figure 8.7. Plots of ln(-ln(1-X_{cr}(t)) as a function of ln(t-tg) based on rheological properties G* according to Liu's model for (a) without, (b) with 200 V/mm 250Hz and (c) 200 V/mm DC electric field aligned samples, whereas $X_{cr}(t) = \frac{G^*(t)-G_0^*}{G^*(max)-G_0^*}$. The open circles are the experimental data and the solid red lines are the corresponding fits.

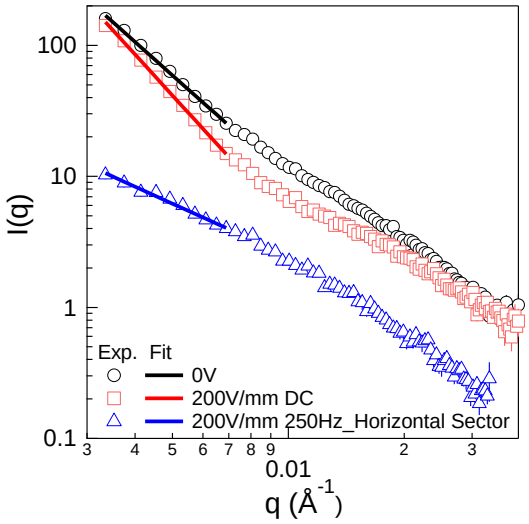

Figure 8.8. Reduced 1-D profile of SANS data using customized sample cell depicted in Figure 3 with neutron beam perpendicular to the electric field. The 2-D pattern at 200V/mm 250Hz electric field is reduced by sector integration along horizontal direction. For 0V and 200V/mm DC samples, the 1-D profile is obtained by circular integration. The regions from 0.0033 to 0.007 Å^{-1} are fitted with power law to obtain the fractal dimension (D_f^S).

8.2.6 *Dielectric spectroscopy and FEM analysis*

Dielectric loss, imaginary and real part of conductivity obtained from dielectric spectroscopy measurement are shown in Figure 8.9 as supplement of dielectric permittivity in Figure 6 (b).

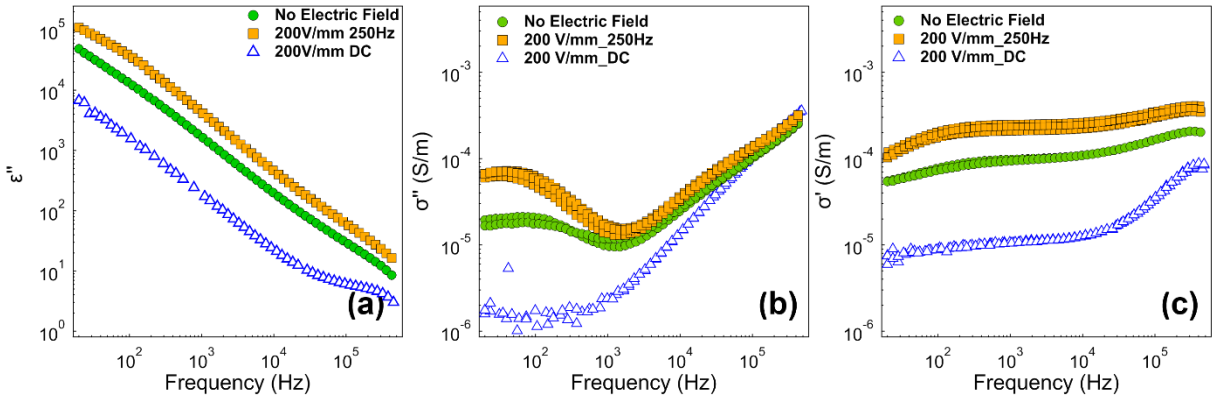

Figure 8.9. (a) Dielectric loss, (b) imaginary and (c) real part of conductivity as a function of frequency. The data was obtained from the dielectric spectroscopy of P3HT organogel in Figure 9 in the main text.

The simulation of electric field gradient distribution between two electrodes was conducted *via* COMSOL Multiphysics software, shown in Figure 8.10. The electrostatics physics module was used and all of the simulations were performed in 2-D domains. The profiles corresponding to the parallel-plate electrodes were directly imported from an experimental profilometer roughness measurement. The Maxwell's Equation was used as the governing equation. The system was meshed with free triangular shape of element sizes between 6 nm and 3 μm. Charge conservation

and electrode potentials were used as boundary conditions. Continuity relation was applied for the transition between adjacent materials.

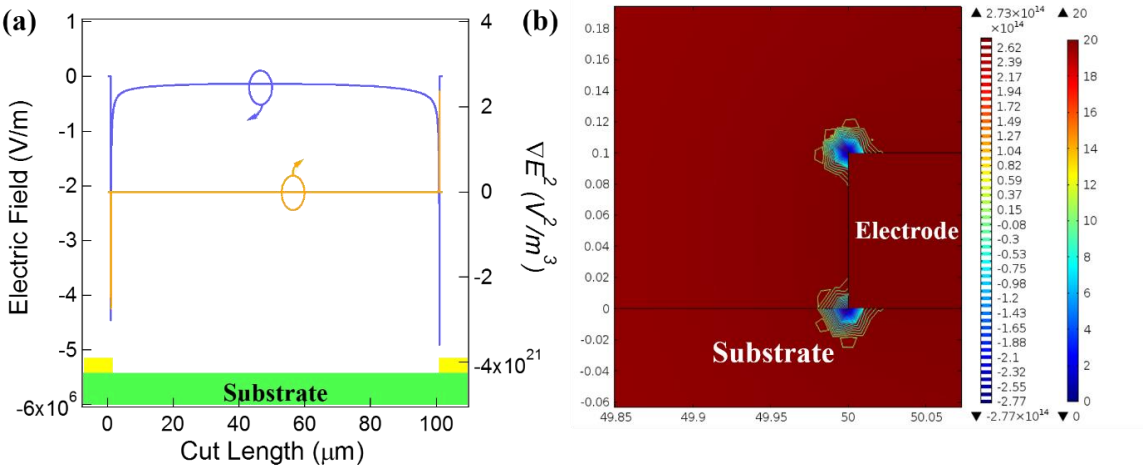

Figure 8.10. (a) Simulations of electric field and gradient of electric field squared distributions between two planar electrodes with a 100 μm gap under 20V electrical potential. (b) 2-D potential distribution and electric field contours simulated by COMSOL.

In both SANS and rheology measurements, the electrodes applying electric fields were parallel plates with a ~1 mm separation distance. Although two perfectly flat parallel plates lead to ideally uniform electric field gradient, local electric field gradients, serving to nucleate initial fibers, can be induced by roughness of the electrodes. A Bruker OM-Dektak XT Profilometer was used to measure the roughness of the Ti plates that were used for SANS measurements. The scan length was 3mm and three different positions were measured on the plates and averaged to extract a representative roughness value. The root mean square roughness of the titanium plates used for SANS measurement was 3.92 ± 0.23 μm. The electric field for a rough plate was also simulated by FEM and the gradient of electric field squared, ∇E^2, was plotted in Figure 8.11. The overall magnitude of ∇E^2 dropped by about six orders of magnitude when compared to that of the planar

electrodes used in microscopy as shown in Figure 8.10. Still, the DEP force would still be large enough to transport the nanofibers when they grow to be large. It is also important to note that the roughness of the electrodes only determines the electric field gradient at initial stages. The electric field would be significantly distorted as soon as some nanofibers start to grow and this further accelerates assembly.

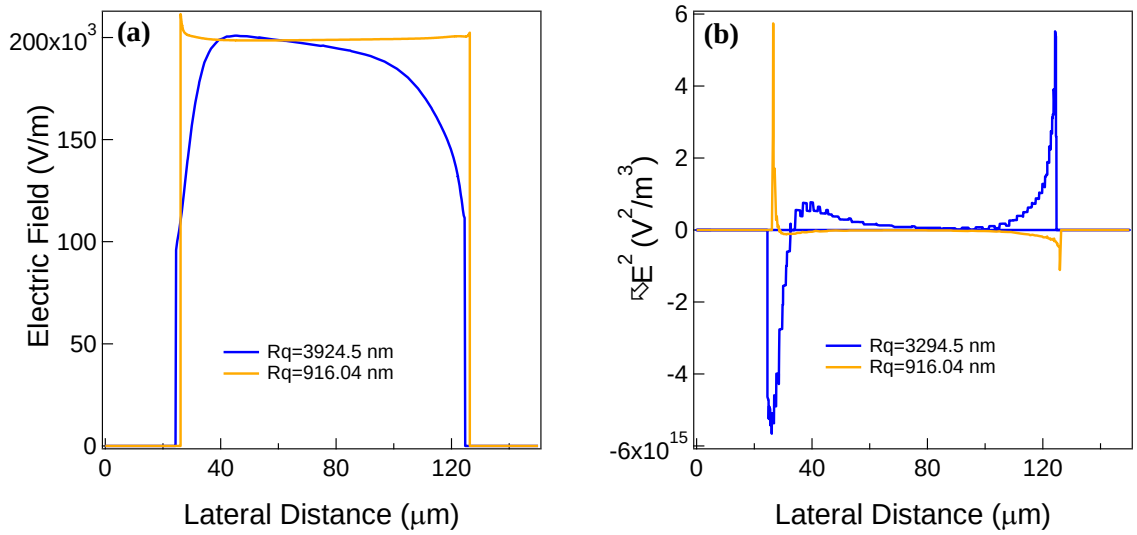

Figure 8.11. (a) Simulations of electric field distribution between two parallel plates with different roughness separated by 100 μm under 20V electric potential. (b) Simulations of the gradient of electric field squared between two parallel plates with different roughness separated by 100 μm under 20V electric potential. The roughness was measured with profilometer and the profile was used as the edge of the electrodes. The magnitude of the gradient of electric field squared dropped by six order of magnitudes compared to planar geometry in Figure 8.10 (a).

8.2.7 *Dielectric force calculations*

The real part of Clausius-Mossotti function, which is shown in Figure 8.12 (a), was used to calculate DEP force in Figure 8 (main text). According to Equation-6 in the main text, this factor

determines the signs of torque at x, y, and z directions. These are plotted in Figure 8.12 (b) as a function of frequency.

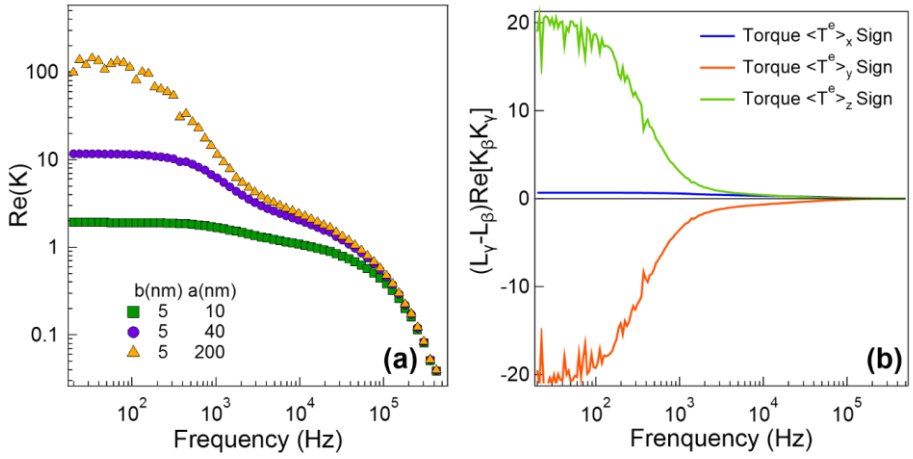

Figure 8.12. (a) Comparison of the real part of Clausius-Mossotti function for fully dissolved P3HT coil and nanofibers with different sizes. Radius of gyration is used to describe the size of fully dissolved polymer chains. "a" represents the length and "b" denotes the radius of the nanofibers. (b) Factor $(L_\gamma-L_\beta)Re[\underline{K}_\beta\underline{K}_\gamma]$ as a function of frequency determines the sign of the torques for different axis. The blackline indicates "0" torque, which separates positive and negative signs.

8.2.8 *Zeta Potential*

Zeta potential measurements were performed on a Zetasizer Nano HT from Malvern Instruments (Worchestershire, U.K.) using a 1 cm path length quartz dip cell with 633 nm wavelength laser. The P3HT samples were made in 0.3 mg/ml concentrations in 45 wt% dodecane mixed with 55 wt% dichlorobenzene and diluted by 40 times for the measurements in Figure 8.13. The samples were prepared in ambient air or in an argon filled glovebox. A sphere shape was assumed and the Huckel electrokinetic model was used in calculating zeta potential values.

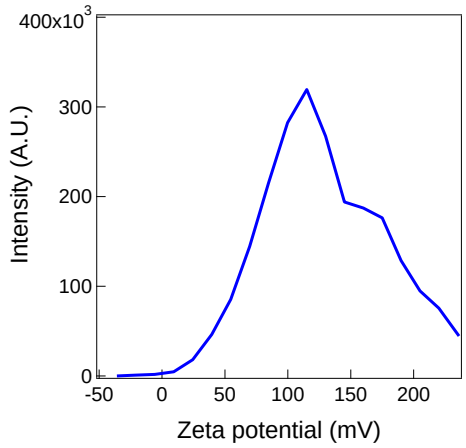

Figure 8.13. Zeta potential measurement of 1 mg/ml P3HT colloidal network prepared in 25 wt% dodecane mixed with 75 wt% dichlorobenzene.

8.2.9 *Time Resolved SANS*

Time-resolved SANS data are shown in Figure 8.14 with and without electric fields. The slope of the low-q region (0.0037 to 0.007 $Å^{-1}$) showed a slight decrease from the beginning to the end of the gelation process. The exponent (slope in log-log plot) at the early stage indicates the presence of some large scale heterogeneous structures. Since these aggregates are large, they scatter with a large exponent due to Porod scattering (i.e. q^{-4}). A combined model of large spheres (i.e. aggregates) and dissolved polymer was used to fit the scattering profile at early stages in Figure 8.14 (c) (300s) and to estimate the amount of aggregation that would lead to this low-q increase. The fit estimated that a very small amount of aggregates (i.e. 0.65% of the total vol% of polymer) with 63 nm in radius was enough to reproduce scattering profile. As the sample crystallizes and nanofibers form, the scattering is rapidly dominated by these emerging nanostructures and the exponent at low-q is reduced. The origin of the aggregates could be contaminants in polymer samples, such as insoluble polymer or residual catalyst. Another possible cause of the low-q signal is due to the error in

correcting empty cell scattering, since the rough electrodes also have large features (>1 μm) that can contribute to low-q scattering. Great efforts have been made to correct for it by increasing empty cell counting time and by measuring every empty cell for each corresponding sample, but the excess signal was not fully eliminated. However, it is important to note that the initial large aggregates at low-q region do not affect the cross-sectional dimensions extrapolated from parallelpiped model, which is performed at mid and high-q region (0.01 ~ 0.3 $Å^{-1}$) in Figure 8.14.

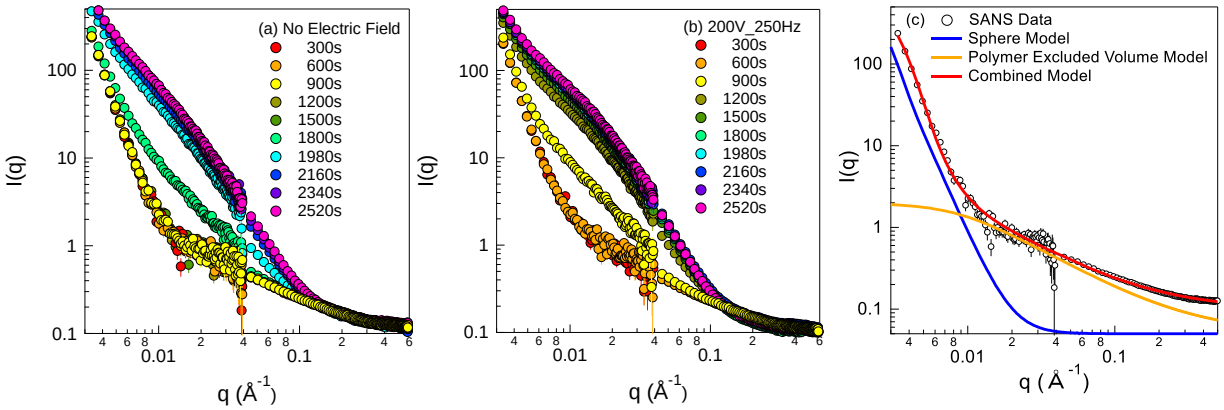

Figure 8.14. SANS of gelation process (a) without and (b) with electric field as a function of time with 30 mg/ml P3HT in 25 wt% dodecane and 75 wt% 1,2-dichlorobenzene in the dielectric cell that has been reported before.[14,15] (c) SANS data of 30 mg/ml P3HT in a mixed solution of 25 wt% dodecane and 75 wt% 1,2-dichlorobenzene collected at 300s and the corresponding fitting using combined model of sphere and polymer excluded volume model.

8.2.10 *UV-vis Spectroscopy*

A Thermo Evolution 300 UV-Vis spectrophotometer was used to record the absorption spectra at wavelength between 300 and 800 nm. 30 mg/ml P3HT samples dissolved in 25% wt dodecane mixed with 1,2-dichlorobenzene was loaded between two parallel plates and experiment performed in the same way as the rheology measurement described in the main context. After allowing gelation for 3 hrs, a small amount of sample was taken out to disperse at a concentration

below 0.1 mg/ml in the same solvent used to prepare the gel. Redissolved samples were prepared by heating up the dispersed fibers to ~80 °C to fully dissolve them. Filtrate curves were obtained by filtering dispersed samples with 200 nm pore size syringe filters (VWR, Radnor, PA). Concentration were determined using Beer's law by fitting the peak absorbance at ~450 nm of the fully dissolved P3HT to extract extinction coefficient.

UV-Vis spectroscopy was also utilized to indirectly probe for structural changes caused by the electric fields. UV-Vis spectra are shown in Figure 8.15 where the solid fraction of fibers was also calculated and compared. The method used for calculating fiber fractions, which was similar to that used in previous publications, consist of filtration and separation of the dissolved fraction.[16] The main absorbance peak in the dissolved state ($\lambda \sim 450$ nm) for a fully dissolved sample ($A_{redissolved}$) and for the extracted supernatant after filtration ($A_{filtered}$) were used to calculate the fiber/solid fraction using equation (3.1). The absorption spectra for crystalline, re-dissolved, and filtered samples are all shown in Figure 8.15. A small increase of the solid fraction from 79.3% to 84.7% was observed after applying an electric field. According to Clark and coworkers,[17] the ratio of the 0-0 and 0-1 peak absorbance can be used to calculate the free exciton bandwidth (W). Values of W for samples formed with and without electric field were 31.2 and 47.1 meV, respectively. Lower W values suggest a higher order for the interchain π-π stacking. Thus, samples without electric field showed relatively higher order of the π-π stacking than those with electric field.

$$\phi_s = 1 - \frac{A_{filtered}}{A_{redissolved}} \qquad (8.1)$$

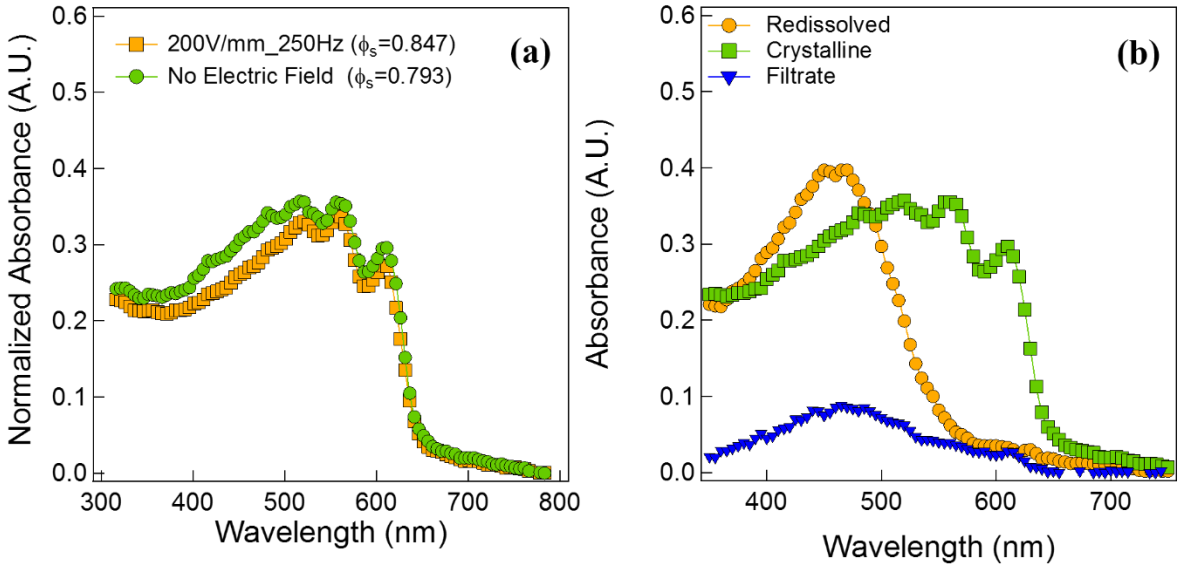

Figure 8.15. (a) Absorption spectra for a fraction of 30 mg/ml P3HT samples formed in rheology measurement with 200 V/mm 250Hz and without electric field alignment at room temperature. (b) Absorption spectrum for P3HT that was redissolved at 80 ºC, crystalized in solution, as well as the supernatant of the solution with solid P3HT removed by filtration.

8.3 SUPPORTING INFORMATION FOR CHAPTER 4

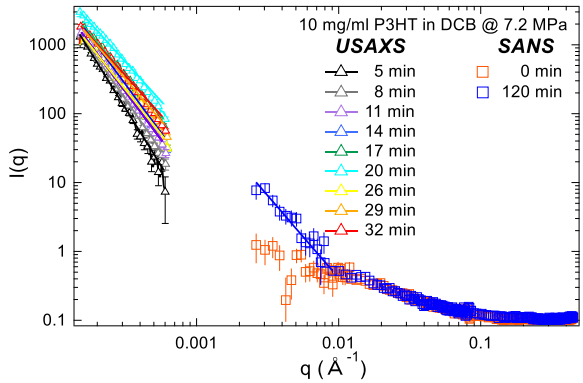

Figure 8.16. Power law fitting results of USAXS and SANS at low q range (< 0.01 $Å^{-1}$). The open symbols represent data points and solid lines are the corresponding power law fitting.

8.4 REFERENCES

(1) Ensikat, H. J.; Ditsche-kuru, P.; Neinhuis, C.; Barthlott, W. Superhydrophobicity in Perfection: The Outstanding Properties of the Lotus Leaf. **2011**, 152–161 DOI: 10.3762/bjnano.2.19.

(2) Yang, H.; Liang, F.; Chen, Y.; Wang, Q.; Qu, X.; Yang, Z. Lotus Leaf Inspired Robust Superhydrophobic Coating from Strawberry-like Janus Particles. *NPG Asia Mater* **2015**, *7* (4), e176 DOI: 10.1038/am.2015.33.

(3) Vukusic, P.; Sambles, J. R. Photonic Structures in Biology. *Nature* **2003**, *424* (6950), 852–855 DOI: 10.1038/nature01941.

(4) Srinivasarao, M. Nano-Optics in the Biological World: Beetles, Butterflies, Birds, and Moths. *Chem. Rev.* **1999**, *99* (7), 1935–1961 DOI: 10.1021/cr970080y.

(5) Potyrailo, R. a.; Ghiradella, H.; Vertiatchikh, A.; Dovidenko, K.; Cournoyer, J. R.; Olson,

E. Morpho Butterfly Wing Scales Demonstrate Highly Selective Vapour Response. *Nat. Photonics* **2007**, *1* (2), 123–128 DOI: 10.1038/nphoton.2007.2.

(6) Cranford, S. W.; Tarakanova, A.; Pugno, N. M.; Buehler, M. J. Nonlinear Material Behaviour of Spider Silk Yields Robust Webs. *Nature* **2012**, *482* (7383), 72–76 DOI: 10.1038/nature10739.

(7) Römer, L.; Scheibel, T. The Elaborate Structure of Spider Silk: Structure and Function of a Natural High Performance Fiber. *Prion* **2008**, *2* (4), 154–161 DOI: 10.4161/pri.2.4.7490.

(8) Aoyanagi, Y.; Okumura, K. Simple Model for the Mechanics of Spider Webs. *Phys. Rev. Lett.* **2010**, *104* (3), 1–4 DOI: 10.1103/PhysRevLett.104.038102.

(9) Miniaci, M.; Krushynska, A.; Movchan, A. B.; Bosia, F.; Pugno, N. M. Spider Web-Inspired Acoustic Metamaterials. *Appl. Phys. Lett.* **2016**, *109* (7) DOI: 10.1063/1.4961307.

(10) Xi, Y.; Pozzo, L. D. Electric Field Directed Formation of Aligned Conjugated Polymer Fibers. *Soft Matter* **2017**, *13*, 3894–3908 DOI: 10.1039/C7SM00485K.

(11) Obrzut, J.; Page, K. A. Electrical Conductivity and Relaxation in Poly(3-Hexylthiophene). *Phys. Rev. B* **2009**, *80* (19), 195211 DOI: 10.1103/PhysRevB.80.195211.

(12) Singh, R.; Singh, R. K.; Kumar, J.; Kant, R.; Kumar, V. The Origin of DC Electrical Conduction and Dielectric Relaxation in Pristine and Doped Poly (3-Hexylthiophene) Films. **2010**, *48*, 1047–1053 DOI: 10.1002/POLB.

(13) Okutan, M.; San, S. E.; Alpaslan, Z.; Demir, A. Electrical Properties of Zn-Phthalocyanine and Poly (3-Hexylthiophene) Doped Nematic Liquid Crystal. **2011**, *2011* (2) DOI: 10.1155/2011/729085.

(14) Newbloom, G. M.; Weigandt, K. M.; Pozzo, D. C. Structure and Property Development of Poly(3-Hexylthiophene) Organogels Probed with Combined Rheology, Conductivity and Small Angle Neutron Scattering. *Soft Matter* **2012**, *8* (34), 8854 DOI: 10.1039/c2sm26114f.

(15) Newbloom, G. M.; Weigandt, K. M.; Pozzo, D. C. Electrical, Mechanical, and Structural Characterization of Self-Assembly in Poly(3-Hexylthiophene) Organogel Networks. *Macromolecules* **2012**, *45*, 3452–3462 DOI: 10.1021/ma202564k.

(16) Newbloom, G. M.; Kim, F. S.; Jenekhe, S. a.; Pozzo, D. C. Mesoscale Morphology and Charge Transport in Colloidal Networks of Poly(3-Hexylthiophene). *Macromolecules* **2011**, *44* (10), 3801–3809 DOI: 10.1021/ma2000515.

(17) Clark, J.; Chang, J. F.; Spano, F. C.; Friend, R. H.; Silva, C. Determining Exciton Bandwidth and Film Microstructure in Polythiophene Films Using Linear Absorption Spectroscopy. *Appl. Phys. Lett.* **2009**, *94* (16), 2007–2010 DOI: 10.1063/1.3110904.

Chapter 9. Conclusions and outlook

9.1 Key Results

The enhancement of electrical properties of conjugated polymers generally includes the exploration of new conjugated polymers by molecular design or the engineering of assembly for existing conjugated polymers to form desired large structures. In this dissertation, both directed- and self- assembly have been demonstrated to be effective in forming ordered structures.

In Chapter 3, we demonstrated that electric field can be effectively used to align conjugated polymers into uni-directional fibers. By applying SANS, optical microscopy, and atomic force microscopy to characterize the structures, it was concluded that alignment can be achieved from nanometer to micrometer scales. The electric field frequency, amplitude, polymer concentration, poor solvent ratio, as well as molecular structures of the polymers are investigated to form a correlation between controllable parameters and the resulted alignment. The optimum condition and molecular design rules are proposed to form effective alignment. The mechanism for alignment is proposed to be dielectrophoresis. The combined effect from electrophoresis, dielectrophoresis, and crystallization of conjugated polymers is the cause for the existence of the optimum alignment conditions for the above controllable parameters.

Chapter 4 presented a method to form nanofibers in commonly believed ‘good’ solvents using acoustic wave. The size and fraction of the nanofibers are carefully characterized by SANS and sTEM. It is found that the dissolved state in ‘good’ solvent is only a local minimum in the energy landscape, which kinetically trap polymers and keep them from forming aggregations. The acoustic wave provides energy to overcome the barrier to form assembly, even using the best solvent for conjugated polymers. The choice of solvent can change the length and aggregation type

of the assembled structures. A correlation between the polymer fractions in fiber form is formed with the peak negative pressure of the acoustic wave. The formation of cavitation is the fundamental reason for the assembly.

In Chapter 5, self-assembly using poor solvents with different polarity is presented. Nanoribbons can be formed with polar poor solvents, while the addition of nonpolar solvent only leads to the formation of aggregates with arbitrary shape. Methanol induces the formation of a different crystalline structure and the hole mobility can be enhanced with this polymorph. This type of crystalline structures can be induced by methanol in different conjugated polymers. It is proposed that the poor solvent molecule interaction with polymer and good solvent molecule is the reason for this polarity dependent self-assembly.

In chapter 6 and 7, conjugated polymers with different dopant and different monomer composition are synthesized. The electrochemical activity is evaluated as solid electrode materials for printable battery applications. Their structures are characterized by SANS, BET, and SEM to correlate with the charge storage capacities. The organometallic salt used to initiate polymerization are also found redox active both as a solid-state material or dispersed in organic solvent. This work provides a way to form versatile materials that the structures can be easily tuned during synthesis.

To continue the above work, several directions are proposed. The preliminary data is collected along with some discussions. Basically, electric field can be combined with flexible substrate for wearable devices that require aligned structures. Acoustic field can also be explored as a general method to direct the assembly of both macro- and small molecules.

9.2 ELASTOMER EMBEDDED WITH ALIGNED CONDUCTIVE FIBERS

Bioelectronics attract a lot of attention because they possess both electrical and flexible mechanical properties within the same device. They can mimic the signaling in biology and potentially replace organs or tissues in human bodies. They can also be used as sensors to detect and record external stimuli. It has been an emerging research area to develop wearable electronic devices that is flexible and ideally stretchable. Examples include electronic skins, biosensors, and organic electrochemical transistors (OECTs). [1] Conjugated polymer is a good candidate for such devices. The assembly of P3HT into nanofibers can further enhance the charge transport for a much longer distance compared to single polymer chains. Such assembly does not compromise the mechanical properties of the resulting film. Recently work have successfully demonstrated that by integrating P3HT nanofibers into a elastomer matrix to enhance the electrical performance in a flexible and stretchable film. [2,3] As the electric field has been demonstrated to align P3HT nanofibers along one direction, it can enhance the charge transport in one direction while suppressing that in the perpendicular direction. By integrating the aligned structure into the flexible and stretchable substrates, it is potentially useful for controlling signal transporting in a favorable direction and it can also be used for biosensors that detect stretches or bending in a certain direction. Preliminary work of transferring aligned fibers to flexible PDMS substrate is shown in Figure 9.1. The fibers are very well aligned with electric field. A relatively low concentration of 1 mg/ml P3HT was used in a binary solvent mixture of 25% dodecane and balanced with 1,2-dichlorobenzene following the same procedure as described in Chapter 3. In fact, alignment can be further improved by decoupling the self-assembly process from alignment. The self-assembly can be achieved either by using mixing poor solvents to induce assembly or by sonication in good solvents (1,2-dichlorobenzene). The sample solution can be aged for days to weeks to ensure complete assembly.

Then the preformed colloidal network can be casted onto electrodes with AC electric field alignment. The elastomer layer was formed by using commercially available Dow Corning (Midland, MI, USA) Sylgard 184 kit. Both the base and crosslinker are dissolved into hexane to allow fast evaporation of solvents during curing. The base to crosslinker mixing ratio of 10:1 is used. It is important to note that the elastomer mixture should be casted after the alignment is completed, but before the solvent is completely dried. This way, high quality alignment is maintained and at the same time good adhesion between polymer and elastomer layer can be achieved as well. After curing at 80˚C for a few hours, the aligned P3HT can be peeled off easily, which can be used for further processing of devices.

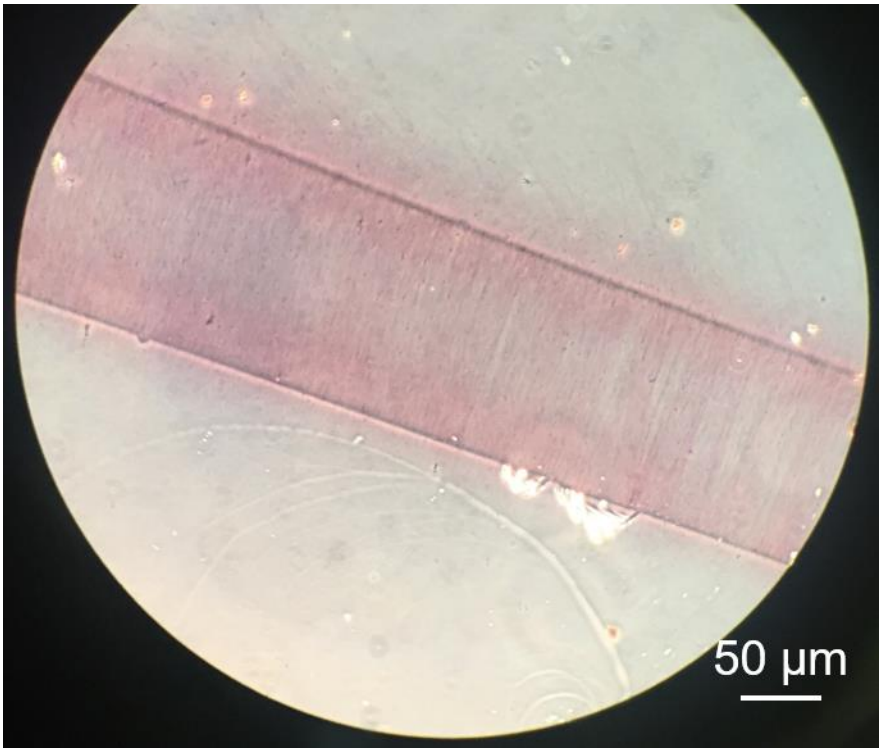

Figure 9.1. Optical microscopy image of aligned P3HT fibers that is transferred to PDMS substrates. The alignment is achieved by using 1 mg/ml P3HT in 25 wt% dodecane and 75 wt% 1,2-dichlorobenzene under 160 V/mm and 250 Hz electric field between two pre-patterned silver electrodes.

9.3 USING SONICATION AS AN EFFECTIVE TOOL TO ENHANCE THE MOBILITY OF DIFFERENT CONJUGATED POLYMERS

Chapter 4 uses poly (3-hexylthiophene) (P3HT) as a model system to study the mechanism of induced crystallization by ultrasound. Not only in P3HT, ultrasound can assist assembly in other conjugated polymers to further improve their charge transport. Below are some preliminary results of enhanced device mobility from different conjugated polymers. We have developed a detailed

understanding of how assembly is induced by acoustic wave. It is also important to further explore how much this step can enhance the mobility in a device for different polymers.

Figure 9.2 shows UV-vis spectra of 3 mg/ml PBTTT with and without 30 min sonication in bath. After sonication, the absorption peak red shifted by 9.5 nm. New absorption peaks start to develop at 574 nm and 623 nm, indicating assembly of polymer chain. In order to measure the charge carrier mobility enhancement in conjugated polymer poly[2,5-bis(3-tetradecylthiophen-2-yl)thieno[3,2-b]thiophene] (PBTTT), bottom gate bottom contact organic field effect transistors (OFETs) are fabricated to probe the charge transport before and after sonication is applied. Since PBTTT has a high tendency to self-assemble in solutions, a good solution (dichlorobenzene) and a relative low concentration (2 mg/ml) is used to minimize the assembly in solution without ultrasound. The transfer curves of 5 devices of each condition are plotted in Figure 9.3 (a) before and after sonication. The drain current increases by almost one order of magnitude when the device is turned on. The calculated saturation mobilities are summarized in Figure 9.3 (b). An enhancement of mobility of about 10 times is observed for polymer solutions after sonication. The threshold voltage also shifts towards 0 V after sonication.

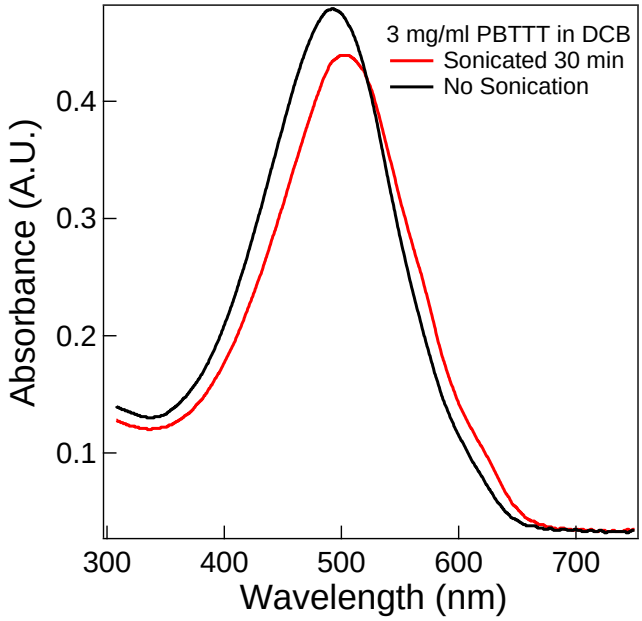

Figure 9.2. UV-vis spectra of 3 mg/ml PBTTT sonicated in 1,2-Dichlorobenzene with and without 30 min sonication.

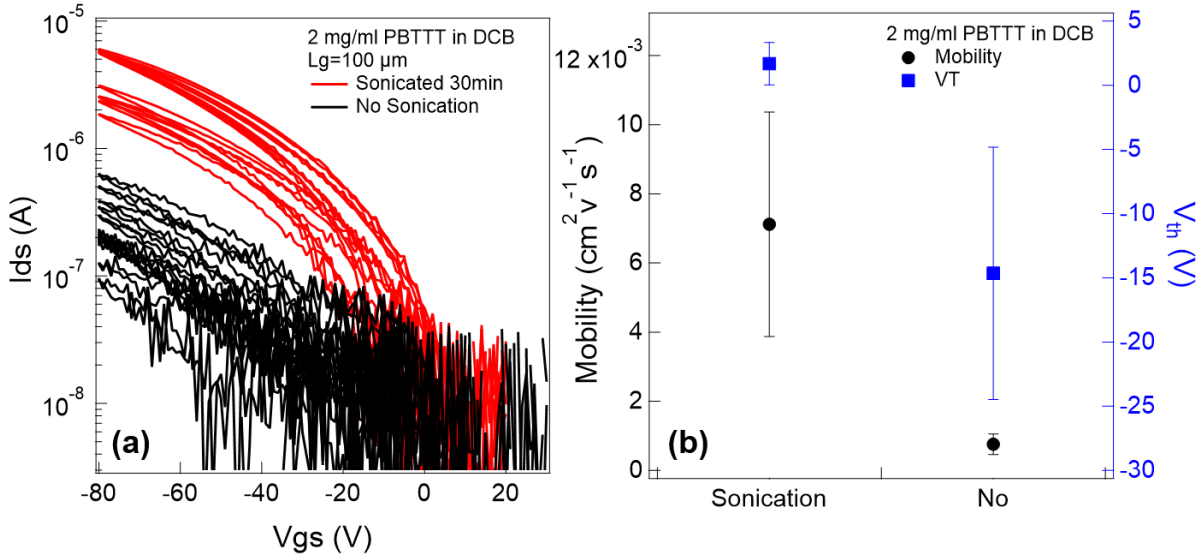

Figure 9.3. (a) I-V characteristics of organic field effect transistors (OFETs) fabricated from 2 mg/ml PBTTT in DCB with sonication and without sonication. (b) The comparison of mobility and threshold voltage between sonicated and samples without sonication.

Not only homopolymers, the effect of sonication also appears in donor-acceptor conjugated polymers. Poly[2,5-(2-octyldodecyl)-3,6-diketopyrrolopyrrole-alt-5,5-(2,5-di(thien-2-yl)thieno[3,2 b]thiophene)] (DPPDTT) was dissolved in chloroform at 2 mg/ml in both 1,2-dichlorobenzen and chloroform, which are both good solvents for this polymer. The UV-vis spectra are collected after sonicating in a bath or sonication by a tip and shown in Figure 9.4. A longer isonation time leads to more blue shifts of the major absorption peak, indicating structural or conformational change of donor acceptor polymer chain within the solution. In chloroform, similar direction of wavelength shift is observed as well.

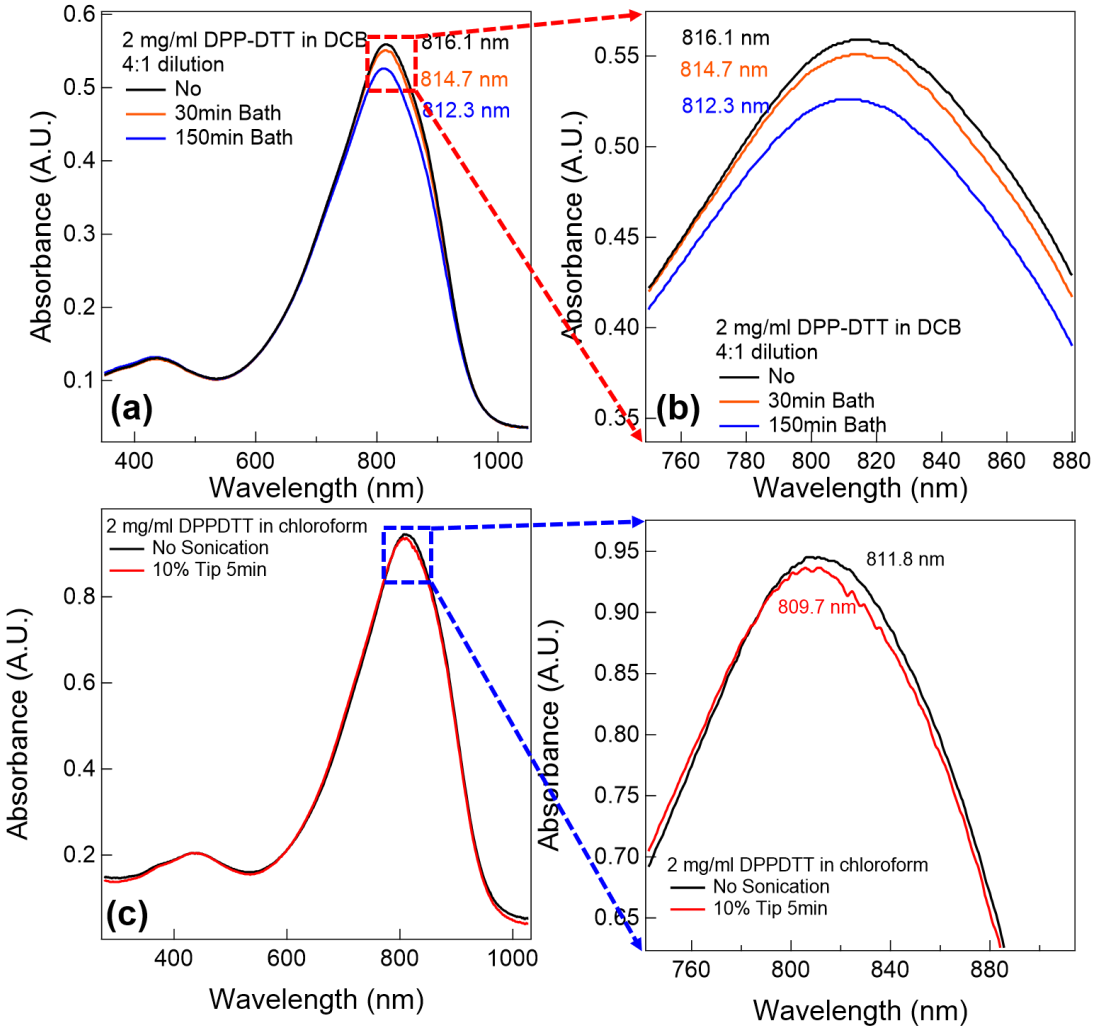

Figure 9.4. UV-vis spectra of 2 mg/ml DPPDTT (a) in 1,2-dichlorobenzene after sonicating in sonication bath and (c) in chloroform after sonicating with a sonication tip. (b) and (d) are enlarged image around absorption peak area.

Another strategy to take advantage of sonication induced assembly, especially in solvents that have high cavitation threshold, is to incorporate a small amount of immiscible solvent that has a relatively low cavitation threshold, which can serve as the seeds for cavitation to occur. The increased number of cavitation events can arrange the polymer chains into conformations that can

easily form π-π stacking. Perfluorohexane is a good candidate for inducing cavitation at low peak negative pressure, since the boiling point for perfluorohexane is only 56 ˚C. By incorporating immiscible perfluorohexane, an increase of drain current is observed for OFET devices in **Figure 9.5**. The calculated mobility increased by about 1.5 times after sonication.

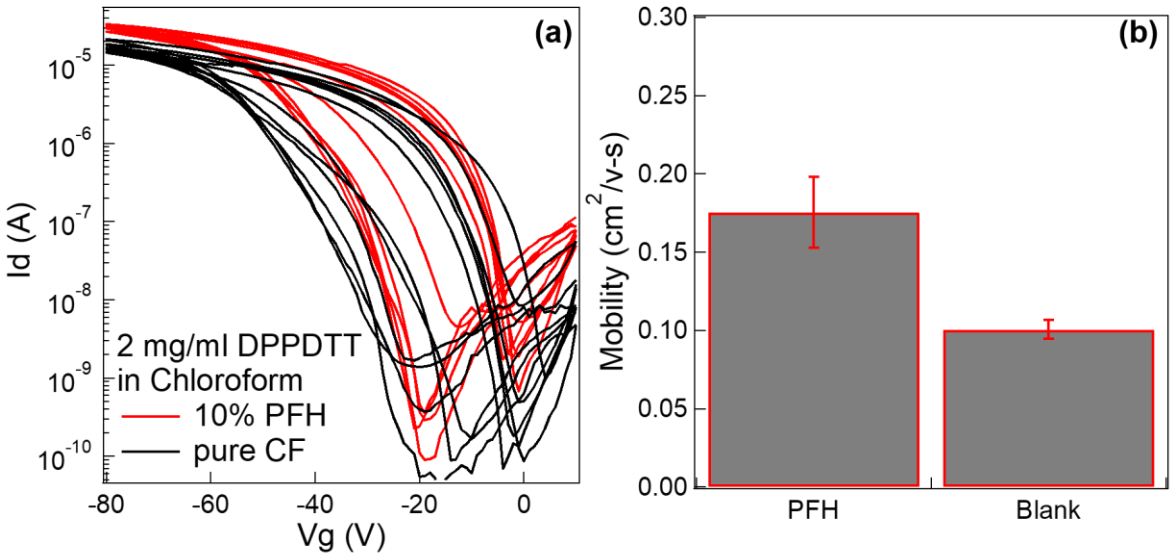

Figure 9.5. (a) A comparison of transfer curves of 2 mg/ml DPPDTT in chloroform with that of adding 10% perfluorohexane to induce assembly. (b) The calculated saturation mobility of samples prepared in the two conditions. The standard deviations are calculated from six devices of each condition.

9.4 Effect of Ultrasound on Water Soluble Macromolecules

Water soluble conjugated polymers (WSCPs) have attracted a lot of attention because they allow 'green' solvent processing and are biocompatible. [4–6] They can be used for diagnosis, imaging and therapy because they are electrochemically or electromechanically responsive to external stimuli. [6] They are also used for electron transport layer, as they can avoid interfacial mixing of the solution deposition of sequential layers, which results in improved charge injection for optoelectronic

devices. [7] Although WSCPs possess so many advantages, they still suffer from poor charge transport when compared to their organic solvent processible counterparts. Hole mobility extrapolated from measurement in organic field-effect transistors (OFET) yielded a value of 10^{-5} $cm^2V^{-1}s^{-1}$ and a low power conversion efficiency (PCE) of 0.015% from a working photovoltaic device. [5,8] In comparison, conjugated polymers processed from organic solvents have already demonstrated mobility of above 0.1 $cm^2V^{-1}s^{-1}$ and PCE above 10%. In order to overcome this limitation, self-assembly can be used to assist polymer chains to form long rang order for better charge transport. The effect of ultrasound assisted assembly is investigated in WSCPs. Poly[2-(3-thienyl)ethyloxy-4-butylsulfonate] sodium salt (PTEBS) is used as a model system for understanding how ultrasound wave can change its structure in solution. The molecular structure of this polymer is depicted in Figure 9.6 (b). A well-defined acoustic wave with 7.2 MPa peak negative pressure is utilized with 20% duty cycle for 2hrs. The UV-vis spectra are recorded for the sample with ultrasound irradiated and for that without any ultrasound treatment. A red shift of 11.2 nm is observed for solutions with ultrasound irradiation. A color change is also observed in the optical microscopic image in the inset of Figure 9.6 (a). Small angle neutron scattering (SANS) is performed on samples with and without ultrasound application. The fresh sample does not have enough statistics. Based on the scattering profile between 0.015 $Å^{-1}$ and 0.03 $Å^{-1}$, it is possible that there is some structure change after ultrasound irradiation.

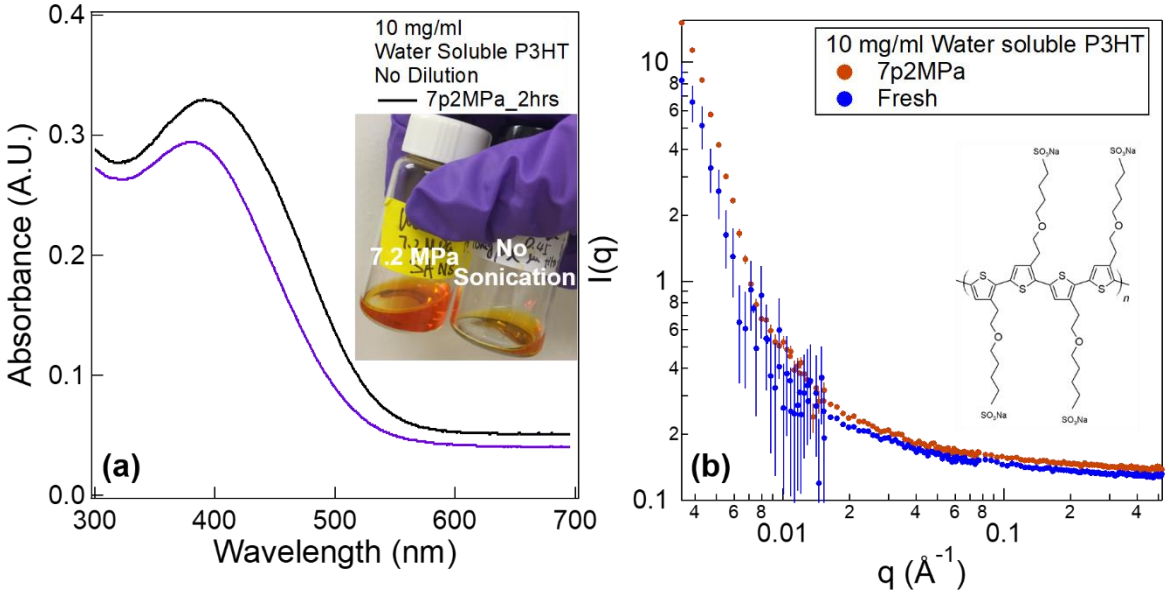

Figure 9.6. (a) UV-vis spectra of 10 mg/ml water soluble P3HT with and without 7.2 MPa ultrasound application for 150 min. The inset picture shows optical images of the colore change with and without ultrasound application. (b) Corresponding 1-D small angle neutron scattering (SANS) profiles of 10 mg/ml polymer solution with and without ultrasound application. The inset schematic image shows the molecular structure of the polymer.

In contrast, the effect of ultrasound treatment on water soluble polymer without π orbital interaction is investigated using poly (vinyl alcohol) (PVA). **Figure 9.7** shows both UV-vis and small angle x-ray scattering (SAXS) of the PVA solution with and without 30 min sonication in bath. For UV-vis measurement, molecular weights of both 31 kDa and 61 kDa PVA are used. The absorption peaks are located between 320 nm and 340 nm, which is shown in the inset image in **Figure 9.7** (a). No obvious change is observed after sonication application for both UV-vis and SAXS measurement. This indicates that the molecular structure is important for acoustic field directed assembly. Strong interchain interaction may be a prerequisite for acoustic directed assembly to occur.

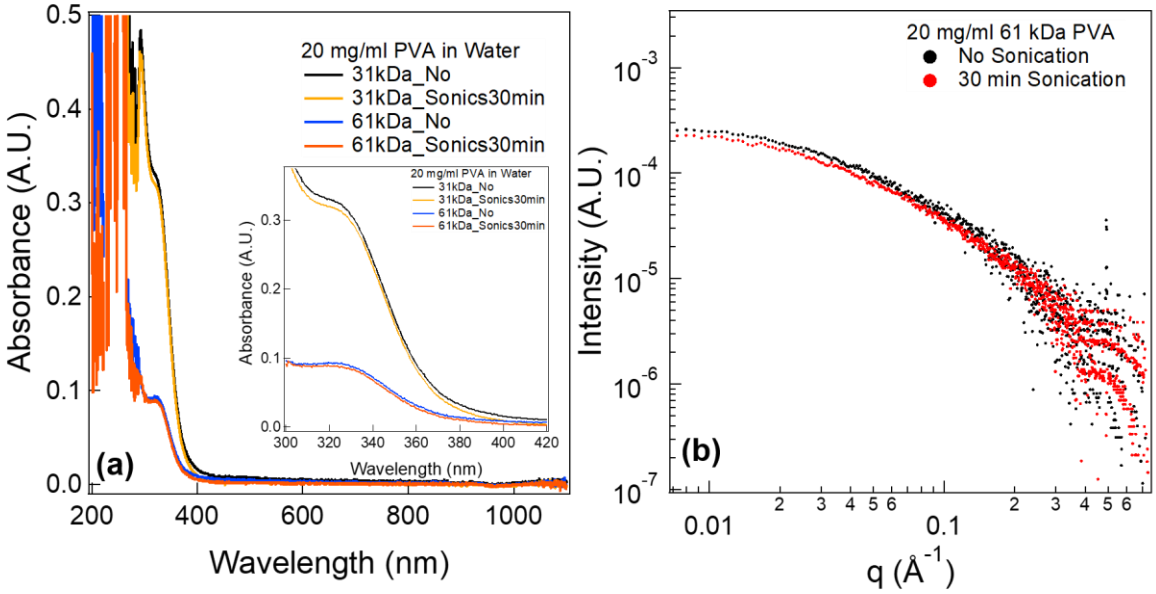

Figure 9.7. (a) UV-vis of 20 mg/ml PVA with two different molecular weights with and without application of 30 min sonication in bath. The inset image shows the enlarge figure around absorption peaks. (b) Small angle x-ray scattering of 61 kDa PVA samples with and without 30 min sonication in bath.

Besides water soluble conjugated polymers, proteins can also be assembled under ultrasound. The crystallization of protein is important for structure characterization using x-ray scattering. Figure 9.8 (a) and (b) show 10 mg/ml and 100 mg/ml lysozyme in water under a sweep of varied ultrasound pressures. For 10 mg/ml sample, an increase in intensity and a change of slope is observed after ultrasound application at the low-q region. This indicates that the formation of a larger structure is intrigued by acoustic wave. With higher lysozyme concentration, the data becomes less noisy and a small increase appears after 2 MPa pressure application. At higher pressures, the change of slope becomes more obvious. It is interesting to note that when lysozyme is dissolved into stock solution made of sodium chloride and sodium acetate, which is usually used in biological experiments, the effect of ultrasound is changed. In Figure 9.8 (c), a decrease of both the intensity and the slope at low-q region are observed with low peak negative pressures. Starting

from 6 MPa, the intensity starts to gradually increase. After the pressure sweep, the scattering curve almost overlaps with the starting point. More investigations are needed to identify the structural change that alters the scattering profiles during ultrasound application. The scattering profiles of the stock solution under ultrasound is shown in (d), which does not show much change by varying the peak negative pressure.

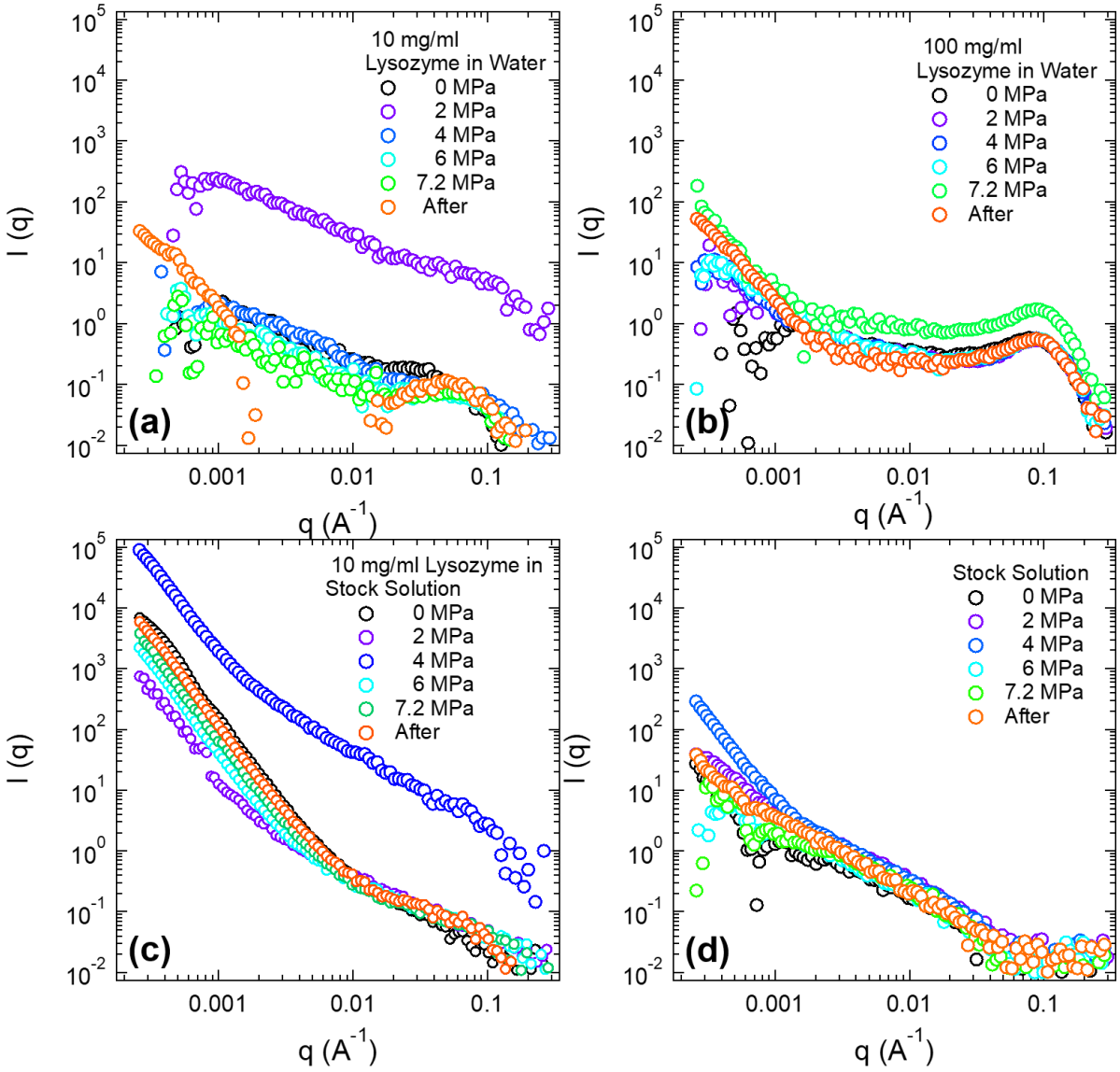

Figure 9.8. Ultra-small angle x-ray scattering profiles of (a) 10 mg/ml and (b) 100 mg/ml Lysozyme dissolved in water, as well as (c) 10 mg/ml lysozyme in stock solution and (d) pure stock solution under ultrasound with different peak negative pressures. The stock solution is prepared with 200 mM sodium acetate and 25 mg/ml sodium chloride in water.

9.5 EFFECT OF ULTRASOUND ON SMALL MOLECULES

Small bulky molecular can assemble into very ordered sheets or nanoribbons using reprecipitation method by mixing poor solvents to good solvents to induce assembly.[9,10] It has been found that during this assembly using reprecipitation method of PCBM, acoustic wave can induce better ordered nanoribbons.[11] The effect of structural change of this molecule using well characterized acoustic wave is investigated in Figure 9.9. The PCBM sample was dissolved in 1,2-dichlorobenzene at 5 mg/ml. Then methanol is added into PCBM solution with 1:1 volume ratio. The solution is divided into two groups. One is used for control without application of any ultrasound. The other one is irradiated with ultrasound of 6.8 MPa peak negative pressure in the sample environment that is described in Chapter 4. A sharp absorption peak is observed at ~ 430 nm, followed by a large and broad absorption peak between 450 nm and 650 nm. Another small peak is visible at ~700 nm. No obvious color change shows up in both optical photograph and UV-vis absorption spectra.

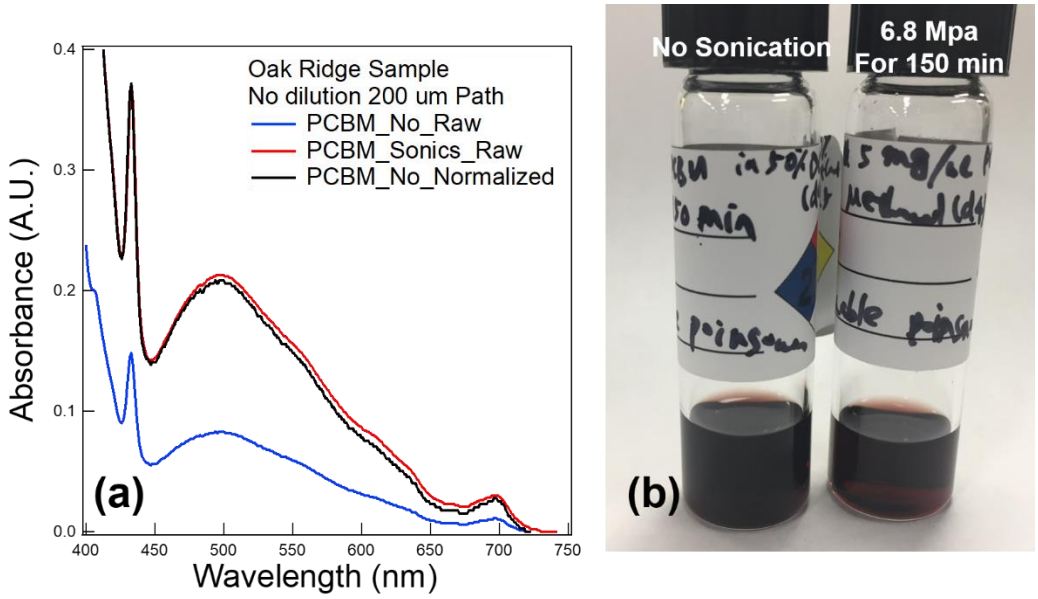

Figure 9.9. (a) UV-vis spectra and (b) microscopic photograph of 2.5 mg/ml PCBM in a mixture of 50 vol% 1,2-dichlorobenzene and 1,2-methanol.

The samples that are irradiated with ultrasound and without any treatment are both characterized by SANS measurement in Figure 9.10. An increase in intensity is observed after ultrasound treatment. It is clear that ultrasound induces structural change of PCBM. The increased intensity can be from the assembled larger structure after ultrasound. This preliminary data highlights the importance of using ultrasound to assist the assembly of small molecules to enhance their charge transport. At the same time, scattering techniques is found to be a great way to characterize the assembled structures, since it is hard to distinguish the sample structures formed with and without ultrasound under sTEM (Figure 9.11). From sTEM images, very thin sheets are observed for both samples. It seems that without sonication, fibril structures coexist with sheets, however, it is not very convincing that structural difference exists in sTEM images. In order to confirm those findings, more investigations are needed. Efforts can be devoted to exploring the mechanism how

ultrasound assists the assembly of this type of small molecules. The level of supersaturation, poor solvent polarity (it is reported that the only methanol helps the formation into nanoribbons with ultrasound [11]), acoustic negative pressure, acoustic wave frequency, as well the molecular structures of PCBM by using different derivatives to understand how the assembled structures are affected.

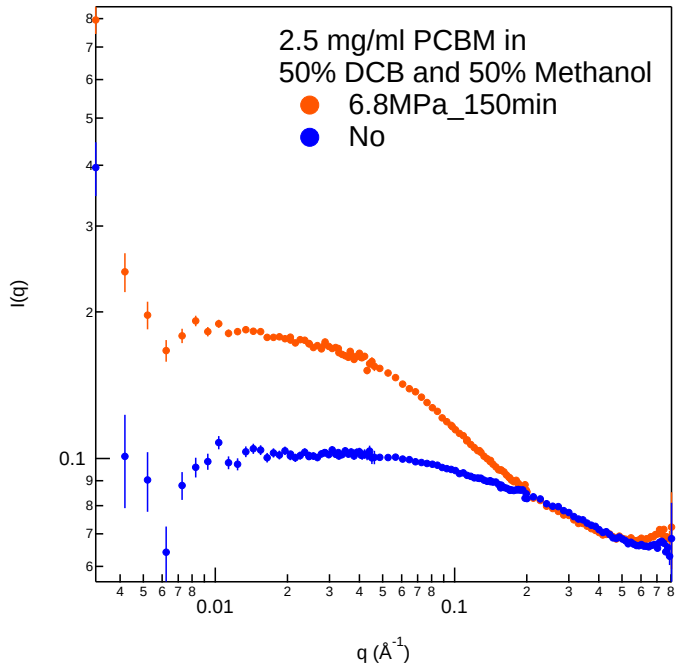

Figure 9.10. 1-D small angle neutron scattering profiles of PCBM sample sonicated with 6.8 MPa and without ultrasound.

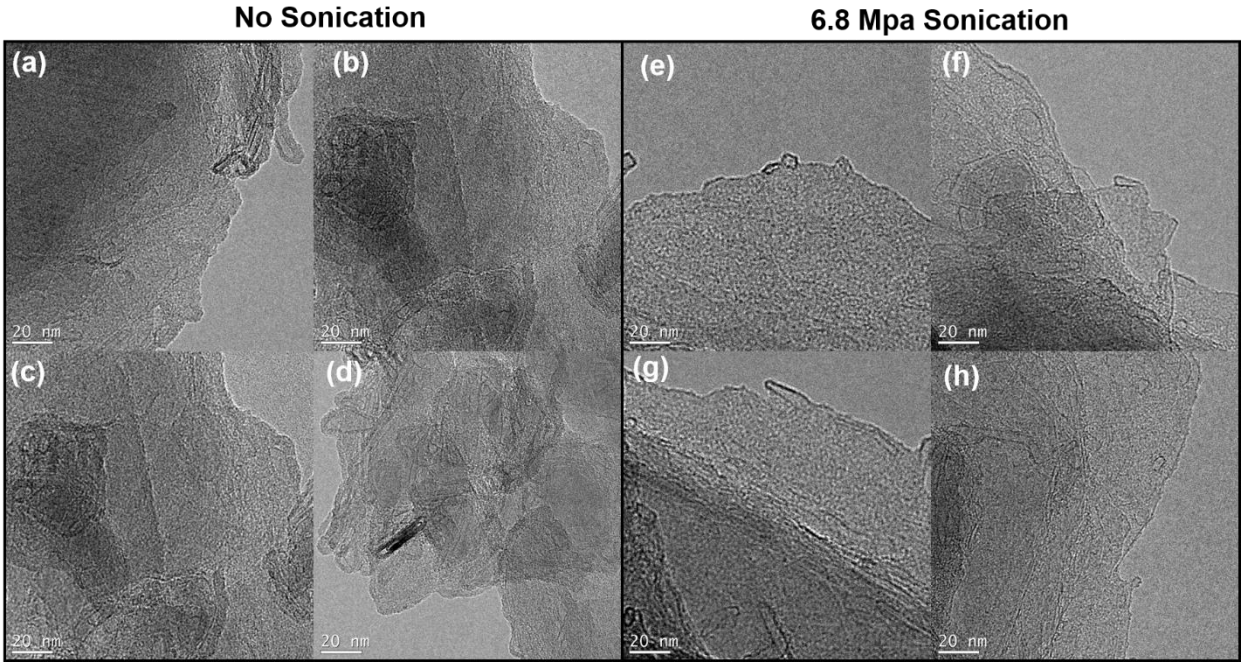

Figure 9.11. sTEM images of PCBM samples with and without ultrasound application.

Bibliography

A Guinier, G. F. Small-Angle Scattering of X-Rays; John Wiley & Sons, Inc., 1955.

Abbel, R.; De Vries, I.; Langen, A.; Kirchner, G.; T'Mannetje, H.; Gorter, H.; Wilson, J.; Groen, P. Toward High Volume Solution Based Roll-to-Roll Processing of OLEDs. J. Mater. Res. 2017, 32 (12), 2219–2229 DOI: 10.1557/jmr.2017.204.

Ahmadi, F.; McLoughlin, I. V.; Chauhan, S.; Ter-Haar, G. Bio-Effects and Safety of Low Intensity, Low Frequency Ultrasonic Exposure. Prog. Biophys. Mol. Biol. 2012 DOI: 10.1016/j.pbiomolbio.2012.01.004.

Ahmed, W.; Kooij, E. S.; Van Silfhout, A.; Poelsema, B. Quantitative Analysis of Gold Nanorod Alignment after Electric Field-Assisted Deposition. Nano Lett. 2009, 9 (11), 3786–3794 DOI: 10.1021/nl901968e.

Alignment, N. I. C.; Defined, H. T. N.; Lithography, N. Nano-Confinement Induced Chain Alignment in Ordered P3HT Nanostructures Defined by Nanoimprint Lithography. 2009, 3 (10), 3085–3090.

Allen, M. J.; Tung, V. C.; Kaner, R. B. Honeycomb Carbon: A Review of Graphene. Chem. Rev. 2010, 110 , 132–145 DOI: 10.1021/cr900070d.

Andersson, P.; Berggren, M.; Kugler, T. Switchable Optical Polarizer Based on Electrochromism in Stretch-Aligned Polyaniline. Appl. Phys. Lett. 2003, 83 (7), 1307 DOI: 10.1063/1.1602556.

Aoyanagi, Y.; Okumura, K. Simple Model for the Mechanics of Spider Webs. Phys. Rev. Lett. 2010, 104 (3), 1–4 DOI: 10.1103/PhysRevLett.104.038102.

Balint, R.; Cassidy, N. J.; Cartmell, S. H. Conductive Polymers: Towards a Smart Biomaterial for Tissue Engineering. Acta Biomater. 2014, 10 (6), 2341–2353 DOI: 10.1016/j.actbio.2014.02.015.

Battaglia, C.; Cuevas, A.; Wolf, S. De. Environmental Science Status and Perspectives. Energy Environ. Sci. 2016, 9, 1552–1576 DOI: 10.1039/C5EE03380B.

Beachley, V.; Wen, X. Effect of Electrospinning Parameters on the Nanofiber Diameter and Length. Mater. Sci. Eng. C 2009, 29 (3), 663–668 DOI: 10.1016/j.msec.2008.10.037.

Bhardwaj, N.; Kundu, S. C. Electrospinning : A Fascinating Fi Ber Fabrication Technique. 2010, 28, 325–347 DOI: 10.1016/j.biotechadv.2010.01.004.

Bhattacharyya, D.; Howden, R. M.; Borrelli, D. C.; Gleason, K. K. Vapor Phase Oxidative Synthesis of Conjugated Polymers and Applications. J. Polym. Sci. Part B Polym. Phys. 2012, 50 (19), 1329–1351 DOI: 10.1002/polb.23138.

Biomechanical, H. Hybrid Nanogenerator for Concurrently. 2010, 4 (7), 3647–3652.

Brinkmann, M.; Aldakov, D.; Chandezon, F. Fabrication of Oriented and Periodic Hybrid Nanostructures of Regioregular Poly(3-Hexylthiophene) and CdSe Nanocrystals by Directional Epitaxial Solidification. Adv. Mater. 2007, 19 (22), 3819–3823 DOI: 10.1002/adma.200700311.

Brown, R. B.; Audet, J. Current Techniques for Single-Cell Lysis. J. R. Soc. Interface 2008, 5 (Suppl_2), S131–S138 DOI: 10.1098/rsif.2008.0009.focus.

Burt, J. P. H.; Al-ameen, T. A. K.; Pethig, R. An Optical Dielectrophoresis Spectrometer for Low -Frequency Measurements on Colloidal Suspensions. J. Phys. E Sci. Instrum. 1989, 22, 952–957 DOI: 10.1088/0022-3735/22/11/011.

Buzzeo, M. C.; Hardacre, C.; Compton, R. G. Extended Electrochemical Windows Made Accessible by Room Temperature Ionic Liquid/Organic Solvent Electrolyte Systems. ChemPhysChem 2006, 7 (1), 176–180 DOI: 10.1002/cphc.200500361.

Cao, Y.; Colaneri, N.; Heeger, a. J.; Smith, P. ‘“Plastic”’ Infrared Polarizers from Uniaxially Oriented Polyaniline Blends. Appl. Phys. Lett. 1994, 65 (16), 2001 DOI: 10.1063/1.112843.

Caupin, F.; Herbert, E. Cavitation in Water: A Review. Comptes Rendus Phys. 2006, 7 (9–10), 1000–1017 DOI: 10.1016/j.crhy.2006.10.015.

Chang, W.-S.; Link, S.; Yethiraj, A.; Barbara, P. F. Single Molecule Spectroscopy of Conjugated Polymer Chains in an Electric Field-Aligned Liquid Crystal. J. Phys. Chem. B 2008, 112, 448–453 DOI: 10.1021/jp076345m.

Charba, A.; Mumtaz, M.; Brochon, C.; Cramail, H.; Hadziioannou, G.; Cloutet, E. Preparation of Water-Free PEDOT Dispersions in the Presence of Reactive Polyisoprene Stabilizers. Langmuir 2014, 30 (42), 12474–12482 DOI: 10.1021/la502480r.

Chaudhari, S. R.; Griffin, J. M.; Broch, K.; Lesage, A.; Lemaur, V.; Dudenko, D.; Olivier, Y.; Sirringhaus, H.; Emsley, L.; Grey, C. P. Donor–acceptor Stacking Arrangements in Bulk and Thin-Film High-Mobility Conjugated Polymers Characterized Using Molecular Modelling and MAS and Surface-Enhanced Solid-State NMR Spectroscopy. Chem. Sci. 2017, 8 (4), 3126–3136 DOI: 10.1039/C7SC00053G.

Chen, M. S.; Lee, O. P.; Niskala, J. R.; Yiu, A. T.; Tassone, C. J.; Schmidt, K.; Beaujuge, P. M.; Onishi, S. S.; Toney, M. F.; Zettl, A.; Fréchet, J. M. J. Enhanced Solid-State Order and Field-Effect Hole Mobility through Control of Nanoscale Polymer Aggregation. J. Am. Chem. Soc. 2013, 135 (51), 19229–19236 DOI: 10.1021/ja4088665.

Chen, W.-R.; Butler, P. D.; Magid, L. J. Incorporating Intermicellar Interactions in the Fitting of SANS Data from Cationic Wormlike Micelles. Langmuir 2006, 22 (15), 6539–6548 DOI: 10.1021/la0530440.

Cheng, Q.; Gregan, E.; Byrne, H. Ultrasound-Assisted SWNTs Dispersion : Effects of Sonication Parameters and Solvent Properties Ultrasound-Assisted SWNTs Dispersion : Effects of Sonication Parameters and Solvent Properties. J. Phys. Chem. C 2010, 114 (19), 8821–8827.

Cho, J. H.; Lee, J.; Xia, Y.; Kim, B.; He, Y.; Renn, M. J.; Lodge, T. P.; Daniel Frisbie, C. Printable Ion-Gel Gate Dielectrics for Low-Voltage Polymer Thin-Film Transistors on Plastic. Nat. Mater. 2008, 7 (11), 900–906 DOI: 10.1038/nmat2291.

Choi, M.; Kim, Y.; Ha, C. Polymers for Flexible Displays : From Material Selection to Device Applications. 2008, 33, 581–630 DOI: 10.1016/j.progpolymsci.2007.11.004.

Chortos, A.; Bao, Z. Skin-Inspired Electronic Devices. Biochem. Pharmacol. 2014, 17 (7), 321–331 DOI: 10.1016/j.mattod.2014.05.006.

Chortos, A.; Liu, J.; Bao, Z. Pursuing Prosthetic Electronic Skin. Nat. Mater. 2016, No. July, 1–14 DOI: 10.1038/nmat4671.

Chou, H.; Nguyen, A.; Chortos, A.; To, J. W. F.; Lu, C.; Mei, J.; Kurosawa, T.; Bae, W.; Tok, J. B.; Bao, Z. Tactile Sensing. Nat. Commun. 2015, 6, 1–10 DOI: 10.1038/ncomms9011.

Chu, P.; Wang, G.; Fu, B.; Choi, D.; Park, J. O.; Srinivasarao, M.; Reichmanis, E. Synergistic Effect of Regioregular and Regiorandom Poly (3-Hexylthiophene) Blends for High Performance Flexible Organic Field Effect Transistors. 2016, 1–12 DOI: 10.1002/aelm.201500384.

Cimrová, V.; Remmers, M.; Neher, D.; Wegner, G. Polarized Light Emission from LEDs Prepared by the Langmuir-Blodgett Technique. Adv. Mater. 1996, 8 (2), 146–149 DOI: 10.1002/adma.19960080209.

Clark, J.; Chang, J. F.; Spano, F. C.; Friend, R. H.; Silva, C. Determining Exciton Bandwidth and Film Microstructure in Polythiophene Films Using Linear Absorption Spectroscopy. Appl. Phys. Lett. 2009, 94 (16), 2007–2010 DOI: 10.1063/1.3110904.

Coakley, B. K. M.; Srinivasan, B. S.; Ziebarth, J. M.; Goh, C.; Liu, Y.; Mcgehee, M. D. Enhanced Hole Mobility in Regioregular Polythiophene Infiltrated in Straight Nanopores **. 2005, 1927–1932 DOI: 10.1002/adfm.200500364.

Cranford, S. W.; Tarakanova, A.; Pugno, N. M.; Buehler, M. J. Nonlinear Material Behaviour of Spider Silk Yields Robust Webs. Nature 2012, 482 (7383), 72–76 DOI: 10.1038/nature10739.

Crespo, R.; Martins, P. M.; Gales, L.; Rocha, F.; Damas, A. M. Potential Use of Ultrasound to Promote Protein Crystallization. J. Appl. Crystallogr. 2010, 43 (6), 1419–1425 DOI: 10.1107/S0021889810040951.

Crossland, E. J. W.; Tremel, K.; Fischer, F.; Rahimi, K.; Reiter, G.; Steiner, U.; Ludwigs, S. Anisotropic Charge Transport in Spherulitic Poly(3-Hexylthiophene) Films. Adv. Mater. 2012, 24 (6), 839–844 DOI: 10.1002/adma.201104284.

Czechowska-Biskup, R.; Rokita, B.; Lotfy, S.; Ulanski, P.; Rosiak, J. M. Degradation of Chitosan and Starch by 360-KHz Ultrasound. Carbohydr. Polym. 2005, 60 (2), 175–184 DOI: 10.1016/j.carbpol.2004.12.001.

Dale A. C. Brownson, C. E. B. The Handbook of Graphene Electrochemistry; 2014.

Das, P. R.; Komsiyska, L.; Osters, O.; Wittstock, G. PEDOT: PSS as a Functional Binder for Cathodes in Lithium Ion Batteries. J. Electrochem. Soc. 2015, 162 (4), A674–A678 DOI: 10.1149/2.0581504jes.

De La Iglesia, P.; Jaeger, V. W.; Xi, Y.; Pfaendtner, J.; Pozzo, L. D. Structure Characterization and Properties of Metal-Surfactant Complexes Dispersed in Organic Solvents. Langmuir 2015, 31 (33), 9006–9016 DOI: 10.1021/acs.langmuir.5b02071.

Dear, J. P.; Field, J. E. A Study of the Collapse of Arrays of Cavities. J. Fluid Mech. 1988, 190 (1), 409 DOI: 10.1017/S0022112088001387.

Diao, Y.; Tee, B. C.-K.; Giri, G.; Xu, J.; Kim, D. H.; Becerril, H. a; Stoltenberg, R. M.; Lee, T. H.; Xue, G.; Mannsfeld, S. C. B.; Bao, Z. Solution Coating of Large-Area Organic Semiconductor Thin Films with Aligned Single-Crystalline Domains. Nat. Mater. 2013, 12 (7), 665–671 DOI: 10.1038/nmat3650.

Dolev, M. MBE Growth of Ultra-Low Disorder 2DEG with Mobility Exceeding. 2009, 311, 1658–1661 DOI: 10.1016/j.jcrysgro.2008.09.151.

Elum, Z. A.; Momodu, A. S. Climate Change Mitigation and Renewable Energy for Sustainable Development in Nigeria: A Discourse Approach. Renew. Sustain. Energy Rev. 2017, 76 (March), 72–80 DOI: 10.1016/j.rser.2017.03.040.

Ensikat, H. J.; Ditsche-kuru, P.; Neinhuis, C.; Barthlott, W. Superhydrophobicity in Perfection: The Outstanding Properties of the Lotus Leaf. 2011, 152–161 DOI: 10.3762/bjnano.2.19.

Ferdous, S.; Liu, F.; Wang, D.; Russell, T. P. Solvent-Polarity-Induced Active Layer Morphology Control in Crystalline Diketopyrrolopyrrole-Based Low Band Gap Polymer Photovoltaics. Adv. Energy Mater. 2014, 4 (2), 1–10 DOI: 10.1002/aenm.201300834.

Fischer, F. S. U.; Tremel, K.; Sommer, M.; Crossland, E. J. W.; Ludwigs, S. Directed Crystallization of Poly(3-Hexylthiophene) in Micrometre Channels under

Confinement and in Electric Fields. Nanoscale 2012, 4 (6), 2138–2144 DOI: 10.1039/c2nr12037b.

Gaikwad, A. M.; Steingart, D. A.; Nga Ng, T.; Schwartz, D. E.; Whiting, G. L. A Flexible High Potential Printed Battery for Powering Printed Electronics. Appl. Phys. Lett. 2013, 102 (23) DOI: 10.1063/1.4810974.

Gaikwad, S. G.; Pandit, A. B. Ultrasound Emulsification: Effect of Ultrasonic and Physicochemical Properties on Dispersed Phase Volume and Droplet Size. Ultrason. Sonochem. 2008, 15 (4), 554–563 DOI: 10.1016/j.ultsonch.2007.06.011.

Galagan, Y.; Fledderus, H.; Gorter, H.; Mannetje, H.; Shanmugam, S.; Mandamparambil, R.; Bosman, J. Roll-to-Roll Slot – Die Coated Organic Photovoltaic (OPV) Modules with High Geometrical Fill Factors. 2015, 834–842 DOI: 10.1002/ente.201500150.

Geng, J.; Zhou, E.; Li, G.; Lam, J. W. Y.; Tang, B. Z. Electric-Field-Induced Molecular Alignment of Side-Chain Liquid-Crystalline Polyacetylenes Containing Biphenyl Mesogens. J. Polym. Sci. Part B Polym. Phys. 2004, 42, 1333–1341 DOI: 10.1002/polb.20021.

George, O. Principles of Polymerization; John Wiley & Sons, Inc., 2004.

Godbert, N.; Burn, P. L.; Gilmour, S.; Markham, J. P. J.; Samuel, I. D. W. Polarized Organic Electroluminescence: Ordering from the Top. Appl. Phys. Lett. 2003, 83 (26), 5347 DOI: 10.1063/1.1632025.

Gopinadhan, M.; Choo, Y.; Osuji, C. O. Strong Orientational Coupling of Block Copolymer Microdomains to Smectic Layering Revealed by Magnetic Field Alignment. 2016 DOI: 10.1021/acsmacrolett.5b00924.

Gracia-Espino, E.; Barzegar, H. R.; Sharifi, T.; Yan, A.; Zettl, A.; Wågberg, T. Fabrication of One-Dimensional Zigzag [6,6]-Phenyl-C 61 -Butyric Acid Methyl Ester Nanoribbons from Two-Dimensional Nanosheets. ACS Nano 2015, 9 (10), 10516–10522 DOI: 10.1021/acsnano.5b04972.

H. Benoit. La Diffusion de La Lumiere Par Des Macromolecules En Chaines En Solution Dans Un Bon Solvant. Comptes Rendus 1957, 245, 2244–2247.

Hah, J. H.; Mayya, S.; Hata, M.; Jang, Y.-K.; Kim, H.-W.; Ryoo, M.; Woo, S.-G.; Cho, H.-K.; Moon, J.-T. Converging Lithography by Combination of Electrostatic Layer-by-Layer Self-Assembly and 193 Nm Photolithography: Top-down Meets Bottom-Up. J. Vac. Sci. Technol. B Microelectron. Nanom. Struct. 2006, 24 (5), 2209 DOI: 10.1116/1.2244541.

Hammouda, B. Probing Nanoscale Structures-The SANS Toolbox.

Hammouda, B. SANS from Homogeneous Polymer Mixtures - A Unified Overview. Adv. Polym. Sci. 1993, 106, 87–133.

Han, Y.; Guo, Y.; Chang, Y.; Geng, Y.; Su, Z. Chain Folding in Poly(3-Hexylthiophene) Crystals. Macromolecules 2014, 47 (11), 3708–3712 DOI: 10.1021/ma5006149.

Hatchett, D. W.; Josowicz, M.; Janata, J. Acid Doping of Polyaniline: Spectroscopic and Electrochemical Studies. J. Phys. Chem. B 1999, 103 (50), 10992–10998 DOI: 10.1021/jp991110z.

He, Z.; Xiao, B.; Liu, F.; Wu, H.; Yang, Y.; Xiao, S.; Wang, C.; Russell, T. P.; Cao, Y. Single-Junction Polymer Solar Cells with High Efficiency and Photovoltage. Nat. Photonics 2015, 9 (3), 174–179 DOI: 10.1038/nphoton.2015.6.

Herrmann, B. W. A. Review New Materials ± The Potential of Modern Synthetic Chemistry *. 1998, 549–558 DOI: 10.1002.

Hilbert, M.; Lopez, P. The World's Technological Capacity to Store, Communicate, and Compute Information. Science (80-.). 2011, 332 (6025), 60–65 DOI: 10.1126/science.1200970.

Ho, C. C.; Evans, J. W.; Wright, P. K. Direct Write Dispenser Printing of a Zinc Microbattery with an Ionic Liquid Gel Electrolyte. J. Micromechanics Microengineering 2010, 20 (10), 104009 DOI: 10.1088/0960-1317/20/10/104009.

Hofmann, S.; Ducati, C.; Neill, R. J.; Piscanec, S.; Ferrari, A. C.; Geng, J.; Dunin-Borkowski, R. E.; Robertson, J. Gold Catalyzed Growth of Silicon Nanowires by Plasma Enhanced Chemical Vapor Deposition. J. Appl. Phys. 2003, 94 (9), 6005–6012 DOI: 10.1063/1.1614432.

Hou, D.; Chang, H. Ac Field Enhanced Protein Crystallization. 2014, 23–25 DOI: 10.1063/1.2938887.

Hu, H.; Zhao, K.; Fernandes, N.; Boufflet, P.; Bannock, J. H.; Yu, L.; de Mello, J. C.; Stingelin, N.; Heeney, M.; Giannelis, E. P.; Amassian, A. Entanglements in Marginal Solutions: A Means of Tuning Pre-Aggregation of Conjugated Polymers with Positive Implications for Charge Transport. J. Mater. Chem. C 2015, 3 (28), 7394–7404 DOI: 10.1039/C5TC01425E.

Hu, L.; Li, J.; Liu, J.; Grüner, G.; Marks, T. Flexible Organic Light-Emitting Diodes with Transparent Carbon Nanotube Electrodes: Problems and Solutions. Nanotechnology 2010, 21 (15), 155202 DOI: 10.1088/0957-4484/21/15/155202.

Hu, Z.; Muls, B.; Gence, L.; Serban, D. a.; Hofkens, J.; Melinte, S.; Nysten, B.; Demoustier-Champagne, S.; Jonas, A. M. High-Throughput Fabrication of Organic Nanowire Devices with Preferential Internal Alignment and Improved Performance. Nano Lett. 2007, 7 (12), 3639–3644 DOI: 10.1021/nl071869j.

Hu, Z.; Willard, A. P.; Ono, R. J.; Bielawski, C. W.; Rossky, P. J.; Vanden Bout, D. A. An Insight into Non-Emissive Excited States in Conjugated Polymers. Nat. Commun. 2015, 6, 1–9 DOI: 10.1038/ncomms9246.

Hutchins, D. O.; Weidner, T.; Baio, J.; Polishak, B.; Acton, O.; Cernetic, N.; Ma, H.; Jen, A. K.-Y. Effects of Self-Assembled Monolayer Structural Order, Surface Homogeneity and Surface Energy on Pentacene Morphology and Thin Film Transistor Device Performance. J. Mater. Chem. C 2013, 1 (1), 101–113 DOI: 10.1039/C2TC00378C.

Iglesia, P. D. La; Pozzo, D. C. Effects of Supersaturation on the Structure and Properties of Poly(9,9-Dioctyl Fluorene) Organogels. Soft Matter 2013, 9 (47), 11214 DOI: 10.1039/c3sm51753e.

Ilavsky, J.; Jemian, P. R. Irena: Tool Suite for Modeling and Analysis of Small-Angle Scattering. J. Appl. Crystallogr. 2009, 42 (2), 347–353 DOI: 10.1107/S0021889809002222.

Ilavsky, J.; Jemian, P. R.; Allen, A. J.; Zhang, F.; Levine, L. E.; Long, G. G. Ultra-Small-Angle X-Ray Scattering at the Advanced Photon Source. J. Appl. Crystallogr. 2009, 42 (3), 469–479 DOI: 10.1107/S0021889809008802.

Israelavhvili, J. N. No Title. In Intermolecular and surface forces; 2009; p 628.

Jamshidi, A.; Pauzauskie, P. J.; Schuck, P. J.; Ohta, A. T.; Chiou, P.-Y.; Chou, J.; Yang, P.; Wu, M. C. Dynamic Manipulation and Separation of Individual Semiconducting and Metallic Nanowires. Nat. Photonics 2008, 2, 86–89 DOI: 10.1038/nphoton.2007.277.

Jang, J.; Oh, J. Y.; Kim, S. K.; Choi, Y. J.; Yoon, S. Y.; Kim, C. O. No Title. Nature 1998, 395 (6701), 481–483 DOI: 10.1038/26711.

Jiang, S.; Duan, G.; Kuhn, U.; Mörl, M.; Altstädt, V.; Yarin, A. L.; Greiner, A. Spongy Gels by a Top-Down Approach from Polymer Fibrous Sponges. Angew. Chemie - Int. Ed. 2017, 56 (12), 3285–3288 DOI: 10.1002/anie.201611787.

Jiang, Z. GIXSGUI : A MATLAB Toolbox for Grazing-Incidence X-Ray Scattering Data Visualization and Reduction, and Indexing of Buried Three-Dimensional Periodic Nanostructured Films. J. Appl. Crystallogr. 2015, 48 (3), 917–926 DOI: 10.1107/S1600576715004434.

Jiang, Z.; Li, X.; Strzalka, J.; Sprung, M.; Sun, T.; Sandy, A. R.; Narayanan, S.; Lee, D. R.; Wang, J. The Dedicated High-Resolution Grazing-Incidence X-Ray Scattering Beamline 8-ID-E at the Advanced Photon Source. J. Synchrotron Radiat. 2012, 19 (4), 627–636 DOI: 10.1107/S0909049512022017.

Jones, T. B. Electromechanics of Particles; Cambridge University Press, 1995.

Jose da Silva, W.; Kim, H. P.; Rashid bin Mohd Yusoff, A.; Jang, J. Transparent Flexible Organic Solar Cells with 6.87% Efficiency Manufactured by an All-Solution Process. Nanoscale 2013, 5 (19), 9324 DOI: 10.1039/c3nr03011c.

Kaddami, H.; Raihane, M. Electric Field Alignment of Nano Fi Brillated Cellulose (NFC) in Silicone Oil: Impact on Electrical Properties. ACS Appl. Mater. Interfaces 2014, 6 (12), 9418–9425.

Kaltenbrunner, M.; White, M. S.; Głowacki, E. D.; Sekitani, T.; Someya, T.; Sariciftci, N. S.; Bauer, S. Ultrathin and Lightweight Organic Solar Cells with High Flexibility. Nat. Commun. 2012, 3 (1), 770 DOI: 10.1038/ncomms1772.

Kim, D. H.; Han, J. T.; Park, Y. D.; Jang, Y.; Cho, J. H.; Hwang, M.; Cho, K. Single-Crystal Polythiophene Microwires Grown by Self-Assembly. Adv. Mater. 2006, 18 (6), 719–723 DOI: 10.1002/adma.200502442.

Kim, J.; Park, H.-S.; Kim, T.-H.; Yeol Kim, S.; Song, H.-K. An Inter-Tangled Network of Redox-Active and Conducting Polymers as a Cathode for Ultrafast Rechargeable Batteries. Phys. Chem. Chem. Phys. 2014, 16 (11), 5295 DOI: 10.1039/c3cp54624a.

Kiriy, N.; Jähne, E.; Adler, H. J.; Schneider, M.; Kiriy, A.; Gorodyska, G.; Minko, S.; Jehnichen, D.; Simon, P.; Fokin, A. A.; Stamm, M. One-Dimensional Aggregation of Regioregular Polyalkylthiophenes. Nano Lett. 2003, 3 (6), 707–712 DOI: 10.1021/nl0341032.

Kitayama, H.; Yoshimura, Y.; So, M.; Sakurai, K.; Yagi, H.; Goto, Y. A Common Mechanism Underlying Amyloid Fibrillation and Protein Crystallization Revealed by the Effects of Ultrasonication. Biochim. Biophys. Acta - Proteins Proteomics 2013, 1834 (12), 2640–2646 DOI: 10.1016/j.bbapap.2013.09.016.

Kleinhenz, N.; Persson, N.; Xue, Z.; Chu, P. H.; Wang, G.; Yuan, Z.; McBride, M. A.; Choi, D.; Grover, M. A.; Reichmanis, E. Ordering of Poly(3-Hexylthiophene) in Solutions and Films: Effects of Fiber Length and Grain Boundaries on Anisotropy and Mobility. Chem. Mater. 2016, 28 (11), 3905–3913 DOI: 10.1021/acs.chemmater.6b01163.

Kline, S. R. Reduction and Analysis of SANS and USANS Data Using IGOR Pro. J. Appl. Crystallogr. 2006, 39 (6), 895–900 DOI: 10.1107/S0021889806035059.

Kumar, R.; Shin, J.; Yin, L.; You, J.-M.; Meng, Y. S.; Wang, J. All-Printed, Stretchable Zn-Ag 2 O Rechargeable Battery via Hyperelastic Binder for Self-Powering Wearable Electronics. Adv. Energy Mater. 2017, 7 (8), 1602096 DOI: 10.1002/aenm.201602096.

Kurotani, M.; Hirasawa, I. Polymorph Control of Sulfamerazine by Ultrasonic Irradiation. J. Cryst. Growth 2008, 310 (21), 4576–4580 DOI: 10.1016/j.jcrysgro.2008.08.002.

Lang, C.; Fang, J.; Shao, H.; Ding, X.; Lin, T. High-Sensitivity Acoustic Sensors from Nanofibre Webs. Nat. Commun. 2016, 7, 11108 DOI: 10.1038/ncomms11108.

Lee, M.; Hong, J.; Lopez, J.; Sun, Y.; Feng, D.; Lim, K.; Chueh, W. C.; Toney, M. F.; Cui, Y.; Bao, Z. High-Performance Sodium-Organic Battery by Realizing Four-Sodium Storage in Disodium Rhodizonate. Nat. Energy 2017, 2 (11), 861–868 DOI: 10.1038/s41560-017-0014-y.

Lee, M.; Jeon, H.; Jang, M.; Yang, H. A Physicochemical Approach Toward Extending Conjugation and the Ordering of Solution-Processable Semiconducting Polymers. ACS Appl. Mater. Interfaces 2016, 8 (7), 4819–4827 DOI: 10.1021/acsami.5b12552.

Lei, Y.; Deng, P.; Li, J.; Lin, M.; Zhu, F.; Ng, T.; Lee, C.; Ong, B. S. Solution-Processed Donor-Acceptor Polymer Nanowire Network Semiconductors For High-Performance Field-Effect Transistors. Sci. Rep. 2016, 6 (1), 24476 DOI: 10.1038/srep24476.

Lei, Y.; Deng, P.; Zhang, Q.; Xiong, Z.; Li, Q.; Mai, J.; Lu, X.; Zhu, X.; Ong, B. S. Hydrocarbons-Driven Crystallization of Polymer Semiconductors for Low-Temperature Fabrication of High-Performance Organic Field-Effect Transistors. Adv. Funct. Mater. 2018, 28 (15), 1–9 DOI: 10.1002/adfm.201706372.

Leung, P.; Shah, A. A.; Sanz, L.; Flox, C.; Morante, J. R.; Xu, Q.; Mohamed, M. R.; Ponce de León, C.; Walsh, F. C. Recent Developments in Organic Redox Flow Batteries: A Critical Review. J. Power Sources 2017, 360, 243–283 DOI: 10.1016/j.jpowsour.2017.05.057.

Li, J.; Zhao, Y.; Tan, H. S.; Guo, Y.; Di, C.-A.; Yu, G.; Liu, Y.; Lin, M.; Lim, S. H.; Zhou, Y.; Su, H.; Ong, B. S. A Stable Solution-Processed Polymer Semiconductor with Record High-Mobility for Printed Transistors. Sci. Rep. 2012, 2, 754 DOI: 10.1038/srep00754.

Li, J.-H.; Xi, Y.; Pozzo, L. D.; Xu, J.-T.; Luscombe, C. K. Macroscopically Aligned Nanowire Arrays of π-Conjugated Polymers via Shear-Enhanced Crystallization. J. Mater. Chem. C 2017 DOI: 10.1039/C7TC01419H.

Li, J.-H.; Xi, Y.; Pozzo, L. D.; Xu, J.-T.; Luscombe, C. K. Macroscopically Aligned Nanowire Arrays of π-Conjugated Polymers via Shear-Enhanced Crystallization. J. Mater. Chem. C 2017 DOI: 10.1039/C7TC01419H.

Li, J.-L.; Yuan, B.; Liu, X.-Y.; Xu, H.-Y. Microengineering of Supramolecular Soft Materials by Design of the Crystalline Fiber Networks. Cryst. Growth Des. 2002, 10 (6), 2699–2706 DOI: 10.1021/cg100188w.

Li, S.; Xu, Q.; Uchaker, E.; Cao, X.; Cao, G. Comparison of Amorphous, Pseudohexagonal and Orthorhombic Nb 2 O 5 for High-Rate Lithium Ion Insertion. CrystEngComm 2016, 18 (14), 2532–2540 DOI: 10.1039/C5CE02069G.

Lim, J. A.; Liu, F.; Ferdous, S.; Muthukumar, M.; Briseno, A. L. Polymer Semiconductor Crystals. Mater. Today 2010, 13 (5), 14–24 DOI: 10.1016/S1369-7021(10)70080-8.

Lin, C.-Y.; Schick, M. Self-Consistent Field Study of the Alignment by an Electric Field of a Cylindrical Phase of Block Copolymer. J. Chem. Phys. 2006, 125 (3), 34902 DOI: 10.1063/1.2214718.

Lin, F.; Zhu, Z.; Zhou, X.; Qiu, W.; Niu, C.; Hu, J.; Dahal, K.; Wang, Y.; Zhao, Z.; Ren, Z.; Litvinov, D.; Liu, Z.; Wang, Z. M.; Bao, J. Orientation Control of Graphene Flakes by Magnetic Field: Broad Device Applications of Macroscopically Aligned Graphene. Adv. Mater. 2017, 29 (1), 1–6 DOI: 10.1002/adma.201604453.

Lin, M. C.; Gong, M.; Lu, B.; Wu, Y.; Wang, D. Y.; Guan, M.; Angell, M.; Chen, C.; Yang, J.; Hwang, B. J.; Dai, H. An Ultrafast Rechargeable Aluminium-Ion Battery. Nature 2015, 520 (7547), 325–328 DOI: 10.1038/nature14340.

Lipomi, D. J.; Bao, Z. Stretchable, Elastic Materials and Devices for Solar Energy Conversion. Energy Environ. Sci. 2011, 4 (9), 3314 DOI: 10.1039/c1ee01881g.

Liu, J.; Arif, M.; Zou, J.; Khondaker, S. I.; Zhai, L. Controlling Poly(3-Hexylthiophene) Crystal Dimension: Nanowhiskers and Nanoribbons. Macromolecules 2009, 42 (24), 9390–9393 DOI: 10.1021/ma901955c.

Liu, L.; Lo, C.-F.; Xi, Y.; Ren, F.; Pearton, S. J.; Laboutin, O.; Cao, Y.; Johnson, J. W.; Kravchenko, I. I. Effect of Buffer Structures on AlGaN/GaN High Electron Mobility Transistor Reliability. J. Vac. Sci. Technol. B Microelectron. Nanom. Struct. 2013, 31 (1), 011805.

Liu, Q.; Shinkle, A. A.; Li, Y.; Monroe, C. W.; Thompson, L. T.; Sleightholme, A. E. S. Non-Aqueous Chromium Acetylacetonate Electrolyte for Redox Flow Batteries. Electrochem. commun. 2010, 12 (11), 1634–1637 DOI: 10.1016/j.elecom.2010.09.013.

Liu, X. Y.; Sawant, P. D. Mechanism of the Formation of Self-Organized Microstructures in Soft Functional Materials. Adv. Mater. 2002, 14 (6), 421–426 DOI: 10.1002/1521-4095(20020318)14:6<421::AID-ADMA421>3.0.CO;2-7.

Liu, X. Y.; Sawant, P. D.; Tan, W. B.; Noor, I. B. M.; Pramesti, C.; Chen, B. H. Creating New Supramolecular Materials by Architecture of Three-Dimensional Nanocrystal Fiber Networks. J. Am. Chem. Soc. 2002, 124 (50), 15055–15063 DOI: 10.1021/ja0206137.

Lo, C. F.; Xi, Y.; Liu, L.; Pearton, S. J.; Doré, S.; Hsu, C. H.; Dabiran, A. M.; Chow, P. P.; Ren, F. Effect of Temperature on CO Sensing Response in Air Ambient by Using Zno Nanorod-Gated AlGaN/GaN High Electron Mobility Transistors. Sensors Actuators, B Chem. 2013, 176, 708–712.

Löffler, S.; Libberton, B.; Richter-Dahlfors, A. Organic Bioelectronic Tools for Biomedical Applications. Electronics 2015, 4 (4), 879–908 DOI: 10.3390/electronics4040879.

Luo, C.; Kyaw, A. K. K.; Perez, L. a.; Patel, S.; Wang, M.; Grimm, B.; Bazan, G. C.; Kramer, E. J.; Heeger, A. J. General Strategy for Self-Assembly of Highly Oriented Nanocrystalline Semiconducting Polymers with High Mobility. Nano Lett. 2014, 14 (5), 2764–2771 DOI: 10.1021/nl500758w.

Luo, C.; Kyaw, K. K.; Perez, L. a; Patel, S.; Wang, M.; Grimm, B.; Bazan, G. C.; Kramer, E. J.; Heeger, A. J. General Strategy for Self-Assembly of Highly Oriented Nanocrystalline Semiconducting Polymers with High Mobility. Nano Lett. 2014, 14, 2764 DOI: 10.1021/nl500758w.

Luo, H.; Yu, C.; Liu, Z.; Zhang, G.; Geng, H.; Yi, Y.; Broch, K.; Hu, Y.; Sadhanala, A.; Jiang, L.; Qi, P.; Cai, Z.; Sirringhaus, H.; Zhang, D. Remarkable Enhancement of Charge Carrier Mobility of Conjugated Polymer Field-Effect Transistors upon Incorporating an Ionic Additive. Sci. Adv. 2016, 2 (May), e1600076 DOI: 10.1126/sciadv.1600076.

Lvovich, V. F. Impedance Spectroscopy; John Wiley & Sons, Inc., 2012.

Machui, F.; Langner, S.; Zhu, X.; Abbott, S.; Brabec, C. J. Determination of the P3HT:PCBM Solubility Parameters via a Binary Solvent Gradient Method: Impact of Solubility on the Photovoltaic Performance. Sol. Energy Mater. Sol. Cells 2012, 100, 138–146 DOI: 10.1016/j.solmat.2012.01.005.

Marzouk, J.; Lucas, B.; Trigaud, T.; Pothier, A.; Bouclé, J.; Ratier, B. Simple Strategy to Tune the Charge Transport Properties of Conjugated Polymer/Carbon Nanotube Composites Using an Electric Field Assisted Deposition Technique. Polym. Int. 2014, 63 (February), 1378–1386 DOI: 10.1002/pi.4686.

Mas-Torrent, M.; Boer, D. Den; Durkut, M.; Hadley, P.; Schenning, a P. H. J. Field Effect Transistors Based on Poly(3-Hexylthiophene) at Different Length Scales. Nanotechnology 2004, 15 (4), S265–S269 DOI: 10.1088/0957-4484/15/4/028.

Mazzio, K. A.; Rice, A. H.; Durban, M. M.; Luscombe, C. K. Effect of Regioregularity on Charge Transport and Structural and Excitonic Coherence in Poly(3-Hexylthiophene) Nanowires. J. Phys. Chem. C 2015, 119 (27), 14911–14918 DOI: 10.1021/acs.jpcc.5b02914.

McCulloch, B.; Ho, V.; Hoarfrost, M.; Stanley, C.; Do, C.; Heller, W. T.; Segalman, R. A. Polymer Chain Shape of Poly(3-Alkylthiophenes) in Solution Using Small-Angle Neutron Scattering. Macromolecules 2013, 46 (5), 1899–1907 DOI: 10.1021/ma302463d.

Michor, E. L.; Berg, J. C. The Particle Charging Behavior of Ion-Exchanged Surfactants in Apolar Media. Colloids Surfaces A Physicochem. Eng. Asp. 2017, 512, 1–6 DOI: 10.1016/j.colsurfa.2016.10.032.

Mike, J. F.; Lutkenhaus, J. L. Recent Advances in Conjugated Polymer Energy Storage. J. Polym. Sci. Part B Polym. Phys. 2013, 51 (7), 468–480 DOI: 10.1002/polb.23256.

Miniaci, M.; Krushynska, A.; Movchan, A. B.; Bosia, F.; Pugno, N. M. Spider Web-Inspired Acoustic Metamaterials. Appl. Phys. Lett. 2016, 109 (7) DOI: 10.1063/1.4961307.

Mittelbach, P.; Porod, G. No Title. Acta Phys. Austriaca 1961, 14, 185–211.

Mohtasham, J. Review Article-Renewable Energies. Energy Procedia 2015, 74, 1289–1297 DOI: 10.1016/j.egypro.2015.07.774.

Molina-lopez, F.; Yan, H.; Gu, X.; Kim, Y.; Toney, M. F.; Bao, Z. Electric Field Tuning Molecular Packing and Electrical Properties of Solution-Shearing Coated Organic Semiconducting Thin Films. Adv. Funct. Mater. 2017 DOI: 10.1002/adfm.201605503.

Muccini, M. A Bright Future for Organic Field-Effect Transistors. Nat. Mater. 2006, 5 (8), 605–613 DOI: 10.1038/nmat1699.

Müllen, K.; Pisula, W. Donor–Acceptor Polymers. J. Am. Chem. Soc. 2015, 137 (30), 9503–9505 DOI: 10.1021/jacs.5b07015.

Müller, C.; Aghamohammadi, M.; Himmelberger, S.; Sonar, P.; Garriga, M.; Salleo, A.; Campoy-Quiles, M. One-Step Macroscopic Alignment of Conjugated Polymer Systems by Epitaxial Crystallization during Spin-Coating. Adv. Funct. Mater. 2013, 23 (19), 2368–2377 DOI: 10.1002/adfm.201202983.

Müller, C.; Garriga, M. Patterned Optical Anisotropy in Woven Conjugated Polymer Systems Patterned Optical Anisotropy in Woven Conjugated Polymer Systems. 2012, 171907, 1–5 DOI: 10.1063/1.4764518.

Neppiras, E. A. Acoustic Cavitation Series: Part One. Acoustic Cavitation: An Introduction. Ultrasonics 2017, 22 (1), 3894–3908 DOI: 10.1016/0041-624X(84)90057-X.

Newbloom, G. M.; de la Iglesia, P.; Pozzo, L. D. Controlled Gelation of Poly(3-Alkylthiophene)s in Bulk and in Thin-Films Using Low Volatility Solvent/Poor-Solvent Mixtures. Soft Matter 2014, 10 (44), 8945–8954 DOI: 10.1039/c4sm00960f.

Newbloom, G. M.; Hoffmann, S. M.; West, A. F.; Gile, M. C.; Sista, P.; Cheung, H. C.; Luscombe, C. K.; Pfaendtner, J.; Pozzo, L. D. Solvatochromism and Conformational Changes in Fully Dissolved Poly(3-Alkylthiophene)S. Langmuir 2015, 31 (1), 458–468 DOI: 10.1021/la503666x.

Newbloom, G. M.; Hoffmann, S. M.; West, A. F.; Gile, M. C.; Sista, P.; Cheung, H. K. C.; Luscombe, C. K.; Pfaendtner, J.; Pozzo, L. D. Solvatochromism and Conformational Changes in Fully Dissolved Poly(3-Alkylthiophene)S. Langmuir 2015, 31 (1), 458–468 DOI: 10.1021/la503666x.

Newbloom, G. M.; Kim, F. S.; Jenekhe, S. a.; Pozzo, D. C. Mesoscale Morphology and Charge Transport in Colloidal Networks of Poly(3-Hexylthiophene). Macromolecules 2011, 44 (10), 3801–3809 DOI: 10.1021/ma2000515.

Newbloom, G. M.; Weigandt, K. M.; Pozzo, D. C. Electrical, Mechanical, and Structural Characterization of Self-Assembly in Poly(3-Hexylthiophene) Organogel Networks. Macromolecules 2012, 45, 3452–3462 DOI: 10.1021/ma202564k.

Newbloom, G. M.; Weigandt, K. M.; Pozzo, D. C. Structure and Property Development of Poly(3-Hexylthiophene) Organogels Probed with Combined Rheology, Conductivity and Small Angle Neutron Scattering. Soft Matter 2012, 8 (34), 8854 DOI: 10.1039/c2sm26114f.

Niedzialek, D.; Lemaur, V.; Dudenko, D.; Shu, J.; Hansen, M. R.; Andreasen, J. W.; Pisula, W.; Müllen, K.; Cornil, J.; Beljonne, D. Probing the Relation between Charge Transport and Supramolecular Organization down to Ångström Resolution in a Benzothiadiazole- Cyclopentadithiophene Copolymer. Adv. Mater. 2013, 25 (13), 1939–1947 DOI: 10.1002/adma.201201058.

Niles, E. T.; Roehling, J. D.; Yamagata, H.; Wise, A. J.; Spano, F. C.; Moulé, A. J.; Grey, J. K. J-Aggregate Behavior in Poly-3-Hexylthiophene Nanofibers. J. Phys. Chem. Lett. 2012, 3 (2), 259–263 DOI: 10.1021/jz201509h.

No Title https://www.nobelprize.org/.

No Title. In Scanning Transmission Electron Microscopy Imaging and Analysis; 2011.

Noriega, R.; Rivnay, J.; Vandewal, K.; Koch, F. P. V.; Stingelin, N.; Smith, P.; Toney, M. F.; Salleo, A. A General Relationship between Disorder, Aggregation and Charge Transport in Conjugated Polymers. Nat. Mater. 2013, 12 (11), 1038–1044 DOI: 10.1038/nmat3722.

Obrzut, J.; Page, K. A. Electrical Conductivity and Relaxation in Poly(3-Hexylthiophene). Phys. Rev. B 2009, 80 (19), 195211 DOI: 10.1103/PhysRevB.80.195211.

Oh, J. Y.; Rondeau-Gagné, S.; Chiu, Y.-C.; Chortos, A.; Lissel, F.; Wang, G.-J. N.; Schroeder, B. C.; Kurosawa, T.; Lopez, J.; Katsumata, T.; Xu, J.; Zhu, C.; Gu, X.; Bae, W.-G.; Kim, Y.; Jin, L.; Chung, J. W.; Tok, J. B.-H.; Bao, Z. Intrinsically Stretchable and Healable Semiconducting Polymer for Organic Transistors. Nature 2016, 539 (7629), 411–415 DOI: 10.1038/nature20102.

Okutan, M.; San, S. E.; Alpaslan, Z.; Demir, A. Electrical Properties of Zn-Phthalocyanine and Poly (3-Hexylthiophene) Doped Nematic Liquid Crystal. 2011, 2011 (2) DOI: 10.1155/2011/729085.

Oliva-Avilés, a I.; Avilés, F.; Sosa, V.; Oliva, a I.; Gamboa, F. Dynamics of Carbon Nanotube Alignment by Electric Fields. Nanotechnology 2012, 23 (46), 465710 DOI: 10.1088/0957-4484/23/46/465710.

Olszowka, V.; Hund, M.; Kuntermann, V.; Scherdel, S.; Tsarkova, L.; Böker, A. Electric Field Alignment of a Block Copolymer Nanopattern: Direct Observation of the Microscopic Mechanism. ACS Nano 2009, 3 (5), 1091–1096 DOI: 10.1021/nn900081u.

P. Butler, G. Alina, R. C. Hernandez, M. Doucet, A. Jackson, P. Kienzle, S. K. and J. Z. SASView for Small Angle Scattering Analysis http://www.sasview.org/.

P. Mittelbach, G. P. X-Ray Low-Angle Scattering by Dilute Scattering Colloidal Systems. The Calculation of Scattering Curves of Parallelepipeds. Acta Phys. Austriaca 1961, 14, 185–211.

Pablo, de la I. Structure-Property Relationships of SelfAssembled Conjugated Polymers, University of Washington, 2015.

Pedersen, J. S.; Schurtenberger, P. Scattering Functions of Semiflexible Polymers with and without Excluded Volume Effects. Macromolecules 1996, 29 (23), 7602–7612 DOI: 10.1021/ma9607630.

Peng, H.; Sun, X.; Cai, F.; Chen, X.; Zhu, Y.; Liao, G.; Chen, D.; Li, Q.; Lu, Y.; Zhu, Y.; Jia, Q. Electrochromatic Carbon Nanotube/Polydiacetylene Nanocomposite Fibres. Nat. Nanotechnol. 2009, 4 (11), 738–741 DOI: 10.1038/nnano.2009.264.

Persano, L.; Dagdeviren, C.; Su, Y.; Zhang, Y.; Girardo, S.; Pisignano, D.; Huang, Y.; Rogers, J. a. High Performance Piezoelectric Devices Based on Aligned Arrays of Nanofibers of Poly(Vinylidenefluoride-Co-Trifluoroethylene). Nat. Commun. 2013, 4, 1633 DOI: 10.1038/ncomms2639.

Pethig, R. Dielectrophoresis: Status of the Theory, Technology, and Applications. Biomicrofluidics 2010, 4 (2), 022811 DOI: 10.1063/1.3456626.

Phan, H.; Ford, M. J.; Lill, A. T.; Wang, M.; Bazan, G. C.; Nguyen, T.-Q. Electrical Double-Slope Nonideality in Organic Field-Effect Transistors. Adv. Funct. Mater. 2018, 28 (17), 1707221 DOI: 10.1002/adfm.201707221.

Philippova, O. E.; Shibaev, A. V.; Muravlev, D. A.; Mityuk, D. Y. Structure and Rheology of Solutions and Gels of Stiff Polyelectrolyte at High Salt Concentration. Macromolecules 2016, 49 (16), 6031–6040 DOI: 10.1021/acs.macromol.6b01392.

Potyrailo, R. a.; Ghiradella, H.; Vertiatchikh, A.; Dovidenko, K.; Cournoyer, J. R.; Olson, E. Morpho Butterfly Wing Scales Demonstrate Highly Selective Vapour Response. Nat. Photonics 2007, 1 (2), 123–128 DOI: 10.1038/nphoton.2007.2.

Pusey, P. N. Introduction to Scattering Experiments. In Neutrons, x-rays and light: scaattering methods applied to soft condensed matter.

Qiao, Q.; Su, L.; Beck, J.; McLeskey, J. T. Characteristics of Water-Soluble Polythiophene: TiO 2 Composite and Its Application in Photovoltaics. J. Appl. Phys. 2005, 98 (9) DOI: 10.1063/1.2130517.

Qie, L.; Yuan, L.-X.; Zhang, W.-X.; Chen, W.-M.; Huang, Y.-H. Revisit of Polypyrrole as Cathode Material for Lithium-Ion Battery. J. Electrochem. Soc. 2012, 159 (10), A1624–A1629 DOI: 10.1149/2.042210jes.

Richards, J. J.; Scherbarth, A. D.; Wagner, N. J.; Butler, P. D. Mixed Ionic/Electronic Conducting Surface Layers Adsorbed on Colloidal Silica for Flow Battery Applications. ACS Appl. Mater. Interfaces 2016, 8 (36), 24089–24096 DOI: 10.1021/acsami.6b07372.

Roman Nayuk, K. H. Formfactors of Hollow and Massive Rectangular Parallelepipeds at Variable Degree of Anisometry. Zeitschrift für Phys. Chemie 2012, 226, 837–854.

Römer, L.; Scheibel, T. The Elaborate Structure of Spider Silk: Structure and Function of a Natural High Performance Fiber. Prion 2008, 2 (4), 154–161 DOI: 10.4161/pri.2.4.7490.

Rossi, D.; Jamshidi, R.; Saffari, N.; Kuhn, S.; Gavriilidis, A.; Mazzei, L. Continuous-Flow Sonocrystallization in Droplet-Based Microfluidics. Cryst. Growth Des. 2015, 15 (11), 5519–5529 DOI: 10.1021/acs.cgd.5b01153.

Ruecroft, G.; Hipkiss, D.; Ly, T.; Maxted, N.; Cains, P. W. Sonocrystallization:? The Use of Ultrasound for Improved Industrial Crystallization. Org. Process Res. Dev. 2005, 9 (6), 923–932 DOI: 10.1021/op050109x.

Ruecroft, G.; others. Sonocrystallization: The Use of Ultrasound for Improved Industrial Crystallization. Org.Proc.Res.Dev. 2005, 9 (6), 923–932.

Scharsich, C.; Lohwasser, R. H.; Sommer, M.; Asawapirom, U.; Scherf, U.; Thelakkat, M.; Neher, D.; Köhler, A. Control of Aggregate Formation in Poly(3-Hexylthiophene) by Solvent, Molecular Weight, and Synthetic Method. J. Polym. Sci. Part B Polym. Phys. 2012, 50 (6), 442–453 DOI: 10.1002/polb.23022.

Schneider, C. a; Rasband, W. S.; Eliceiri, K. W. NIH Image to ImageJ: 25 Years of Image Analysis. Nat. Methods 2012, 9 (7), 671–675 DOI: 10.1038/nmeth.2089.

Sekine, C.; Tsubata, Y.; Yamada, T.; Kitano, M.; Doi, S. Recent Progress of High Performance Polymer OLED and OPV Materials for Organic Printed Electronics. Sci. Technol. Adv. Mater. 2014, 15 (3), 034203 DOI: 10.1088/1468-6996/15/3/034203.

Senthil Kumar, M.; Lee, S. H.; Kim, T. Y.; Kim, T. H.; Song, S. M.; Yang, J. W.; Nahm, K. S.; Suh, E. K. DC Electric Field Assisted Alignment of Carbon Nanotubes on Metal Electrodes. Solid. State. Electron. 2003, 47 (11), 2075–2080 DOI: 10.1016/S0038-1101(03)00258-2.

Shao, L.; Jeon, J. W.; Lutkenhaus, J. L. Polyaniline/Vanadium Pentoxide Layer-by-Layer Electrodes for Energy Storage. Chem. Mater. 2012, 24 (1), 181–189 DOI: 10.1021/cm202774n.

Shao, M.; He, Y.; Hong, K.; Rouleau, C. M.; Geohegan, D. B.; Xiao, K. A Water-Soluble Polythiophene for Organic Field-Effect Transistors. Polym. Chem. 2013, 4 (20), 5270 DOI: 10.1039/c2py21020g.

Shin, H.; Seo, S.; Park, C.; Na, J.; Han, M.; Kim, E. Energy Saving Electrochromic Windows from Bistable Low-HOMO Level Conjugated Polymers. Energy Environ. Sci. 2016, 9 (1), 117–122 DOI: 10.1039/C5EE03160E.

Shinkle, A. A.; Sleightholme, A. E. S.; Griffith, L. D.; Thompson, L. T.; Monroe, C. W. Degradation Mechanisms in the Non-Aqueous Vanadium Acetylacetonate Redox Flow Battery. J. Power Sources 2012, 206, 490–496 DOI: 10.1016/j.jpowsour.2010.12.096.

Simon, D. T.; Gabrielsson, E. O.; Tybrandt, K.; Berggren, M. Organic Bioelectronics: Bridging the Signaling Gap between Biology and Technology. Chem. Rev. 2016, 116 (21), 13009–13041 DOI: 10.1021/acs.chemrev.6b00146.

Simon, D. T.; Gabrielsson, E. O.; Tybrandt, K.; Berggren, M. Organic Bioelectronics: Bridging the Signaling Gap between Biology and Technology. Chem. Rev. 2016, 116 (21), 13009–13041 DOI: 10.1021/acs.chemrev.6b00146.

Singh, N.; Galande, C.; Miranda, A.; Mathkar, A.; Gao, W.; Reddy, A. L. M.; Vlad, A.; Ajayan, P. M. Paintable Battery. Sci. Rep. 2012, 2, 6–10 DOI: 10.1038/srep00481.

Singh, R.; Singh, R. K.; Kumar, J.; Kant, R.; Kumar, V. The Origin of DC Electrical Conduction and Dielectric Relaxation in Pristine and Doped Poly (3-Hexylthiophene) Films. 2010, 48, 1047–1053 DOI: 10.1002/POLB.

Smith, P. a.; Nordquist, C. D.; Jackson, T. N.; Mayer, T. S.; Martin, B. R.; Mbindyo, J.; Mallouk, T. E. Electric-Field Assisted Assembly and Alignment of Metallic Nanowires. Appl. Phys. Lett. 2000, 77 (9), 1399–1401 DOI: 10.1063/1.1290272.

Søndergaard, R.; Hösel, M.; Angmo, D.; Larsen-olsen, T. T.; Krebs, F. C. Roll-to-Roll Fabrication of Polymer Solar Cells As the Performance in Terms of Power Conversion Efficiency and Operational. Mater. Today 2012, 15 (1–2), 36–49 DOI: 10.1016/S1369-7021(12)70019-6.

Song, E.; Kang, B.; Choi, H. H.; Sin, D. H.; Lee, H.; Lee, W. H.; Cho, K. Stretchable and Transparent Organic Semiconducting Thin Film with Conjugated Polymer Nanowires Embedded in an Elastomeric Matrix. 2016, 1–8 DOI: 10.1002/aelm.201500250.

Song, H. K.; Palmore, G. T. R. Redox-Active Polypyrrole: Toward Polymer-Based Batteries. Adv. Mater. 2006, 18 (13), 1764–1768 DOI: 10.1002/adma.200600375.

Song, Z.; Zhou, H. Towards Sustainable and Versatile Energy Storage Devices: An Overview of Organic Electrode Materials. Energy Environ. Sci. 2013, 6 (8), 2280 DOI: 10.1039/c3ee40709h.

Spano, F. C. Absorption in Regio-Regular Poly(3-Hexyl)Thiophene Thin Films: Fermi Resonances, Interband Coupling and Disorder. Chem. Phys. 2006, 325 (1), 22–35 DOI: 10.1016/j.chemphys.2005.08.019.

Sponer, J. Dependence of the Cavitation Threshold on the Ultrasonic Frequency. Czechoslov. J. Phys. 1990, 40 (10), 1123–1132 DOI: 10.1007/BF01597973.

Srinivasarao, M. Nano-Optics in the Biological World: Beetles, Butterflies, Birds, and Moths. Chem. Rev. 1999, 99 (7), 1935–1961 DOI: 10.1021/cr970080y.

Street, R. A. Unraveling Charge Transport in Conjugated Polymers. Science (80-.). 2013, 341 (6150), 1072–1073 DOI: 10.1126/science.1242935.

Sulas, D. B.; Yao, K.; Intemann, J. J.; Williams, S. T.; Li, C.-Z.; Chueh, C.-C.; Richards, J. J.; Xi, Y.; Pozzo, L. D.; Schlenker, C. W.; Jen, A. K.-Y.; Ginger, D. S. Open-Circuit Voltage Losses in Selenium-Substituted Organic Photovoltaic Devices from Increased Density of Charge-Transfer States. Chem. Mater. 2015, 27 (19), 6583–6591 DOI: 10.1021/acs.chemmater.5b02133.

Sun, K.; Wei, T. S.; Ahn, B. Y.; Seo, J. Y.; Dillon, S. J.; Lewis, J. A. 3D Printing of Interdigitated Li-Ion Microbattery Architectures. Adv. Mater. 2013, 25 (33), 4539–4543 DOI: 10.1002/adma.201301036.

Sun, X.; Chen, T.; Yang, Z.; Peng, H. The Alignment of Carbon Nanotubes: An Effective Route To Extend Their Excellent Properties to Macroscopic Scale. Acc. Chem. Res. 2013, 46 (2), 539–549 DOI: 10.1021/ar300221r.

Suslick, K. S.; Didenko, Y.; Fang, M. M.; Hyeon, T.; Kolbeck, K. J.; McNamara III, W. B.; Mdleleni, M. M.; Wong, M. Acoustic Cavitation and Its Consequences. Philos. Trans. R. Soc. A 1999, 357 (1927), 335–353 DOI: 10.1098/rsta.1999.0330.

T. G. Leighton. The Acoustic Bubble; Academic Press, 1997.

Tamura, K.; Akutagawa, N.; Satoh, M.; Wada, J.; Masuda, T. Charge/Discharge Properties of Organometallic Batteries Fabricated with Ferrocene-Containing Polymers. Macromol. Rapid Commun. 2008, 29 (24), 1944–1949 DOI: 10.1002/marc.200800526.

Thomas, A. K.; Garcia, J. A.; Ulibarri-Sanchez, J.; Gao, J.; Grey, J. K. High Intrachain Order Promotes Triplet Formation from Recombination of Long-Lived Polarons in Poly(3-Hexylthiophene) J-Aggregate Nanofibers. ACS Nano 2014, 8 (10), 10559–10568 DOI: 10.1021/nn5040026.

Tomita, Y.; Shima, A. Mechanisms of Impulsive Pressure Generation and Damage Pit Formation by Bubble Collapse. J. Fluid Mech. 1986, 169 (1), 535 DOI: 10.1017/S0022112086000745.

Transmission Electron Microscopy https://cmrf.research.uiowa.edu/transmission-electron-microscopy.

Treat, N. D.; Nekuda Malik, J. A.; Reid, O.; Yu, L.; Shuttle, C. G.; Rumbles, G.; Hawker, C. J.; Chabinyc, M. L.; Smith, P.; Stingelin, N. Microstructure Formation in Molecular and Polymer Semiconductors Assisted by Nucleation Agents. Nat. Mater. 2013, 12 (7), 628–633 DOI: 10.1038/nmat3655.

Trebbin, M.; Steinhauser, D.; Perlich, J.; Buffet, A.; Roth, S. V; Zimmermann, W. Anisotropic Particles Align Perpendicular to the Fl Ow Direction in Narrow Microchannels. 2013, 110 (17) DOI: 10.1073/pnas.1219340110.

Ural, A.; Li, Y.; Dai, H. Electric-Field-Aligned Growth of Single-Walled Carbon Nanotubes on Surfaces. Appl. Phys. Lett. 2002, 81 (18), 3464 DOI: 10.1063/1.1518773.

Vaz, P. D.; Nolasco, M. M.; Gil, F. P. S. C.; Ribeiro-Claro, P. J. A.; Tomkinson, J. Hydrogen-Bond Dynamics of C□H···O Interactions: The Chloroform···Acetone Case. Chem. - A Eur. J. 2010, 16 (30), 9010–9017 DOI: 10.1002/chem.201000479.

Velev, O. D.; Bhatt, K. H. On-Chip Micromanipulation and Assembly of Colloidal Particles by Electric Fields. Soft Matter 2006, 2 (9), 738 DOI: 10.1039/b605052b.

Vidor, F. F.; Meyers, T.; Hilleringmann, U. Flexible Electronics: Integration Processes for Organic and Inorganic Semiconductor-Based Thin-Film Transistors. 2015, 480–506 DOI: 10.3390/electronics4030480.

Vohra, V.; Arrighetti, G.; Barba, L.; Higashimine, K.; Porzio, W.; Murata, H. Enhanced Vertical Concentration Gradient in Rubbed P3HT:PCBM Graded Bilayer Solar Cells. J. Phys. Chem. Lett. 2012, 3 (13), 1820–1823 DOI: 10.1021/jz300710a.

Volder, M. F. L. De; De Volder, M. F. L.; Tawfick, S. H.; Baughman, R. H.; Hart, a. J. Carbon Nanotubes: Present and Future Commercial Applications. Science (80-.). 2013, 339 (6119), 535–539 DOI: 10.1126/science.1222453.

Vukusic, P.; Sambles, J. R. Photonic Structures in Biology. Nature 2003, 424 (6950), 852–855 DOI: 10.1038/nature01941.

Wang, W.; Luo, Q.; Li, B.; Wei, X.; Li, L.; Yang, Z. Recent Progress in Redox Flow Battery Research and Development. Adv. Funct. Mater. 2013, 23 (8), 970–986 DOI: 10.1002/adfm.201200694.

Wang, W.; Sun, X.; Wu, W.; Peng, H.; Yu, Y. Photoinduced Deformation of Crosslinked Liquid-Crystalline Polymer Film Oriented by a Highly Aligned Carbon Nanotube Sheet. Angew. Chemie - Int. Ed. 2012, 51 (19), 4644–4647 DOI: 10.1002/anie.201200723.

Whipps, H. How the iron age changed the world https://www.livescience.com/2339-iron-age-changed-world.html.

Whitehead, K. S.; Grell, M.; Bradley, D. D. C.; Jandke, M.; Strohriegl, P. Highly Polarized Blue Electroluminescence from Homogeneously Aligned Films of Poly(9,9-Dioctylfluorene). Appl. Phys. Lett. 2000, 76 (20), 2946–2948 DOI: 10.1063/1.126525.

Wu, C.-H.; Chueh, C.-C.; Xi, Y.-Y.; Zhong, H.-L.; Gao, G.-P.; Wang, Z.-H.; Pozzo, L. D.; Wen, T.-C.; Jen, A. K.-Y. Influence of Molecular Geometry of Perylene Diimide Dimers and Polymers on Bulk Heterojunction Morphology Toward High-Performance Nonfullerene Polymer Solar Cells. Adv. Funct. Mater. 2015, 25 (33), 5326–5332 DOI: 10.1002/adfm.201501971.

Xi, Y.; Liu, L.; Ren, F.; Pearton, S. J.; Kim, J.; Dabiran, A.; Chow, P. P. Methane Detection Using Pt-Gated AlGaN/GaN High Electron Mobility Transistor Based Schottky Diodes. J. Vac. Sci. Technol. B Microelectron. Nanom. Struct. 2013, 31 (3), 032203.

Xi, Y.; Pozzo, L. D. Electric Field Directed Formation of Aligned Conjugated Polymer Fibers. Soft Matter 2017, 13, 3894–3908 DOI: 10.1039/C7SM00485K.

Xie, Z.; Liu, Q.; Chang, Z.; Zhang, X. The Developments and Challenges of Cerium Half-Cell in Zinc-Cerium Redox Flow Battery for Energy Storage. Electrochim. Acta 2013, 90, 695–704 DOI: 10.1016/j.electacta.2012.12.066.

Xu, T.; Zhu, Y.; Gido, S. P.; Russel, T. P. Electric Field Alignment of Symmetric Diblock Copolymer Thin Films. Macromolecules 2004, 37 (7), 2625–2629 DOI: 10.1007/978-1-4020-6330-5_6.

Yan, J. Y.; Patey, G. N. Heterogeneous Ice Nucleation Induced by Electric Fields. J. Phys. Chem. Lett. 2011, 2 (20), 2555–2559 DOI: 10.1021/jz201113m.

Yang, H.; Liang, F.; Chen, Y.; Wang, Q.; Qu, X.; Yang, Z. Lotus Leaf Inspired Robust Superhydrophobic Coating from Strawberry-like Janus Particles. NPG Asia Mater 2015, 7 (4), e176 DOI: 10.1038/am.2015.33.

Yousefi, N.; Sun, X.; Lin, X.; Shen, X.; Jia, J.; Zhang, B.; Tang, B.; Chan, M.; Kim, J. K. Highly Aligned Graphene/Polymer Nanocomposites with Excellent Dielectric Properties for High-Performance Electromagnetic Interference Shielding. Adv. Mater. 2014, 26 (31), 5480–5487 DOI: 10.1002/adma.201305293.

Yu, D.; Yang, Y.; Chen, Z.; Tao, Y.; Liu, Y. Recent Progress on Thin- Fi Lm Encapsulation Technologies for Organic Electronic Devices. Opt. Commun. 2016, 362, 43–49 DOI: 10.1016/j.optcom.2015.08.021.

Yuryev, Y.; Wood-Adams, P. M. Crystallization of Poly(L-/D-Lactide) in the Presence of Electric Fields. Macromol. Chem. Phys. 2012, 213 (6), 635–642 DOI: 10.1002/macp.201100448.

Zamarayeva, A. M.; Ostfeld, A. E.; Wang, M.; Duey, J. K.; Deckman, I.; Lechêne, B. P.; Davies, G.; Steingart, D. A.; Arias, A. C. Flexible and Stretchable Power Sources for Wearable Electronics. Sci. Adv. 2017, 3 (6), e1602051 DOI: 10.1126/sciadv.1602051.

Zeiger, B.; Suslick, K. Sonofragmentation of Molecular Crystals: Observations and Modeling. Proc. Meet. Acoust. 2013, 19, 045089 DOI: 10.1121/1.4800930.

Zhang, C. Y.; Wang, Y.; Schubert, R.; Liu, Y.; Wang, M. Y.; Chen, D.; Guo, Y. Z.; Dong, C.; Lu, H. M.; Liu, Y. M.; Wu, Z. Q.; Betzel, C.; Yin, D. C. Effect of Audible Sound on Protein Crystallization. Cryst. Growth Des. 2016, 16 (2), 705–713 DOI: 10.1021/acs.cgd.5b01268.

Zhang, D.; Lan, H.; Li, Y. The Application of a Non-Aqueous Bis(Acetylacetone)Ethylenediamine Cobalt Electrolyte in Redox Flow Battery. J. Power Sources 2012, 217, 199–203 DOI: 10.1016/j.jpowsour.2012.06.038.

Zhao, K.; Khan, H. U.; Li, R.; Su, Y.; Amassian, A. Entanglement of Conjugated Polymer Chains Influences Molecular Self-Assembly and Carrier Transport. Adv. Funct. Mater. 2013, 23 (48), 6024–6035 DOI: 10.1002/adfm.201301007.

Zheng, L.; Han, Y. Solvated Crystals Based on [6,6]-Phenyl-C 61 -Butyric Acid Methyl Ester (PCBM) with the Hexagonal Structure and Their Phase Transformation. J. Phys. Chem. B 2012, 116 (5), 1598–1604 DOI: 10.1021/jp210937h.

Zheng, Y.-Q.; Yao, Z.-F.; Lei, T.; Dou, J.-H.; Yang, C.-Y.; Zou, L.; Meng, X.; Ma, W.; Wang, J.-Y.; Pei, J. Unraveling the Solution-State Supramolecular Structures of Donor-Acceptor Polymers and Their Influence on Solid-State Morphology and Charge-Transport Properties. Adv. Mater. 2017, 1701072, 1701072 DOI: 10.1002/adma.201701072.

Zheng, Z.; Yim, K. H.; Saifullah, M. S. M.; Welland, M. E.; Friend, R. H.; Kim, J. S.; Huck, W. T. S. Uniaxial Alignment of Liquid-Crystalline Conjugated Polymers by Nanoconfinement. Nano Lett. 2007, 7, 987–992 DOI: 10.1021/nl070022k.

Zhu, C.; Liu, L.; Yang, Q.; Lv, F.; Wang, S. Water-Soluble Conjugated Polymers for Imaging, Diagnosis, and Therapy. Chem. Rev. 2012, 112 (8), 4687–4735 DOI: 10.1021/cr200263w.

Zhu, R.; Kumar, A.; Yang, Y. Polarizing Organic Photovoltaics. Adv. Mater. 2011, 23 (36), 4193–4198 DOI: 10.1002/adma.201101514.

Zijlstra, P.; van Stee, M.; Verhart, N.; Gu, Z.; Orrit, M. Rotational Diffusion and Alignment of Short Gold Nanorods in an External Electric Field. Phys. Chem. Chem. Phys. 2012, 14 (13), 4584–4588 DOI: 10.1039/c2cp24092k.

Zou, Z.; Zhu, C.; Li, Y.; Lei, X.; Zhang, W.; Xiao, J. Rehealable, Fully Recyclable, and Malleable Electronic Skin Enabled by Dynamic Covalent Thermoset Nanocomposite. Sci. Adv. 2018, 4 (2), eaaq0508 DOI: 10.1126/sciadv.aaq0508

Curriculum Vitae

Yuyin Xi

xiyuyin@uw.edu ● (206)-455-3322

EDUCATION

- **PhD student** in Chemical Engineering, University of Washington, USA.
  Sep. 2013~ Present.
  Advisor: Prof. Lilo D. Pozzo
  Committee members: Christine K. Luscombe, Stuart Adler, and Lih Lin
  Dissertation title: "Structure Engineering of Self- and Directed-Assembled conjugated polymers"
  GPA: 3.90/4.00
- **Master of Science** in Chemical Engineering**,** University of Florida, USA.
  Aug. 2011~ Dec. 2012.
  Advisor: Prof. Fan Ren
  GPA: 3.93/4.00
- **Bachelor of Science** in Chemical Engineering, Nanjing University of Technology, China.
  Sep. 2007~ Jun. 2011.

  GPA: 90.5/100.0

RESEARCH EXPERIENCE

Research Assistant, Department of Chemical Engineering, University of Washington, Seattle, WA, Jan.2014~Present.

- Structure and properties investigation of conjugated polymers (TEM, SEM, AFM, SANS, SAXS) under external stimuli (electric and acoustic fields), to improve charge transport.
- Synthesis of metallic complex and solution processable conjugated polymers (PEDOT, PPy) for printable battery applications, a study using molecular dopants to tune the structure, thus their properties.

Research Assistant, Department of Chemical Engineering, University of Florida, Gainesville, FL, Dec. 2011~Jun. 2013.

- Reliability study of circular shaped AlGaN/GaN high electron mobility field effect transistors (HEMTs).
- Chemical gas (H_2, CO, CH_4) detection using AlGaN/GaN HEMTs to develop chemical sensors and enhance response time.

SKILL SET

- Proficient in scattering experiments and nano-structure analysis, including small angle neutron

scattering (SANS), and small angle x-ray scattering (SAXS).
- Experienced with typical cleanroom processes, such as photo mask design, photolithography, metal evaporation and plasma enhanced chemical vapor deposition (PECVD), as well as transistor fabrication and characterization.
- Experienced with self-assembly and directed-assembly process of macromolecules, as well as wet chemical synthesis.
- Familiar with various microscopy techniques, such as TEM, SEM, and AFM.

TEACHING EXPERIENCE

Teaching Assistant:

- Interfacial Phenomena Laboratory, Department of Chemical Engineering, University of Washington, Seattle, WA, Sep. 2016~Dec. 2016.
- Interfacial Phenomena Laboratory, Department of Chemical Engineering, University of Washington, Seattle, WA, Sep. 2015~Dec. 2015.
- Unit Operation Laboratory, Department of Chemical Engineering, University of Washington, Seattle, WA, Mar. 2014~Jun. 2014.
- Unit Operation Laboratory, Department of Chemical Engineering, University of Florida, Gainesville, FL, May. 2012~Dec. 2012.

AWARDS

1. Graduate Excellence Award in polymer science, *American Chemical Society*, San Francisco, CA, 2017
2. Top 10 2012-2013 *JVST B* articles read and cited the most in 2014: with the title of "Dependence on proton energy of degradation of AlGaN/GaN high electron mobility transistors"
3. Top 20 most downloaded articles of *Journal of Vacuum Science & Technology* in April, 2013, with the title of "Study of hydrogen detection response time at room temperature with Pt-gated diodes fabricated on AlGaN/GaN hetero-structure"
4. Top 20 most read articles of *Journal of Vacuum Science & Technology* in January, 2013, with the tile of "Effect of buffer structures on AlGaN/GaN high electron mobility transistor reliability"
5. Third prize of the student poster session in *Ann Symp. Florida Chapter of the AVS Science and Technology Society (FLAVS)* with the tile of "Study of hydrogen detection response time at room temperature with Pt-gated diodes fabricated on AlGaN/GaN hetero-structure" Orlando, FL, Mar. 2013
6. Achievement Award, University of Florida, Gainesville, FL, September 2011
7. Special Award of comprehensive school scholarships (the highest award in university), Nanjing University of Technology, 2008, 2009, 2010
8. Third prize of the National College English Contest, national foreign language teaching in colleges and universities steering committee of ministry of education, China, Dec. 2009
9. Second Prize of Mathematical Modeling Contest, Nanjing University of Technology, Jun. 2009

10. Second prize of Calculus Contest, Jiangsu Province, Jun. 2008

FUNDED PROPOSALS & FELLOWSHIPS

- Neutron scattering proposal titled "Self-assembly of donor-acceptor conjugated polymers induced by miscible poor solvents", Funded by NIST. Mar. 2018
- Synchrotron proposal titled "Static and time-resolved investigation of chain orientation of electric field aligned conjugated polymers", Funded by ANL. Dec. 2017
- Neutron scattering proposal titled "In-Situ SANS investigation of Polymer Conformation Change in Solution triggered by acoustic wave: Amplitude and Frequency Study", Funded by ORNL. May 2017
- Neutron scattering proposal titled "Investigation of Acoustic Wave Directed Assembly of Water Soluble Conjugated Polymers", Funded by NIST. Mar. 2017
- Neutron scattering proposal titled "Investigation of Ultrasound Excitation on the Conformation of Dilute Conjugated Polymers in Solutions", Funded by NIST. Sep. 2016
- Neutron scattering proposal titled "RheoSANS of Poly(3-hexylthiophene) Alignment Under Electric Field with Varied Concentrations", Funded by NIST. Feb. 2016
- Neutron scattering proposal titled "TR-SANS of Poly[4-(4,4-dihexadecyl-4H-cyclopenta[1,2-b:5,4-b'] dithiophen-2-yl)-alt-[1,2,5]-thiadiazolo[3,4-c] pyridine] (PCDTPT) Conjugated Polymer Alignment Under Electric Field", Funded by NIST. Jun. 2015
- Neutron scattering proposal titled "In-Situ TR-SANS-Dielectric Spectroscopy of Poly(3-hexylthiophene) Conjugated Polymer Organogels under high electric field", Funded by NIST. Oct. 2014
- Neutron scattering proposal titled "TR-SANS of the Synthesis and Self-Assembly of Organic Dispersible PEDOT-Surfactant Complexes", Funded by NIST. Oct. 2014
- Clean Energy Institute Fellowship, University of Washington, Seattle WA, 2015.
- Jagjeet and Janice Bindra Endowed and Chemical Endowed Fellowship, University of Washington, Seattle, WA. September 2013.
- First Prize of HQCEC Scholarship (Typically for graduate students, while awarded to me as undergraduate student), China Huanqiu Contracting & Engineering Corporation, Jun. 2010
- National Scholarship, Chinese ministry of education, China, Nov. 2008

MEMBERSHIP & SOCIETY

- American chemical society (ACS)
- Institute of electrical and electronics engineers (IEEE)
- American Institute of chemical engineers (AIChE)

PUBLICATIONS

1. **Yuyin Xi**, et al., "Sonocrystallization of Conjugated Polymers with Ultrasound Fields" *Soft Matter*, accepted, (2018).
2. **Yuyin Xi**, et al., "Electric Field Directed Formation of Aligned Conjugated Polymer Fibers" *Soft Matter*, **13**, 21, 3894, (2017).
3. **Yuyin Xi** *et al*., "Effect of 5 MeV proton radiation on DC performance and reliability of circular-shaped AlGaN/GaN high electron mobility transistors" *Journal of Vacuum Science & Technology B* **32,** 012201(2014).
4. **Yuyin Xi** *et al*., "Methane detection using Pt-gated AlGaN/GaN high electron mobility transistor based Schottky diodes" *Journal of Vacuum Science & Technology B* **31**, 032203(2013).
5. **Yuyin Xi** *et al*., "Study of hydrogen detection response time at room temperature with Pt-gated diodes fabricated on AlGaN/GaN hetero-structure" *Journal of Vacuum Science & Technology B* **31**, 032202(2013).
6. Chen Zou, **Yuyin Xi** et al., "A Highly Sensitive UV–vis–NIR All-Inorganic Perovskite Quantum Dot Phototransistor Based on a Layered Heterojunction" *Advanced Optical Materials*, 1800324, (2018).
7. David S. Li, Yi-Ting Lee, **Yuyin Xi**, et al., "A Small-Angle Scattering Environment for In Situ Ultrasound Studies" *Soft Matter*, accepted, (2018).
8. Jiangsheng Yu, **Yuyin Xi** et al., "Boosting Performance of Inverted Organic Solar Cells by Using a Planar Coronene based Electron-transporting Layer" *Nano Energy*, **39**, 454, (2017).
9. Jun-Huan Li, **Yuyin Xi** et al., "Macroscopically aligned nanowire arrays of π-conjugated polymers via shear-enhanced crystallization" *Journal of Materials Chemistry C*, **5**, 21, 5128, (2017).
10. Jiangsheng Yu, **Yuyin Xi**, et al., "A Room-Temperature Processable PDI-based Electron-Transporting Layer for Enhanced Performance in PDI-Based Non-Fullerene Solar Cells", *Advanced Materials Interfaces*, **3**, 18 (2016).
11. Dana B. Sulas, Kai Yao, Jeremy J. Intemann, Spencer T. Williams, Chang-Zhi Li, Chu-Chen Chueh, Jeffrey J. Richards, **Yuyin Xi**, et al., "Open-Circuit Voltage Losses in Selenium-Substituted Organic Photovoltaic Devices from Increased Density of Charge-Transfer States" *Chemistry of Materials*, **27** (19), 6583, (2015).
    ACS Editors' Choice.
12. Pablo de la Iglesia, Vance Jaeger, **Yuyin Xi**, et al., "Structure Characterization and Properties of Metal-Surfactant Complexes Dispersed in Organic Solvents" *Langmuir* **31**(33), 9006 (2015).
13. Chen-Hao Wu, Chu-Chen Chueh, **Yuyin Xi**, et al., "Influence of Molecular Geometry of Perylene Diimide Dimers and Polymers on Bulk Heterojunction Morphology Towards High-Performance Non-Fullerene Polymer Solar Cells" *Advanced Functional Materials*, **25**, 5326 (2015).
14. Lu Liu, **Yuyin Xi** *et al*., "Characteristics of gate leakage current and breakdown voltage of AlGaN/GaN high electron mobility transistors after postprocess annealing" *Journal of Vacuum Science & Technology B* **32**(5), 052201-1(2014).
15. Lu Liu, Ya-Hsi Hwang, **Yuyin Xi**, *et al*., "Study on the effects of proton irradiation on the dc characteristics of AlGaN/GaN high electron mobility transistors with source field plate" *Journal of Vacuum Science & Technology B* **32**(2), 022202-1 (2014).

16. Chien-Fong Lo, **Yuyin Xi** *et al*., "Effect of temperature on CO sensing response in air ambient by using ZnO nanorod-gated AlGaN/GaN high electron mobility transistors" *Sensors and Actuators, B,* **176**, 708(2013).
17. Lu Liu, Camilo Velez Cuervo, **Yuyin Xi** *et al*., "Impact of proton irradiation on dc performance of AlGaN/GaN high electron mobility transistors" *Journal of Vacuum Science & Technology B* **31**,042202(2013).
18. L. Liu, C. F. Lo, **Y. Y. Xi** *et al*., "Dependence on proton energy of degradation of AlGaN/GaN high electron mobility transistors" *Journal of Vacuum Science & Technology B* **31**, 022201(2013).
19. L. Liu, C. F. Lo, **Y. Y. Xi** *et al*., "Effect of buffer structures on AlGaN/GaN high electron mobility transistor reliability" *Journal of Vacuum Science & Technology B* **31**, 0011805(2013).
20. C. Schwarz, A. Yadav, M. Shatkhin, E. Flitsiyan, L. Chemyak, V. kasiyan, L. Liu, **Y. Y. Xi** *et al*., "Effects of gamma irradiation on AlGaN/GaN HEMT high electron mobility devices" *Applied Physics Letters,* **102**, 062102(2013).
21. Erin Patrick, Mark E. Law, Lu Liu, Camilo Velez Cuervo, **Yuyin Xi** *et al*., "Modeling Proton Irradiation in AlGaN/GaN HEMTs: Understanding the Increase of Critical Voltage" *Nuclear Science, IEEE Transactions on,* **60**, 4103(2013).
22. D J Cheney, E A Douglas, L Liu, C F Lo, **Y Y Xi**, *et al*., "Reliability studies of AlGaN/GaN high electron mobility transistors" *Semiconductor Science and Technology,* **28**, 074019(2013).
23. Chen bin, Jiang Yongxiang, **Xi Yuyin** *et al*., "Application of Sagging Control Resin in Orange-Peel Coatings" *Paint & Coatings Industry* **40,** 11(2010).

PRESENTATIONS

1. **Yuyin Xi** et al., "Acoustic Wave Directed Assembly of Conjugated Polymers", *IEEE International Ultrasonics Symposium, Washington D.C., Sep. 2017*
2. **Yuyin Xi** et al., "Acoustic Field Directed Assembly of Conjugated Polymers", *91th ACS colloid & Surface Science Symposium, New York, NY, Jul. 2017*
3. **Yuyin Xi** et al., "Directed Structure Manipulation of Conjugated Polymers with External Fields", *ACS 253rd National Meeting & Exhibition, San Francisco, CA, Apr. 2017*
4. **Yuyin Xi** et al., "Directed Assembly of Conjugated Polymers under Electric Field", *Orcas 2016: International Conference on Energy Conversion & Storage, Seattle, WA, Sep. 2016*
5. **Yuyin Xi** et al., "Electric Field Alignment of Conjugated polymers", *90th ACS colloid & Surface Science Symposium, Cambridge, MA, Jun. 2016*
6. **Yuyin Xi** et al., *"*Structure and Properties of P3HT Organogels Aligned under Electric Fields*" Gordon Research Conference, Ventura, CA, Feb. 2016*
7. **Yuyin Xi** et al., *"Electric Field Alignment of Poly(3-hexylthiophene) (P3HT) Organogels" Annual meeting of American Institute of Chemical Engineers (AIChE), Salt Lake City, UT, Nov. 2015*
8. **Yuyin Xi** et al., "Macroscopic growth of aligned poly(3-hexylthiophene) under electric field" 12th International Symposium on Functional π-Electron Systems (Fπ-12), *University of Washington, Seattle, USA, 2015*
9. **Yuyin Xi** et al., "Organic electrode materials for printable battery applications" *Graduate Student Symposium VII, University of Washington, Seattle WA, Sep. 2014*
10. **Yuyin Xi** *et al.*, "Response time study of hydrogen detection with Pt-gated AlGaN/GaN based diodes", *55th Electronic Materials Conference (EMC), South Bend, IN, June. 2013*

11. Chien-Fong Lo, **Yuyin Xi** *et al.*, "Effect of Temperature on CO detection Sensitivity in Air Ambient by Using ZnO Nanorod-Gated AlGaN/GaN High Electron Mobility Transistors", *55th Electronic Materials Conference (EMC), South Bend, IN, June. 2013*
12. L. Liu, C. F. Lo, **Y. Y. Xi** et al., "The effect of Proton Irradiation on the Reliability of InAlN/GaN High Electron Mobility Transistors", *55th Electronic Materials Conference (EMC), South Bend, IN, June. 2013*
13. L. Liu, C. F. Lo, **Y. Y. Xi** et al., "The Improvement of the Reliability of AlGaN/GaN High Mobility Transistors by Employing Different Buffer Structures", *55th Electronic Materials Conference (EMC), South Bend, IN, June. 2013*
14. **Yuyin Xi** *et al*., "Study of hydrogen detection response time at room temperature with Pt-gated diodes fabricated on AlGaN/GaN hetero-structure" *Ann Symp. Florida Chapter of the AVS Science and Technology Society (FLAVS), Orlando, Mar. 2013*
15. Chien-Fong Lo, **Yuyin Xi** *et al*., "Effect of temperature on CO sensing response in air ambient by using ZnO nanorod-gated AlGaN/GaN high electron mobility transistors" *Ann Symp. Florida Chapter of the AVS Science and Technology Society (FLAVS), Orlando, Mar. 2013*
16. Chien-Fong Lo, **Yuyin Xi** *et al*., "The effect of ambient temperature on CO sensing of ZnO nanorod-gated AlGaN/GaN high electron mobility transistor (HEMT) sensors" *NanoFlorida 2012, Tampa, Sep. 2012*
17. L. Liu, C. F. Lo, **Y. Y. Xi** *et al.*, "The effects of proton irradiation on the reliability of InAlN/GaN high electron mobility transistors", *Reliability of Compound Semiconductors Workshop (ROCS), Boston, MA, Apr.2012*
18. **Yuyin Xi** *et al*., "ZnO nanorod-gated AlGaN/GaN high electron mobility transistor based sensor for methane sensing" *Ann Symp. Florida Chapter of the AVS Science and Technology Society (FLAVS), Orlando, Mar. 2012*